

Optimalisatie van erosiebescherming voor monopile funderingen
en kwantificeren van golfoploop

Invloed van offshore windturbines op lokale stromingscondities

Optimisation of Scour Protection Design for Monopiles
and Quantification of Wave Run-Up

Engineering the Influence of an Offshore Wind Turbine on Local Flow Conditions

Leen De Vos

Promotoren: prof. dr. ir. J. De Rouck, prof. dr. ir. P. Troch
Proefschrift ingediend tot het behalen van de graad van
Doctor in de Ingenieurswetenschappen: Bouwkunde

Vakgroep Civiele Techniek
Voorzitter: prof. dr. ir. J. De Rouck
Faculteit Ingenieurswetenschappen
Academiejaar 2007 - 2008



ISBN 978-90-8578-218-6
NUR 956
Wettelijk depot: D/2008/10.500/37

Promotor

Prof. dr. ir. Julien De Rouck
Prof. dr. ir. P. Troch

Onderzoeksinstelling

Afdeling Weg- en Waterbouwkunde
Vakgroep Civiele Techniek
Faculteit Ingenieurswetenschappen
Universiteit Gent
Technologiepark 904
B-9052 Zwijnaarde

Tel: +32 9 264 65 89
Fax: +32 9 264 5837
Website: <http://awww.ugent.be>

Doctoraatsbeurs gefinancierd door

Het Fonds voor Wetenschappelijk Onderzoek (FWO) - Vlaanderen

Copyright © Leen De Vos

Alle rechten voorbehouden . Dit werk of delen ervan mogen onder geen enkele voorwaarde en ook niet voor persoonlijk gebruik worden uitgeleend, gekopieerd of op één of andere manier vermenigvuldigd worden zonder voorafgaande schriftelijke toestemming van de auteur of de promotoren.

words of thanks

As this work reaches the end, a couple of people deserve part of the credit. To them I want to say... THANK YOU!

My promoter Prof. dr. ir. Julien De Rouck, I would like to thank for the opportunity he gave me to work at his department, for the possibilities to go abroad and expand my knowledge, for his good advice and the pleasant working environment.

To my co-promoter Prof. dr. ir. Peter Troch I would like to say thanks for answering my (many) questions. His willingness to always make time for advice and suggestions made a huge difference.

Prof. dr. ir. Peter Frigaard I would like to thank for his hospitality and the terrific guidance during my stay at Aalborg University, for the time (both at and outside of work) which he made for me, notwithstanding his very busy life. His extensive knowledge and enthusiasm lie at the basis of this work.

My colleagues at work, I would like to thank for the five pleasant years: Amélie, Anny, Bart, Corneel, Dave, Dieter, Dogan, Ellen, Etienne, Hadewych, Hans, Jonas, Jimmy, Kurt, Lander, Lien, Ludo, Nathalie, Philippe, Pieter D.W., Pieter M., Stefaan, Tingqui, Willem and Wouter. A special thanks should go to the technical staff at our department, who proved to be indispensable during my experiments and for learning me what they know: thank you Herman, Herwin, Sam and Tom! Tom, your help with the PIV experiments and the user interface is much appreciated! A special thanks to my roommates at work as well, for the pleasant atmosphere and the help with little (or bigger) problems, chronologically: Cathy, Jan, Charlotte en Griet!

To my colleagues and friends at Aalborg University, who made my stay at Aalborg a never-to-be-forgotten experience: thank you Palle (roomy!), Brian and Lucia. Thank as well to Anja, Diego, Jens Peter, Jørgen, Kurt, Lars, Michael, Morten, Pernille, Thomas...

A word of thanks goes out to the students who performed a master thesis under my supervision. Their hard work provided input needed for my PhD: thank you Dries, Elke and Frederik, Jef and Tim.

Dr. James Sutherland and dr. Richard Whitehouse are gratefully acknowledged for their efforts in compiling the data set necessary for validating the study. To Erik Damgaard I would like to say thank you for inviting me at DHI and supervising my stay at the DHI main office.

The financial support of the Research Foundation – Flanders is gratefully acknowledged, as well as the logistic support of Hydraulic Research Laboratory.

For everybody from my volleyball club, the time we spent together created a nice diversion... Thanks for waiting for me when I was late ... Now you know why ☺

Mum and Dad, thanks for teaching me what is important in life. Your support throughout my studies and these last 5 years mean more to me than it sometimes appears. To Jan and Sarah, Joke and Gert, thanks for the time we always spend together.

To my daughter Marie-Lore, thank you for getting my spirit up every time I look at you after a hard days work. The hours we spend together are worth more than anything... you are our princess.

To my husband Pieter: no words can describe what you have done for me, but I will give it a go... thanks for listening to my thoughts, sitting with me during the evenings when I was running tests, reading the texts over and over again, improving the writing, supporting me while I was working late hours and just... being there for me.

Leen, June 2008

INDEX

Samenvatting – Summary

List of symbols

PART I: SCOUR AROUND MONOPILE FOUNDATIONS

Chapter 0: Introduction

0.1	Offshore wind	0-1
0.2	Objective and approach of the study	0-3
0.3	Thesis outline	0-4

Chapter 1: State of the art in scour research

1.0	Introduction	1-1
1.1	Sediment transport	1-1
1.1.1	Bed shear-stress and boundary layers	1-3
1.1.1.1	Steady uniform flow	1-5
1.1.1.2	Wave boundary layer and wave induced bed shear-stress .	1-7
1.1.1.3	Wave-current boundary layer interaction.....	1-10
1.1.2	Threshold of motion	1-12
1.1.3	Transport equations	1-16
1.2	Flow around a monopile foundation	1-17
1.2.1	Downflow in front of the pile.....	1-18
1.2.2	Horseshoe vortex.....	1-18
1.2.3	Lee-wake vortex shedding.....	1-23
1.2.4	Streamline contraction.....	1-28
1.3	Scour around a monopile foundation	1-30
1.3.1	General description of scour development	1-31
1.3.1.1	Local scour versus global scour	1-31
1.3.1.2	Equilibrium scour depth and time-scaling of scour	1-31
1.3.1.3	Clear-water scour versus live-bed scour	1-32
1.3.2	Scour depth around a vertical pile	1-33
1.3.2.1	Scour depth in steady current	1-33

1.3.2.2	Scour depth in waves.....	1-39
1.3.2.3	Scour depth in combined current and waves.....	1-40
1.3.2.4	Scour depth in cohesive soils.....	1-41
1.3.3	Extent of scour.....	1-42
1.4	Conclusions.....	1-43
	References.....	1-44

Chapter 2. Evaluation of the effect of scour on foundation design

2.0	Introduction.....	2-1
2.1	Loads on a vertical pile in a marine environment.....	2-2
2.1.1	Wave Loads.....	2-3
2.1.1.1	Non-breaking waves.....	2-3
2.1.1.2	Breaking waves.....	2-5
2.1.2	Current load.....	2-6
2.1.3	Wind load.....	2-7
2.1.4	Loads in the example cases.....	2-11
2.2	Bending moment.....	2-12
2.3	Soil mechanics.....	2-14
2.3.1	Lateral bearing capacity.....	2-14
2.3.2	Axial bearing capacity.....	2-18
2.4	Dynamic behaviour.....	2-19
2.4.1	Eigenfrequency.....	2-19
2.4.2	Fatigue.....	2-22
2.5	Free spanning of cables.....	2-23
2.6	Conclusions.....	2-24
	References.....	2-25

PART II: SCOUR PROTECTION AROUND MONOPILE FOUNDATIONS

Chapter 3: State of the art in scour protection design

3.0	Introduction.....	3-1
------------	--------------------------	------------

3.1	Basic principles of scour protection	3-1
3.1.1	Need for scour protection.....	3-2
3.1.2	Failure modes.....	3-4
3.2	Environmental and structural parameters	3-5
3.2.1	Environmental parameters	3-6
3.2.1.1	Water depth	3-6
3.2.1.2	Wave characteristics.....	3-6
3.2.1.3	Flow characteristics	3-17
3.2.1.4	Sediment characteristics	3-18
3.2.2	Structural parameters	3-20
3.2.2.1	Density	3-20
3.2.2.2	Individual stone size and weight.....	3-21
3.2.2.3	Stone grading	3-22
3.2.2.4	Stone shape	3-24
3.2.2.5	Settling velocity	3-24
3.3	Existing design criteria for scour protections around cylindrical monopiles	3-24
3.3.1	Required stone size.....	3-24
3.3.2	Radial extent and thickness of the scour protection	3-29
3.3.3	OPTI-PILE project	3-31
3.3.4	Existing offshore wind farms and their scour protection design	3-34
3.4	Physical modelling of scour protection	3-34
3.4.1	Laboratory or model effects.....	3-35
3.4.2	Scale effects.....	3-36
3.5	Conclusions	3-39
	References	3-40

Chapter 4. Experimental research on scour protection design around a monopile foundation

4.0.	Introduction	4-1
4.1.	Experimental set-up	4-1
4.1.1.	General description of set-up and model	4-1
4.1.2.	Hydraulic conditions	4-4
4.1.3.	Scour protection characteristics	4-5
4.1.4.	Bed profiling.....	4-7
4.1.5.	Model and scale effects.....	4-9
4.2.	Development of static stability criterion	4-11
4.2.1.	Test conditions	4-12
4.2.2.	Analysis	4-14
4.2.3.	Derivation of new prediction tool for statically stable scour protection around monopile foundations	4-15

4.2.3.1	Regular waves	4-15
4.2.3.2	Adjustment for irregular waves	4-22
4.2.4.	Comparison and validation of formula and results	4-24
4.3.	Including damage number in the stability criterion	4-27
4.3.1.	Accepting local damage	4-27
4.3.2.	Tests conditions	4-29
4.3.3.	Analysis	4-32
4.3.3.1.	Damage definition	4-33
4.3.3.2.	Repeatability	4-37
4.3.3.3.	Acceptable damage criterion	4-39
4.3.3.4.	Influence of governing variables	4-41
4.3.3.5.	Location of damage	4-59
4.3.4.	Derivation of new prediction tool for scour protections around monopile foundations	4-60
4.3.5.	Comparison and validation of formula and results	4-72
4.3.5.1.	Comparison with OPTI-PILE results	4-73
4.3.5.2.	Comparison of required stone size with different formulae	4-76
4.4.	Radial extent of a scour protection	4-77
4.4.1.	Disturbance of the flow: impact area	4-78
4.4.1.1.	Amplification	4-78
4.4.1.2.	PIV measurements	4-80
4.4.1.3.	Scour protection tests	4-84
4.4.2.	Edge scour	4-84
4.4.2.1.	Dimensions of edge scour	4-85
4.4.2.2.	Effect of edge scour on lateral bearing capacity	4-87
4.4.3.	Recommendations	4-93
4.5.	Conclusions	4-94
References	4-96

PART III: WAVE RUN-UP

Chapter 5. State of the art in wave run-up on monopiles

5.0	Introduction	5-1
5.1	Analytical models for wave run-up	5-2
5.1.1	Velocity stagnation head calculations	5-2
5.1.2	Diffraction theory	5-2
5.2	Previous experimental studies and semi-empirical run-up formulae	5-3
5.2.1	Wave run-up and forces on a cylinder in regular and random waves	5-3
5.2.2	Wave run-up on columns due to regular waves	5-5

5.2.3	Wave run-up of random waves on a small circular pier	5-5
References	5-7

Chapter 6. Experimental research on wave run-up on a monopile foundation

6.0	Introduction	6-1
6.1	Experimental set-up	6-1
6.1.1	Description of set-up and model	6-1
6.1.2	Wave conditions	6-4
6.1.3	Definition of run-up	6-5
6.2	Analysis of wave run-up experiments	6-5
6.2.1	Dimensionless quantities.....	6-5
6.2.2	Regular wave test results.....	6-5
6.2.3	Irregular wave experimental results	6-13
6.2.4	Variation of run-up around the pile.....	6-19
6.3	Evaluation of run-up formula	6-21
6.4	Conclusions	6-22
References	6-24

PART IV: PREDICTION TOOL

Chapter 7: Practical implementation of prediction tool

7.0	Introduction	7-1
7.1	Statically stable scour protection without stone movement .	7-1
7.2	Stable scour protection with prescribed damage level	7-6
7.3	Filter characteristics	7-10
7.4	Wave run-up	7-11
7.5	Practical use of prediction tool	7-12

Chapter 8 : Conclusions and recommendations

8.1	Conclusions	8-1
8.2	Recommendations	8-2

APPENDICES

Appendix I: Filter criteria

I.1.	Granular filter.....	1
I.1.1.	Geometrically closed filters.....	2
I.1.2.	Geometrically open filters	3
I.2.	Geotextile filters.....	5
	References	6

Appendix II: Installation of steady current circuit

II.1.	Pump circuit	1
II.2.	Vertical distribution of the current	3

Appendix III: Scour tests

III.1.	$u = 0.07$ m/s	1
III.2.	$u = 0.14$ m/s	1
III.3.	$u = 0.21$ m/s	2
III.4.	$u = 0.28$ m/s	4
	References	6

Appendix IV: Influence of steady current on wave characteristics

IV.1.	Change of wave length and wave height	1
IV.2.	Wave attenuation	2
IV.3.	Wave breaking and blocking.....	2

References 3

Appendix V: 3D EPro measurements

Appendix VI: Pictures of dynamic scour protection tests

Appendix VII: PIV experiments

VII.1. PIV equipment 1
VII.1.1. Seeding 1
VII.1.2. Camera 2
VII.1.3. Laser 2
VII.1.4. Synchronizer 2
VII.2. Set-up 3
VII.2.1. Wave gauges..... 4
VII.2.2. Structure and PIV equipment..... 6
VII.3. Image capturing 8
VII.4. Repeatability 8
VII.5. Data analysis 9
References13

Samenvatting

De voorraad fossiele energiebronnen is hoe dan ook eindig. Derhalve is zoeken naar hernieuwbare energiebronnen meer dan zinvol. Bovendien helpen ze om te voldoen aan de Kyoto norm en zo de opwarming van de aarde tegen te gaan. Windenergie is één van de groene energiebronnen die het verst staat in zijn ontwikkeling en kan een belangrijke bijdrage leveren tot een beter milieu. De uitbouw van de windenergie naar locaties op zee is een logische ontwikkeling. De eigenschappen van wind op zee t.o.v. wind over land zijn immers optimaler voor het opwekken van energie en bovendien zijn vele van de beste onshore locaties voor windenergie al bezet in een al volgebouwd Europa. Hoewel de mogelijkheden op zee groot zijn, zijn er bijkomende moeilijkheden bij het bouwen van windturbinefunderingen in zee, die ervoor zorgen dat windenergie op zee nog een stuk duurder uitvalt dan op land. Ook al is de zorg voor de omgeving een belangrijke drijfveer, voor degenen die met energieproductie bezig zijn gaat het vooral om opbrengst. Om van offshore energie een winstgevende industrie te maken - een noodzaak om een verdere uitbouw ervan te garanderen - moet elk onderdeel van het ontwerp geoptimaliseerd worden. Twee aspecten die hiertoe een bijdrage kunnen leveren worden behandeld in deze thesis: de noodzaak en het ontwerp van een erosiebescherming en de golfoploop tegen de paal.

Door de verstoring van de stroming die de paal teweegbrengt, ontstaat lokaal erosie aan de basis van de fundering. De erosiediepte kan oplopen tot ongeveer twee keer de paaldiameter en heeft ernstige gevolgen voor de stabiliteit en het dynamisch gedrag van de fundering. Enkele berekeningen tonen aan dat de invloed van de erosie op het ontwerp meer dan significant is. Bijna steeds wordt ervoor geadviseerd om een erosiebescherming aan te leggen en zo de stabiliteit van de fundering te garanderen. Een dergelijke erosiebescherming bestaat meestal uit breuksteen die geplaatst wordt rondom de fundering van de windturbine. Het doel van deze erosiebescherming is niet om erosie volledig te vermijden, maar wel om ze op een voldoende afstand van de fundering te houden. Hoewel reeds vele offshore windmolenparken gebouwd werden, bestaan er tot op heden weinig tot geen formules om de benodigde grootte van de stenen te bepalen in een omgeving waar een gecombineerde actie van golven en stroming de belasting uitmaakt. Voor het ontwerpen en plaatsen van de erosiebeschermingen rond bestaande windmolens worden steeds fysische modelproeven uitgevoerd om het vaak ruimschoots conservatieve ontwerp te toetsen. Ervaring is dus reeds voorhanden, maar wordt omwille van confidentialiteit vaak niet prijsgegeven.

In deze thesis werd vooral experimenteel werk verricht. Het doel was een ontwerpformule te ontwikkelen om de benodigde grootte van de deklaagstenen van een erosiebescherming rond een monopile fundering te bepalen onder een gecombineerde belasting van golven en stroming. Hierbij werd enerzijds uitgegaan van een conservatieve benadering, waarbij geen beweging van de stenen toegelaten wordt. Dit is de traditionele uitgangsmethode en een optimalisatie van de gebruikelijke ontwerpprocedure werd beoogd. Deze traditionele ontwerpprocedure maakt gebruik van de bodemschuifspanning, deze

is de kracht die per oppervlakte eenheid door de stroming op de bodem wordt uitgeoefend en is evenredig met de het kwadraat van de stroomsnelheid. Wanneer de bodemschuifspanning een zekere grenswaarde overschrijdt, wordt een korrel (of steen) meegenomen door de stroming. Wanneer de waarde van de bodemschuifspanning weer daalt, valt de korrel (of steen) terug op de bodem. De grenswaarde wordt de kritieke bodemschuifspanning genoemd en deze wordt bepaald door de eigenschappen van de steen (afmetingen en dichtheid). Door de verstoring die de paal veroorzaakt op de stroming (veroorzaakt door de permanente stroming en de golven), neemt de bodemschuifspanning lokaal sterk toe, zodat grotere stenen (met een grotere kritieke bodemschuifspanning) gebruikt dienen te worden. De lokale toename van de bodemschuifspanning rond de paal wordt gekwantificeerd door een amplificatiefactor, die toe te passen is op de onverstoorde bodemschuifspanning (die aanwezig is wanneer er geen paal in de stroming staat). De amplificatiefactor verschilt echter voor golven en stroming en het is onduidelijk welke waarde er best voor aan te nemen in een omgeving waar zowel golven en stroming samen voorkomen. In de experimentele opstelling werd onderzocht welke golfkarakteristieken begin van beweging veroorzaakten bij verschillende opgelegde stroomsnelheden. Hierbij werden voor de golven de golfhoogte en de golfperiode als de belangrijkste parameters aanschouwd. Voor de analyse werd gebruik gemaakt van de onverstoorde bodemschuifspanning en de kritieke bodemschuifspanning van de geteste stenen. Er werd een lineaire relatie gevonden tussen de kritieke bodemschuifspanning τ_{cr} en de bodemschuifspanning veroorzaakt door stroming τ_c en golven τ_w . De formule wordt dimensieloos gemaakt door gebruik te maken van de paaldiameter D , de relatieve dichtheid van de stenen Δ , de zwaartekrachtversnelling g en de dichtheid van het water ρ_w :

$$\frac{\tau_{cr}}{\rho_w \Delta g D} = 0.001 + 3.303 \frac{\tau_c}{\rho_w \Delta g D} + 1.015 \frac{\tau_w}{\rho_w \Delta g D} \quad (4.6)$$

Anderzijds werd uitgegaan van een meer economische benadering, waarbij kleinere steendiameters gebruikt worden en (beperkte) beweging toegelaten wordt van de stenen uit de toplaag. Proefreeksen met in totaal 5000 golven werden toegepast op 6 verschillende erosiebeschermingen. De volgende parameters werden gevarieerd: steendiameter, steendichtheid, gradatie, filter type, golfhoogte en golfperiode, stroomsnelheid, waterdiepte en stromingsrichting. De bodemprofielen werden voor elke test opgemeten met een contactvrije laser-profiler en de opmeting werd herhaald na 1000 golven, 3000 golven en 5000 golven. Een schadegetal werd gedefinieerd waarbij de erosiebescherming werd opgedeeld in subzones voor de analyse en schadedefinitie. Een duidelijke relatie werd gevonden tussen het opgemeten schadegetal en een visuele schadebeoordeling. De bodemschuifspanning bleek een minder goede parameter voor het inschatten van de grootte van de schade. Volgende formule werd afgeleid voor het bepalen van het schadegetal:

$$\frac{S_{3D}}{N^{b_0}} = a_0 \frac{U_m^3 T_{m-1,0}^2}{\sqrt{gd} (s-1)^{3/2} D_{n50}^2} + a_1 \left(a_2 + a_3 \frac{\left(\frac{U_c}{w_s}\right)^2 (U_c + a_4 U_m)^2 \sqrt{d}}{g D_{n50}^{3/2}} \right) \quad (4.30)$$

waarbij S_{3D} het schadegetal is, N het aantal golven, U_m de horizontale orbitaalsnelheid aan de bodem, veroorzaakt door de golven, $T_{m-1,0}$ de karakteristieke golfperiode, g de gravitaire versnelling, d de waterdiepte, s de relatieve steendichtheid, D_{n50} de nominale steendiameter, U_c de gemiddelde stroomsnelheid over de diepte en w_s de valsnelheid van de stenen. De parameters b_0 , a_0 , a_2 en a_3 werden door fitting bepaald en zijn respectievelijk gelijk aan 0.24300, 0.00076, -0.02200 en 0.00790. De parameters a_1 en a_4 hangen af van de verhouding van stroomsnelheid tot steendiameter en van de stromingsrichting en zijn bepaald als:

$$a_1 = 0 \quad \text{voor} \quad \frac{U_c}{\sqrt{g D_{n50}}} < 0.92 \quad \text{en voor golven die met de stroming mee lopen} \quad (4.28)$$

$$a_1 = 1 \quad \text{voor} \quad \frac{U_c}{\sqrt{g D_{n50}}} \geq 0.92 \quad \text{of voor golven die tegen de stroming in lopen}$$

$$a_4 = 1 \quad \text{voor golven die met de stroming mee lopen} \quad (4.29)$$

$$a_4 = \frac{Ur}{6.4} \quad \text{voor golven die tegen de stroming in lopen}$$

waarbij Ur het Ursell getal is ($= HL^2/d^3$).

Eén van de opvallendste resultaten is dat de schade groter is wanneer de golven tegen de stroming in lopen, waarbij de invloed blijkt af te hangen van de graad van niet-lineariteit van de golven. Een andere belangrijke conclusie is dat de stroomsnelheid slechts vanaf een bepaalde waarde invloed heeft op de ontwikkelde schade.

Voor gegeven stromings- en golfkarakteristieken, ontwikkelt de schade naar een vast schadegetal. Enkele proeven werden uitgevoerd om te zien of het gevormde profiel stabiel bleef wanneer er nog een verdere belasting op uitgeoefend wordt. Er ontwikkelde zich een erosiekuil wanneer een constante stroming met hoge snelheid werd toegepast op een sterk beschadigd profiel, waarbij een granulaire filter of geen filter was toegepast. Dit betekent dat er zich, bij de toegepaste diktes van de toplaag, geen stabiel profiel ontwikkelt wanneer de schade te groot wordt.

Slechts één paaldiameter werd getest, nl. $D = 0.1\text{m}$ op schaal 1/50. Zonder verdere proeven is het aangewezen de resultaten niet te ver buiten de beproefde range te gebruiken.

Bij het ontwerp van een erosiebescherming speelt ook de uitgestrektheid van de bescherming in het horizontale vlak een belangrijke rol bij het prijskaartje. Verder ontwikkelt zich aan de rand van de bescherming steeds randerosie, die de stabiliteit van de erosiebescherming in het gedrang kan brengen. Een berekening toont aan dat de randerosie slechts een beperkte invloed heeft op de laterale draagkracht van de fundering wanneer de diameter van de erosiebescherming groter is dan $5D$ en de randerosie in oppervlakte beperkt blijft. Om de stabiliteit van de erosiebescherming te garanderen wanneer de randerosie kuilen diep worden, dient extra materiaal toegevoegd te worden.

Een tweede aspect dat onderzocht werd in het kader van deze thesis is de golfoploop tegen de paal. Door de verstoring die de paal veroorzaakt op de golven, lopen golven hoog op tegen de paal. Deze hoge golfoploop veroorzaakte onverwachte schade aan het toegangsplatform van de Horns Rev windmolen funderingen. Experimenteel onderzoek werd uitgevoerd om de grootte van de golfoploop te kunnen inschatten voor verschillende golfcondities. Een formule werd afgeleid om de golfoploop te berekenen:

$$R_{u2\%} = \eta_{\max} + m \frac{u^2}{2g} \quad (6.3)$$

Waarbij $R_{u2\%}$ de golfoploop is die in 2% van de gevallen overschreden wordt, η_{\max} de maximale verheffing, berekend met een tweede orde theorie van Stokes en u de snelheid in de golftop, ook berekend met de tweede orde theorie van Stokes. Het blijkt dat het type fundering een invloed heeft op de golfoploop, waarbij opmerkelijk hogere golfoploop gevonden werd in het geval van een gravitaire fundering. De factor m bedraagt dan ook 2.71 in het geval van een monopile fundering en 4.45 in het geval van een conusvormige gravitaire fundering.

Summary

Renewable energy sources are being considered to meet the requirements of the Kyoto protocol thus helping to stop global warming. Wind energy is one of the most mature green energy sources and could possibly contribute significantly in attaining a better environment. The expansion of wind energy to offshore locations is a logical development. The characteristics of sea winds versus mainland winds are more optimal for energy generation. Moreover, the best onshore locations for wind energy parks are already occupied in the densely populated Europe. Even though the possibilities at sea are considerable, the added difficulty of building offshore wind turbine foundations result in offshore wind energy remaining more costly than its onshore equivalent. Notwithstanding the fact that care for the environment is an important motive, cost efficiency remains even more important in energy production. In order to transform offshore energy into a profitable industry – a necessity to guarantee its further expansion – every part of the design of wind turbines must be optimized. Two aspects that can contribute to this are treated in this thesis: the importance and design of an erosion protection and the pile wave run-up.

The disruption of the current caused by the presence of the pile induces local scour at the foundation's base. The scour depth can amount to two times the pile diameter, seriously affecting the stability and dynamical behaviour of the foundation. Some calculations show that scour significantly affects the design. Virtually in every case a scour protection is opted for to guarantee the foundation's stability. Such scour protections usually consist of rip-rap material placed around the wind turbines' foundation. The goal of the scour protection is not to avoid scour completely yet to shun scour from within a certain perimeter around the foundation. Even though multiple offshore wind farms were already built little to no formulae are available at present to calculate the required stone size in a combined wave and current climate. While designing and constructing the scour protections of existing wind farms, physical model tests were always performed in order to assess the often overly conservative design. So experience already exists on the subject but remains confidential.

This thesis mainly concerns experimental work. The goal was to develop a design formula to determine the required stone size of a scour protection around a monopile foundation for combined wave and current loadings. Two approaches were considered. First, the conservative method, whereby no stone movement is allowed. This is the traditional method, but an optimization of the usual design procedure was targeted. The design method uses the bed shear stress, which represents the force per area exerted on the bed by the waves and current and is proportional to the square of the flow velocity. When the bed shear stress exceeds a certain boundary value, a grain or rock can be trailed by the current. When the bed shear stress value diminishes, the grain or rock resettles on the bottom. The boundary value is called the critical bed shear stress and is defined by the stone properties (dimensions and density). The local increase in bed shear stress caused by the pile's disruption of the flow is quantified by an amplification factor which is applied to the bed shear stress that is present when

no pile were installed (undisturbed bed shear stress). The amplification factor differs for waves and currents and it is unclear which value should be used in a combined wave-current climate. During the experiments it was observed what set of wave characteristics were connected to initiation of motion for different current velocities. Here, wave height and wave period were considered the most important wave characteristics.

A linear relationship was found between the critical bed shear stress τ_{cr} and the bed shear stress caused by current τ_c and waves τ_w , respectively. The formula was made dimensionless using the pile diameter D , the stones' relative density Δ , the gravitational acceleration g and the density of the water ρ_w :

$$\frac{\tau_{cr}}{\rho_w \Delta g D} = 0.001 + 3.303 \frac{\tau_c}{\rho_w \Delta g D} + 1.015 \frac{\tau_w}{\rho_w \Delta g D} \quad (4.6)$$

τ_{cr} in this equation represents the required critical bed shear stress for the $D_{67.5}$ of the scour protection armour layer.

A second method that was followed uses a more economical approach, in which smaller stone diameters are used and limited stone motion is allowed for top layer stones. Test series of 5000 waves in total were performed for 6 different scour protections. The following parameters were varied during the tests: stone diameter, stone density, stone grading, type of filter, wave height, wave period, current velocity, water depth and direction of the current. The bed profiles were registered before each test and consecutive measurements of the profile were made after 1000, 3000 and 5000 waves. A damage number was defined in which the scour protections' surface was divided into sub areas for analysis and damage definition. A clear relationship was found between the measured damaged number and a visual damage assessment. Bed shear stress was found to be a moderate estimator for the damage's magnitude. The following formula was derived to determine the damage number:

$$\frac{S_{3D}}{N^{b_0}} = a_0 \frac{U_m^3 T_{m-1,0}^2}{\sqrt{gd} (s-1)^{3/2} D_{n50}^2} + a_1 \left(a_2 + a_3 \frac{\left(\frac{U_c}{w_s} \right)^2 (U_c + a_4 U_m)^2 \sqrt{d}}{g D_{n50}^{3/2}} \right) \quad (4.30)$$

in which S_{3D} is the damage number, N the number of waves, U_m the horizontal orbital velocity at the bottom, caused by waves, $T_{m-1,0}$ the characteristic wave period, g the gravitational acceleration, d the water depth, s the relative stone density, D_{n50} the nominal stone diameter, U_c the current velocity averaged over the water depth and w_s the fall velocity.

The parameters b_0 , a_0 , a_2 and a_3 were determined through fitting and are equal to 0.24300, 0.00076, -0.02200 en 0.00790 respectively. The parameters a_1 en

a_4 depend on both the current velocity/stone diameter ratio and the current direction and are determined as:

$$a_1 = 0 \quad \text{for } \frac{U_c}{\sqrt{gD_{n50}}} < 0.92 \text{ and waves following current} \quad (4.28)$$

$$a_1 = 1 \quad \text{for } \frac{U_c}{\sqrt{gD_{n50}}} \geq 0.92 \text{ or waves opposing current}$$

$$a_4 = 1 \quad \text{for waves following current} \quad (4.29)$$

$$a_4 = \frac{Ur}{6.4} \quad \text{for waves opposing current}$$

with Ur the Ursell number = HL^2/d^3 .

One of the most striking results is that the damage is larger when waves oppose the current, a phenomenon where the magnitude of this influence depends on the non-linearity of the waves. Another important conclusion is that the current velocity only influences the damage development when it exceeds a certain value.

Scour protection damage is shown to evolve to a fixed level for a given set of wave characteristics and current. Some tests were performed to assess the stability of the profile that was formed when further subjecting it to wave and current loading. It was found that a scour hole develops when a constant high velocity current was applied to a highly damaged profile while using either a granular filter or no filter layer. This indicates that no stable profile develops in case of excessive damage for the tested top layer thicknesses.

Only one pile diameter was tested, i.e. $D = 0.1\text{m}$ on 1/50 scale. In absence of further testing it is advised no to use the presented results when operating far outside the tested range.

In designing scour protections the horizontal extent of the protection highly influences the eventual cost. Moreover, in any case, edge scour develops at the rim of the scour protection. Calculations show that the edge scour's influence on the lateral bearing capacity are limited when the scour protection's diameter exceeds $5D$. In order to guarantee the scour protection's stability when edge scour holes develop, extra material needs to be added.

A second aspect in optimizing wind turbines' design which was investigated in light of this thesis is wave run-up on the pile. Due to the disruption of the waves by the pile, waves tend to run up highly onto the pile. High run-up was the cause of unexpected damage of the entrance platforms of the Horns Rev wind turbines. Experimental research was performed to estimate the magnitude of wave run-up under different wave conditions. The following formula was derived to calculate the wave run-up:

$$R_{u2\%} = \eta_{\max} + m \frac{u^2}{2g} \quad (6.3)$$

in which $R_{u2\%}$ is the wave run-up which is exceeded by 2% of the waves, η_{max} is the maximum elevation, calculated with a second order theory of Stokes, and u is the velocity in the wave crest, calculated likewise. It was found that the foundation type influences wave run-up, whereby a significantly higher run-up was found in case of a gravitational foundation. The factor m equals 2.71 in the case of a monopile foundation and 4.45 in case of a cone shaped gravitational foundation.

List of symbols

A	=	Amplitude of the horizontal component of the orbital motion of the water particles	[m]
A'	=	Horizontally projected area of a grain particle	[m ²]
A_{disk}	=	Area taken up by the rotor disk	[m ²]
A_{pile}	=	Surface of the pile subject to wind loading	[m ²]
A_s	=	Area of the pile shaft	[m ²]
A_t	=	Area of the pile tip	[m ²]
A_0	=	Dimensionless parameter describing the ratio of the distance which the water particles move during one quarter cycle of the oscillation to the cylinder diameter	[-]
a	=	Wave amplitude	[m]
a	=	Cylinder radius	[m]
b	=	Induction factor	[-]
C	=	Clay content of the soil	[-]
C	=	Chézy coefficient	m ^{1/2} /s
C	=	Wave celerity = L/T_w	[m/s]
C_D	=	Drag coefficient	[-]
$C_{D,b}$	=	Drag coefficient of a turbine blade	[-]
$C_{D,w,pile}$	=	Drag coefficient of a pile for air flow	[-]
$C_{L,b}$	=	Lift coefficient of a turbine blade	[-]
C_M	=	Inertia coefficient	[-]
C_P	=	Power coefficient	[-]
C_S	=	Slamming coefficient	[-]
C_s	=	Stability coefficient	[-]
C_v	=	Velocity distribution coefficient	[-]
C_0	=	Coefficient	[-]
c_a	=	Aerofoil chord length	[m]
D	=	Pile diameter	[m]
D_{av}	=	Average pile diameter = $D - t_w$	[m]
D_i	=	Inner pile diameter	[m]
D_o	=	Outer pile diameter	[m]
D_s	=	Representative value of the stone size	[m]

D_{s30}	=	Stone size of an equivalent sphere of which 30% of the stones is finer by weight	[m]
D_{50}	=	Median stone size for the scour protection	[m]
D_*	=	Dimensionless grain size	[-]
d	=	Water depth	[m]
d_{Base}	=	Representative diameter for the base material	[m]
d_{bx}	=	Particle size of the filter for which x% by weight of the base material is smaller	[m]
d_{cr}	=	Critical grain diameter	[m]
d_{Filter}	=	Representative diameter for filter material	[m]
d_{fx}	=	Particle size of the filter for which x% by weight of the filter material is smaller	[m]
d_s	=	Sediment grain diameter	[m]
d_{50}	=	Median sediment grain diameter	[m]
E	=	Modulus of elasticity	[N/m ²]
E_{py}	=	Soil modulus	[N/m ²]
Fr	=	Froude number	[-]
F_D	=	Drag force	[N]
$F_{D,b}$	=	Drag force on a wind turbine's blade	[N]
$F_{D,w,pile}$	=	Drag force on a pile, caused by wind	[N]
F_I	=	Impact force	[N]
F_L	=	Lift force	[N]
$F_{L,b}$	=	Lift force on a wind turbine's blade	[N]
F_M	=	Inertia force	[N]
F_{Mor}	=	Total non breaking wave load on a vertical pile	[N]
F_S	=	Frictional force between grains due to contact	[N]
F_s	=	Safety factor	[-]
F_{tot}	=	Total force on an offshore wind turbine	[N]
F_{wind}	=	Force caused by the wind on a wind turbine	[N]
$F_{wind,b}$	=	Force caused by the wind on the rotor blades	[N]
$F_{wind,stop}$	=	Axial force caused by the wind on the rotor blades during an emergency stop	[N]
f	=	Unit skin friction of soil	[N/m ²]
f	=	Wave frequency	[1/s]

f_c	=	Current friction coefficient	[-]
f_D	=	Drag force per unit length	[N/m]
f_M	=	Inertia force per unit length	[N/m]
f_{Mor}	=	Total non-breaking wave load per unit length at a certain height on the pile	[N/m]
f_v	=	Vortex-shedding frequency	[1/s]
f_w	=	Wave friction factor	[-]
f_{1nat}	=	First eigenfrequency of a structure	[1/s]
g	=	Acceleration due to gravity = 9.81 m/s ²	[m/s ²]
h	=	Height of wave flume	[m]
H	=	Wave height	[m]
H_b	=	Breaking wave height	[m]
H_m	=	Mean wave height	[m]
H_{m0}	=	Significant wave height, based on the spectral density	[m]
H_{max}	=	Maximum wave height	[m]
H_r	=	Ripple height	[m]
H_{rms}	=	Root-mean-square wave height	[m]
H_s	=	Significant wave height = average of 1/3rd highest waves	[m]
$H_{s,d}$	=	Significant design wave height	[m]
H_u	=	Ultimate horizontal load for a monopile foundation	[N]
H_0	=	Deep water wave height	[m]
$H_{2\%}$	=	Wave height exceeded by 2% of the waves	[m]
I	=	Moment of inertia	[m ⁴]
KC	=	Keulegan Carpenter number	[-]
K_1	=	Sideslope correction factor	[-]
K_S	=	Slope correction factor	[-]
K_T	=	Turbulence correction factor	[-]
K_Y	=	Depth correction factor	[-]
K_σ	=	correction factor depending on grain size distribution	[-]
k	=	Wave number	[-]
k_s	=	$2.5 d_{50}$ or $(0.5 - 1) H_r$; bottom roughness	[m]
L	=	Wave length, calculated as $L = \frac{gT^2}{2\pi} \tanh\left(\frac{2\pi d}{L}\right)$	[m]
L_b	=	Rotor blade length	[m]

L_p	=	Length of pile above the bottom	[m]
L_s	=	Length of scour protection, defined as the distance between edge of pile and edge of scour protection	[m]
L_0	=	Deep water wave length	[m]
l	=	Length of wave flume	[m]
M_{Mor}	=	Moment on a pile near the bed, calculated with Morison equation	[Nm]
M_{tot}	=	Total maximum moment at the bed	[Nm]
M'_{tot}	=	Increased moment at the bed due to scour	[Nm]
M_u	=	Ultimate moment at the bed for a monopile foundation	[N]
m	=	Weight of stones	[kg]
m	=	Coefficient	[-]
m_{top}	=	Turbine mass on top of the pile	[kg]
N	=	Number of cycles to failure	[-]
N_b	=	Number of rotor blades	[-]
n_f	=	Porosity of filter material	[-]
$O_{\%}$	=	characteristic opening for geotextile filter for which % of the pores are smaller	[m]
P	=	Power output of a wind turbine	[W]
p_{ult}	=	Ultimate soil resistance	[N/m]
Q_d	=	Design axial load carrying capacity of a pile foundation	[N]
Q_s	=	Shaft friction capacity of a pile foundation	[N]
Q_t	=	End-bearing capacity of a pile foundation	[N]
Q_u	=	Ultimate axial load carrying capacity of a pile foundation	[N]
q	=	Flow discharge per unit width	[m ² /s]
q_b	=	Volumetric transport rate	[m ² /s]
q_t	=	Unit tip bearing capacity	[N/m ²]
R	=	Hydraulic radius of a channel	[m]
Re	=	Reynolds number	[-]
Re_A	=	Wave amplitude Reynolds number	[-]
Re_D	=	$\frac{U \cdot D}{\nu}$ = Pile Reynolds number	[-]
Re_*	=	Grain Reynolds number	[-]
R_u	=	Run-up on up-wave side of structure	[m]
R_{us}	=	Significant run-up height on the up-wave side of structure	[m]

$R_{u\max}$	=	Maximum run-up height on the up-wave side of structure	[m]
$R_{u2\%}$	=	2% excess run-up height on the up-wave side of structure	[m]
$\overline{R}_{u2\%}$	=	average of run-up values higher than the 2% excess run-up height;	[m]
r_I	=	Moment arm for impact force of breaking wave	[m]
r_{Mor}	=	Moment arm for the non breaking wave load	[m]
r_{tot}	=	Total moment arm	[m]
r_{wind}	=	Moment arm for the wind load	[m]
r_0	=	Relative turbulence intensity at edge of scour protection	[-]
S	=	Scour depth	[m]
S	=	Stress	[N/m ²]
S_c	=	Equilibrium scour depth in a current alone case	[m]
S_e	=	Equilibrium scour depth	[m]
S_{edge}	=	Edge scour depth	[m]
S_f	=	Safety factor	[-]
$S(f)$	=	Spectral density	[m ² /s]
St	=	Strouhal number	[-]
$Stab$	=	Stability parameter, defined in the OPTI-PILE project as $\theta_{\max} / \theta_{cr}$	[-]
s	=	Relative density of the stone, ratio of the densities of sediment and water ρ_s / ρ_w	[-]
s	=	Wave steepness H/L	[-]
s_0	=	Deep water wave steepness H_0/L_0	[-]
T	=	Time scale of the scour process, representing the time period during which substantial scour develops	[s]
T_p	=	Peak period in irregular waves	[s]
T_r	=	Return period	[years]
T_w	=	Wave period	[s]
$T_{w,r}$	=	Wave period with regards to a moving reference frame	[s]
T_z	=	Mean zero crossing wave period	[s]
T_0	=	Duration of a wave measurement	[s]
TI	=	Parameter characterising the turbulence intensity	[-]
t	=	Time	[s]
t_e	=	Time for a scour hole to develop until its equilibrium	[days]

t_s	=	Thickness of armour layer	[m]
t_w	=	Wall thickness of a pile	[m]
t_0	=	Pile penetration depth	[m]
U	=	Velocity	[m/s]
Ur	=	Ursell number = HL^2/d^3	[-]
U_b	=	The current velocity at a height of 0.1d above the bottom	[m/s]
U_c	=	Steady current velocity	[m/s]
U_{cr}	=	Critical current velocity	[m/s]
$U_{c,S}$	=	Decreased flow velocity to account for Scour depth	[m/s]
U_{cw}	=	Velocity ratio $U_c/U_c + U_w$	[-]
U_{lp}	=	velocity at which the live-bed peak scour depth occurs	[m/s]
U_m	=	Maximum value of the horizontal orbital velocity	[m/s]
U_w	=	Horizontal orbital wave velocity	[m/s]
$U_{10\%}$	=	Orbital velocity amplitude, exceeded by 10% of the waves	[m/s]
u	=	Horizontal component of wave velocity	[m/s]
u_f	=	Velocity at the interface armour layer – filter layer	[m/s]
$u_{f,cr}$	=	Critical velocity	[m/s]
u_t	=	Flow velocity in the top layer of a scour protection	[m/s]
u_*	=	Friction or shear velocity	[m/s]
u_{*cr}	=	Critical shear velocity, corresponding with the threshold of motion	[m/s]
\dot{u}	=	Horizontal particle acceleration due to wave action	[m/s ²]
V_{disk}	=	Wind velocity near the rotor	[m/s]
V_{eS}	=	Volume of soil per unit width, lost by edge scour	[m ³ /m]
V_r	=	Ratio of the steady flow velocity to the maximum value of the horizontal orbital velocity	[-]
V_{rel}	=	Relative wind speed over a rotor blade	[m/s]
V_{rot}	=	Rotation velocity of a wind turbine's rotor	[m/s]
V_w	=	Average wind speed	[m/s]
$V_{w,ext1h}$	=	Extreme hourly wind speed	[m/s]
$V_{w,ext10min}$	=	Extreme 10-minute wind speed	[m/s]
$V_{w,r}$	=	Average wind speed at a height z_r above the sea level	[m/s]

V_0	=	Undisturbed incoming wind velocity	[m/s]
Vol_s	=	Unit volume, occupied by the grains/stones	[m ³]
W	=	Submerged weight of a grain particle	[N]
W	=	Width of scour hole	[m]
W	=	Section modulus of a section	[m ³]
W_p	=	Width of scour hole, perpendicular to current direction	[m]
w	=	Width of wave flume	[m]
w_s	=	Settling or fall velocity	[m/s]
x_s	=	Distance from the pile axis to the separation point at the bed in front of the pile; characteristic length, representing the size of the horseshoe vortex in streamwise direction	[m]
z	=	Distance in the vertical direction, $z = 0$ at the water level	[m]
z_r	=	Reference height above the sea level	[m]
z_0	=	Roughness length	[m]
α	=	Amplification factor of the bed shear-stress	[-]
α	=	Angle of attack of a rotor blade	[°]
α_{down}	=	Downstream angle of scour hole	[°]
α_U	=	Amplification factor of the flow velocity	[-]
α_{up}	=	Upstream angle of scour hole	[°]
β	=	Angle of a sloping bed	[°]
β_m	=	Coefficient	[-]
β_1, β_2	=	upstream and downstream angle of edge scour hole	[°]
γ	=	Density of the soil	[N/m ³]
γ	=	Coefficient	[-]
Δ	=	Relative density of sediment = $(\rho_s - \rho_w) / \rho_w$	[-]
$\Delta_b, \Delta_f, \Delta_t$	=	Relative density of base, filter and top layer material	[-]
Δr	=	Length of a rotor blade element	[m]
δ	=	Boundary layer thickness	[m]
δ_a	=	Horizontal part of active soil pressure coefficient	[-]
δ_p, δ'_p	=	Horizontal part of passive soil pressure coefficient	[-]
ε	=	Angle which the soil makes with the horizontal	[°]
η	=	Water surface elevation	[m]
η_b	=	Distance between wave crest and SWL	[m]
η_{max}	=	Maximum water surface elevation	[m]
θ	=	Shields parameter	[-]

θ_{cr}	=	Critical value of the Shields parameter, corresponding with the initiation of motion at the bed	[-]
$\theta_{cr,b}$	=	Critical Shields parameter for the base material	[-]
θ_{max}	=	Maximum Shields parameter for combined wave and current situation	[-]
κ	=	Von Karman constant	[-]
κ_g	=	Permeability of a geotextile filter	[m/s]
κ_s	=	Permeability of the soil	[m/s]
λ	=	Curling factor	[-]
λ	=	Ratio of blade tip speed to wind speed	[-]
λ_a	=	Active soil pressure coefficient	[-]
λ_n	=	Neutral soil pressure coefficient	[-]
λ_p	=	Passive soil pressure coefficient	[-]
μ	=	Pile mass per meter	[kg/m ³]
μ	=	Stability correction factor	[-]
ν	=	Kinematic viscosity of water	[m ² /s]
ρ_a	=	Density of air	[kg/m ³]
ρ_w	=	Density of water	[kg/m ³]
ρ_s	=	Sediment density	[kg/m ³]
ρ_{steel}	=	Density of steel	[kg/m ³]
σ	=	Standard deviation	[-]
σ	=	Angular frequency in a moving reference frame	[Hz]
σ_v	=	Tensile strength of a material	[N/m ²]
τ_b	=	Bed shear-stress	[N/m ²]
τ_b'	=	Effective bed shear-stress, originating from skin friction	[N/m ²]
τ_b''	=	bed shear-stress, originating from larger bed forms	[N/m ²]
$\tau_{b,c}$	=	Bed shear-stress induced by a steady current	[N/m ²]
$\tau_{b,w}$	=	Bed shear-stress induced by waves	[N/m ²]
$\tau_{b,wc}$	=	Bed shear-stress induced by combined waves and current	[N/m ²]
$\tau_{b,\infty}$	=	Undisturbed bed shear-stress	[N/m ²]
τ_{cr}	=	Critical bed shear-stress, corresponding with the threshold of motion	[N/m ²]
$\tau_{\beta,cr}$	=	Critical bed shear-stress on a slope	[N/m ²]
τ_{∞}	=	Undisturbed bed shear-stress	[N/m ²]

Φ	=	dimensionless bedload transport rate	[-]
ϕ	=	Angle of repose of sediment	[°]
ϕ	=	Angle between wave and current direction	[°]
ψ	=	Angle which the flow makes with the upslope direction	[°]
ψ	=	Angle under which the soil pressure acts on the structure	[°]
ω	=	Angular frequency of a wave = $2\pi/T_w$	[1/s]
ω	=	relative depth below the bed of the rotation point of a monopile in an ultimate limit state calculation	[-]

Chapter 0: Introduction

0.1 Offshore wind

To control the climate change the Kyoto protocol has as an objective to reduce the emission of greenhouse gasses. Two vital steps towards meeting the Kyoto protocol are the reduction of energy consumption and the production of “clean” energy. Within the so-called renewable energy sector, wind energy has already reached a mature stadium and has therefore become the mainstream source of renewable energy in Europe. In the last decade, the extension of wind energy production to offshore locations has significantly increased the capacity of wind power production in Europe. Offshore wind energy production has several advantages compared to onshore production: a higher performance due to a more continuous, uniform and higher wind speed, a vast amount of space and a limited visual pollution when building farshore.

Several offshore projects are currently operational. Other than a few tryout offshore piles, most offshore wind turbines are located in Europe: the early projects were of relatively small scale and placed in shallow or sheltered waters. Together with growing wind turbine capacity, an increase in size of the offshore projects took place. The largest operational project so far is Nysted Offshore wind farm in Denmark. Figure 0-1 shows the location of the currently operational wind farms in Europe, while Table 0-1 lists their specifics in a chronological order.

Table 0-1 shows that both output (and thus size) of the turbines and the applied pile diameter increase over time.



Figure 0-1: Location of operational offshore wind turbine parks in Europe

Table 0-1: Specifics of operational offshore wind parks in Europe

Location	Online	Distance to shore	Foundation type	Number of turbines	Turbine type	Water depth	Pile diameter (monopile)
	[year]	[km]	[-]	[-]	[MW]	[m]	[m]
Vindeby (Denmark)	1991	1.5 – 3	Gravity based	11	0.45	2.5 - 5	-
Lely (Netherlands)	1994	0.8	Monopile	2	0.5	4 - 5	3.2 – 3.7
Tunø Knob (Denmark)	1995	6	Gravity based	10	0.5	3 - 5	-
Dronten (Netherlands)	1996	0.03	Monopile	28	0.6	1 - 2	?
Bockstigen (Sweden)	1998	4	Monopile	5	0.55	5.5 -6.5	2.25
Blyth Offshore (UK)	2000	0.8	Monopile	2	2	6 - 11	3.5
Utgrunden (Sweden)	2000	12	Monopile	7	1.5	7 - 10	3
Middelgrunden (Denmark)	2001	2 – 3	Gravity based	20	2	5-10	-
Yttre Stengrund (Sweden)	2001	5	Monopile	5	2	8	3 - 3.5
Horns Rev (Denmark)	2002	14-20	Monopile	80	2	6 - 14	4
Frederikshaven (Denmark)	2003	0.2	1 bucket foundation, 3 monopiles	4	2.3 – 3	4	?
Samsø (Denmark)	2003	3.5	Monopile	10	2.3	11 - 18	4.2
North Hoyle (UK)	2003	7 – 8	Monopile	30	2	12 - 20	4
Nysted (Denmark)	2004	9	Gravity based	72	2.3	6 - 10	-
Arklow Bank (Ireland)	2004	7 - 12	Monopile	7	3.6	5	5.1
Scroby Sands (UK)	2004	2.3	Monopile	30	2	21 (max)	4.2
Ems-Emden (Germany)	2004	0.03	Like land based	1	4.5	2 (max)	-
Kentish flats (UK)	2005	8 - 10	Monopile	30	3	5	4
Breitling (Germany)	2006	0.5	Like land based	1	2.5	2	-
Barrow (UK)	2006	7	Monopile	30	3	15-20	4.75
Beatrice (Moray Firth) (Scotland)	2007	25	Lattice towers	2	5	45	-
Egmond aan zee (Netherlands)	2007	10	Monopile	36	3	19-22	4.6
Burbo (UK)	2007	6.4	Monopile	25	3.6	1-8	4.7
Lillgrund (Sweden)	2007	7	Gravity based	48	2.3	4-8	-
Q7 (Netherlands)	2008	23	Monopile	60	2	20-24	4

Several offshore parks are still under construction or in planning phase, among which the Thorntonbank in front of the Belgian coast. The planned projects' total capacity exceeds 30 GW. Figure 0-2 shows a picture of the largest operational wind farm so far: the Nysted Offshore wind park.



Figure 0-2: View of the largest operational wind farm: wind park Nysted Offshore; © Siemens press picture

0.2 Objective and approach of the study

Together with new opportunities, offshore wind farms raise new engineering challenges. Due to the additional difficulties, offshore wind energy production costs still significantly exceed those of onshore wind production. When an expansion of the offshore production is aspired, the cost of offshore wind energy production needs to be reduced. This can be achieved by identifying and optimizing the critical design parameters. Two topics specifically related to the offshore placement of wind turbine foundations are tackled in this thesis, both related to the disturbance of the flow due to the pile's presence.

The first topic relates to the erosion of bottom material around the foundation of the wind turbines, caused by the local increase of the wave and current induced flow velocities by the pile's presence. When a scour hole is allowed to develop, this has a considerable impact on the stability and dynamic behaviour of the wind turbine. When significant scour is expected, usually a scour protection is placed to avoid erosion of the soil close to the foundation thus guaranteeing stability and acceptable dynamic behaviour of the monopile. Although much experience exists on scour protection around bridge piers (which are placed in a current alone situation), at present, little design guidelines exist for the specific case of a scour protection around a monopile foundation subjected to a combined wave and current loading. The objective of this thesis is to find a relationship between loading conditions and damage development for a scour protection existing of loose rocks, thus leading to an optimization of the scour protection design for monopile foundations. Due to the difficult physical

processes involved in flow disturbance and displacement of bed protection material at the base of a foundation, mainly small scale experimental research was used to achieve this goal. Only monopile foundations were considered in this part of the study. As can be concluded from Table 0-1, monopile foundations cover 80% of the currently installed offshore power production.

The second topic is related to the wave run-up on the wind turbines support structure. Due to the obstruction caused by the pile, waves that hit the pile cause water run-up levels which can rise significantly above the wave crest elevation. High wave run-up levels in turn lead to additional loading on access constructions such as access platform, door and ladder... Unexpectedly high run-up levels on some of the existing wind turbines led to high damage of these components. The first step in estimating the loading which is exerted on these parts is knowing the correct run-up level which can be expected. Again, a physical scale model study was performed to investigate the run-up levels and the distribution of the run-up around the pile under different wave conditions. For this part of the study, both a monopile foundation and a cone shaped gravity based foundation were investigated.

0.3 Thesis outline

This thesis is structured in the logical order of cause and event. The first Part gives an overview of the processes related to scour around monopile foundations. Chapter 1 discusses the general considerations on sediment transport and the influence of a vertical, cylindrical pile on the flow, as these lie at the basis of the scour development. At the end of this chapter, an overview is given of the empirical relations to determine the expected scour depth and extent. In chapter 2, the influence of the developed scour hole on the monopile foundation design is considered. The topics which are covered in this chapter are the increase of the moment near the sea bottom, the decrease in lateral bearing capacity, the change in dynamic behaviour and the free spanning of the cables.

Part II deals with the scour protection design. In chapter 3, the general principles of a scour protection design are discussed, together with the parameters which have an influence on the scour protection design. The existing design methods for scour protections and the problems encountered when using small scale modelling are treated at the end of this chapter. In chapter 4, scale model tests on the scour protection around a monopile foundation are described, together with the analysis and resulting design formulae. The chapter finishes with the discussion of the required radial extent of a scour protection, based on existing knowledge and calculations of the influence of edge effects on the pile's bearing capacity.

Part III deals with the wave run-up problem. In chapter 5, the state of the art on run-up is discussed, whereas the experiments and their results are discussed in chapter 6.

In part IV, the resulting design equations are repeated and implemented in a new software tool in chapter 7, which also includes the practical use of the software tool.

Chapter 8 summarizes the conclusions and ends with recommendations for further research on scour protection design.

PART I. SCOUR AROUND MONOPILE FOUNDATIONS

Chapter 1: State of the art in scour research

1.0 Introduction

Any structure, placed within a marine environment, has an influence on the local flow conditions. This change in flow pattern both increases the local sediment transport capacity, leading to scour and determines the scour protection design. Therefore, a summary of the existing research on flow patterns around a vertical cylinder is indispensable in this thesis.

Furthermore this chapter gives a summary of the research performed on scour around a single, slender vertical pile in a steady current, in a wave field and in a combined wave and current situation.

Any chapter describing a scour process should address the basics of sediment transport. The first part of this chapter is thus written to that effect. The treatment of the inception of motion will also prove to be valuable for the scour protection design (Chapter 3).

1.1 Sediment transport

Sediment transport lies at the basis of scour around structures placed in a marine environment. In such an environment, sediment can be moved by a current (tidal, wind or wave driven), waves or a combination of both. Many authors address the processes determining the behaviour of non-cohesive sediment in combined current-wave conditions, including Fredsøe and Deigaard (1992), Nielsen (1992), van Rijn (1993), Soulsby (1997), Liu (2001), among others.

The sediment transport is caused by the basic processes of entrainment, transportation and deposition (Figure 1-1, Soulsby (1997)). These three basic processes take place at the same time.

Entrainment results from the friction which is exerted on the sea bed by the current and/or waves, with the possibility of grains going into suspension due to turbulent diffusion. In section 1.1.1, the friction exerted on the sea bottom, caused by current and/or waves is described, followed by a description of the initiation of motion of sediment.

Transport takes place by bedload transport (rolling, hopping and sliding) and by suspended transport. The former playing a dominant role for slow flows and/or large grains, while the latter is dominant for larger flow velocities and/or sufficiently small grains. The suspended transport can be much higher than the bedload transport.

Deposition takes place when a grain comes to rest in the bedload transport or settles down from suspension.

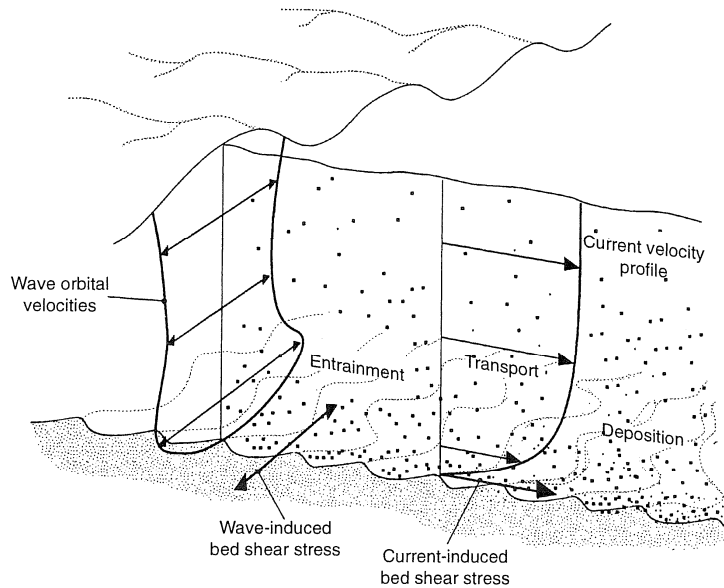


Figure 1-1: Sketch of marine sediment transport processes; Soulsby (1997)

The sediment transport rate is defined as the amount of sediment which passes through a vertical plane of unit width perpendicular to the flow per unit of time [kg/(ms) or m³/(ms)] (Figure 1-2). The sediment transport capacity is defined as the amount of sediment a flow can carry under equilibrium conditions per unit width perpendicular to the flow and per unit of time [kg/(ms) or m³/(ms)].

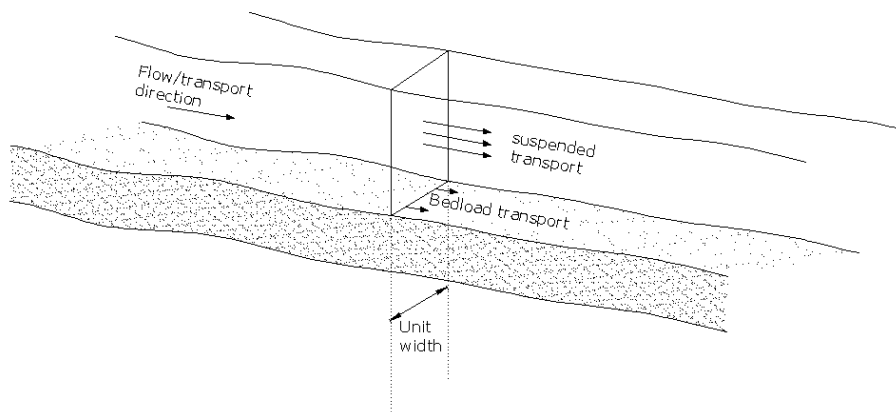


Figure 1-2: Definition of sediment transport rate; after Soulsby (1997)

Erosion or accretion in one area occurs when the net transport which enters this area differs from the net transport which leaves the area. This implies that erosion only appears when there is a difference in transport rate. To calculate the transport rate in an area, the hydrodynamic distributions of the currents and the waves and the dependent quantities, such as bed shear-stresses need to be known.

The bed shear-stress is the frictional force which is exerted by the flow per unit area of bed and is one of the most important terms when it comes to sediment transport. Consequently, attention is given to the determination of the bed shear-stress in this chapter.

An important note should be made on the accuracy of the sediment transport prediction. Due to the complexity and the interaction of the different processes, the biological effects and the uncertainty in most of the input parameters (water density ρ_w , kinematic viscosity of water ν , sediment density ρ_s , grain size and distribution, water depth d , current velocity U_c , current direction, wave height H_s , wave period T_p , wave direction) the prediction of sediment transport is an inexact science, resulting in considerable inaccuracies. The uncertainties in the input parameters are due to both measurement errors and the fact that they vary in time (Soulsby (1997)).

Dou and Jones (2000) mention that sediment transport formulae which are developed for general scour in an unobstructed flow field, are not appropriate to calculate local scour. They define an effective sediment transport capacity of the flow, which accounts for diving currents, strong vortices and high turbulence. Their formula for local sediment transport adds a term to the traditional sediment transport formula, which is derived from experimental data. As the formula is only to be applied in numerical models, we do not elaborate on it here. Their observation that general sediment transport formulae are not ideal to describe local scour is the main reason why they are not described within this chapter. Only the physical background of sediment transport is treated, in combination with the concept of initiation of motion.

1.1.1 Bed shear-stress and boundary layers

As mentioned above, the bed shear-stress τ_b [N/m²] is the frictional force which is exerted by the flow per unit area of bed. It is also often expressed as the friction velocity u_* [m/s], which is defined as:

$$u_* = \sqrt{\frac{\tau_b}{\rho_w}} \quad (1.1)$$

Often, the dimensionless form of the bed shear-stress is used and its relationship to the sediment properties is expressed by the Shields parameter θ , which is roughly the ratio of the load on a grain to the gravitational force that resists movement:

$$\theta = \frac{\tau_b}{g(\rho_s - \rho_w)d_s} = \frac{\tau_b}{\rho_w g \Delta d_s} = \frac{u_*^2}{g(s-1)d_s} \quad (1.2)$$

in which $g = 9.81$ m/s² is the acceleration due to gravity; ρ_s and ρ_w are the densities of the sediment grains and the water respectively; $s = \rho_s/\rho_w$ is the

specific density i.e. the ratio of the densities of sediment and water; $\Delta = s - 1$ and d_s is the sediment grain diameter.

With respect to sediment transport, the most important part of the flow is the boundary layer flow. The bottom boundary layer is intuitively defined as the layer inside which the flow is significantly influenced by the bed (Nielsen (1992)). Several derivations of the boundary layer thickness exist (Fredsoe and Deigaard (1992)), a commonly accepted definition is the distance from the boundary surface to the point where the local velocity equals $0.995U_c$, with U_c the steady flow velocity (Figure 1-3).

Due to the short life time of wave velocities, waves have much smaller boundary layer thicknesses than a steady current. As the bed shear-stresses are larger for smaller boundary layer thicknesses for the same free stream velocity U_c and the ability of the flow to transport sediment mainly depends on the bed shear-stresses, waves will tend to dominate over the current with respect to sediment entrainment. However, as waves create an orbital velocity (which goes back and forward), the currents are still dominant in transporting the entrained sediments (Nielsen (1992)).

The bed shear-stresses and boundary layers are treated consecutively for:

- a steady current
- a wave field
- a combined wave and current field

As sediment transport is the cause of scour, this subject is treated here, but understanding the forces which are exerted on the bed is also indispensable for the design of a scour protection (chapters 3 and 4).

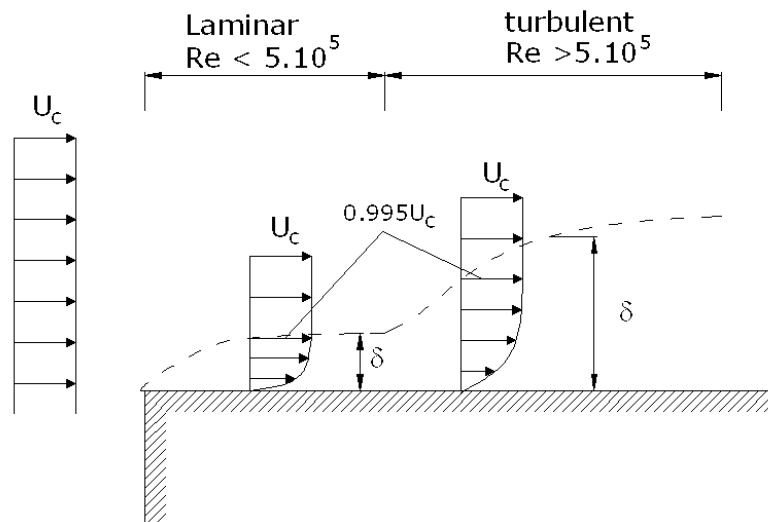


Figure 1-3: Definition of boundary layer thickness; after Liu (2001)

1.1.1.1 Steady uniform flow

One of the most elementary and best known cases of wall flow is the uniform flow in a channel. The bottom shear-stress $\tau_{b,c}$ related to the current alone case, depends on the flow velocity and the bottom roughness. Typically, the average flow velocity U_c is used to calculate $\tau_{b,c}$:

$$\tau_{b,c} = \frac{1}{2} \rho_w f_c U_c^2 \quad (1.3)$$

with f_c a dimensionless friction coefficient of the bed. For a hydraulically rough flow, f_c is determined by the bed roughness k_s and the water depth d . For a hydraulically smooth flow, f_c is determined by the water depth d and the friction velocity u_* (Liu (2001)):

$$f_c = \frac{2g}{C^2} = \frac{2g}{\left(\frac{\sqrt{g}}{\kappa} \ln \left(\frac{d}{z_0 e} \right) \right)^2} = \begin{cases} \frac{0.06}{\left(\log \left(\frac{12d}{3.3 \frac{\nu}{u_*}} \right) \right)^2}, & \text{hydr. smooth flow: } \frac{u_* k_s}{\nu} \leq 5 \\ \frac{0.06}{\left(\log \left(\frac{12d}{k_s} \right) \right)^2}, & \text{hydr. rough flow: } \frac{u_* k_s}{\nu} \geq 70 \end{cases} \quad (1.4)$$

with C the Chézy coefficient [\sqrt{m}/s]; z_0 the roughness length, corresponding to the elevation above the bed with zero velocity (equation (1.6)); $\kappa = 0.4$, the Von Karman constant; ν the kinematic viscosity of water and $e = 2.718$.

In a hydraulically smooth flow ($u_* k_s / \nu \leq 5$), the bed roughness is so small that roughness elements stay within the viscous sublayer and they do not affect the velocity distribution. In a hydraulically rough flow ($u_* k_s / \nu \geq 70$), there is no viscous sublayer and the flow velocity does not depend on viscosity. In a transitional flow $5 \leq u_* k_s / \nu \leq 70$, the velocity distribution is affected by both the bed roughness and viscosity (Liu (2001)).

The value of the bottom roughness k_s depends on the presence of ripples: a widely used value when no ripples are present is $k_s = 2.5d_{50}$, with d_{50} the median sediment grain diameter. When ripples are present, $k_s = (0.5 - 1)H_r$, with H_r the ripple height (Liu (2001)).

A steady current flowing over a seabed most often has a boundary layer with a thickness that covers a large part of the water depth. Measurements of the velocity distribution in a steady, uniform, turbulent boundary layer correspond very well to the logarithmic profile (Nielsen (1992), Soulsby (1997), Liu (2001)):

$$U(z) = \frac{u_*}{\kappa} \ln \left(\frac{z}{z_0} \right) \quad (1.5)$$

in which $\kappa = 0.4$ is the Von Karman constant and z_0 is the roughness length, corresponding with the elevation above the bed with zero velocity. This is in fact not realistic, but it reflects the fact that equation (1.5) gives a horizontally uniform description (Nielsen (1992)).

Colebrook and White (1937) studied pipe flows and a comparison of their results with the results from Nikuradse led to:

$$z_0 = \frac{k_s}{30} + \frac{\nu}{9u_*} \quad (1.6)$$

This equation simplifies to the well known value for a hydraulically rough flow:

$$z_0 = \frac{k_s}{30}, \quad \frac{u_* k_s}{\nu} \geq 70 \quad (1.7)$$

and in case of a hydraulically smooth flow:

$$z_0 = \frac{\nu}{9u_*}, \quad \frac{u_* k_s}{\nu} \leq 5 \quad (1.8)$$

For a hydraulically rough flow with a boundary layer which establishes over the entire depth, equations (1.5) and (1.7) lead to the conclusion that the average velocity is measured at a height of $0.368d \approx 0.4d$ above the bed, with d the water depth.

When ripples are present, the total bed shear-stress increases compared to the bed shear-stress over a flat bed and can be presented as:

$$\tau_b = \tau'_b + \tau''_b \quad (1.9)$$

in which τ'_b is called the effective shear-stress and originates from skin friction and τ''_b originates from form pressure of the ripples or larger bed forms.

To calculate τ'_b , $k_s = 2.5d_{50}$ is used in equation (1.4). To calculate the total shear-stress, k_s is taken as the ripple height H_r (or a value between $0.5H_r$ and H_r). To calculate the threshold of motion, the bed-load transport or sediment entrainment only the skin friction τ'_b is active in moving the sediment (Soulsby (1997), Liu (2001), Madsen and Wood (2002)).

1.1.1.2 Wave boundary layer and wave induced bed shear-stress

Waves in a sufficiently small water depth ($d/L < 1/2$) produce an oscillatory horizontal velocity at the sea bed. The amplitude of this horizontal velocity just above the bed U_m can be derived with linear wave theory as:

$$U_m = \frac{\pi H}{T_w} \cdot \frac{1}{\sinh\left(\frac{2\pi d}{L}\right)} \quad (1.10)$$

in which H represents the wave height, T_w is the wave period, d is the water depth and L is the wave length.

Frictional effects near the bed create an oscillatory boundary layer. In this boundary layer, the wave orbital velocity amplitude increases rapidly from zero at the bed to the value of U_m at the top of the boundary layer. The wave boundary layer remains thin (O(mm) – O(cm)), because the flow reverses before the layer can grow in a vertical direction, in contrast to the boundary layer of a steady current, which can be meters or tens of meters thick (Nielsen (1992)). This causes the bed shear-stress to be significantly larger in the case of waves with amplitude U_m of the orbital velocity than in the case of a steady current with depth-averaged velocity U_c , when U_m equals U_c .

In the case of waves, the bed shear-stress is oscillatory and has an amplitude $\tau_{b,w}$ which is obtained through the use of a wave friction factor f_w :

$$\tau_{b,w} = \frac{1}{2} \rho_w f_w U_m^2 \quad (1.11)$$

Several expressions for the wave friction factor exist (Nielsen (1992), Fredsøe and Deigaard (1992), Soulsby (1997)) and are cited here. As will be explained in section 1.1.1.3, the wave friction factor has a dominant role in the combined wave and current climate and a correct estimate of its value is important.

Fredsøe and Deigaard (1992) calculate a theoretical solution for the wave friction factor over a rough bed with a momentum method, obtaining a theoretical expression for the wave friction factor f_w and the wave boundary layer thickness δ :

$$f_w = 0.04 \left(\frac{A}{k_s} \right)^{-1/4}, \quad \frac{A}{k_s} > 50 \quad (1.12)$$

$$\frac{\delta}{k_s} = 0.09 \left(\frac{A}{k_s} \right)^{0.82} \quad (1.13)$$

with k_s the sediment roughness and A the amplitude of the wave orbital motion at the bed:

$$A = \frac{U_m T_w}{2\pi} \quad (1.14)$$

In case of small values of the ratio of the orbital amplitude and the bottom roughness A/k_s , the approximation suggested by Kamphuis is withheld for the wave friction factor:

$$f_w = 0.4 \left(\frac{A}{k_s} \right)^{-0.75}, \quad \frac{A}{k_s} < 50 \quad (1.15)$$

A recent study of Dixer et al. (2008) suggests an adjustment to f_w and δ for small values of A/k_s (\sim equations (1.15) and (1.13)), based on new experimental results:

$$f_w = 0.32 \left(\frac{A}{k_s} \right)^{-0.8}, \quad 0.2 < \frac{A}{k_s} < 10 \quad (1.16)$$

$$\frac{\delta}{k_s} = 0.08 \left(\left(\frac{A}{k_s} \right)^{0.82} + 1 \right), \quad 0.5 < \frac{A}{k_s} < 5000 \quad (1.17)$$

In case of a smooth bed, Fredsøe and Deigaard (1992) calculate the following expressions for the wave friction factor and the boundary layer thickness:

$$f_w = 0.035 \text{Re}_A^{-0.16} \quad (1.18)$$

$$\frac{\delta}{A} = 0.086 \text{Re}_A^{-0.11} \quad (1.19)$$

both are now solely depending on the amplitude Reynolds number Re_A :

$$\text{Re}_A = \frac{U_m A}{\nu} \quad (1.20)$$

In general, a sand bed exposed to waves will be hydraulically rough, when the waves are sufficiently large for the sediment to move. Moreover, a scour protection is also hydraulically rough, so equations (1.18) – (1.19) which are valid for a smooth bed, are only given to be complete.

Nielsen (1992) suggests equation (1.21) for the wave friction factor in case of a rough turbulent flow and equation (1.22) in case of a smooth bed:

$$f_w = \exp \left[5.5 \left(\frac{k_s}{A} \right)^{0.2} - 6.3 \right] \quad (1.21)$$

$$f_w = \frac{2}{\sqrt{\frac{A^2 \omega}{\nu}}} \quad (1.22)$$

in which ω represents the angular frequency of the waves = $2\pi/T_w$.

Soulsby (1997) gives the following expression for the wave friction factor in the case of a rough bed:

$$f_w = 1.39 \left(\frac{A}{z_0} \right)^{-0.52} \quad (1.23)$$

for all values of A/k_s , with z_0 the bed roughness length = $d_{50}/12$ for hydrodynamical rough flows.

In case of a smooth bed, Soulsby (1997) suggests:

$$f_w = B \text{Re}_A^{-N} \quad (1.24)$$

with: $B = 2, \quad N = 0.5 \quad \text{for } \text{Re}_A \leq 5 \cdot 10^5 \text{ (laminar)}$
 $B = 0.0521, \quad N = 0.187 \quad \text{for } \text{Re}_A \leq 5 \cdot 10^5 \text{ (smooth turbulent)}$

which leads to the same expression for a laminar flow over a smooth bed as the one from Nielsen (1992) (equation (1.22)).

A typical feature of an oscillatory boundary layer is that the bed shear-stress $\tau_{b,w}$ is ahead of the velocity $u_w(t)$ (Nielsen (1992), Dixen et al. (2008)):

$$u_w(t) = U_m \cdot \cos(\omega t) \quad (1.25)$$

The phase difference varies between 10-30° in measurements of Dixen et al. (2008) (compared to 45°, which is given by the laminar solution) and seems to be independent of the value of A/k_s . The measurements of Dixen et al. (2008) and others are presented in Figure 1-4, together with the laminar solution.

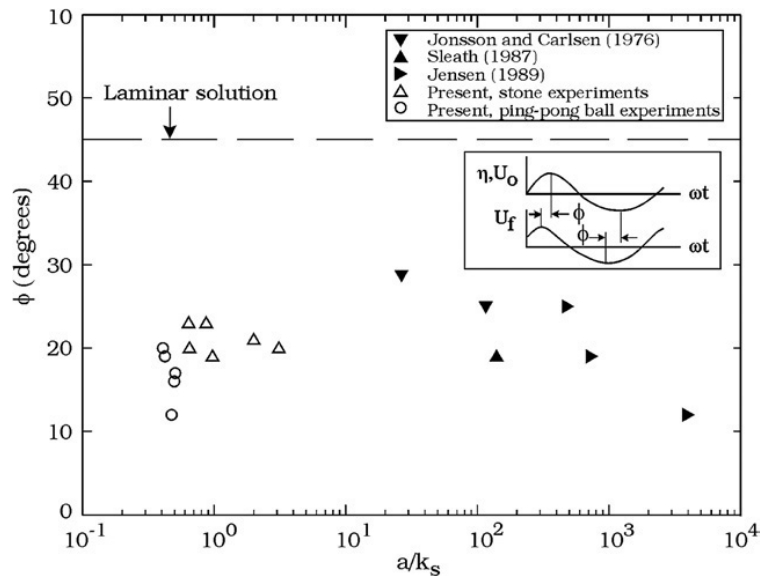


Figure 1-4: Phase lead of the friction velocity over the free-surface elevation; Dixen et al. (2008)

1.1.1.3 Wave-current boundary layer interaction

In most marine environments, both currents and waves occur simultaneously. Difficulties arise because these interact, so that their combined influence is not the same as a linear sum of their separate influences. Only the interaction of the wave and current boundary layers are treated here. The changes in wave height and length which occur when waves travel through a flow field are disregarded here. These are discussed in Appendix III.

The velocity profile in a combined flow is commonly split into three parts (Fredsoe and Deigaard (1992), Nielsen (1992)): an upper zone, in which the current dominates the turbulence characteristics and which covers the largest part of the water depth, a transitional zone and a wave dominated zone near the bed. The location of the three zones is shown in Figure 1-5.

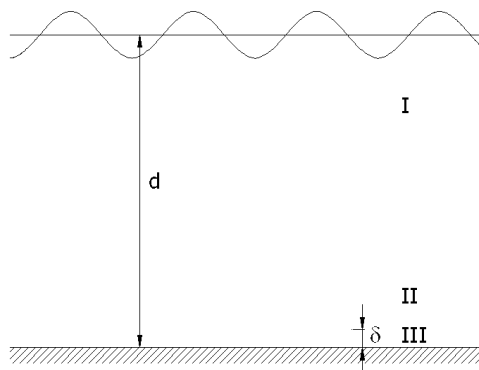


Figure 1-5: Definition sketch and location of different zones of turbulence; after Fredsoe and Deigaard (1992)

The change in the turbulent structure due to the presence of the waves causes a modification in the vertical distribution of the mean current profile. The changes in the mean velocity profile due to the interaction between waves and a current were investigated by Delgado Blanco et al. (2004) and Umeyama (2005), showing that the mean velocity for waves following a current behaves differently than in the case of waves opposing a current. The former leads to a reduced current towards the free surface, whereas the latter leads to an increase of the current towards the free surface, compared with the logarithmic velocity profile of a current alone case.

As mentioned above, bed shear-stresses differ from a simple linear composition of the bed shear stresses for waves and currents due to a non-linear interaction between the wave and current boundary layers. Delgado Blanco et al. (2004) found that, in contrary to the free surface flow velocity, the influence of a following (opposing) current leads to an increase (decrease) in near bed velocities. Delgado Blanco et al. (2004) found that for their experiments the measured bed shear stresses in combined waves and currents were about one order of magnitude larger than those found for currents alone.

Several different theories and models have been proposed to calculate the bed shear-stress $\tau_{b,wc}$ in combined waves and current, leading to considerable differences in the predicted bed shear-stress. These are summarized below.

Fredsøe and Deigaard (1992) suggest for the case where waves coexist with a weak, parallel current that the boundary layer thickness is determined by the wave motion only (equation (1.13) or equation (1.19)). This results in a mean bed shear-stress τ_m :

$$\tau_m = \frac{2}{\pi} \rho_w f_w U_m U_\delta \quad (1.26)$$

with

$$U_\delta = C - \sqrt{C^2 - U_c^2} \quad (1.27)$$

and

$$C = U_c + \frac{1}{\pi} f_w U_m \left(6.2 + \frac{1}{\kappa} \ln \left(\frac{d}{30\delta} \right) \right)^2 \quad (1.28)$$

in which U_c represents the average current velocity; f_w is the wave friction factor according to equation (1.12), equation (1.15) or equation (1.18); U_m according to equation (1.10); δ according to equation (1.13) or equation (1.19) and $\kappa = 0.4$, the Von Karman constant.

The resulting maximum bed shear-stress according to Fredsøe and Deigaard (1992) is:

$$\tau_{\max} = \frac{1}{2} \rho_w f_w (U_m + U_\delta) \cdot |U_m + U_\delta| \quad (1.29)$$

with U_m according to equation (1.10) and U_δ according to equation (1.27).

Soulsby (1997) compared the mean (τ_m) and maximum (τ_{max}) bed shear-stresses during a wave cycle. Based on a dataset of 131 points two simple equations are derived, which according to Soulsby (1997) give an almost as good fit as the best theoretical models:

$$\tau_m = \tau_c \left[1 + 1.2 \left(\frac{\tau_w}{\tau_c + \tau_w} \right)^{3.2} \right] \quad (1.30)$$

$$\tau_{max} = \left[(\tau_m + \tau_w \cos \phi)^2 + (\tau_w \sin \phi)^2 \right]^{1/2} \quad (1.31)$$

with ϕ the angle between the wave and current direction.

According to Soulsby (1997), the calculation of τ_m is necessary to determine sediment diffusion, whereas the calculation of τ_{max} is necessary to determine the threshold of motion.

1.1.2 Threshold of motion

The threshold of a particle's motion is attained when the driving forces become larger than the stabilizing forces. Figure 1-6 illustrates the forces acting on a grain, resting on the bed and loaded by a flow velocity. The driving forces are the horizontal drag force F_D , which consists of a friction drag and a form drag, and a vertical lift force F_L . The size of the drag force depends on the particle Reynolds number and the particle's shape. If A' is the projected area of the grain on the horizontal plane, the bottom shear-stress τ_b is:

$$\tau_b = \frac{F_D}{A'} \quad (1.32)$$

The stabilizing forces are the submerged weight W of the grain and the reaction forces F_s between the grain and the surrounding grains.

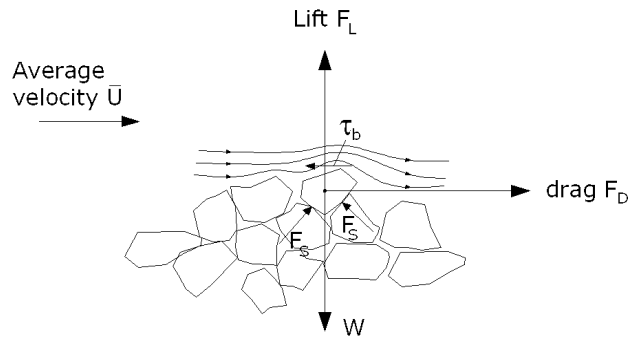


Figure 1-6: Forces acting on a sediment grain, resting on the bed

The forces mentioned above do however not give all the necessary information to know when a grain will be entrained. Additional information is needed on the duration of the forces which act on the grain particle: the force should last long enough to entrain a particle. Furthermore the correlation between drag and lift force and the location of the point on which the forces apply are important. Finally, the movement of the particle will influence the forces which act on it (Hofland (2005)).

The thesis of Shields (1936) is the best-known and most used in research on the threshold of motion in uniform flow. He defined the parameter θ_{cr} for the threshold of motion as the Shields parameter at which some particles can be seen displacing at each moment and at each part of the bed:

$$\theta_{cr} = \frac{\tau_{cr}}{g(\rho_s - \rho_w)d_s} = \frac{u_{*cr}^2}{g\Delta d_s} \quad (1.33)$$

with τ_{cr} the threshold bed shear-stress, d_s the sediment grain diameter, u_{*cr} the critical shear velocity and $\Delta = (\rho_s - \rho_w) / \rho_w$. When the critical Shields parameter is exceeded or in other words when the bed shear stress exceeds the critical bed shear stress, stones will be moved by the flow.

The original Shields curve, which plots the Shields parameter (equation (1.2)) as a function of the grain Reynolds number Re_* (equation (1.34)) is given in Figure 1-7. The grain Reynolds number Re_* indicates whether the grain protrudes into the turbulent boundary layer or stays within the viscous sub-layer and is defined as:

$$Re_* = \frac{u_* d_s}{\nu} \quad (1.34)$$

For large values of Re_* , the critical Shields parameter reaches a constant value of 0.056. Because $u_* = \sqrt{\tau_b / \rho_w}$ depends on the bed shear-stress, the main

disadvantage of the Shields diagram is that the bed shear-stress appears on both axes.

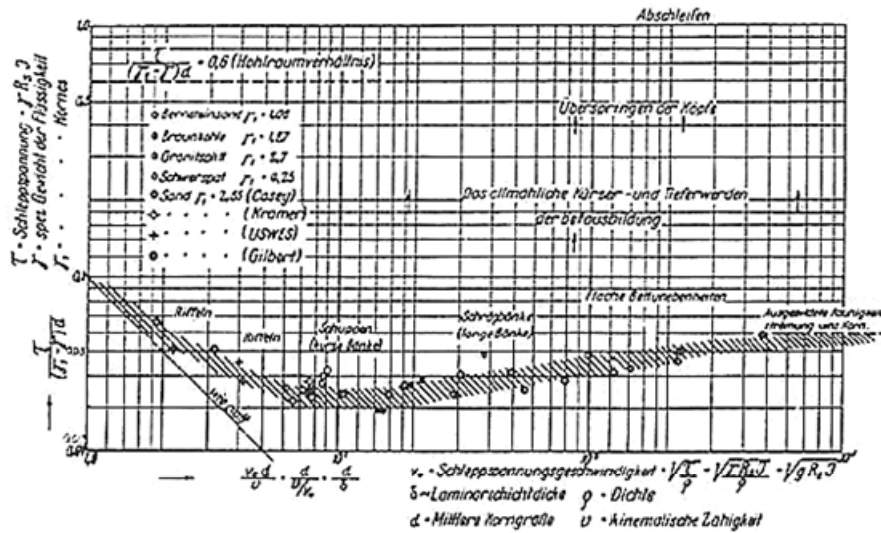


Figure 1-7: Original Shields curve: the Shields parameter is plotted against the particle Reynolds number Re_* ; Shields (1936)

In CIRIA/CUR (1991) it is described how both Grant and Komar & Miller have shown independently in 1975 that the results for initiation of motion for unsteady flow (waves) are in reasonable agreement with the Shields curve determined for steady flow (current) when the wave friction factor, defined in equation (1.11), is used.

Soulsby (1997) transformed the original Shields curve into Figure 1-8, where θ_{cr} is plotted against the dimensionless grain size D_* given by equation (1.35). The curve is valid for both waves and currents.

$$D_* = \left[\frac{g(s-1)}{\nu^2} \right]^{1/3} d_s \quad (1.35)$$

Soulsby and Whitehouse (1997) propose the following improved expression for the threshold Shields parameter, shown in Figure 1-8:

$$\theta_{cr} = \frac{0.30}{1+1.2D_*} + 0.055 \left[1 - \exp(-0.020D_*) \right] \quad (1.36)$$

with the remark that equation (1.36) can only be used for the initiation of motion on an initially flat bed (Soulsby (1997)). If the bed is rippled, equation (1.36) applies only to the skin friction component of the bed shear-stress τ'_b

(see equation (1.9)). Contrary to the use of the original Shields diagram, equation (1.36) allows a quick calculation of the critical grain size.

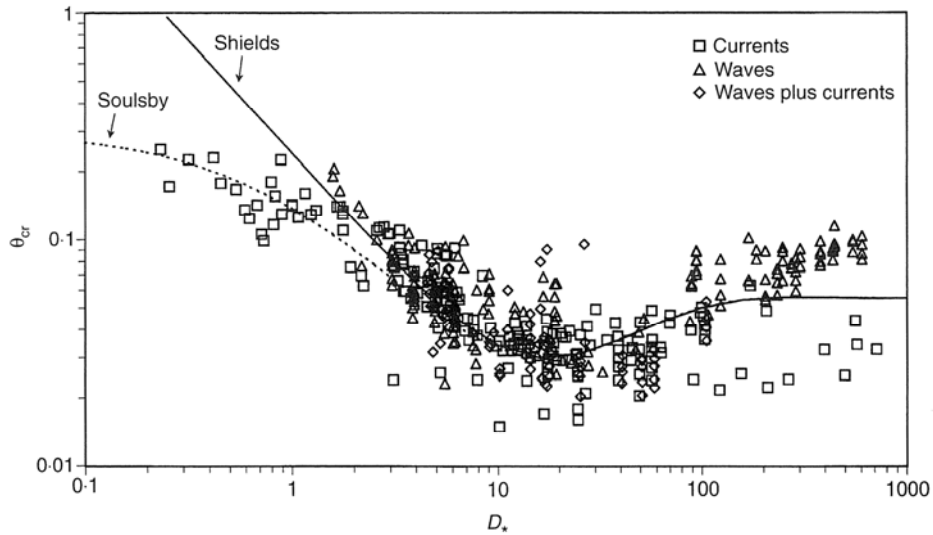


Figure 1-8: Adapted Shields curve, plotting the critical Shields parameter against the dimensionless grain size D_* for the threshold of sediment motion beneath waves and/or currents; Soulsby (1997)

Hoffmans and Verheij (1997) note that, because of the non-uniform distribution of the mixtures, Shields drew not a single curve, but a broad belt. They present another variation on the Shields curve, shown in Figure 1-9. They also plot the Shields parameter versus the dimensionless grain size D_* (equation (1.35)). The plot shows that the Shields criterion actually corresponds with the initiation of motion over the entire bed. Occasional particle movement may occur at some locations for much smaller values of the Shields parameter.

When the sediments are placed on a sloping bed, an extra force component is added by gravity, which may increase or decrease the threshold of motion, depending on whether the flow is up or down the slope. The gravity force should be added vectorially to the shear-stress force from the flow to calculate the threshold of motion for a sediment grain on a sloping bed and the following expression gives the ratio of the critical bed shear-stress on a slope $\tau_{\beta,cr}$ to the critical bed shear-stress on a horizontal bottom τ_{cr} (Soulsby (1997)):

$$\frac{\tau_{\beta,cr}}{\tau_{cr}} = \frac{\cos \psi \sin \beta + (\cos^2 \beta \tan^2 \phi - \sin^2 \psi \sin^2 \beta)^{1/2}}{\tan \phi} \quad (1.37)$$

with β the angle of the slope with the horizontal, ϕ the angle of repose of the sediment and ψ the angle which the flow makes with the upslope direction.

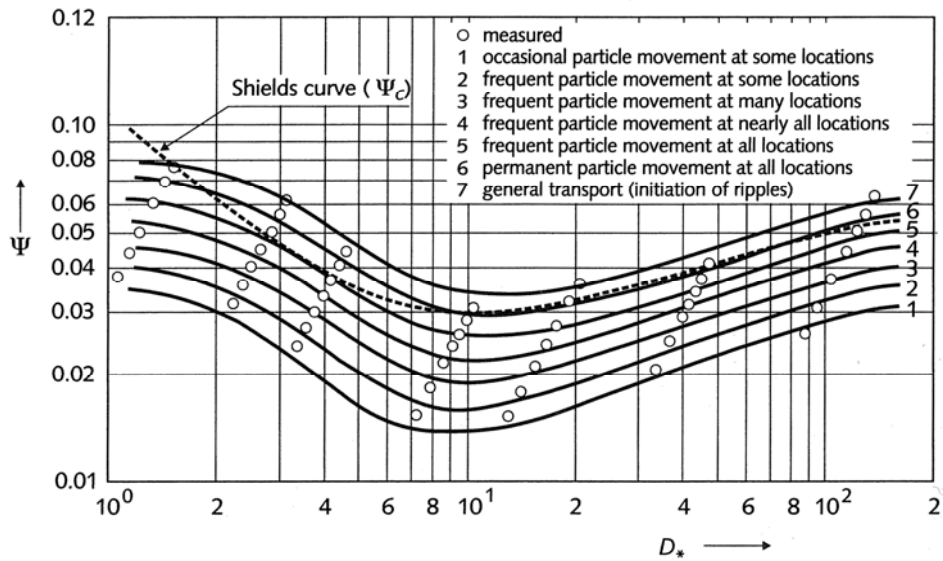


Figure 1-9: Modified Shields diagram; Hoffmans and Verheij (1997)

1.1.3 Transport equations

In chapter 3 and 4, describing the design of a scour protection, emphasis is put on the design of a scour protection, where a certain amount of movement of the bed material (i.e. damage) is allowed. Therefore it is useful to describe the basics of bedload transport here. Suspended transport plays a less important role when it comes to damage of a scour protection and is therefore not considered. Suspended transport does play a role in the development of a scour hole, but most often empirical relations are used to calculate the scour depth (see section 1.3), which makes it unnecessary to describe the different suspended load formulae.

Most bedload transport formulae use the dimensionless transport rate Φ , defined as:

$$\Phi = \frac{q_b}{\sqrt{g(s-1)d_s^3}} \quad (1.38)$$

in which q_b represents the volumetric transport rate = the volume of grains moving per unit time and per unit width of the bed [$\text{m}^3/(\text{ms}) = \text{m}^2/\text{s}$].

Most bedload transport formulae can be expressed as a function of the Shields parameter θ and the critical Shields parameter θ_{cr} :

$$\Phi = \text{function}(\theta, \theta_{cr}) \quad (1.39)$$

Several formulae exist for the case of a steady current alone, a wave alone or combined waves and current. A reference is made to Fredsøe and Deigaard (1992), van Rijn (1993), Nielsen (1992) or Soulsby (1997).

1.2 Flow around a monopile foundation

Extensive research has been performed on the influence of a single vertical pile on the flow pattern in a steady current (Melville and Raudkivi (1977), Hjorth (1975); Baker (1979); Dargahi (1989); Sumer et al. (1997); Sumer and Fredsøe (1997); Sumer and Fredsøe (2002); amongst others) and several investigations exist on the flow pattern around a vertical pile in a wave field (Sumer and Fredsøe (1997); Sumer and Fredsøe (2002)). Limited information is available on the flow pattern in a combined wave and current case (Umeda et al. (2003); Sumer et al. (1997)). The main findings of the research on flow patterns around a single vertical pile is described in this paragraph.

Breusers and Raudkivi (1991) and Sumer and Fredsøe (2002) give a clear description of the flow pattern around a single vertical pile. When a vertical pile is placed on a sea bed, the flow experiences the following changes (Figure 1-10):

- a downflow is formed in front of the pile
- a horseshoe vortex originates in front of the pile
- a vortex flow pattern is formed at the lee-side of the pile (usually accompanied by vortex shedding)
- the streamlines are contracted at the side edges of the pile

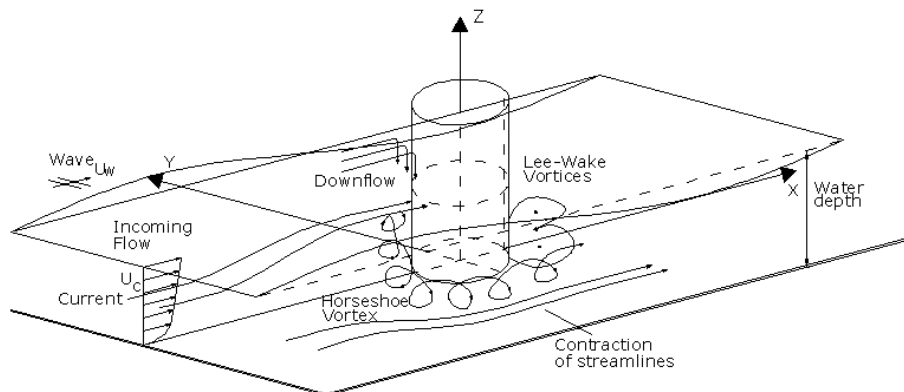


Figure 1-10: Definition sketch of the flow-structure interaction for a vertical cylinder

The changes in the flow pattern, described above, generally create an increase (1) in the bed shear-stress and (2) in the turbulence level near the structure, both leading to an increase in local sediment transport capacity near the structure. At this moment, much more is known about part (1) than about part (2), although Ali and Karim (2002) and Bollaert and Hofland (2004) conclude

that the degree of turbulence intensity contributes significantly in the scouring process, especially in an obstructed field.

The increase in the bed shear-stress is traditionally expressed in terms of a so-called amplification factor α , which is defined by

$$\alpha = \frac{\tau_b}{\tau_\infty} \quad (1.40)$$

in which τ_b and τ_∞ represent the actual and the undisturbed bed shear-stress, respectively.

1.2.1 Downflow in front of the pile

The downflow originates as the flow comes to rest at the front of the pile. Since the velocity U decreases from the surface downwards (logarithmic velocity profile), the stagnation pressure ($\rho_w U^2/2$) also decreases from the surface down, creating a downward pressure gradient (Breusers and Raudkivi (1991)).

1.2.2 Horseshoe vortex

From a sediment transport point of view, the horseshoe vortex plays an important role in a steady current environment. According to Sumer and Fredsøe (2002), the horseshoe vortex is formed by the rotation of the incoming flow; the boundary layer of the bed upstream of the pile experiences a three-dimensional separation caused by the adverse pressure gradient which is induced by the presence of the structure itself. The separated boundary layer forms a spiral vortex (horseshoe vortex) around the structure and then trails off downstream. The distance from separation point to the center of the pile x_s (Figure 1-11) characterizes the size of the horseshoe vortex. According to Breusers and Raudkivi (1991), the horseshoe vortex develops as a result of the separation of the flow at the upstream edge of the scour hole and is thus a consequence of the scour, not the cause of it. They do mention however that it does aid in transporting sediment away from the scour hole. Kobayashi (1992) concludes from a numerical simulation in which he compares the flow pattern on a flat bed with the flow pattern in a scour hole that the scour hole has a significant influence on the shedding and deformation processes of large vortices.

In the case of a steady current, the horseshoe vortex has been investigated intensively, using different visualization techniques (e.g. Hjorth (1975); Baker (1979); Dargahi (1989); Sumer and Fredsøe (2002)).

In Sumer and Fredsøe (2002) it is noted that both the existence of an incoming boundary layer and the separation of the boundary layer (caused by a sufficiently strong pressure gradient) are necessary to form the horseshoe vortex. For a circular pile in a steady current, the characteristics of the vortex system upstream of the pile depend mainly on the following parameters δ/D and

Re_D (Baker (1979)). With δ/D = the ratio of the bed boundary layer thickness δ to pile diameter D and Re_D = the pile Reynolds number:

$$Re_D = \frac{U \cdot D}{\nu} \quad (1.41)$$

in which U = the velocity at the outer edge of the boundary layer (Figure 1-11).

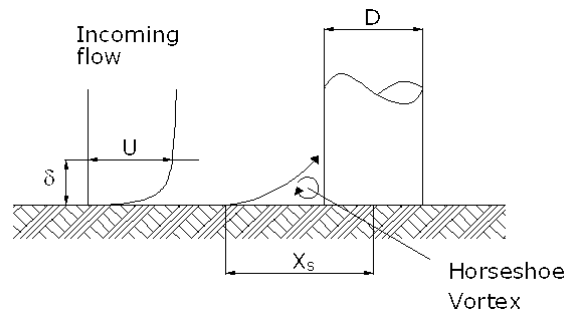


Figure 1-11: Definition of boundary layer thickness, incoming flow velocity and separation point

The influence of the boundary layer to pile size ratio δ/D is such that the smaller δ/D , the smaller the horseshoe vortex. For very small values of δ/D the boundary layer may not separate at all. Similar to the effect of δ/D , the (pile) Reynolds number Re_D influences the size of the horseshoe vortex. The smaller Re_D , the smaller the horseshoe vortex and for very small values of Re_D , the horseshoe vortex may not be separated at all. In Sumer and Fredsøe (2002) it is noted however that in case of a turbulent boundary layer, the role of the Reynolds number may be reversed, i.e. the size of the horseshoe vortex may decrease with increasing Reynolds number. This is due to an increase in the momentum exchange between the fluid layers in a turbulent boundary layer, which may lead to a delay in the boundary layer separation.

The amplification of the bed shear-stress in a steady current due to the presence of the horseshoe vortex is presented in Figure 1-12. The maximum measured value of the amplification mounts up to 7, but generally varies around 5.

In the case of waves, the Keulegan Carpenter number KC is added to the list of parameters influencing the horseshoe vortex (Sumer and Fredsøe (2002)). The Keulegan Carpenter number is defined as:

$$KC = \frac{U_m \cdot T_w}{D} = \frac{2\pi A}{D} \quad (1.42)$$

in which U_m = the maximum value of the undisturbed horizontal orbital velocity at the bed (1.10), T_w = the wave period and A is the amplitude of the undisturbed horizontal orbital motion at the bed, cf. equation (1.14).

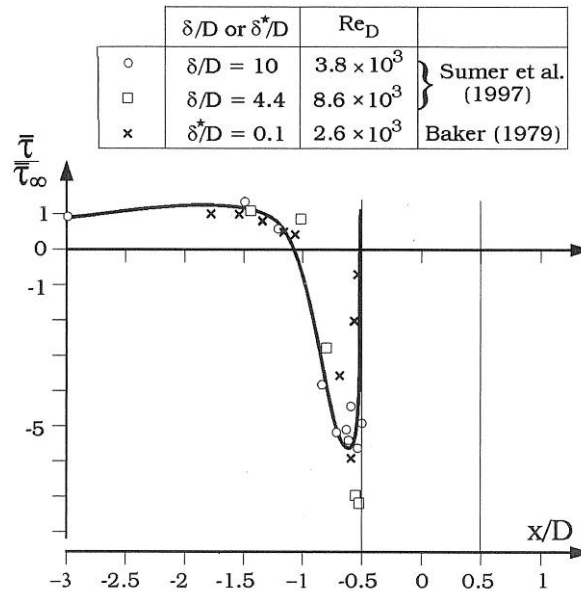


Figure 1-12: Bed shear-stress at the horseshoe-vortex side of the pile. $X = 0$ represents the center of the pile; Sumer and Fredsøe (2002)

The expression of KC shows that it is proportional to the ratio of the amplitude of the horizontal orbital velocity and the pile diameter, which means that for small KC numbers, the orbital motion is small compared to the pile size. For very small values of KC , the horseshoe vortex may not be formed. For very large KC numbers however, the amplitude of the orbital motion is high enough to resemble a steady current (Sumer and Fredsøe (2002)).

Sumer et al. (1997) investigated the influence of the KC number on the flow characteristics and found that no horseshoe vortex is formed when $KC < 6$ (or $A < D$), even though lee-wake vortex shedding occurs for values of KC larger than 1.1 (see section 1.2.3). This is due to the adverse pressure gradient in front of the pile, which is a factor 5 smaller than the pressure gradient over the surface of the pile, explaining why the formation of a horseshoe vortex is postponed until a KC value of 6 is reached. The results of the study of Sumer et al. (1997) are shown in Figure 1-13. In the figure, $\omega t = 0^\circ - 180^\circ$ corresponds with the crest of the wave.

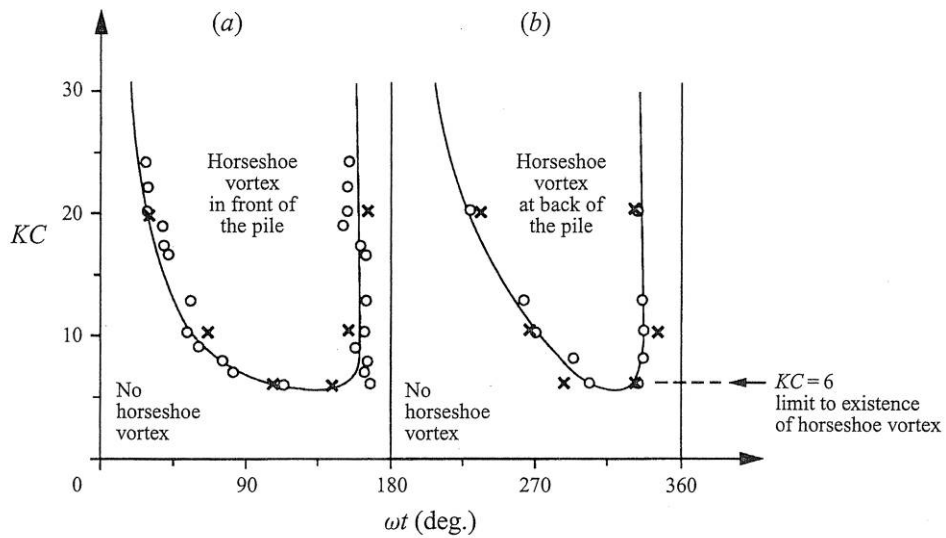


Figure 1-13: Horseshoe vortex as a function of wave phase ωt ; Sumer et al. (1997)

The horseshoe vortex is formed in each half cycle of the wave period and disappears each time the flow is reversed, to reappear on the other side of the pile. The life span of the horseshoe vortex depends on the KC number, with an increasing life span for an increasing KC number. Again the increase of the life span is linked to the necessary adverse pressure gradient, which is maintained over a longer period when KC increases.

The location of the separation point as a function of the KC number is shown in Figure 1-14 (Sumer et al. (1997)).

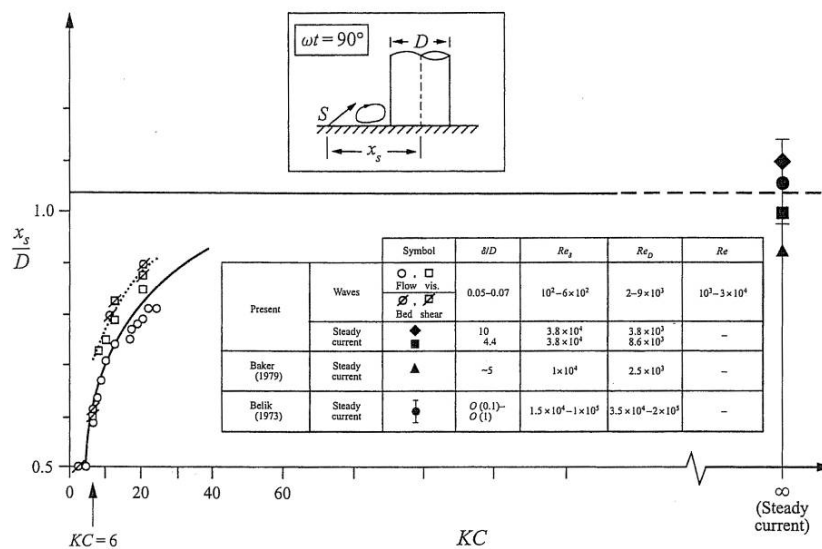


Figure 1-14: Location of separation point for a circular, vertical pile; $\omega t = 90^\circ$ (○) and $\omega t = 270^\circ$ (□); Sumer et al. (1997)

In Figure 1-14, a difference can be noted between the two half cycles, with generally a larger vortex size during the passage of the wave trough. This is attributed to the asymmetry between the two half periods of the waves. The distance between the separation point and the center of the pile first goes through a steep increase with increasing KC number and tends towards an asymptotic value.

The amplification of the bed shear-stress due to the formation of the horseshoe vortex, on the horseshoe side of the pile is shown in Figure 1-15 for $\omega t = 90^\circ$ and $\omega t = 270^\circ$ (as in Figure 1-14). The amplification is much smaller in the case of waves than in the case of a steady current, due to a stronger presence of the horseshoe vortex in a steady current.

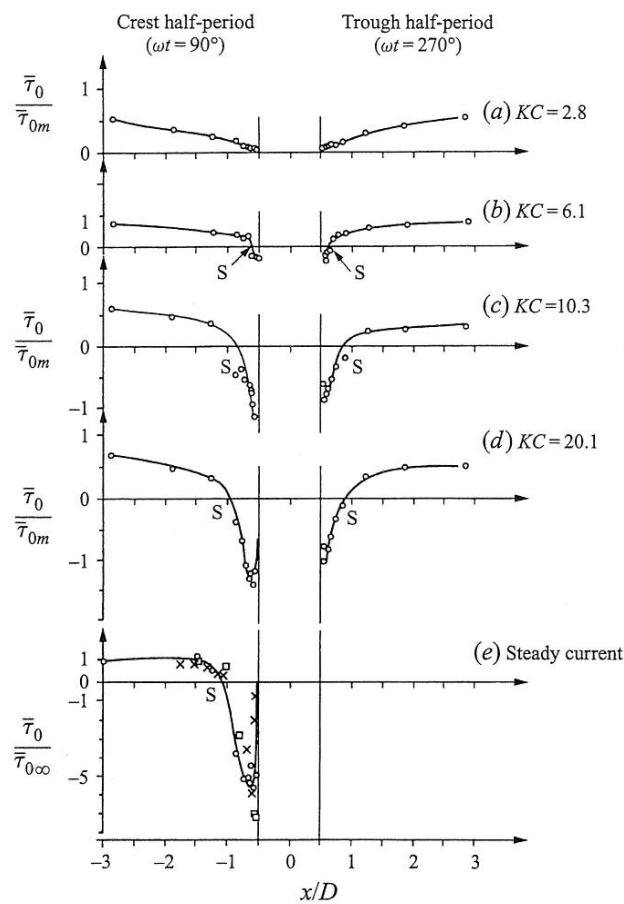


Figure 1-15: Bed shear-stress at the horseshoe side of single circular pile for different KC numbers and a steady current. $x =$ Baker (1979); Sumer et al. (1997)

In case of combined waves and current, the results of Sumer et al. (1997) show that a horseshoe vortex is formed for decreasing values of the KC number with increasing current velocity and that the life span of the horseshoe vortex is

increased for an increasing current velocity. Umeda et al. (2003) performed a numerical study on the flow field around a single vertical pile and they found that, when the oscillatory flow and the steady flow work in the same direction, the enhanced velocity produces a strong horseshoe vortex in front of the cylinder. When the oscillatory flow and the steady flow work in the opposite direction, no horseshoe vortex is formed at the downstream side of the pile. According to Umeda et al. (2003), the formation of the horseshoe vortex in a combined wave and current flow field depends on the velocity ratio of the steady flow to the oscillatory flow V_r ($V_r = U_c/U_m$) and on the KC number. For a KC number = 10 and a small velocity ratio ($V_r = 0.5$), the horseshoe vortex appears between $t/T_w = 3/24$ and $t/T_w = 14/24$. When the velocity ratio $V_r = 1.5$ while $KC = 10$, the life span of the horseshoe vortex reaches about five-sixths of a whole cycle (from $t/T_w = -3/24$ till $t/T_w = 17/24$). For a smaller KC number ($KC = 2.5$), the life span of the horseshoe vortex and the number of shed vortices decreases. Their results are plotted together with the results from Sumer et al. (1997) in Figure 1-16. The streamwise extent of the horseshoe vortex is presented herein as a function of a dimensionless parameter A_0 , which represents the ratio of the distance over which the water particles move during one quarter cycle of the oscillation to the cylinder diameter and is defined as:

$$A_0 = KC \cdot \frac{2 + \pi V_r}{4\pi} \quad (1.43)$$

No horseshoe vortex exists for $A_0 < 0.5$.

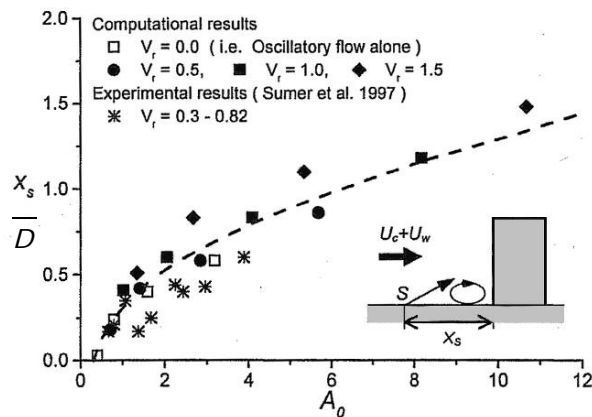


Figure 1-16: Separation distance of the horseshoe vortex; Umeda et al. (2003)

1.2.3 Lee-wake vortex shedding

Sumer and Fredsøe (1997) give a comprehensive description of the vortex formation and vortex shedding at the lee-side of a circular pile in a steady current and in oscillatory flows. Their main conclusions are summarized here. Sufficient attention is given to the lee-wake vortices as it is noted in Sumer and Fredsøe (2002) that in the case of a wave field, the lee-wake vortex shedding is

essential for the scour process, in contrast to the steady current case, where the horseshoe vortex mainly determines the scour process. In case of a steady current, the pile Reynolds number determines the lee-wake vortex flow. The flow changes strongly when the pile Reynolds number increases. A summary of the flow regime around a smooth, vertical pile as a function of the pile Reynolds number Re_D is given in Figure 1-17.

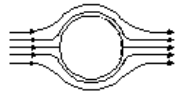





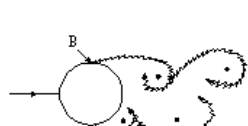


a)		No separation. Creeping flow	$Re_D < 5$
b)		A fixed pair of symmetric vortices	$5 < Re_D < 40$
c)		Laminar vortex street	$40 < Re_D < 200$
d)		Transition to turbulence in the wake	$200 < Re_D < 300$
e)		Wake completely turbulent A: Laminar boundary layer separation	$300 < Re_D < 3 \times 10^5$ Subcritical
f)		A: Laminar boundary layer separation B: Turbulent boundary layer separation: but boundary layer turbulent	$3 \times 10^5 < Re_D < 3.5 \times 10^5$ Critical (Lower transition)
g)		B: Turbulent boundary layer separation: boundary layer partly laminar partly turbulent	$3.5 \times 10^5 < Re_D < 1.5 \times 10^6$ Supercritical
h)		C: boundary layer completely turbulent at one side	$1.5 \times 10^6 < Re_D < 4 \times 10^6$ Upper transition
i)		C: boundary layer completely turbulent at two sides	$4 \times 10^6 < Re_D$ Transcritical

Figure 1-17: Lee-wake flow regime around a smooth, circular pile in steady current as a function of Re_D ; after Sumer and Fredsøe (1997)

The vortex shedding frequency is represented by the dimensionless Strouhal number St , defined as:

$$St = \frac{f_v D}{U_c} \quad (1.44)$$

with f_v the vortex-shedding frequency, D the pile diameter and U_c the flow velocity.

The normalised vortex shedding frequency is a function of Re_D and the relative surface roughness k_s/D , as illustrated in Figure 1-18 and Figure 1-19.

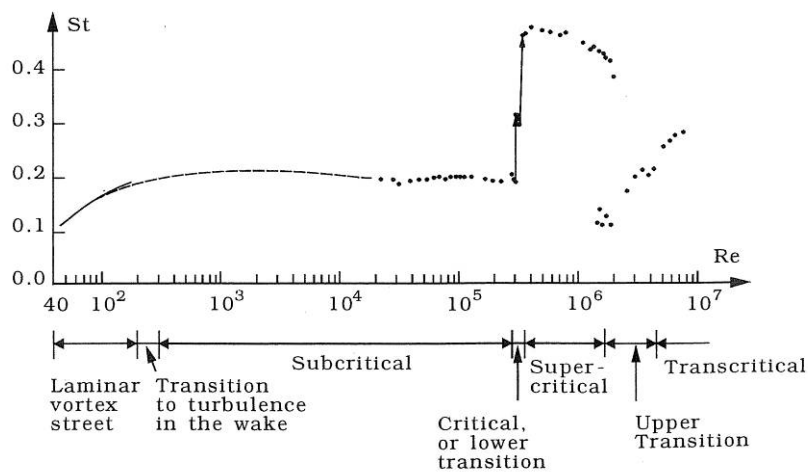


Figure 1-18: Strouhal number of a vertical cylindrical pile as a function of pile Reynolds number, data from Williamson (solid line, 1989), Roshko (dashed curve, 1961) and Schewe (dots, 1983); from Sumer and Fredsøe (1997)

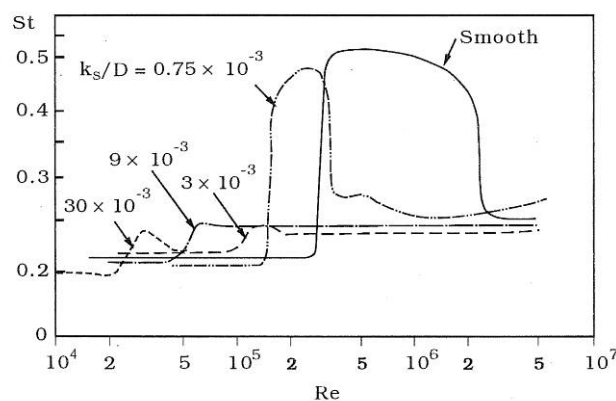


Figure 1-19: Effect of surface roughness on vortex shedding frequency; from Sumer and Fredsøe (1997)

In the case of waves, the KC number comes up as an additional parameter which influences the lee-wake vortex-shedding, as it does for the horseshoe vortex. Figure 1-20 summarizes the flow regimes for increasing KC numbers. In Sumer and Fredsøe (1997) it is noted that the flow regimes in Figure 1-20 may change when the Re_D number changes. This is illustrated in Figure 1-21 and Figure 1-22.


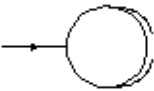
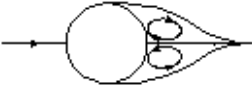



 <p>a.</p>	<p>No separation. Creeping (laminar) flow</p>	<p>$KC < 1.1$</p>
 <p>b.</p>	<p>Separation with Honji vortices</p>	<p>$1.1 < KC < 1.6$</p>
 <p>c.</p>	<p>A pair of symmetric vortices.</p>	<p>$1.6 < KC < 2.1$</p>
 <p>d.</p>	<p>A pair of symmetric vortices. Turbulence over the cylinder surface (A)</p>	<p>$2.1 < KC < 4$</p>
 <p>e.</p>	<p>A pair of asymmetric vortices</p>	<p>$4 < KC < 7$</p>
 <p>f.</p>	<p>Vortex shedding</p>	<p>$7 < KC$ Shedding regimes</p>

Figure 1-20: Lee-wake flow regime around a smooth, circular pile in oscillatory flow as a function of KC number ($Re = 10^3$); after Sumer and Fredsøe (1997)

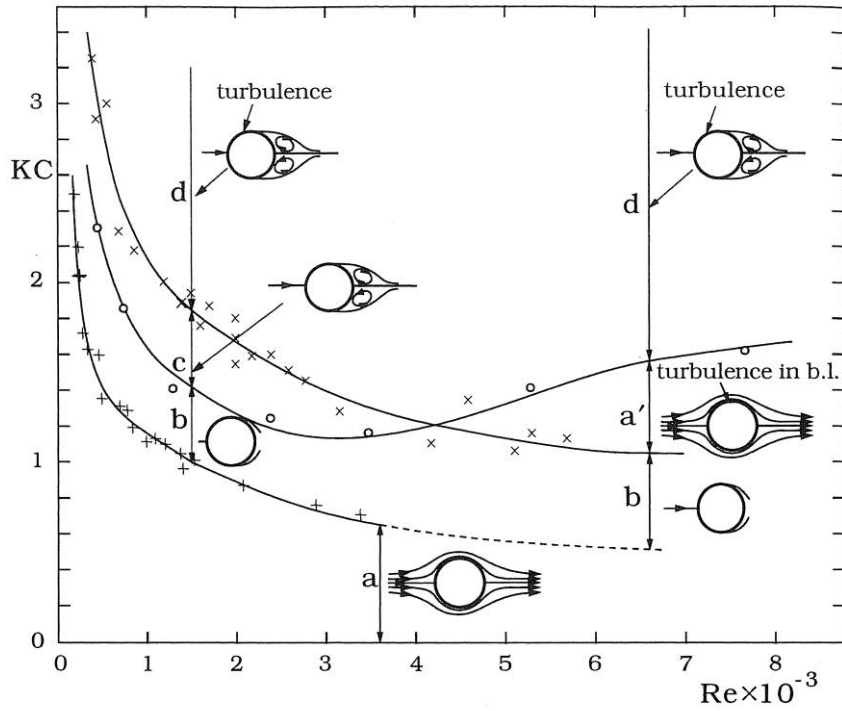


Figure 1-21: Vortex shedding regimes around a smooth, circular cylinder in oscillatory flow for small KC numbers ($KC < 3$); from Sumer and Fredsøe (1997)

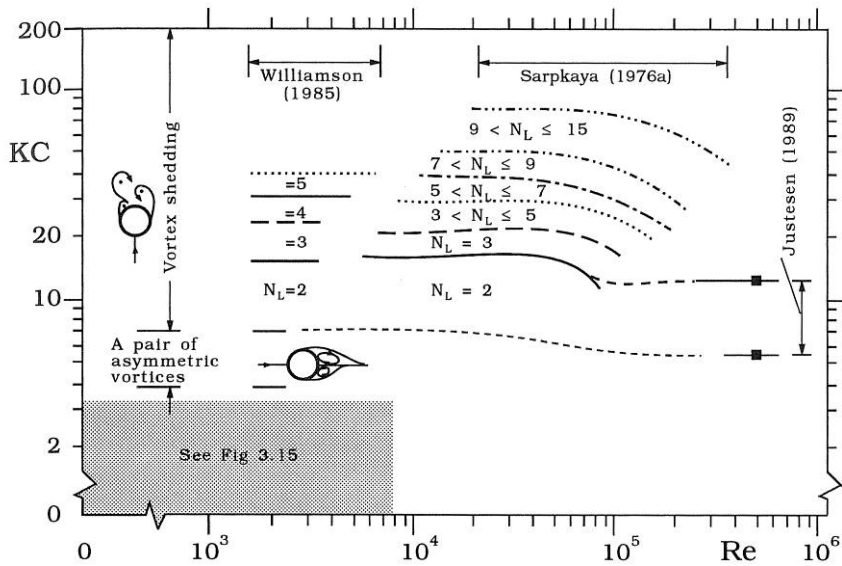


Figure 1-22: Shedding regimes around a smooth, circular cylinder; Sumer and Fredsøe (1997)

1.2.4 Streamline contraction

When combining the effect of the streamlines' contraction with the horseshoe vortex, the amplification factor for a steady current increases from $O(5)$ to $O(10)$ (Sumer and Fredsøe (2002), Figure 1-23).

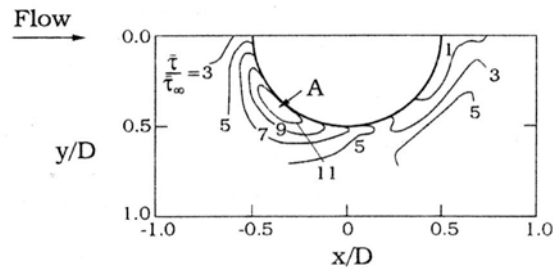


Figure 1-23: Amplification of bed shear-stress due to the presence of a single, vertical pile. $D = 0.075$ m, $U = 0.3$ m/s, $d = 0.2$ m, $\delta/D = 2.7$, $Re_D = 2.3 \times 10^4$; Sumer and Fredsøe (2002), originally from Hjorth (1975)

The effect of the contraction of the streamlines in case of a wave field is shown in Figure 1-24. The figure shows the combined effect of an increase in the bed shear-stress due to a contraction of the streamlines and the formation of the horseshoe vortex. When comparing Figure 1-23 and Figure 1-24, we see that the amplification of the bed shear-stress $\alpha = O(10)$ in case of a steady current, while it is $\alpha = O(4)$ in the case of waves. In Sumer and Fredsøe (2002), this is attributed to the stronger presence of the horseshoe vortex in case of a steady current.

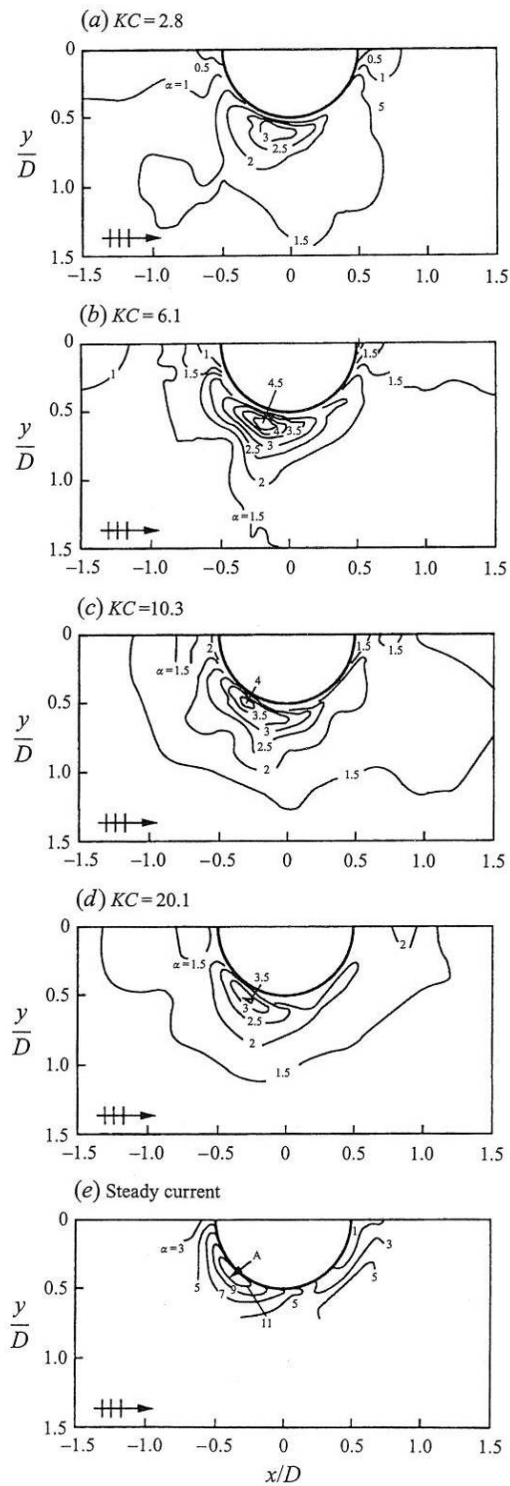


Figure 1-24: Amplification of bed shear-stress for different KC numbers; Sumer et al. (1997)

1.3 Scour around a monopile foundation

As described in the introduction, the changes in the flow pattern, caused by a structure placed within the flow, will increase the local sediment transport capacity and thus induce local erosion around this structure when it is placed on an erodable bottom. The term scour is used to denote the erosion caused by a structure as opposed to other erosion processes. This paragraph is dedicated to local scour around monopile foundations, as knowledge of the design scour depth is essential to assess the necessity of a scour protection. Figure 1-25 gives a definition sketch of a typical scour hole around a monopile foundation in a steady flow. The shape of a scour hole can basically be represented by a truncated cone, which is however slightly asymmetrical around the pile axis.

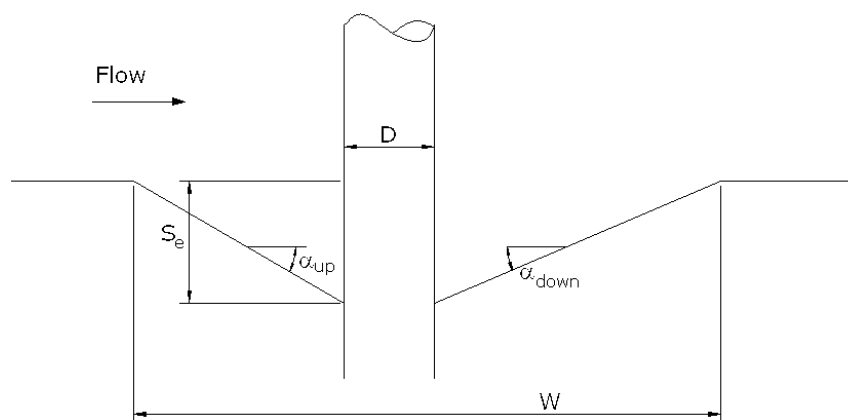


Figure 1-25: Definition sketch of scour dimensions

Local scour around cylindrical piles has been studied extensively, both in uniform flow and in oscillatory flow (waves). Scour around bridge piers (uniform flow) has been studied elaborately, as it is one of the main causes of bridge failures (Hjorth (1975), Breusers and Raudkivi (1991), Kobayashi and Oda (1994), Chiew (1995), Hoffmans and Verheij (1997), May et al. (2002), Ballio et al. (2004), Kho et al. (2004), Link and Zanke (2004a), Link and Zanke (2004b), Mashahir et al. (2004)). In the marine environment, the study of local scour becomes more complex due to the time-varying nature of the flow. Recently, many researchers focussed on the local scour around vertical piles in a marine environment (uniform current and waves, tidal currents): Kawata and Tsuchiya (1988), Saito et al. (1990), Hoffmans and Verheij (1997), Whitehouse (1998), Sumer et al. (1992b), Sumer and Fredsøe (1999), Carreiras et al. (2000), Sumer and Fredsøe (2001), Sumer and Fredsøe (2002), Myrhaug and Rue (2003), den Boon et al. (2004), Harris et al. (2004), Roulund et al. (2005), Gothel and Zielke (2006), Jensen et al. (2006), Whitehouse et al. (2006), Sumer et al. (2007)

It is not the scope of this thesis to give a complete overview of all the available references on scour around vertical piles, but rather to give a summary of the physics influencing the scour process and to provide some formulae to calculate the dimensions of a scour hole. A clear overview of the scour process around a

vertical pile in a marine environment is provided by Whitehouse (1998) and Sumer and Fredsøe (2002).

1.3.1 General description of scour development

1.3.1.1 Local scour versus global scour

When studying scour around an offshore structure, two main types of scour can be identified: one related to the local influence of the structure on the flow pattern, termed local scour, and one related to the overall seabed movement, termed global scour. Global scour can be caused by either global seabed movement i.e. sand waves or a more general influence of a composite structure, like a jack-up platform on the flow pattern. Because global scour is very site specific, only local scour, caused by a single vertical cylinder is discussed, although global scour can have a considerable effect on the foundation design, and the scour protection design needs to be adapted (e.g. Hansen and Gislason (2005)).

1.3.1.2 Equilibrium scour depth and time-scaling of scour

After a pile is installed in the seabed, it takes some time for the scour hole to develop and reach its equilibrium stage (Figure 1-26).

Although generally it is the equilibrium scour depth which is most interesting for the design, it is recommended to have an insight in the time development of the scour hole, for example to estimate whether the equilibrium scour depth will be reached during a storm period (applicable for cohesive soils), to assess the time-window for the installation of a scour protection or to assess the installation time in the case where the developed scour hole is backfilled with scour protection material (e.g. Hansen and Gislason (2005), Cefas (2006)).

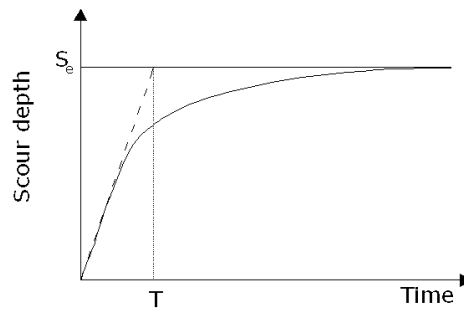


Figure 1-26: Time development of scour depth

Several formulae exist to account for the time-development of the scour hole. The following relationship is suggested by Sumer et al. (1992a) for the depth of the scour hole as a function of time $S(t)$:

$$S(t) = S_e \left(1 - \exp(-t/T)\right) \quad (1.45)$$

in which S_e is the equilibrium scour depth and the parameter T is defined as the time scale of the scour process, which represents the time during which a substantial amount of the scour hole has developed (Figure 1-26).

In Whitehouse (1998) the time scale T in equation (1.45) is defined as the time which is necessary to develop a scour depth which has 63% of the equilibrium value.

In Melville and Chiew (1999), the time evolution of a set of scour tests is well represented by:

$$\frac{S(t)}{S_e} = \exp \left\{ -0.03 \left| \frac{U_{cr}}{U} \ln \left(\frac{t}{t_e} \right) \right|^{1.6} \right\} \quad (1.46)$$

in which U represents the average current velocity; U_{cr} is the critical flow velocity and t_e is the time for the equilibrium scour depth to develop:

$$\begin{aligned} t_e (\text{days}) &= 48.26 \frac{D}{U} \left(\frac{U}{U_{cr}} - 0.4 \right) & \frac{d}{D} > 6 \\ t_e (\text{days}) &= 30.89 \frac{D}{U} \left(\frac{U}{U_{cr}} - 0.4 \right) \left(\frac{d}{D} \right)^{0.25} & \frac{d}{D} \leq 6 \end{aligned} \quad (1.47)$$

In Ballio et al. (2004) it is concluded that the time to reach equilibrium in live-bed situations rapidly decreases with increasing flow velocities.

1.3.1.3 Clear-water scour versus live-bed scour

A distinction is made between clear-water scour, with no sediment transport outside the influenced pile zone ($\theta < \theta_{cr}$ away from the pile) and live-bed scour, where sediment transport exists over the entire bed ($\theta > \theta_{cr}$ everywhere).

Clear-water scour depends strongly on the Shields parameter θ (Figure 1-27, Breusers and Raudkivi (1991), Sumer and Fredsøe (2002)). For very small values of θ , the amplified bed shear-stress near the pile is too small to induce sediment transport and there is no scour around the pile. Once scour is initiated, the scour depth increases rapidly with θ and reaches a maximum for $\theta = \theta_{cr}$ in the undisturbed area. At that moment, sediment transport is initiated over the whole bed, and the live-bed scour regime starts. The live-bed scour varies only slightly with θ as variations in θ result in a changed sediment transport both in and outside the scour hole. Figure 1-27 shows that the equilibrium clear-water scour develops slower than live-bed scour, but has a higher maximum equilibrium depth. Breusers and Raudkivi (1991) note that the maximum equilibrium clear-water scour depth is approximately 10% higher than the (mean) live-bed equilibrium scour depth.

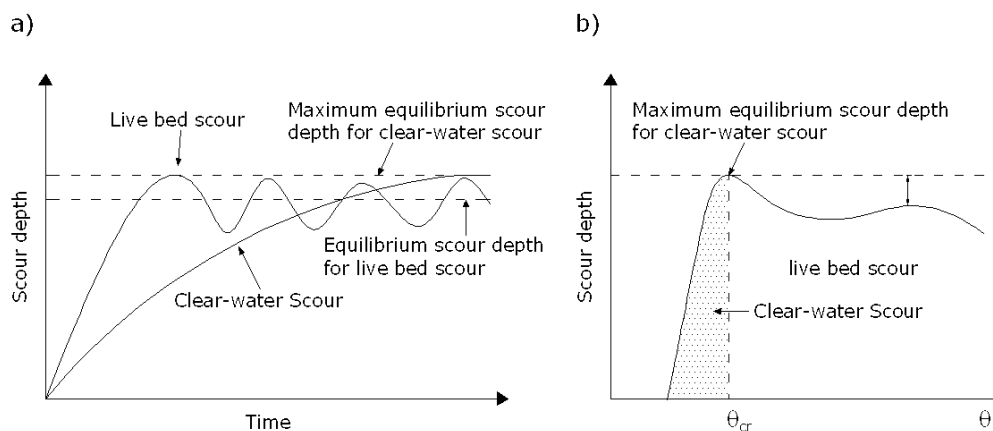


Figure 1-27: Equilibrium scour depth in clear-water scour versus live-bed scour; after Breusers and Raudkivi (1991)

1.3.2 Scour depth around a vertical pile

One of the most important parameters regarding scour for the design of the foundation is the maximum scour depth which is to be expected in the lifespan of the foundation. Most scour relations are derived from experimental data. Comparison between laboratory and field measurements however (Lee et al. (2004)) and comparison of calculations with measured prototype scour holes (Harris et al. (2004), LICEngineering (2004), Rudolph et al. (2004), Cefas (2006), Noormets et al. (2006)) show a fairly good agreement between empirically predicted scour depths and prototype scour depths.

Most scour formulae are developed to assess the maximum scour depth in non-cohesive soils. In this paragraph scour in steady currents, scour in waves and scour in combined waves and currents are treated successively. A separate paragraph is devoted to scour in cohesive soils, as the behaviour is quite different of that of non-cohesive soils and research on this topic has only started very recently.

Although for the dynamic behaviour of the structure, the time variation of the scour depth plays an important role, only limited knowledge is available on this subject. It is acknowledged that the most frequently occurring scour depth is less than the maximum scour depth given by the equations following below (Whitehouse (1998), Thomsen (2006)).

1.3.2.1 Scour depth in steady current

Many laboratory studies have been performed to measure local scour around vertical structures, such as bridge piers, in a steady current. Below, a summary of the most used scour formulae is given.

In Breusers and Raudkivi (1991), relationship (1.48) is suggested for the clear-water equilibrium scour depth S_e and equation (1.49) for the equilibrium live-bed scour depth:

$$\frac{S_e}{D} = 2.3 \cdot K_s K_\sigma K_\alpha K_{si} K_d \quad (1.48)$$

$$\frac{S_e}{D} = 2.3 \cdot K_s K_\alpha K_{si} K_d \quad (1.49)$$

with:

K_s a pier shape factor = 1 for cylindrical piles

K_σ a factor depending on grain size distribution $\sigma_g = d_{84}/d_{50}$ (Figure 1-28)

K_α a pier alignment factor = 1 for a cylindrical pile

K_{si} a pier size factor = 1 for the relevant values of D/d_{50} in a marine environment

K_d , a flow depth factor = 1 for $d/D > 3$, according to Figure 1-29 for $d/D < 3$.

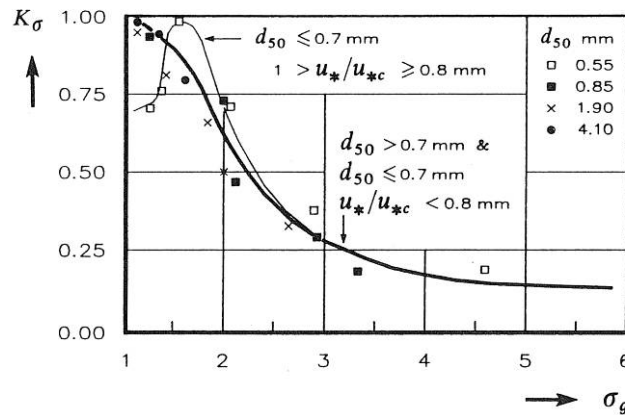


Figure 1-28: K_σ as a function of the geometric standard deviation of the particle size distribution $\sigma_g = d_{84}/d_{50}$; Breusers and Raudkivi (1991)

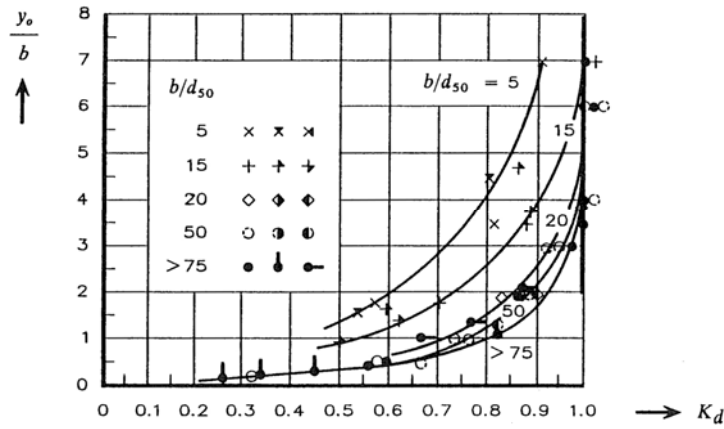


Figure 1-29: K_d as a function of the water depth to pile size ratio (from Breusers and Raudkivi (1991))

In Sumer et al. (1992b), the following, currently frequently used relationship, is suggested, valid for live-bed scour:

$$\frac{S_e}{D} = 1.3 + \sigma_s \quad (1.50)$$

with σ_s the standard deviation of the scour depth = 0.7.

Chiew (1995) found the following empirical relationship for the equilibrium clear-water scour depth:

$$\frac{S_e}{D} = 3.77 \frac{U_c}{U_{cr}} - 1.13 \quad \text{for } 0.3 \leq \frac{U_c}{U_{cr}} \leq 1 \quad (1.51)$$

in which U_c is the depth averaged velocity and U_{cr} is the critical velocity. This formula leads to a maximum value of $S_e/D = 2.64$. Although most found that scour developed once $U_c/U_{cr} > 0.5$, Chiew (1995) finds that motion is initiated once $U_c/U_{cr} > 0.3$.

Melville (1997) suggests to calculate the equilibrium scour depth S_e as:

$$S_e = K_{yD} K_I K_d K_S K_\alpha K_G \quad (1.52)$$

in which K_{yD} depends on the pile size to flow depth D/d :

$$\begin{aligned}
K_{yD} &= 2.4D && \text{for } \frac{D}{d} < 0.7 \\
K_{yD} &= 2\sqrt{dD} && \text{for } 0.7 < \frac{D}{d} < 5 \\
K_{yD} &= 4.5d && \text{for } \frac{D}{d} > 5
\end{aligned} \tag{1.53}$$

and K_I depends on the flow intensity:

$$\begin{aligned}
K_I &= \frac{U_c}{U_{cr}} && \text{for } \frac{U_c}{U_{cr}} < 1 \\
K_I &= 1 && \text{for } \frac{U_c}{U_{cr}} > 1
\end{aligned} \tag{1.54}$$

with U_c the mean current velocity and U_{cr} the critical velocity.

K_d depends on the pile size to particle size ratio $\frac{D}{d_{50}}$:

$$\begin{aligned}
K_d &= 0.57 \log \left(2.24 \frac{D}{d_{50}} \right) && \text{for } \frac{D}{d_{50}} < 25 \\
K_d &= 1 && \text{for } \frac{D}{d_{50}} > 1
\end{aligned} \tag{1.55}$$

K_s accounts for the shape of the pile = 1 for a cylindrical pile.

K_α accounts for the alignment of the pile = 1 for a cylindrical pile.

And K_G accounts for the channel geometry = 1 for a wide channel (sea).

The critical velocity U_{cr} is defined as (1.56) in Melville (1997):

$$\frac{U_{cr}}{u_{*cr}} = 5.75 \log \left(5.53 \frac{d}{d_{50}} \right) \tag{1.56}$$

$$\begin{aligned}
\text{with } u_{*cr} &= 0.0115 + 0.0125d_{50}^{1.4}, && 0.1 \text{ mm} < d_{50} < 1 \text{ mm} \\
u_{*cr} &= 0.0305d_{50}^{0.5} - 0.0065d_{50}^{-1}, && 1 \text{ mm} < d_{50} < 100 \text{ mm}
\end{aligned} \tag{1.57}$$

where u_{*cr} is in m/s and d_{50} is in mm.

In Whitehouse (1998), the same expression for live-bed scour (1.50) is retained as in Sumer et al. (1992b). For clear-water scour, the following is suggested:

$$\frac{S_e}{D} = 1.3 \left[2 \sqrt{\frac{\theta}{\theta_{cr}}} - 1 \right] \quad (1.58)$$

in which θ and θ_{cr} respectively are the Shields parameter and the critical Shields parameter (equations (1.2) and (1.33)).

In Hoffmans and Verheij (1997), equation (1.59) is used for clear-water scour ($0.5 < U_c/U_{cr} < 1$), and equation (1.60) gives the equilibrium steady current scour depth in a live-bed situation. When the mean approach velocity is smaller than half of the critical velocity, no scouring will be predicted.

$$\frac{S_e}{D} = 2K_i \left(2 \frac{U_c}{U_{cr}} - 1 \right) \cdot \tanh \left(\frac{d}{D} \right) \quad (1.59)$$

$$\frac{S_e}{D} = 1.5K_i \tanh \left(\frac{d}{D} \right) \quad (1.60)$$

in which K_i is a correction factor, depending on pile shape, influence of group of piles, gradation of bed material and factor for orientation of the flow:

$$K_i = K_s K_\alpha K_\sigma K_{gr} \quad (1.61)$$

with K_s , K_α , K_σ as in (1.49) and K_{gr} a factor to be applied for a group of piers = 1 for a single pile.

In Schiereck (2001), the following equation is proposed:

$$\frac{S_e}{D} = 2K_s K_\alpha K_U \tanh \left(\frac{d}{D} \right) \quad (1.62)$$

with again K_s a shape factor = 1 for a cylinder, K_α a factor for the angle of attack = 1 for a cylindrical pile and K_U a velocity factor:

$$\begin{aligned}
K_U &= 0 && \text{for } \frac{U_c}{U_{cr}} < 0.5 \\
K_U &= 2 \frac{U_c}{U_{cr}} - 1 && \text{for } 0.5 < \frac{U_c}{U_{cr}} < 1 \\
K_U &= 1 && \text{for } \frac{U_c}{U_{cr}} > 1
\end{aligned} \tag{1.63}$$

Sheppard and Miller Jr (2006) give equation (1.64) for the clear-water scour range ($0.47 \leq U_c/U_{cr} \leq 1$), equation (1.65) for the live-bed scour range, up to the live-bed peak ($1 < U_c/U_{cr} \leq U_{lp}/U_{cr}$) and equation (1.66) for the live-bed scour range above the live-bed peak ($U_c/U_{cr} > U_{lp}/U_{cr}$):

$$\frac{S_e}{D} = 2.5 f_1 \left(\frac{d}{D} \right) f_2 \left(\frac{D}{d_{50}} \right) \left\{ 1 - 1.75 \left[\ln \left(\frac{U_c}{U_{cr}} \right) \right]^2 \right\} \tag{1.64}$$

$$\frac{S_e}{D} = f_1 \left(\frac{d}{D} \right) \left[2.2 \left(\frac{U_c/U_{cr} - 1}{U_{lp}/U_{cr} - 1} \right) + 2.5 f_2 \left(\frac{D}{d_{50}} \right) \left(\frac{U_{lp}/U_{cr} - U_c/U_{cr}}{U_{lp}/U_{cr} - 1} \right) \right] \tag{1.65}$$

$$\frac{S_e}{D} = 2.2 f_1 \left(\frac{d}{D} \right) \tag{1.66}$$

with

$$f_1 \left(\frac{d}{D} \right) \equiv \tanh \left[\left(\frac{d}{D} \right)^{0.4} \right] \tag{1.67}$$

$$f_2 \left(\frac{D}{d_{50}} \right) \equiv \frac{D/d_{50}}{0.4(D/d_{50})^{1.2} + 10.6(D/d_{50})^{-0.13}} \tag{1.68}$$

The value of U_{lp} is the velocity at the live-bed scour peak and is called the "live-bed peak velocity". According to Sheppard and Miller Jr (2006) it can be calculated by simultaneously fulfilling the following criteria (according to van Rijn (1993)):

$$\begin{aligned}
Fr &= \frac{U_c}{\sqrt{gd}} > 0.8 \\
\frac{\tau_b - \tau_{cr}}{\tau_{cr}} &> 25
\end{aligned} \tag{1.69}$$

1.3.2.2 Scour depth in waves

Due to diffraction effects, local scour due to waves around slender piles differs strongly from scour around large piles (Sumer and Fredsøe (2002)). It is commonly accepted that diffraction effects around a vertical cylinder become important when the pile diameter to wave length ratio $D/L > 0.2$ (Isaacson (1979)), or $KC > O(1)$ (Sumer and Fredsøe (2002)). In this paragraph, only scour around slender piles is considered, as a monopile foundation for an offshore wind turbine always has a value of D/L which is significantly smaller than 0.2 in storm conditions.

As mentioned before, the formation of the horseshoe vortex undergoes substantial changes and the lee-wake vortices contribute significantly to the transportation of sediment in the case of waves (Kawata and Tsuchiya (1988), Sumer and Fredsøe (1999)). As both phenomena depend strongly on the KC number, it is expected and confirmed (Sumer and Fredsøe (1999)) that the KC number (equation (1.3)) is critical when it comes to the formation of the local scour hole around a vertical pile.

Sumer et al. (1992b) deduce the following empirical equation for the scour depth in regular waves:

$$\frac{S_e}{D} = A \left\{ 1 - \exp \left[-B(KC - C) \right] \right\}, \quad KC \geq 6 \quad (1.70)$$

with $A = 1.3$, $B = 0.03$ and $C = 6$ for vertical cylindrical piles. Equation (1.70) is valid for live-bed conditions. For large values of KC , the scour depth tends towards the equilibrium scour depth for a steady current. For smaller values of KC , the scour depth is smaller in the case of waves, than it is in the case of a steady current.

For KC numbers, smaller than 6, Sumer et al. (1992b) conclude that the scour depth is practically nil. De Moor and Janda (2005) however found values of $S_e/D = 0.2$ for KC numbers smaller than 6.

For irregular waves, Sumer and Fredsøe (2001) found that their empirical formula (1.70) can be used for irregular waves, provided that the KC number is calculated as:

$$KC = \frac{U_m T_p}{D} \quad (1.71)$$

with T_p the irregular wave peak period and U_m defined as:

$$U_m = \sqrt{2} \sigma_U \quad (1.72)$$

with σ_U the root mean square value of the orbital velocity U_w at the bed:

$$\sigma_U^2 = \int_0^{\infty} S(f) df \quad (1.73)$$

in which $S(f)$ = the power spectrum of U_w and f is the frequency.

Carreiras et al. (2000) conclude from their experimental results that a better fit was found when in equation (1.30) $B = 0.06$ and The Keulegan Carpenter number KC is calculated as:

$$KC = \frac{2\pi A}{D} \quad (1.74)$$

with A the stroke of the motion close to the bottom, computed by integrating the measured local velocity.

A statistical approach is used by Myrhaug and Rue (2003) to describe scour around a vertical pile in irregular waves. They conclude that the 1/10th value (average value of 1/10th highest scour depths) of the estimated scour depth $(S/D)_{1/10}$ gives the best result compared to the method of Sumer and Fredsøe (2001), described above.

Kobayashi and Oda (1994) investigated the location and magnitude of the maximum scour depth for waves in the clear-water regime. They distinguish three different scour types. They found a distinct relationship between scour type and depth and KC -number, but noticed a poor relationship between the maximum scour depth and the Shields parameter.

1.3.2.3 Scour depth in combined current and waves

Generally, it is accepted that when waves are superimposed on a current, the depth of the scour hole decreases. On the other hand, both Kawata and Tsuchiya (1988) and Sumer and Fredsøe (2001) note that for small KC numbers, even a slight current superimposed on the waves can significantly increase the scour depth.

The scour depth in combined waves and current depends both on the KC number and on the dimensionless parameter U_{cw} (Sumer and Fredsøe (2001)):

$$U_{cw} = \frac{U_c}{U_c + U_m} \quad (1.75)$$

with U_c the current velocity and U_m the amplitude of the wave orbital velocity near the bottom in case of regular waves or equation (1.72) in case of irregular waves.

For a small value of U_{cw} , the lee-wake vortices play an important role, as for large U_{cw} values, the horseshoe vortex is predominant. According to Sumer and Fredsøe (2002), for small values of U_{cw} , the scour depth tends towards the wave alone case (equation (1.70)), whereas for large values of U_{cw} , the scour depth

tends towards equation (1.50). According to Sumer and Fredsøe (2002), the direction of the current (following or opposing the waves) does not have a large influence on the scour depth.

Sumer and Fredsøe (2002) suggest the following expression to assess the scour depth in combined waves and current:

$$\frac{S}{D} = \frac{S_c}{D} \left[1 - \exp\{-B(KC - C)\} \right], \quad KC \geq C \quad (1.76)$$

with S_c the equilibrium scour depth in the current alone case and the following expression for the parameters B and C :

$$B = 0.03 + \frac{3}{4} U_{cw}^{2.6} \quad (1.77)$$

$$C = 6 \exp(-4.7 U_{cw}) \quad (1.78)$$

Sumer and Fredsøe (2002) note however that expressions (1.76) to (1.78) are only valid for a live-bed regime and for $KC \leq 30$.

Whitehouse et al. (2006) found however that in some cases the scour depth does not decrease when a wave is superimposed on a current. Even though $U_{cw} \approx 0.5$, they found $S_e/D = 1.5$ for a combined wave and current situation, which however still lies within the value suggested by equation (1.50).

As mentioned above, it is generally accepted that the scour depth around a single pile decreases when waves are superimposed on a current. In the case of breaking waves superimposed on a current however, there is some uncertainty concerning the local scour depth. Bijker and de Bruyn (1988) measured scour depths in combined breaking waves and current which are larger than scour depths in steady currents. Both Carreiras et al. (2000) and Jensen et al. (2006) observe however that the scour pattern in breaking wave experiments is a combination of local scour and larger scale bed dynamics, leading to the conclusion that breaking waves do not increase the local scour when superimposed on a steady current.

1.3.2.4 Scour depth in cohesive soils

It is only since very recently that local scour around vertical cylinders in cohesive soils is investigated (Kho et al. (2004), Sumer et al. (2004), Sumer et al. (2007)). Both experiments in a steady current (Kho et al. (2004)) and in waves (Sumer et al. (2004)) show that the local scour depth in cohesive soils is remarkably larger than in the case of non-cohesive soils, with an increase in scour depth as a function of clay and silt content.

Sumer et al. (2004) and Sumer et al. (2007) note that the increase in scour depth strongly depends on the relative density of the silt. In Sumer et al. (2004), the scour depth in waves was increased with a factor 1.6 – 2 compared

to scour depths in a non-cohesive soil. Furthermore, they noted that the scour depth becomes practically independent of the Shields parameter θ , in a live-bed situation.

Kho et al. (2004) measure values of S/D up till 2.6 and predict values of S_e/D up till 3.7 in steady currents. They suggest the following relationship for the scour depth in cohesive soils:

$$\frac{S_e}{D} = 0.0314C + 1.5265 \quad (1.79)$$

with C the clay content of the soil [%]. Clay contents varying between 0 and 50% were tested and the silt content of the material was in all tests equal to the clay content.

Both studies indicate further that the time-development of the scour process is strongly prolonged in cohesive soils.

Considering the large increase of the scour depth, clearly more research concerning scour in cohesive soils is required.

1.3.3 Extent of scour

The shape of a scour hole can basically be represented by a truncated cone, which is however slightly asymmetrical around the pile axis. The dimensions of the scour hole can be represented by the slopes of the scour hole α_{up} and α_{down} which, together with the scour depth determine the extent of the scour hole W (Figure 1-25):

$$W = D + S_e \left(\cot(\alpha_{up}) + \cot(\alpha_{down}) \right) \quad (1.80)$$

In the case of a steady current, the upstream slope of the scour hole α_{up} is observed to be more or less equal to the angle of internal friction ϕ (Hoffmans and Verheij (1997)), while the downstream slope α_{down} is generally somewhat less steep and approximately equal to 25° according to Sumer and Fredsøe (2002), or approximately equal to $1/2 \alpha_{up}$, according to Hoffmans and Verheij (1997).

The side slope of the scour hole, perpendicular to the flow direction is comparable to α_{up} (and thus the angle of internal friction), which implies that the width of the scour hole in the direction perpendicular to the flow W_p is approximately equal to:

$$W_p = D + 2S_e \cot(\phi) \quad (1.81)$$

In the case of a tidal current, which is strong enough to reach equilibrium scour in one tide, both slopes tend towards a less steep slope, equal to α_{down} (Frigaard and De Vos (2006)).

In the case of cohesive soils, the upstream slope α_{up} of the scour hole becomes steeper (Kho et al. (2004)).

1.4 Conclusions

The frictional force which is exerted by the flow on the bed is characterized by the bed shear-stress [N/m^2], which forms the foundation for the development of this thesis. The bed shear stress is proportional to the square of the flow velocity. It is both the cause of sediment transport and thus of the development of scour around a structure, and a determining factor in the required stone size for the scour protection. A review of the existing formulae to quantify the bed shear-stress is given in this chapter. A clear distinction can be made between the bed shear-stress in a steady current and the bed shear-stress in a wave climate, where the bed shear stress is significantly higher in the latter situation. In most marine environments, both currents and waves occur simultaneously. Difficulties arise because these interact and their combined influence is not the same as a linear sum of their separate influences. Several theories on how to combine the bed shear-stresses in a combined hydrodynamical loading are discussed in this chapter.

When the bed shear-stress exceeds a critical value, grains are entrained by the flow and transport of bed material is initiated. The Shields parameter θ_{cr} is the best-known and most used in research on the threshold of motion in uniform flow. In chapter 4, the Shields parameter is used to determine the entrainment of the stones when a pile is placed in the flow.

When a structure is placed in a flow, it has an influence on the local flow pattern. The flow experiences the following changes when a vertical pile is placed on a sea bed:

- a downflow is formed in front of the pile
- a horseshoe vortex originates in front of the pile
- a vortex flow pattern is formed at the lee-side of the pile (usually accompanied by vortex shedding)
- the streamlines are contracted at the side edges of the pile

Together, these cause an increase in the bed shear stress around the base of the structure. The increase is expressed as an amplification of the undisturbed bed shear-stress and depends on the flow conditions. In a steady current, the amplification of the bed shear-stress can be as much as 10, for a vertical cylindrical pile, where it is approximately equal to 4 in a wave climate.

The increase in bed shear stress causes a local increase in sediment transport capacity, leading to a scour hole around the base of the foundation. The most important parameter to describe the scour is the depth of the scour hole and the most frequently used empirical formulae to determine the scour depth are given at the end of this chapter. According to these formulae, the maximum expected scour depth varies between 1 and 2 times the pile diameter.

References

- Ali, K.H.M. and Karim, O., 2002. Simulation of flow around piers. *Journal of Hydraulic Research*, 40(2): 161-174.
- Baker, C.J., 1979. The laminar horseshoe vortex. *Journal of Fluid Mechanics*, 95: 347-367.
- Ballio, F., Radice, A. and Franzetti, S., 2004. An experimental study of live-bed scour at bridge abutments, *International Conference on Scour and Erosion*, Nanyang University, Nanyang, Singapore. .
- Bijker, E.W. and de Bruyn, C.A., 1988. Erosion around a pile due to current and breaking waves. Publ by ASCE, New York, NY, USA, Malaga, Spain, pp. 1368-1381.
- Bollaert, E. and Hofland, B., 2004. The influence of flow turbulence on particle movement due to jet impingement, *International Conference on Scour and Erosion*, Nanyang University, Nanyang, Singapore.
- Breusers, H.N.C. and Raudkivi, A.J., 1991. *Scouring*. Balkema.
- Carreiras, J., Larroudé, P., Seabra-Santos, F. and Mory, M., 2000. *Wave Scour Around Piles*, Coastal Engineering, Sydney, Australia.
- Cefas, 2006. *Scroby Sands Offshore Wind Farm – Coastal Processes Monitoring*. Final Report for the Department of Trade and Industry. Contract AE0262, Cefas Lowestoft Laboratory, Suffolk.
- Chiew, Y.M., 1995. Mechanics of Riprap Failure at Bridge Piers. *Journal of Hydraulic Engineering*, 121(9): 635-643.
- CIRIA/CUR, 1991. *Manual on the use of rock in coastal and shoreline engineering*. CUR 154.
- Colebrook, C.F. and White, C.M., 1937. Experiments with Fluid Friction in Roughened Pipes. *Proceedings of the Royal Society of London. Series A, Mathematical and Physical Sciences*, 161(906): 367-381.
- Dargahi, B., 1989. The turbulent flow field around a circular cylinder. *Experiments in Fluids*, 8(1): 1-12.
- De Moor, F. and Janda, E., 2005. *Experimenteel onderzoek naar de erosie en erosiebescherming rond palen onder gecombineerde actie van stroming en golven*. MSc Thesis, Ghent University, Ghent, 167 pp.
- Delgado Blanco, M.R., Willems, M., Verhoeven, R., De Mulder, T., R., B. and Monbaliu, J., 2004. 2D experimental study of waves and current contribution to the nearbed velocities and shear stresses field, 23th *International Conference on Offshore Mechanics and Arctic Engineering*, Vancouver, Canada.
- den Boon, J.H., Sutherland, J., Whitehouse, R., Soulsby, R., Stam, C.J.M., Verhoeven, K., Høgedal, M. and Hald, T., 2004. *Scour Behaviour and Scour Protection for Monopile Foundations of Offshore Wind Turbines*, European Wind Energy Conference & exhibition (EWEC), London, UK.
- Dixen, M., Hatipoglu, F., Sumer, B.M. and Fredsøe, J., 2008. Wave boundary layer over a stone-covered bed. *Coastal Engineering*, 55(1): 1-20.
- Dou, X.S. and Jones, J.S., 2000. *A New Sediment Transport Formula for Local Scour Prediction*, Building Partnerships- 2000 Joint Conference on Water Resource Engineering and Water Resources Planning & Management, Minneapolis, Minnesota.
- Fredsøe, J. and Deigaard, R., 1992. *Mechanics of Coastal Sediment Transport*. Advanced series on Ocean Engineering, Vol. 3. World Scientific.

- Frigaard, P. and De Vos, L., 2006. Offshore Wind Turbines situated in areas with Strong Currents: Laboratory Tests, Offshore Wind Turbines situated in areas with Strong Currents. Offshore Center Danmark, Esbjerg, Denmark.
- Gothel, O. and Zielke, W., 2006. Numerical Modelling of Scour at Offshore Wind Turbines. COASTAL ENGINEERING CONFERENCE, 30(3): 2343.
- Hansen, N.-E.O. and Gislason, K., 2005. Movable scour protection on highly erodible sea bottom, International Coastal Symposium.
- Harris, J.M., Herman, W.M. and Cooper, B.S., 2004. Offshore windfarms - an approach to scour assessment, International Conference on Scour and Erosion, Nanyang University, Nanyang, Singapore.
- Hjorth, P., 1975. Studies on the nature of local scour. Institute of Technology, Dept. of Water Resources Engineering.
- Hoffmans, G.J.C.M. and Verheij, H.J., 1997. Scour manual. A.A. Balkema, Rotterdam, Netherlands ; Brookfield, VT, xv, 205 p. pp.
- Hofland, B., 2005. Rock & Roll: Turbulence-induced Damage to Granular Bed Protections. Department of Civil Engineering and Geosciences, Delft University of Technology.
- Isaacson, M., 1979. Wave-induced forces in the diffraction regime. Mechanics of Wave-Induced Forces on Cylinders, ed. TL Shaw, Pitman Advanced Publishing Program: 68-69.
- Jensen, M.S., Juul Larsen, B., Frigaard, P., De Vos, L., Christensen, E.D., Asp Hansen, E., Solberg, T., Hjertager, B.H. and Bove, S., 2006. Offshore Wind Turbines Situated in Areas with Strong Currents, Offshore Center Danmark Esbjerg, Danmark.
- Kawata, Y. and Tsuchiya, Y., 1988. Local scour around cylindrical piles due to waves and currents combined. Publ by ASCE, New York, NY, USA, Malaga, Spain, pp. 1310-1322.
- Kho, K.T., Valentine, E. and Glendinning, S., 2004. An experimental study of local scour around circular bridge piers in cohesive soils, International Conference on Scour and Erosion, Nanyang University, Nanyang, Singapore.
- Kobayashi, T., 1992. 3-D Analysis of Flow around a Vertical Cylinder on a Scoured Bed. Proceedings of the 23rd International Coastal Engineering Conference, 3: 3482-3495.
- Kobayashi, T. and Oda, K., 1994. Experimental study on developing process of local scour around a vertical cylinder. Proc. 24th Coast. Engrg. Conf. ASCE, Newyork: 1284-1297.
- Lee, S., Sturm, T.W., Gotvald, A. and Landers, M., 2004. Comparison of laboratory and field measurements of bridge pier scour, International Conference on Scour and Erosion Nanyang University, Nanyang, Singapore.
- LICengineering, A.S., 2004. Scroby Sands Wind Farm, Offshore foundations series.
- Link, O. and Zanke, U., 2004a. Influence of flow depth on scour at a circular pier in uniform coarse sand, International Conference on Scour and Erosion, Nanyang University, Nanyang, Singapore.
- Link, O. and Zanke, U., 2004b. On the time-dependent scour-hole volume evolution at a circular pier in uniform coarse sand, International Conference on Scour and Erosion, Nanyang University, Nanyang, Singapore.
- Liu, Z., 2001. Sediment transport, Aalborg.

- Madsen, O.S. and Wood, W., 2002. Part III, chapter 6: Sediment transport outside the surf zone, Coastal Engineering Manual. U.S. Army Corps of Engineers, Washington, DC.
- Mashahir, M.B., Zarrati, A.R. and Rezayi, M.J., 2004. Time development of scouring around a bridge pier protected by collar, International Conference on Scour and Erosion, Nanyang University, Nanyang, Singapore.
- May, R.W.P., Ackers, J.C. and Kirby, A.M., 2002. Manual on Scour at Bridges and Other Hydraulic Structures. CIRIA.
- Melville, B.W., 1997. Pier and Abutment Scour: Integrated Approach. Journal of Hydraulic Engineering, 123(2): 125-136.
- Melville, B.W. and Chiew, Y.M., 1999. Time Scale for Local Scour at Bridge Piers. Journal of Hydraulic Engineering, 125(1): 59-65.
- Melville, B.W. and Raudkivi, A.J., 1977. Flow Characteristics in Local Scour at Bridge Piers. Journal of Hydraulic Research, 15(4): 373-380.
- Myrhaug, D. and Rue, H., 2003. Scour below pipelines and around vertical piles in random waves. Coastal Engineering, 48(4): 227-242.
- Nielsen, P., 1992. Coastal Bottom Boundary Layers and Sediment Transport. Advanced Series on Ocean Engineering, Vol. 4. World Scientific.
- Noormets, R., Ernstsens, V.B., Bartholomä, A., Flemming, B.W. and Hebbeln, D., 2006. Implications of bedform dimensions for the prediction of local scour in tidal inlets: a case study from the southern North Sea. Geo-Marine Letters, 26(3): 165-176.
- Roulund, A., Sumer, B.M., Fredsoe, J. and Michelsen, J., 2005. Numerical and experimental investigation of flow and scour around a circular pile. Journal of Fluid Mechanics, 534: 351-401.
- Rudolph, D., Bos, K.J., Luijendijk, A.P., Rietema, K. and Out, J.M.M., 2004. Scour around offshore structures - analysis of field measurements, International Conference on Scour and Erosion, Nanyang University, Nanyang, Singapore.
- Saito, E., Sato, S. and Shibayama, T., 1990. Local Scour Around a Large Circular Cylinder Due to Wave Action, Coastal Engineering, pp. 1795-1804.
- Schiereck, G.J., 2001. Introduction to Bed, Bank and Shore Protection. Delft University Press.
- Sheppard, D.M. and Miller Jr, W., 2006. Live-Bed Local Pier Scour Experiments. Journal of Hydraulic Engineering, 132: 635-642.
- Shields, A., 1936. Anwendung der Aehnlichkeitsmechanik und der Turbulenzforschung auf die Geschiebepbewegung. Preussische Versuchsanstalt für Wasserbau und Schiffbau.
- Soulsby, R., 1997. Dynamics of Marine Sands: A Manual for Practical Applications. Thomas Telford.
- Soulsby, R.L. and Whitehouse, R.J.S., 1997. Threshold of sediment motion in coastal environments, Pacific Coasts and Ports'97, New Zealand, pp. 149-154.
- Sumer, B.M., Christiansen, N. and Fredsoe, J., 1992a. Time scale of scour around a vertical pile. Proc., 2 nd Int. Offshore and Polar Engineering Conf, San Francisco. International Society of Offshore and Polar Engineers(ISOPE), Cupertino, Calif. 3, 308-315.
- Sumer, B.M., Christiansen, N. and Fredsøe, J., 1997. The horseshoe vortex and vortex shedding around a vertical wall-mounted cylinder exposed to waves. Journal of Fluid Mechanics, 332: 41-70.

- Sumer, B.M. and Fredsøe, J., 1997. Hydrodynamics around cylindrical structures. Advanced series on ocean engineering. World Scientific, Singapore ; River Edge, NJ, xviii, 530 p. pp.
- Sumer, B.M. and Fredsøe, J., 1999. Wave scour around structures. Advances in Coastal and Ocean Engineering.
- Sumer, B.M. and Fredsøe, J., 2001. Scour around a Pile in Combined Waves and Current. *Journal of Hydraulic Engineering*, 127(5): 403-411.
- Sumer, B.M. and Fredsøe, J., 2002. The mechanics of scour in the marine environment. Advanced series on ocean engineering. World Scientific, River Edge, N.J., 536 pp.
- Sumer, B.M., Fredsøe, J. and Christiansen, N., 1992b. Scour Around Vertical Pile in Waves. *Journal of Waterway, Port, Coastal and Ocean Engineering*, 118(1): 15-31.
- Sumer, B.M., Hatipoglu, F. and Fredsøe, J., 2004. Wave scour around a vertical circular pile in silt, International Conference on Scour and Erosion, Nanyang University, Nanyang, Singapore.
- Sumer, B.M., Hatipoglu, F. and Fredsøe, J., 2007. Wave Scour around a Pile in Sand, Medium Dense, and Dense Silt. *Journal of Waterway, Port, Coastal, and Ocean Engineering*, 133: 14.
- Thomsen, J.M., 2006. scour in a marine environment characterized by currents and waves. MSc Thesis, Aalborg University, Aalborg, 98 pp.
- Umeda, S., Yuhi, M. and Ishida, H., 2003. Numerical study of three-dimensional flow fields around the base of a vertical cylinder in oscillatory plus mean flow. Coastal Structures 2003 - Proceedings of the Conference. American Society of Civil Engineers, Reston, VA 20191-4400, United States, Portland, OR, United States, pp. 751-763.
- Umeyama, M., 2005. Reynolds Stresses and Velocity Distributions in a Wave-Current Coexisting Environment. *Journal of Waterway, Port, Coastal, and Ocean Engineering*, 131: 203.
- van Rijn, L.C., 1993. Principles of Sediment Transport in Rivers, Estuaries and Coastal Seas. Aqua Publications.
- Whitehouse, R., 1998. Scour at marine structures : a manual for practical applications. Thomas Telford, London, xix, 198 p. pp.
- Whitehouse, R.J.S., Sutherland, J. and O'Brien, D., 2006. Seabed scour assessment for offshore windfarm, International Conference on scour and erosion, Nanyang University, Nanyang, Singapore.

Chapter 2. Evaluation of the effect of scour on foundation design

2.0 Introduction

This chapter will focus on the influence of a scour hole on the wind turbine's foundation design. Four aspects are to be considered:

- an increase of the maximum bending moment;
- a decrease in the pile's bearing capacity;
- an influence on the eigenfrequency of the pile and the resulting fatigue damage;
- free-spanning of the cables.

Today's operational offshore wind turbines (monopiles) have a diameter varying between 3 and 5.1m and are placed in water depths from 2 to 24m (Table 0-1). By way of illustration, two "typical" examples of an offshore wind turbine with monopile foundation are used throughout this chapter to provide the reader with an idea of the magnitude of the loads and the influence of the scour upon them. One of the monopiles is located in shallow water, while the other is located in a considerably larger water depth. The characteristics of the example monopile foundations are listed in Table 2-1.

Table 2-1: "Typical" offshore characteristics

Parameter	Unit	Case 1	Case 2
Pile diameter D	[m]	4.5	4.5
Water depth d	[m]	5	20
Significant wave height H_s	[m/s]	3.7	8
Wave period T_p	[s]	9	12
Keulegan Carpenter number KC	[-]	3.65	3.92
Pile diameter to wave length ratio D/L	[-]	0.07	0.04
Tidal current velocity U_c	[m/s]	1.5	1.5
Average wind speed V_w	[m/s]	8	8
Maximum wind speed $V_{w, \text{extr } 10 \text{ min}}$	[m/s]	50	50

The maximum scour depths which can be expected for the example foundations according to the formulae handed in chapter 1 are given in Table 2-2. As mentioned in chapter 1, the scour depth is largest in the current alone case and it is thus this situation which is considered.

Even when assuming a sediment with $d_{50} = 2\text{mm}$, a live bed situation is reached in both situations ($\theta > \theta_{cr}$). As sediment size is typically smaller than 2 mm, it can thus be assumed that a live bed situation is present independent of the sediment size. Equation (1.60) is calculated assuming a value of 0.75 for the

factor depending on the grain size distribution K_{σ} , following the indications of Hoffmans and Verheij (1997) for natural sand.

Table 2-2: Maximum expected scour depth [m]

Method	Breusers and Raudkivi (1991)	Sumer et al. (1992)	Melville (1997)	Hoffmans and Verheij (1997)	Schiereck (2001)	Sheppard and Miller Jr (2006)
Eq. number	(1.49)	(1.50)	(1.52)	(1.60)	(1.62)	(1.65)
Case 1	8.80	5.85 (+3.15)	9.49	4.07	7.24	5.47
Case 2	10.35	5.85	10.80	5.06	9.00	6.66

The predicted scour depth varies between 4.07m ($S_e/D = 0.90$) and 9.49m ($S_e/D = 2.1$) for case 1 and between 5.06m ($S_e/D = 1.12$) and 10.8m ($S_e/D = 2.4$) for case 2.

In both cases a typical 3.6 MW turbine is considered to calculate the loads on the pile. The characteristics are depicted in Table 2-3 (G.E. Energy (2005); Schmidt (2007)) .

Table 2-3: Characteristics of turbine (3.6MW)

Turbine characteristic	Unit	Value
Hub height above SWL	[m]	70
Power capacity P	[kW]	3600
Rated wind speed	[m/s]	14
Cut-off wind speed	[m/s]	27
Number of blades N_b	[-]	3
Blade length L_b	[m]	55.5
Average airfoil chord length	[m]	4.884
Area of the rotor disk A_{disk}	[m ²]	9677
Rotor speed	[rpm]	8.5 - 15.3
Rotor weight	[ton]	290

2.1 Loads on a vertical pile in a marine environment

The loading which the foundation has to withstand is caused by wind, wave and current action. The knowledge of the various loads is required to assess the influence of the scour on the foundations' design. A deterministic approach is used to calculate the forces. According to Argyriadis et al. (2004) this leads to an overestimation of the maximum overturning moment of the pile compared to the stochastic approach.

2.1.1 Wave loads

To calculate the loads on the foundation, a distinction is made between breaking and non-breaking waves. Wave loads on the monopile foundation are discussed and calculated here while more basic wave characteristics are discussed in chapter 3 (section 3.2.1.2).

2.1.1.1 Non-breaking waves

The Morison equation is an empirical formula used to calculate the hydrodynamic load on a slender vertical pile. Its basic assumption is that the pile is slender, and diffraction of the waves due to the presence of the pile is negligible. As mentioned in section 1.3.2.2, it is commonly accepted that diffraction effects around a vertical cylinder become important when the pile diameter to wave length ratio D/L exceeds 0.2 (Isaacson (1979)). In the two example cases, D/L is respectively equal to 0.07 and 0.02 (Table 2-1), indicating that Morison's equation can be used to calculate the non-breaking wave load on a vertical pile:

$$f_{Mor}(x, z, t) = f_D(x, z, t) + f_M(x, z, t) \quad (2.1)$$

with f_{Mor} the total hydrodynamic load per unit length at a certain height on the pile (Figure 2-1), f_D the drag force, proportional to u^2 and f_M the inertia load, proportional to \dot{u} :

$$f_D(x, z, t) = C_D \frac{\rho_w}{2} D \cdot |u(x, z, t)| \cdot u(x, z, t) \quad (2.2)$$

$$f_M = C_M \frac{\rho_w \pi D^2}{4} \cdot \dot{u}(x, z, t) \quad (2.3)$$

in which C_D represents the drag coefficient; C_M is the inertia coefficient; ρ_w is the density of water; D is the pile diameter; u is the horizontal particle velocity and \dot{u} is the horizontal particle acceleration.

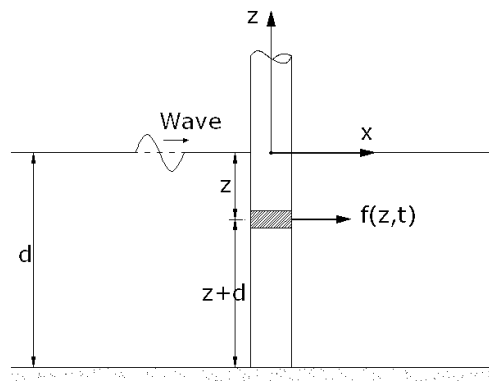


Figure 2-1: Wave forces on a slender vertical pile

The values of C_M and C_D depend on the pile roughness (marine fouling), on the pile Reynolds number and on the Keulegan Carpenter number. In Veritas (2004) it is suggested to take marine fouling into account and to use $C_M = 2$ and $C_D = 1.05$ for a rough surface and a KC number between 3 and 6.

When using linear wave theory, the horizontal particle velocity and acceleration are given by equation (2.4) and equation (2.5) respectively, when the z -axis is defined as in Figure 2-1:

$$u(x, z, t) = \frac{H}{2} \frac{g T_w}{L} \frac{\cosh\left[\frac{2\pi(z+d)}{L}\right]}{\cosh\left(\frac{2\pi d}{L}\right)} \cdot \cos(kx - \omega t) \quad (2.4)$$

$$\dot{u}(x, z, t) = \frac{g\pi H}{L} \frac{\cosh\left(\frac{2\pi(z+d)}{L}\right)}{\cosh\left(\frac{2\pi d}{L}\right)} \sin(kx - \omega t) \quad (2.5)$$

in which g is the gravitational acceleration, H is the wave height, T_w the wave period, L the wave length, d the water depth, k the wave number and ω the angular frequency. The force is calculated in the center of the pile, or $x = 0$, when defined as in Figure 2-1.

Because linear wave theory is only valid below the still water level (SWL), it does not describe the wave kinematics in the wave crest. This can be solved by either assuming a constant particle velocity from the SWL upwards, by applying some kind of wave stretching (Wheeler stretching) or by using a higher order wave theory ((Figure 2-2)).

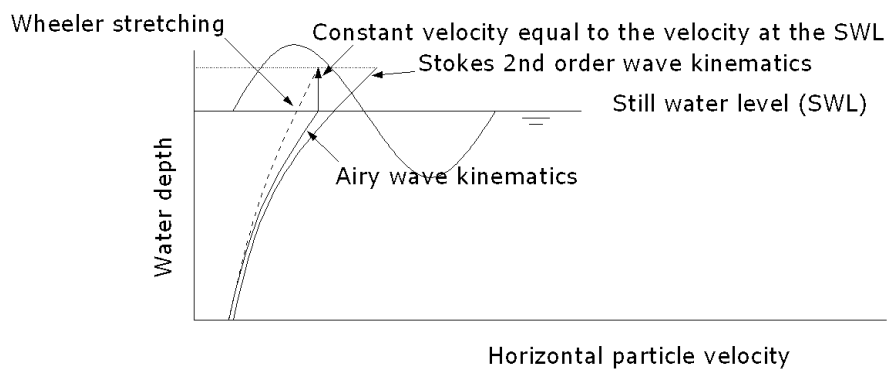


Figure 2-2: Wave kinematics above SWL

Although underestimating the wave forces (Randall et al. (1993)), linear wave theory is applied to calculate the non-breaking wave forces. The main goal of

this chapter is after all to investigate the sensitivity of the structural design to scour and not to calculate the expected forces in detail.

The total force on the pile is calculated by integrating the forces along the length of the pile, from the bottom up to the elevation η :

$$F_{Mor} = \int_{-d}^{\eta} (f_D + f_M) dz = F_D + F_M \quad (2.6)$$

with d the water depth.

The moment M_{Mor} at the sea bed is calculated as:

$$M_{Mor} = \int_{-d}^{\eta} (f_D + f_M) (z + d) dz \quad (2.7)$$

As the pile is not completely fixed near the sea bed, the maximum moment is higher than the moment calculated with equation (2.7) and lies below the sea bed. It is however assumed that equation (2.7) sufficiently approaches the maximum moment for our goal.

For engineering purposes, it is hardly ever the wave force distribution that is important but the maximum force and the maximum moment acting on the pile at the sea bed. The CEM (US Army Corps of Engineers (2002)) hands graphs from which the total maximum drag and inertia forces can be read, according to the stream function theory from Dean. The maximum force is however overestimated when summing the maxima of both F_D and F_M , as the maxima of inertia and drag force do not occur simultaneously. It is therefore more economical to look at the time evolution of both components.

According to Veritas (2004), the outer diameter of the part of the foundation placed under water should be increased due to marine fouling. They recommend an increase of the diameter with 0.1m, for water depths between 0 and 10m, and an increase of 0.09m, for a water depth between 10 and 20m. For both our example cases, the pile diameter is increased with 0.1m to calculate the wave forces.

The results for the non-breaking wave loads are shown in Table 2-4 (p.2-13)

2.1.1.2 Breaking waves

When waves become too steep or the water depth becomes too small, waves might break. In case of a steep slope in front of the structure or when sand banks are present wave breaking should be taken into consideration for the design of offshore foundations. Breaking waves cause a large impact force on the structure, especially in the case of plunging wave breakers.

As the kinematics of breaking waves are not as well understood as those of non-breaking waves, mostly empirical formulae are used to calculate the impact force. Although many experiments have already been performed, uncertainty still remains about the best empirical relationship.

According to Wienke et al. (2000) and Wienke and Oumeraci (2005) an additional impact force F_I can be added to the Morison equation:

$$F = F_D + F_M + F_I \quad (2.8)$$

The impact force can be described as a function of the so-called slamming coefficient C_S :

$$F_I = \frac{1}{2} \lambda \eta_b C_S \rho_w D C^2 \quad (2.9)$$

in which ρ_w is the density of water; D is the pile diameter; $\lambda \eta_b$ represents the impact height of the breaking wave and η_b is the maximum elevation from the SWL (Figure 2-3). The wave's strike zone and resulting impact force are limited to the height $\lambda \eta_b$ and the total wave force is calculated by using the Morison equation (2.6) from $z = -d$ to $z = \eta_b - \lambda \eta_b$ and by computing the impact force on the section that is struck by the nearly vertical part of the wave, $\lambda \eta_b$ (Wiegel (1982)). The curling factor λ depends on the breaker type: according to Wiegel (1982) $\lambda < 0.1$ for spilling breakers (in case of mild slopes), while λ can increase to 0.5 for plunging breakers (in case of a steep slope). Wienke and Oumeraci (2005) suggest to use the wave celerity $C = L/T_w$ as a value for the wave approaching velocity, with L the wave length and T_w the wave period. Different values are given to the slamming coefficient C_S . Two theories are described in Wienke and Oumeraci (2005): the theory of von Karman which results in $C_S = \pi$ and the theory of Wagner, which yields $C_S = 2\pi$. Wienke and Oumeraci (2005) conclude from their experiments that the theory of Wagner is more accurate, resulting in a value of 2π for C_S .

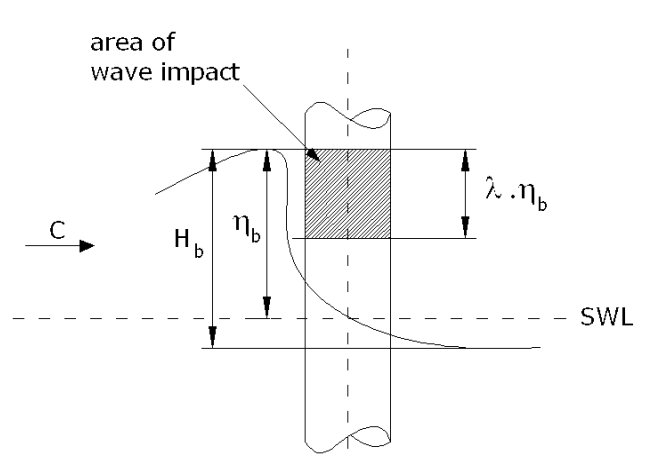


Figure 2-3: Definition sketch of breaking wave impact

To investigate the influence of the scour depth on the moment, caused by the wave impact, we will assume that wave breaking occurs in the case of the

smallest water depth (Table 2-1, Case 1). The maximum elevation in this case is calculated with Fenton's theory in ACES (1992), as this theory is valid for wave heights up till the breaking wave height H_b .

2.1.2 Current load

When a steady current interacts with the waves, the hydrodynamic loading of the current should be included in the Morison equation. As the derivative of a steady current equals zero, a steady current only influences the drag force which acts on the pile. The adjusted drag force is:

$$f_D(x, z, t) = C_D \frac{\rho_w}{2} D \cdot |u(x, z, t) + U_c(z)| \cdot (u(x, z, t) + U_c(z)) \quad (2.10)$$

in which $U_c(z)$ is the steady current velocity at a height z above the bottom. A logarithmic velocity profile is often assumed, given by equation (1.5). The influence of the waves on the velocity profile is discussed in chapter 1 (section 1.1.1.3).

For the example cases, a constant current profile with a flow velocity equal to the average velocity is assumed over the entire water depth. An adjustment of the current profile due to an interaction of waves and current is not taken into account.

2.1.3 Wind load

The wind speed is an important design factor when it comes to offshore wind farms, since it determines the power output of a wind turbine. Most existing offshore wind farm locations have average yearly wind speeds between 8.5 and 10 m/s. The present generation of wind turbines usually starts operating at 3-4 m/s wind speed and shuts down at approximately 25-30 m/s. At that moment, the load on the wind turbine becomes too high and the turbines' blades are rotated until they are parallel with the wind.

Comparable to the flow velocity profile, the wind speed at a certain elevation can be determined by using a logarithmic velocity profile (Van der Tempel (2006)):

$$V_w(z) = V_{w,r} \frac{\ln\left(\frac{z}{z_0}\right)}{\ln\left(\frac{z_r}{z_0}\right)} \quad (2.11)$$

in which $V_w(z)$ is the mean wind speed at a height z above the surface; $V_{w,r}$ is the mean wind speed at the reference height z_r and z_0 is the surface roughness = 0.001 for a rough sea. Equation (2.11) can be used to calculate the velocity at hub height (usually between 65 – 90 m above the SWL)

Extreme winds are obtained by considering a certain return period. Wind speeds are measured during long periods and extrapolation of measured means above a certain threshold yields the required return wind speed (Van der Tempel (2006)). A distinction is made between an extreme hourly mean wind speed and an extreme incident wind speed within a given short time interval. According to Van der Tempel (2006) design standards exist for onshore extreme wind speeds. Offshore sites however always require site-specific analysis. The class with highest wind speed for onshore situation hands a first estimate of the design wind speed. This yields an extreme hourly wind speed $V_{w,ext1h}$ of 10 m/s and an extreme 10-minute mean wind speed $V_{w,ext10min}$ of 50 m/s at hub height (according to IEC, from Van der Tempel (2006)).

The drag force on the pile $F_{D,w,pile}$, caused by the wind can be calculated similar to the current load on the pile as:

$$F_{D,w,pile} = \frac{1}{2} C_{D,w,pile} \rho_a A_{pile} V_w^2 \quad (2.12)$$

with $C_{D,w,pile}$ the drag coefficient of the pile = 0.7 according to Van der Tempel (2006), ρ_a the density of air = 1.25 kg/m³, A_{pile} the surface of the pile subject to wind loading and V_w the velocity of the wind.

The wind forces on the rotor blades cause a large horizontal force on the wind turbine's support structure. When no boundary effects are taken into account (a blade is thought to be infinitely long), the axial load on the blades is caused by the relative wind speed over the blade V_{rel} , which is a combination of incoming wind velocity at the rotor V_{disk} and rotation speed of the blades V_{rot} (Van der Tempel (2006)):

$$V_{rel} = \sqrt{V_{disk}^2 + V_{rot}^2} \quad (2.13)$$

The velocity V_{disk} can be calculated as a function of the undisturbed incoming wind velocity V_0 and the induction factor b (Van der Tempel (2006)):

$$V_{disk} = V_0 (1-b) \quad (2.14)$$

Figure 2-4 shows how the axial load which acts on a blade element is a combination of drag force $F_{D,b}$ and lift force on the blade $F_{L,b}$:

$$F_{D,b} = \frac{1}{2} C_{D,b}(\alpha) \rho_a V_{rel}^2 c_a \Delta r \quad (2.15)$$

$$F_{L,b} = \frac{1}{2} C_{L,b}(\alpha) \rho_a V_{rel}^2 c_a \Delta r \quad (2.16)$$

with $C_{D,b}(\alpha)$ and $C_{L,b}(\alpha)$ respectively the drag coefficient and lift coefficient of the blade, depending on the pitch angle of the blade α ; ρ_a the density of air = 1.25 kg/m³ for a temperature of 10°C; V_{rel} the relative wind speed over the rotor blade (equation (2.13)); c_a the aerofoil chord length and Δr the length of the blade.

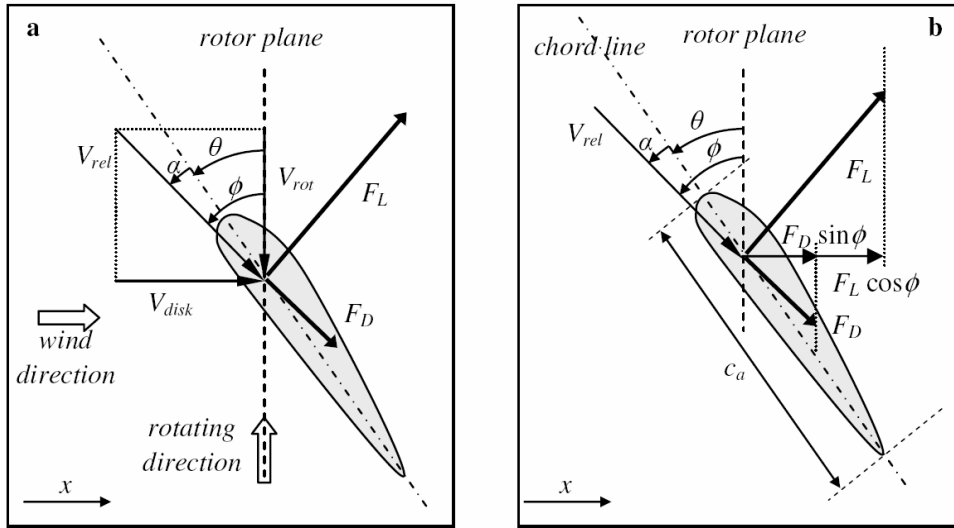


Figure 2-4: Lift and drag load on a blade element; Van der Tempel (2006)

The total horizontal force, caused by the wind on the rotor blades is equal to:

$$F_{wind,b} = N_b \sum_{r=root}^{r=tip} (F_{D,b} \sin \phi + F_{L,b} \cos \phi) \quad (2.17)$$

with N_b the number of blades and ϕ the angle of the relative wind speed over the blade with the rotating plane (Figure 2-4).

The power production can be calculated as:

$$P = F_{wind,b} \cdot V_{disk} \quad (2.18)$$

The power coefficient C_p is defined as the power P divided by the power of the wind which flows through the rotor plane:

$$C_p = \frac{P}{\frac{1}{2} \rho_a V_0^3 A_{disk}} = 4b(1-b)^2 \quad (2.19)$$

with ρ_a the density of air; V_0 the incoming flow velocity; A_{disk} the area taken up by the rotor disk $= \pi L_b^2$, with L_b the length of the blades and b the induction factor (equation (2.14)).

When the power output P and the incoming wind velocity are known, the induction factor can be calculated with equation (2.19). This determines the velocity at the rotor disk V_{disk} through equation (2.14) and the horizontal wind force on the turbine with equation (2.18).

The maximum capacity of a wind turbine is reached at a certain value of the incoming wind speed (= rated wind speed). At that moment the rotor speed is kept constant to maintain the same power output. This can be done in two ways: the blades can be fixed to the hub with blades that will create extra turbulent losses when the wind speed exceeds the rated wind speed or the blades can be pitched into the wind, which is called active stall. In the latter case, the blades are tilted to decrease the angle of attack, leading to much smaller values of the drag coefficient for higher wind velocities (Van der Tempel (2006), Lindenburt and Snel (2003)).

In both cases, the wind turbine is stopped and the blades are placed parallel to the wind direction when the wind velocity exceeds a critical value (cut-off wind speed), thus significantly reducing the force which acts on the wind turbine. Therefore it is not required to consider the highest wind speed to calculate the maximum force on the wind turbine, but only the velocities until the cut-off wind speed. When looking at equation (2.18), we can see that the highest horizontal working load is reached with the smallest velocity leading to the maximum power output.

A high load is also reached when the wind turbine needs an emergency stop at the cut-off wind speed. At that point, the rotation speed of the wind turbine becomes 0 and the angle of attack increases significantly, leading to a high value of ϕ (Figure 2-4). The drag force will give the highest load, which can approximately be calculated as:

$$F_{wind,stop} = N_b \sum_{r=root}^{r=tip} \frac{1}{2} C_D(\alpha) \rho_a V_0^2 c_a \Delta r \quad (2.20)$$

with N_b the number of blades = 3, C_D the drag coefficient, which is equal to a maximum of 1.3 for $\alpha = 90^\circ$, ρ_a the density of air = 1.25 kg/m³, V_0 the incoming wind speed = 27 m/s, c_a the airfoil chord length and Δr the radial location of the blade element.

The turbine characteristics, required to calculate the axial load on the rotor are given in Table 2-3. For the example cases, a 3.6 MW turbine is considered. The cut-off wind speed is 27 m/s and the velocity at which the generator reaches maximum capacity (= rated velocity) is equal to 14 m/s. The maximum rotor speed, needed to calculate the blade section velocity equals 15.3 rpm. The rotor diameter is 111m (blade length = 55.5m). The blades are assumed to be pitch controlled. Figure 2-5 gives the power curves for a 3.6MW GE turbine, showing the power coefficient C_p as a function of the ratio of blade tip speed to wind

speed λ (Miller et al. (2003)). From this curve, the required pitch angle of the blades can be determined.

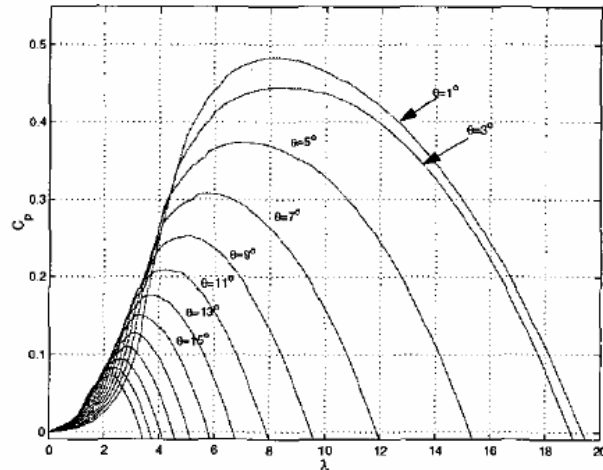


Figure 2-5: Wind power C_p curves for a 3.6MW turbine; Miller et al. (2003)

The total load on the wind turbine, caused by the wind is the sum of the wind load on the pile $F_{D,w,pile}$ and the wind load on the rotor (blades) $F_{wind,b}$:

$$F_{wind} = F_{wind,b} + F_{D,w,pile} \quad (2.21)$$

To calculate the maximum wind load, the same wind velocity is used to calculate the load on the rotor and the load on the pile.

2.1.4 Loads in the example cases

The different loads, moments and moment arms for the two cases are given in Table 2-4. Non-breaking wave loads are calculated with linear wave theory. Breaking wave forces are only considered in case 1 (small water depth). In case 1 it is not the maximum force which is considered for the non-breaking waves, but the force which is present when the breaking wave hits the pile, which is assumed to be when the crest reaches the pile.

The combined load effect of wind and waves is calculated by a linear superposition of the separately calculated loads, as is suggested by Veritas (2004) for a conceptual evaluation. A comparison is made in Argyriadis et al. (2004) between a combination of separately calculated wind and wave loads and a simultaneous analysis of the 1-minute averaged wind speed combined with the extreme wave height. They find a slightly higher overturning moment when the separately calculated forces are combined.

The highest wind load is found for a wind speed of 27 m/s, when an emergency stop is required.

2.2 Bending moment

Due to the increase in pile length, the scour hole will have an influence on the maximum bending moment in the pile. In the CEM (US Army Corps of Engineers (2002)), the maximum moment acting on the pile is calculated as, for a scour hole with depth S_e :

$$M'_{tot} = (r_{tot} + S_e) F_{tot} \quad (2.22)$$

with r_{tot} the total moment arm and F_{tot} the total force in case no scouring had occurred. In reality there will be an increase in F_{tot} as well, as there will be a flow velocity within the scour hole. For the waves, the velocity in the scour hole is kept equal to the bottom velocity (although it will be somewhat lower in reality). The total load is calculated as:

$$F = \int_{-(d+S_e)}^{\eta} (f_D + f_M) dz = F_D + F_M \quad (2.23)$$

with f_D and f_M kept constant from the sea bottom downwards. The total moment is calculated as:

$$M_{tot} = \int_{-(d+S_e)}^{\eta} (f_D + f_M) (z + d + S_e) dz \quad (2.24)$$

Note that the wavelength remains the same, as it is assumed that the extension of the scour hole is not large enough to alter the wave length.

For the current velocity, the flow velocity is kept constant, also in the scour hole. This will somewhat overestimate the load, as the increase in water depth will normally create a local decrease in flow velocity.

For the moment, caused by the breaking wave force and the wind load, it is only the moment arm which increases, and the increased moment is computed as suggested in equation (2.22).

The increased loads and moments are given in Table 2-4, for each case the minimum and maximum expected scour depth from Table 2-2 are taken into account and the increase in % of the maximum moment compared to the cases without scour are given between brackets. An increase between 16.1 and 41.0% is found.

Table 2-4: Case loads, with scour

	Case 1	Case 1	Case 1	Case 2	Case 2	Case 2
	No scour	$S_e = 4.1\text{m}$	$S_e = 9.5\text{m}$	No scour	$S_e = 5.1\text{m}$	$S_e = 10.8\text{m}$
F_{Mor} [kN]	251	412	612	1378	1633	1918
r_{Mor} [m]	3.25	5.61	8.34	12.58	15.31	18.31
F_I [kN]	1057	1057	1057	-	-	-
r_I [m]	7.05	11.15	16.55	-	-	-
F_{wind} [kN]	582	582	582	582	582	582
r_{wind} [m]	68.96	73.06	78.46	83.96	89.06	94.76
F_{tot} [kN]	1890	2051	2251	1960	2215	2500
r_{tot} [m]	25.61	27.6	30.3	33.78	34.69	36.11
M_{tot} [kNm]	48402	56618 (+17.0%)	68261 (+41.0%)	66200	76834 (+16.1%)	90269 (+36.4%)

In Table 2-4, F_{Mor} is the force which causes the maximum moment, for the steady current and non-breaking wave load; r_{Mor} is the moment arm for the current and non-breaking wave load; F_I is the force causing the maximum moment for the breaking wave load; r_I is the moment arm for the breaking wave load; F_{wind} is the maximum force due to the wind load; r_{wind} is the moment arm for the wind load; F_{tot} is the total force; r_{tot} is the total moment arm and M_{tot} is the total maximum moment at the sea bed.

The total maximum moment determines the required section modulus, which is defined as the total moment M_{tot} divided by the tensile strength σ_v . For circular piles:

$$W = \frac{M_{tot}}{\sigma_v} = \frac{\pi(D_o^4 - D_i^4)}{32D} \quad (2.25)$$

in which D_o is the outer pile diameter and D_i is the inner pile diameter; the wall thickness $t_w = (D_o - D_i)/2$ and the tensile strength σ_v for steel is assumed to be 235 N/mm².

When scour is prevented, equation (2.25) leads to a required wall thickness of 12 mm in case 1, and a required wall thickness of 18 mm in case 2, when using the values for the total maximum moment, obtained in Table 2-4. Although the moment at the bottom increases significantly, the required wall thickness does not exceed 25mm even for the largest moment,. Typically, the wall thickness of a pile with that large a diameter will be at least 45mm, due to reasons of dynamic behaviour (Van der Tempel (2006)). Even though no safety factors are considered for the loads, we can conclude that in these cases the wall thickness will not be determined by the maximum bending moment. As the ratio pile diameter to wall thickness is an important parameter for the natural frequency of the monopile structure, it will rather be the fatigue behaviour which determines the wall thickness (section 2.4, Zaaijer (2003)).

2.3 Soil mechanics

An offshore monopile foundation is on the one hand loaded in the axial direction, by the weight of the pile and the turbine, and on the other hand in the lateral direction, due to the action of the waves, current and wind. The axial load which can be carried is determined by the shaft bearing resistance and the tip bearing capacity of the pile. The lateral load is counteracted by the resistance of the surrounding soil to be deformed.

The required embedded length of the pile is determined by the required axial bearing capacity and lateral bearing capacity as well as by the dynamic behaviour of the pile. In this section, we will consider the axial and lateral bearing capacity. The dynamic behaviour is discussed in section 2.4.

2.3.1 Lateral bearing capacity

To calculate the lateral bearing capacity of the pile, the method described in Vandepitte (1979) is used, which allows a manual calculation of the ultimate limit state. Figure 2-6 shows which assumptions which are made: a rotation of the pile at a depth ωt_0 under the bed is assumed. Active and passive soil pressure develop on both sides of the pile and act as shown in Figure 2-6. The neutral soil pressure, working on the sides of the pile also contribute to the soils resistance. A last part of the soil resistance is provided by the passive soil pressure which acts on the sides of the soil mass ABD, which is pushed upwards.

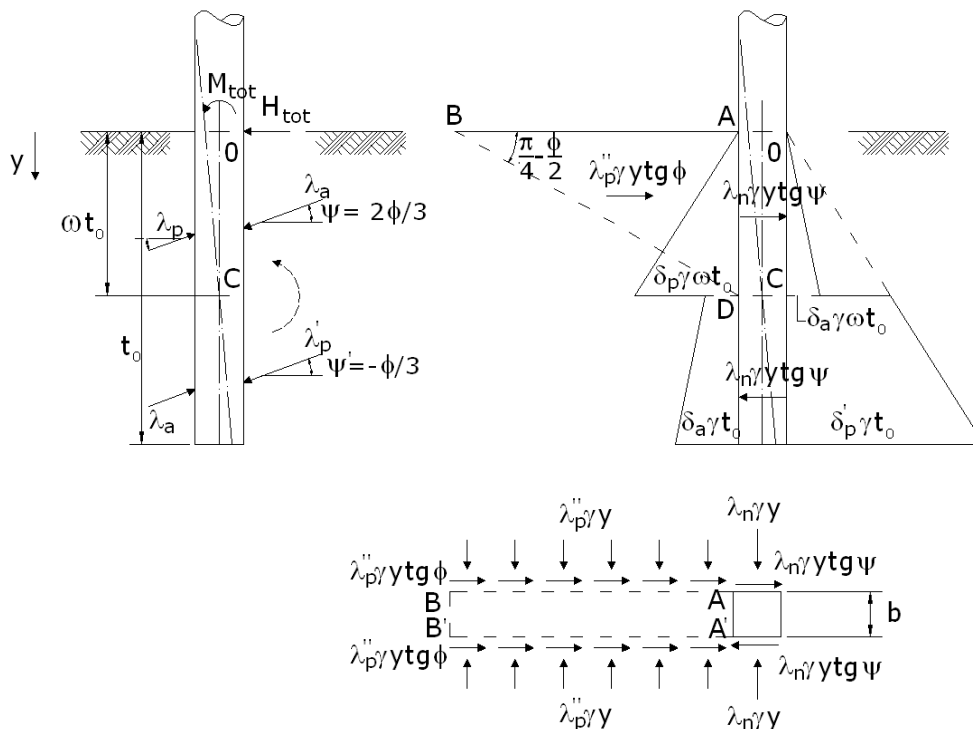


Figure 2-6: Calculation of lateral pile bearing capacity; after Vandepitte (1979)

Based on Figure 2-6, Vandepitte (1979) derives the following equations for the ultimate load H_u and moment M_u :

$$H_u = \frac{1}{6} \gamma t_0^2 \left[3(\delta_p - \delta_a) \omega^2 b - 3(\delta'_p - \delta_a)(1 - \omega^2) b + 6\lambda_n (2\omega^2 - 1) a \cdot \tan \psi + 2\omega^3 \cdot t_0 \cdot \tan \phi \cdot \tan^3 \left(\frac{\pi}{4} + \frac{\phi}{2} \right) \right] \quad (2.26)$$

$$M_u = \frac{1}{6} \gamma t_0^3 \left[-2(\delta_p - \delta_a) \omega^3 b + 2(\delta'_p - \delta_a)(1 - \omega^3) b + 4\lambda_n (1 - 2\omega^3) a \cdot \tan \psi - \omega^4 \cdot t_0 \cdot \tan \phi \cdot \tan^3 \left(\frac{\pi}{4} + \frac{\phi}{2} \right) \right] \quad (2.27)$$

with γ the density of the soil = 10kN/m³ for sand located under water; t_0 the pile penetration depth; δ_p , δ'_p and δ_a respectively the passive and active soil pressure, calculated from equation (2.28) – equation (2.30); λ_n the neutral soil pressure coefficient = 0.5; αt_0 the depth of the rotating point below the bed; b the pile width; ϕ the angle of internal friction and ψ the angle which the active and passive forces make with the horizontal.

$$\delta_p = \lambda_p \cos \psi = \frac{\cos^2 \phi}{\cos \psi \left(1 - \sqrt{\frac{\sin(\phi + \psi) \sin(\phi + \varepsilon)}{\cos \psi \cos \varepsilon}} \right)^2} \cdot \cos \psi \quad (2.28)$$

$$\delta'_p = \lambda'_p \cos \psi' = \frac{\cos^2 \phi}{\cos \psi' \left(1 - \sqrt{\frac{\sin(\phi + \psi') \sin(\phi + \varepsilon)}{\cos \psi' \cos \varepsilon}} \right)^2} \cdot \cos \psi' \quad (2.29)$$

$$\delta_a = \lambda_a \cos \psi = \frac{\cos^2 \phi}{\cos \psi \left(1 + \sqrt{\frac{\sin(\phi + \psi) \sin(\phi - \varepsilon)}{\cos \psi \cos \varepsilon}} \right)^2} \cdot \cos \psi \quad (2.30)$$

with ε the angle which the soil makes with the horizontal = 0 when the bed is horizontal. The angle $\psi = 2\phi/3$, whereas $\psi' = -\phi/3$.

The location of the rotation point C is found by stating that $M_u = r_{tot} \cdot H_u$ when the load H_u acts at a height r_{tot} above the bottom and by substituting equation (2.26) in equation (2.27). The value of H_u can be calculated once ω is known. The required embedded pile length can be calculated from equations (2.26) and

(2.27) by stating that H_u has to be at least equal to the total load on the structure H_{tot} .

To calculate the required pile penetration depth, a sandy soil with an angle of internal friction $\phi = 30^\circ$ is assumed.

The required embedded pile length when no scour is present is 13.9m in case 1 and 15.7m in case 2.

When a scour hole develops, the required embedded pile length increases because:

- the maximum load and moment increase;
- the soil pressure is reduced to zero in the scoured region;
- the effective soil pressure of the soil which is located below the scour hole is reduced due to a reduction of the weight of the soil in the soil layers above

The increased maximum load and moment arm are shown in Table 2-4.

To account for the reduction of the soil resistance, an adaptation is made to the theory provided by Vandepitte (1979). According to Zaijjer and Van der Tempel (2004), the influence of the scour hole on the effective soil pressure is limited in depth, as the weight of the upper layer of soil far away from the pile also presses down on the soil near the pile for large depths. Figure 2-7 shows the difference between global scour, where the effective soil pressure is reduced with the weight of the scoured hole over the entire depth, and local scour, where the influence is limited to an overburden reduction depth as described above. A typical value of the overburden reduction depth is 6 times the pile diameter.

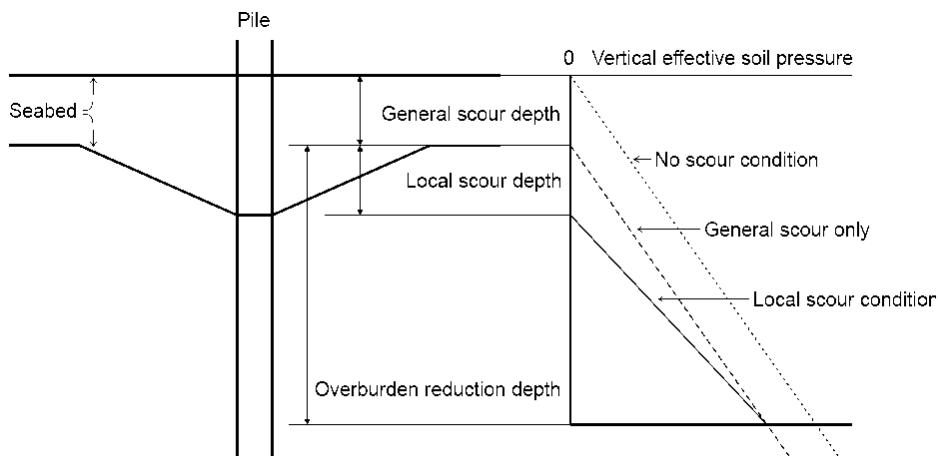


Figure 2-7: Reduction of effective soil pressure due to scour; Zaijjer and Van der Tempel (2004)

The concept shown in Figure 2-7 can be applied to the theory described in Vandepitte (1979). Taking the calculated embedded length into account (approx. 15m), we assume initially that the overburden reduction depth ($6D = 27\text{m}$) is

larger than the pile penetration depth. The rotation point C will in any case be located beneath the scour hole. Figure 2-8 shows how the soil pressures change compared to Figure 2-6. Be aware that the embedded length t'_0 is defined as the length which is located underneath the scour hole. The scour depth should therefore be added to t'_0 in order to obtain the true increased pile length. The ultimate load and moment can now be calculated as:

$$H_u = \frac{1}{6} \gamma t_0'^2 \left[3(\delta_p - \delta_a) \omega^2 b \left(\frac{6D}{6D - S_e} \right) - 3(\delta_p' - \delta_a)(1 - \omega^2) b \left(\frac{6D}{6D - S_e} \right) + 6\lambda_n (2\omega^2 - 1) a \cdot \tan \psi + 2\omega^3 \cdot t'_0 \cdot \tan \phi \cdot \tan^3 \left(\frac{\pi}{4} + \frac{\phi}{2} \right) \right] \quad (2.31)$$

$$M_u = \frac{1}{6} \gamma t_0'^3 \left[-2(\delta_p - \delta_a) \omega^3 b \left(\frac{6D}{6D - S_e} \right) + 2(\delta_p' - \delta_a)(1 - \omega^3) b \left(\frac{6D}{6D - S_e} \right) + 4\lambda_n (1 - 2\omega^3) a \cdot \tan \psi - \omega^4 \cdot t'_0 \cdot \tan \phi \cdot \tan^3 \left(\frac{\pi}{4} + \frac{\phi}{2} \right) \right] \quad (2.32)$$

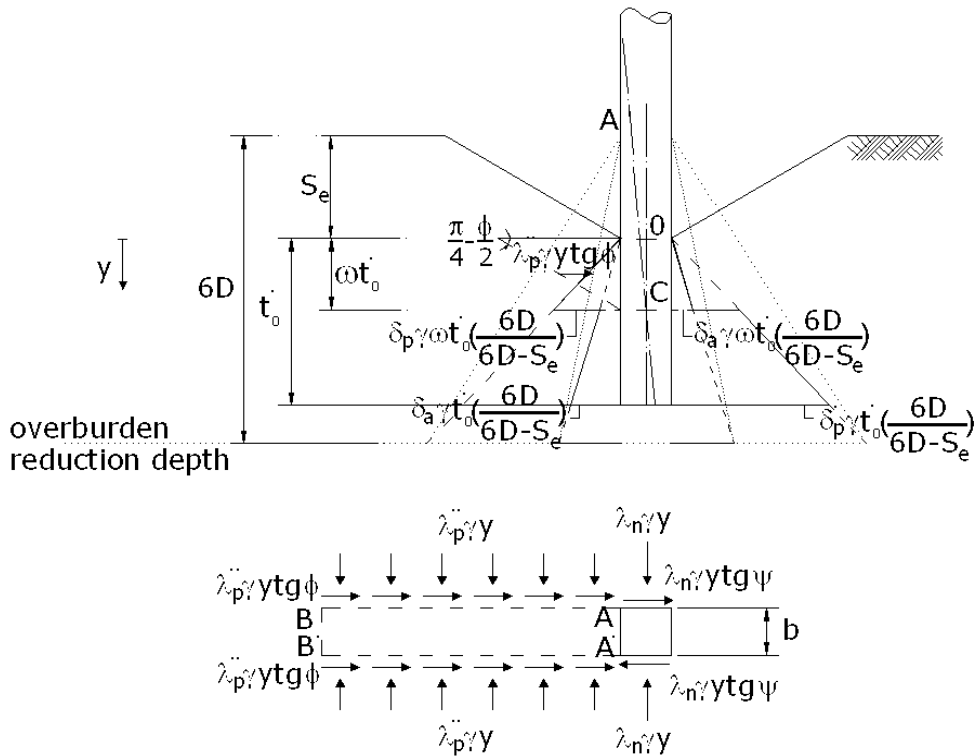


Figure 2-8: Calculation of lateral pile bearing capacity when a scour hole develops

Table 2-5 gives the required pile penetration depth in the example cases (= penetration depth from the original sea bed level). The table shows that the increase in pile length, caused by the scour development, is approximately equal to the scour depth S_e . Note that the assumption that $t_0 < 6D$ is valid in all cases.

Table 2-5: Required pile penetration depth for example cases

	Case 1 no scour	Case 1 $S_e = 4.1\text{m}$	Case 1 $S_e = 9.5\text{m}$	Case 2 no scour	Case 2 $S_e = 5.1\text{m}$	Case 2 $S_e = 10.8\text{m}$
Value of t_0 according to Vandepitte (1979) [m]	14.4	18.7 (+30.0%)	23.8 (+65.3%)	15.8	20.8 (+31.6%)	26.1 (+65.2%)

Nowadays, the soil and pile interaction is usually modelled in more detail, by calculating the real deformation and displacements of the pile and the effective soil pressure belonging to this displacement. For small displacements, the pressure increases linearly (elastic deformation), but for larger displacements the pressure reaches a maximum when the soil is deformed plastically. This is accounted for by the use of so-called p-y curves, which plot the soil resistance against the pile deflection, as shown in Figure 2-9. This problem can no longer be solved analytically (Reese and Van Impe (2001)) and this method is not pursued here. Results given in this section are meant to draw the attention on the phenomenon and to give an indication about the value of the soil pressure and the influence of the scour hole on it.

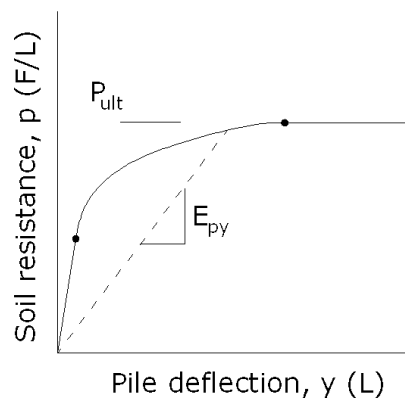


Figure 2-9: Typical p-y curve; after Reese and Van Impe (2001)

2.3.2 Axial bearing capacity

The ultimate axial load carrying capacity of the pile (Q_u) is composed of the end-bearing capacity of the pile (Q_t) and the shaft friction capacity (Q_s). The general equation describing Q_u is (Titi and Abu-Farsakh (1999)):

$$Q_u = Q_t + Q_s = q_t A_t + f A_s \quad (2.33)$$

in which q_t is the unit tip bearing capacity, A_t is the area of the pile tip, f is the unit skin friction, and A_s is the area of the pile shaft. In sands, the end-bearing capacity Q_t dominates. The design load carrying capacity Q_d of the pile can be calculated by dividing the ultimate axial load capacity of the pile by a safety factor.

The axial bearing capacity of a pile depends strongly on the site-specific soil characteristics. For loosely packed sand, the tip bearing resistance varies between 2-4 MPa. Even when assuming the lowest value for q_c (2MPa) and only using the tip bearing capacity, the axial load capacity of the pile amounts to Q_u 31800 kN, which is much more than the load it has to carry (approximately 6000 kN, weight of pile and rotor). Unless locally very soft soil layers are present, it is thus usually not the axial bearing capacity which determines the required pile length.

2.4 Dynamic behaviour

The dynamic behaviour of an offshore wind turbines' support structure is an important design factor, especially for monopiles because they are quite flexible. Two aspects are to be considered. Firstly it is important that resonance of the pile is avoided. This is achieved when the eigenfrequency of the structure does not lie within the excitation frequencies caused by waves, current and wind (due to the shedding of vortices), rotor frequency and blade passing frequency. Secondly, a change in eigenfrequency of the structure can cause a change in dynamic response of the structure, possibly leading to fatigue damage. Due to the different behaviour of offshore wind turbines, compared to other offshore structures, researchers have recently looked into the dynamic behaviour of a monopile structure and the influence of scour on this behaviour (Zaaijer (2003), Westgate and DeJong (2005), Zaaijer (2005), Van Ginhoven (2006)). Their findings are summarized below.

2.4.1 Eigenfrequency

The natural frequency or eigenfrequency of a support structure can be assessed with several methods. Often used are Rayleigh's method which gives an estimate of the upper limit of the first eigenfrequency or finite element methods which model the structure and soil-structure interaction in more detail (Zaaijer (2003) and also yield good results when comparing calculated and measured natural frequencies (Zaaijer (2005)).

The natural frequency of the structure depends strongly on the pile diameter, the pile diameter to wall thickness ratio, the pile length and the soil characteristics (Van Ginhoven (2006)).

The wind turbine and its support structure can be modeled as a flexible pile with a mass m_{top} on top of the pile (Figure 2-10). When the base of the pile is considered fixed in the bed, the first natural frequency f_{1nat} can be calculated as (Van der Tempel (2006)):

$$f_{1nat}^2 = \frac{3.04}{4\pi^2} \frac{EI}{(m_{top} + 0.227\mu L_p) L_p^3} \quad (2.34)$$

with EI the pile's bending stiffness; μ the pile mass per meter and L_p the height of the pile.

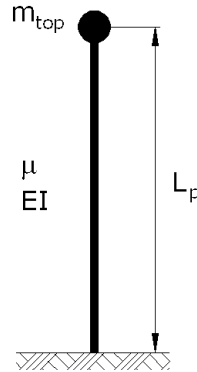


Figure 2-10: Definition sketch of model for the calculation of the natural frequency

Equation (2.34) can be rewritten as (Van der Tempel (2006)):

$$f_{1nat} \cong \frac{D_{av}}{L_p^2} \sqrt{\frac{E}{104 \left(\frac{m_{top}}{\rho_{steel} \pi D_{av} t_w L_p} + 0.227 \right) \rho_{steel}}} \quad (2.35)$$

with D_{av} the average tower diameter ($= D - t_w$), t_w the wall thickness, L_p the length of the pile above the bottom, E the modulus of elasticity of steel $= 210 \cdot 10^9$ N/m² and ρ_{steel} the density of steel $= 7850$ kg/m³.

Initially, a wall thickness of 45mm is assumed. The mass m_{top} is equal to $290 \cdot 10^3$ kg (3.6 MW turbine). The characteristic pile length and first eigenfrequency for each case are given in Table 2-6.

When pile diameter and wall thickness are kept constant, the natural frequency of the pile decreases significantly (up to 17.5%). In reality, the natural frequency of the pile will be somewhat lower than computed in Table 2-6, as the soil properties will always be more flexible than the fixed connection which is used in Figure 2-10.

Table 2-6: First eigenfrequency for the different cases

		Case 1 no scour	Case 1 $S_e = 4.1\text{m}$	Case 1 $S_e = 9.5\text{m}$	Case 2 no scour	Case 2 $S_e = 5.1\text{m}$	Case 2 $S_e = 10.8\text{m}$
L_p	[m]	75	79.1	84.5	90	95.1	100.8
$f_{1\text{nat}}$	[Hz]	0.400	0.367 (-8.3%)	0.330 (-17.6%)	0.298	0.272 (-8.6%)	0.247 (-16.9%)

The excitation frequencies for the different load cases are:

- Waves: 0.04 Hz – 0.33 Hz (25s – 3s), with the highest energy in a zone of 0.07 – 0.17 Hz.
- Current shedding frequency: 0.01 Hz – 0.13 Hz (equation (1.44) and Figure 1-18 for a current speed varying between 0.5 and 2 m/s and a pile diameter of 4.5m)
- Rotor frequency: 0.142 – 0.255 Hz (depends on the rotor type, here 3.6 MW GE turbine)
- Blade passing frequency: 0.425 – 0.765 Hz (three times the rotor frequency, for a 3-bladed rotor)

The excitation frequencies are shown in Figure 2-11 together with the first eigenfrequency of the pile. This shows that for large wind turbines (high hub height and slow rotation of the rotor) the excitation frequencies of the waves and rotor overlap. It is therefore not possible to envision a structure with a natural frequency lying between the rotor frequency and the wave frequency, although this so-called "soft-soft" structure requires much less steel (Van der Tempel (2006)). Figure 2-11 shows that, for case 1, although the natural frequency decreases significantly, the shift does not seem to interfere with any of the excitation frequencies. For case 2 however, the natural frequency overlaps with the excitation frequency of the rotor, requiring a larger wall thickness or pile diameter in case scour is allowed. To maintain the natural frequency of 0.298 Hz in case 2, the wall thickness should increase up to 59 mm, when the scour is 5.1m deep and up to 82mm, when the scour hole is 10.8m deep, resulting in a large increase in weight of the pile. In reality an increase of both pile diameter and wall thickness could be performed to obtain a more economic design. Note however that an increase of the pile diameter again leads to higher loads.

Van der Tempel et al. (2004) calculated the change in natural frequency for another case (2.75MW turbine with 3.5m diameter pile). They obtained a decrease in natural frequency from 0.321 Hz in the case without scour to 0.31 Hz in the case of a scour hole with a depth $S_e = 2.5D$.

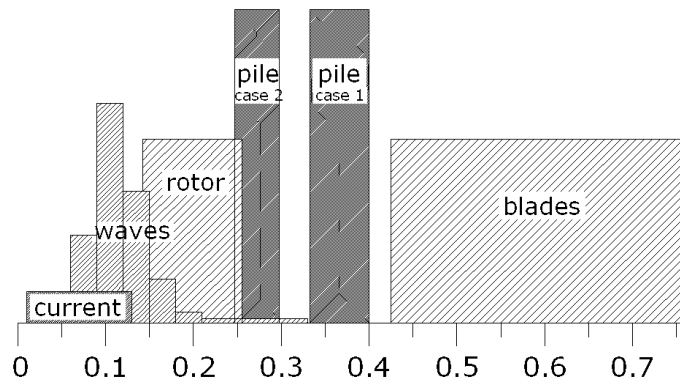


Figure 2-11: Frequency range for waves, current, rotation of the rotor, blade passing and natural

2.4.2 Fatigue

Although the natural frequency of the support structure is designed to avoid direct overlap with the excitation frequencies, amplification of the response also occurs in the neighborhood of the natural frequencies. The fatigue lifetime of offshore wind turbines can therefore be influenced by scour.

Fatigue is progressive structural damage that occurs when a material is subjected to cyclic loading. The maximum stress values are less than the ultimate tensile stress limit, and may be below the yield stress limit of the material. The resistance against fatigue is usually expressed in terms of S-N curves, which gives the number of cycles to failure N against the stress range. An example of such a curve for steel and aluminum is given in Figure 2-12.

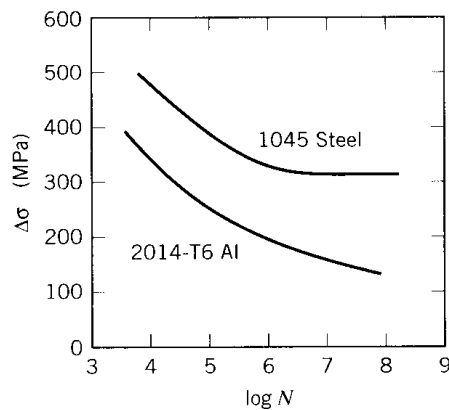


Figure 2-12: Example of S-N curve for aluminum and low-carbon steel; Roylance (2001)

Van der Tempel et al. (2004) performed a rough estimate of the influence of scour on the fatigue life of a monopile foundation. They found that for their case (2.75 MW turbine on monopile foundation in a water depth $d = 20\text{m}$, a pile diameter $D = 3.5\text{m}$, maximum wave height $H = 12.8\text{m}$, wave period $T_w = 9.5\text{s}$, surface current velocity $U_c = 1.1\text{ m/s}$) the fatigue damage increased

dramatically with increasing scour depth: the fatigue life went from 500 years to 120 years for a scour depth $S_e = 2.5D$. Although in this case, fatigue life time still meets the requirements (for structural parts that cannot be inspected, fatigue life should be three times the economic life span, according to Van der Tempel et al. (2004)), this example shows that influences of scour on fatigue life can be important.

2.5 Free spanning of cables

Typically, the transition between the cable in the turbine and the cable trench is done with a J-tube (Figure 2-13). The J-tube is generally made of a hard material and the cables that exit the J-tube near the bottom are normally embedded in a rock armour layer (scour protection).

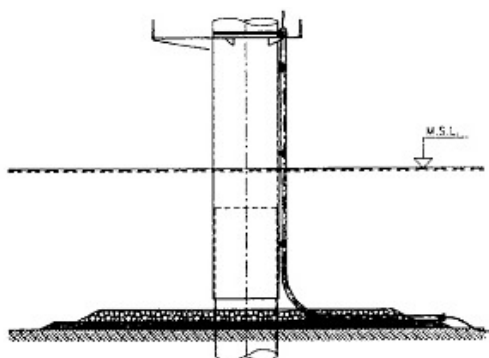


Figure 2-13: Cable transition from pile to sea bed for the Horns Rev wind turbines; <http://www.hornsrev.dk>

When no scour protection is applied, the cables exiting the J-tube will hang loose above the scour hole and will experience damage due to the action of currents and waves.

Zaaijer and Van der Tempel (2004) hand three possible alternatives for the free-spanning of the cable, which are illustrated in Figure 2-14:

- the use of an extended J-tube to cover the extension of the scour hole (Figure 2-14-a);
- the support of the cable with intermediate piles (Figure 2-14-b);
- directional drilling of the cable to avoid a J-tube and enter the cable through the bottom of the monopile (Figure 2-14-c);

Zaaijer and Van der Tempel (2004) mention however that little to no experience exists on this matter. The economic viability of these solutions still has to be established.

When placing a scour protection, the problem of the free-spanning of the cables is solved.

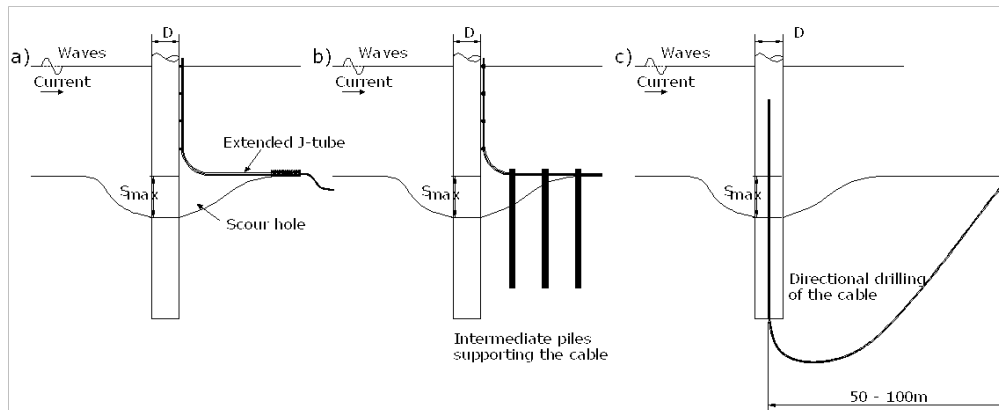


Figure 2-14: Possible solutions for the free-spanning of the cables, after Zaijjer and Van der Tempel (2004)

2.6 Conclusions

It is important to assess the influence of the scour hole on the design of a foundation, as this will determine whether the use of a scour protection is required. Four aspects are considered in this chapter:

- the increase of the maximum bending moment;
- the decrease in the pile's bearing capacity;
- the influence on the eigenfrequency of the pile and the resulting fatigue damage
- the free-spanning of the cables

For each of these aspects, two typical examples of an offshore monopile foundation are used to assess the influence of the scour hole on the design. In the example cases, the increase of the moment near the sea bottom amounts from 16 to 36%. In combination with the decrease in lateral bearing capacity, this leads to a required increase in penetration depth that is almost equal to the depth of the scour hole (an increase of 30% to 65% of the pile's penetration depth). The scour depth also results in a decrease of the eigenfrequency of the pile of 8 to 17.5%, which might be critical for the dynamic behaviour of the support structure. Considering the free-spanning of the cables, some alternative solutions exist, but might be expensive. An assessment of the economical viability of these solutions still has to be made.

This leads to the conclusion that, when large scour depths are to be expected, the impact on the design of the foundation is significant and a scour protection will prove valuable.

References

- ACES, 1992. Automated Coastal Engineering System. Coastal Engineering Research Center, Department of the army, Mississippi.
- Argyriadis, K., Gill, L. and Schwartz, S., 2004. Loads for Offshore Wind Turbines. The 2nd Edition of the GL Wind Guideline, Germanischer Lloyd, Hamburg.
- Breusers, H.N.C. and Raudkivi, A.J., 1991. Scouring. Balkema.
- G.E. Energy, 2005. 3.6 MW Offshore Series Wind Turbine, http://www.gepower.com/prod_serv/products/wind_turbines/en/36mw/index.htm.
- Hoffmans, G.J.C.M. and Verheij, H.J., 1997. Scour manual. A.A. Balkema, Rotterdam, Netherlands ; Brookfield, VT, xv, 205 p. pp.
- Isaacson, M., 1979. Wave-induced forces in the diffraction regime. Mechanics of Wave-Induced Forces on Cylinders, ed. TL Shaw, Pitman Advanced Publishing Program: 68–69.
- Lindenburg, C. and Snel, H., 2003. Aero-elastic stability analysis tools for large wind turbine rotor blades, European Wind Energy Conference, Madrid, Spain.
- Melville, B.W., 1997. Pier and Abutment Scour: Integrated Approach. Journal of Hydraulic Engineering, 123(2): 125-136.
- Miller, N.W., Sanchez-Gasca, J.J., Price, W.W. and Delmerico, R.W., 2003. Dynamic modeling of GE 1.5 and 3.6 MW wind turbine generators for stability simulations. Power Engineering Society General Meeting.
- Randall, R.E., Zhang, J. and Longridge, J.K., 1993. Laser Doppler anemometer measurements of irregular water wave kinematics. Ocean Engineering, 20(6): 541-554.
- Reese, L.C. and Van Impe, W.F., 2001. Single Piles and Pile Groups Under Lateral Loading. Aa Balkema, 463 pp.
- Roylance, D., 2001. Fatigue, lecture notes. Department of Materials Science and Engineering. Massachusetts Institute of Technology.
- Schiereck, G.J., 2001. Introduction to Bed, Bank and Shore Protection. Delft University Press.
- Schmidt, M., 2007. The Economic Optimization of Wind Turbine Design. MSc thesis Thesis, Georgia Institute of Technology, Georgia.
- Sheppard, D.M. and Miller Jr, W., 2006. Live-Bed Local Pier Scour Experiments. Journal of Hydraulic Engineering, 132: 635-642.
- Sumer, B.M., Fredsøe, J. and Christiansen, N., 1992. Scour Around Vertical Pile in Waves. Journal of Waterway, Port, Coastal and Ocean Engineering, 118(1): 15-31.
- Titi, H.H. and Abu-Farsakh, M.Y., 1999. Evaluation of Bearing Capacity of Piles from Cone Penetration Test Data, Louisiana Transportation Research Center, Louisiana.
- US Army Corps of Engineers, 2002. Coastal Engineering Manual. Engineer Manual 1110-2-1100, Washington, D.C. .
- Van der Tempel, J., 2006. Design of Support Structures for Offshore Wind Turbines. PhD Thesis, Technische Universiteit Delft, Delft, 209 pp.
- Van der Tempel, J., Zaaier, M.B. and Subroto, H., 2004. The effects of Scour on the design of Offshore Wind Turbines, 3rd International Conference on Marine Renewable Energy, Blyth, UK.

- Van Ginhoven, J., 2006. Het effect van erosie en grondeigenschappen op het dynamisch gedrag van offshore windturbines, betreffende stalen en betonnen mono paal funderingen. MSc Thesis, Delft University of Technology, Delft, 98 pp.
- Vandepitte, D., 1979. Berekening van constructies I. E. Story-Scientia, Gent, 614 pp.
- Veritas, D., 2004. Design of Offshore Wind Turbine Structures. Offshore Standard DNV-OS- J, 6: 2004.
- Westgate, Z.J. and DeJong, J.T., 2005. Geotechnical considerations for Offshore Wind Turbines, University of California.
- Wiegel, R.L., 1982. Forces induced by breakers on piles, 18 th International Conference on Coastal Engineering. ASCE, pp. 1699-1715.
- Wienke, J. and Oumeraci, H., 2005. Breaking wave impact force on a vertical and inclined slender pile - theoretical and large-scale model investigations. Coastal Engineering(52): 435-462.
- Wienke, J., Sparboom, U. and Oumeraci, H., 2000. Breaking wave impact on a slender cylinder. In: B.L. Edge (Editor), International Conference on Coastal engineering. ASCE, Sydney, Australia.
- Zaaijer, M.B., 2003. Comparison of monopile, tripod, suction bucket and gravity base design for a 6 MW turbine, OWEMES, Naples, Italy.
- Zaaijer, M.B., 2005. Design Methods for Offshore Wind Turbines at Exposed Sites (OWTES); Sensitivity analysis for Foundations of Offshore Wind Turbines, Delft University, Delft.
- Zaaijer, M.B. and Van der Tempel, J., 2004. Scour protection: a necessity or a waste of money?, 43rd IEA Topical Expert Meeting–Critical Issues Regarding Offshore Technology and Deployment, Skaerbaek, Denmark, pp. 43-51.

PART II. SCOUR PROTECTION AROUND MONOPILE FOUNDATIONS

Chapter 3: State of the art in scour protection design

3.0 Introduction

Due to the expected scour depths around monopile foundations and the consequences for the design of the foundation (see chapter 1 and 2), a scour protection is generally applied around an offshore wind turbine foundation.

Different empirical criteria for the design of scour protections in a steady current (bridge piers) exist (Chiew (1995), Hoffmans and Verheij (1997), May et al. (2002)), but the design of scour protections in a combined wave and current environment has only recently been dealt with by den Boon et al. (2004), Hansen and Gislason (2005), Grune et al. (2006), Whitehouse et al. (2006). To the author's knowledge, very few design methods exist other than the method developed in the OPTI-PILE project from E-Connection et al. (2002-2004). The scour protections of most offshore wind parks are designed based on the criteria of the threshold of motion followed by a physical model study (e.g. Kirkegaard et al. (1998)). Most of these results are confidential and therefore only a confined group of people has the knowledge and experience to design scour protections for offshore monopile foundations.

The aim of this chapter is:

- to give a background of general scour protection design (section 3.1);
- to determine the loads upon and the strength of a scour protection (section 3.2);
- to give a review of all existing design criteria for scour protections around monopile foundations in wave, current and combined wave- and current climates (section 3.3);
- to describe physical modelling of scour protections around offshore wind turbines (section 3.4).

3.1 Basic principles of scour protection design

When designing a scour protection, it is important to keep the purpose of the scour protection in mind. Therefore, the design of a protection should be tuned to the project as a part of an integrated design. The resulting design ought to be both effective and efficient (Schierreck (2001)). While effective means that the scour protection fulfills its purpose, efficient means that the cost of the scour protection should be as low as possible. The main purpose of a scour protection around a monopile foundation is to avoid erosion of the soil close to the foundation thus guaranteeing stability and acceptable dynamic behaviour of the monopile. Loose rocks (riprap, see below) are commonly used as scour protection around offshore foundations. The main advantages of riprap are its availability and its low cost. First disadvantage is the wider size distribution of

riprap compared to uniformly graded rocks leading to a less uniform armor layer. Consequently the riprap layer will be more susceptible to damage by strong waves and currents. Secondly, the installation of the riprap layer by dumping leads to less precise positioning.

3.1.1 Need for scour protection

The necessity of a scour protection should always be questioned and alternatives should be considered. To establish whether a scour protection is required, the design loads (see section 3.2) and resulting scour depth should be calculated. Two possible alternatives for a scour protection around monopile foundations are (as adopted from May et al. (2002)):

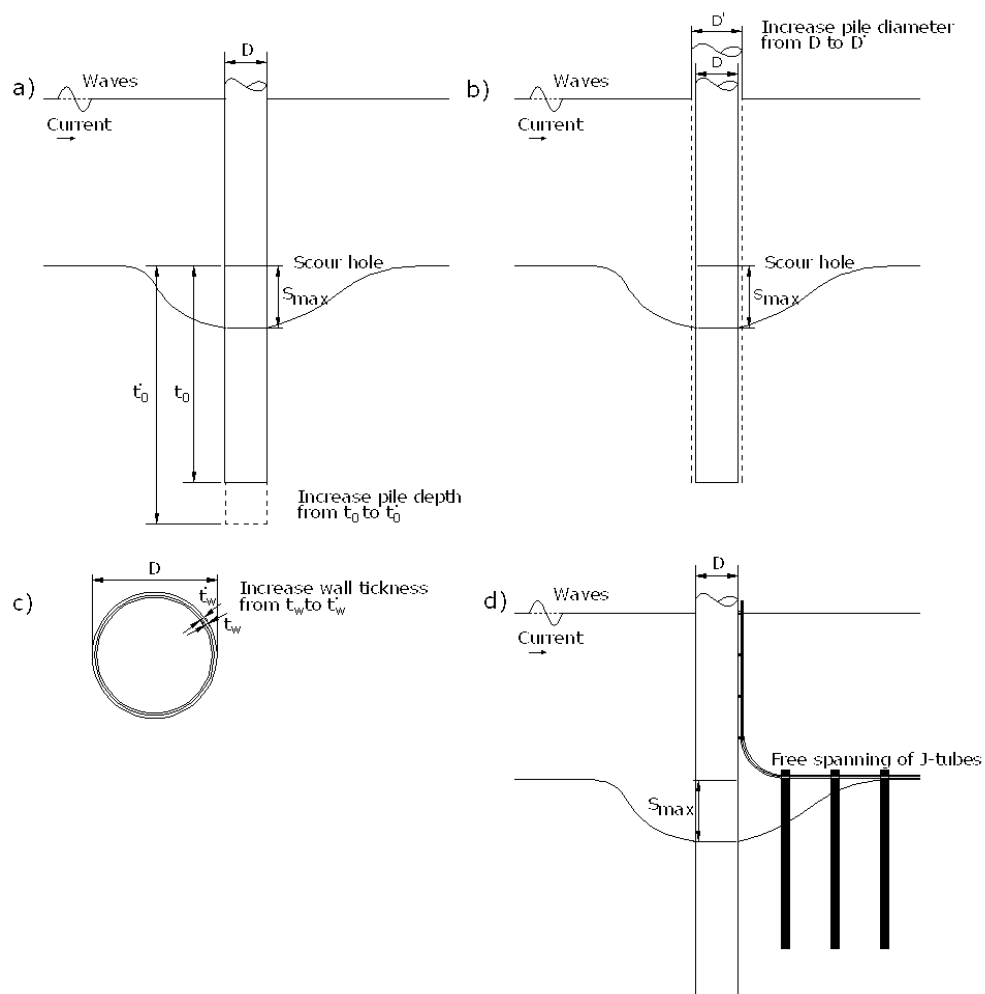


Figure 3-1: possible alternative for a scour protection around a monopile foundation: allowing local scour to develop

- 1) To allow scour around the monopile and take structural measures (Figure 3-1):
 - a) increase the bearing capacity of the pile by driving it deeper into the ground;
 - b) increase the pile diameter or wall thickness to take on a higher bending moment;
 - c) increase the stiffness of the pile by increasing the pile wall thickness to compensate for the increase in eigenfrequency caused by the higher pile length;
 - d) solve the free spanning of the cables: Zaijier and Van der Tempel (2004) hand possible alternatives, which are discussed in chapter 2 (section 2.5). One example is the support of the cable with intermediate piles (see Figure 3-1-d). Zaijier and Van der Tempel (2004) mention however that little experience exists on this matter.

- 2) To take scour reducing measures (Figure 3-2):
 - a) adding a horizontal deflector/collar may significantly reduce the scour depth (Hjorth (1975), Hoffmans and Verheij (1997)). An example of a horizontal collar, placed underneath the original bed is given in Figure 3-2(a). More research however is required to investigate these alternatives before they can become a valuable option;
 - b) Other scour reducing measures, i.e. the use of sacrificial piles or vertical vanes (May et al. (2002)), are sometimes used to reduce bridge scour in rivers but are not suitable for a marine environment, as they require knowledge of the flow direction and are developed for unidirectional flow (Hoffmans and Verheij (1997)).

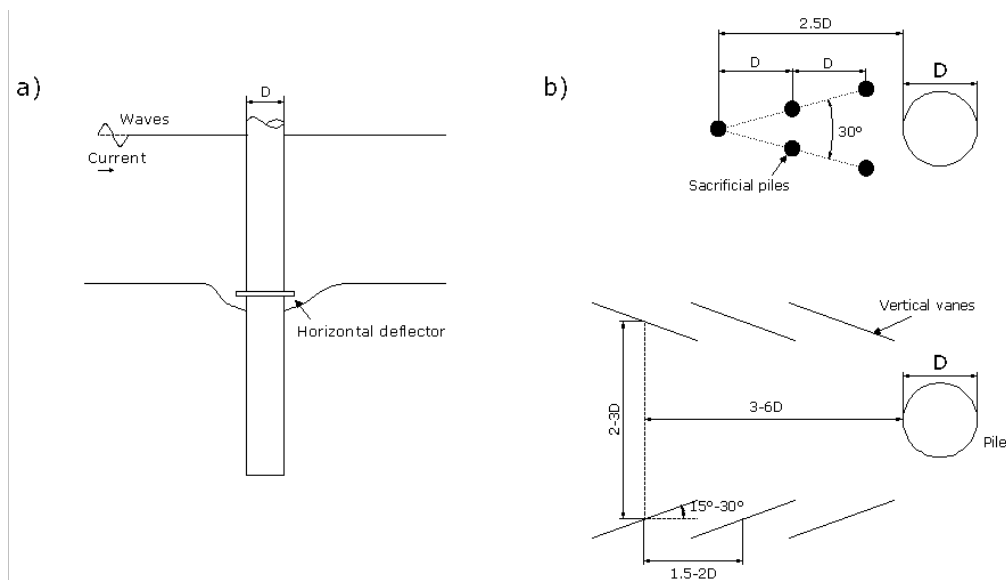


Figure 3-2: possible alternative for a scour protection around a monopile foundation: scour reducing methods; after May et al. (2002)

When the expected scour threatens the stability of the structure and/or the alternatives excessively raise costs, a scour protection is the way to go. Ballast Nedam and Oud (2002) and Herman et al. (2003) weigh the first alternative (scour development) against the application of a scour protection for a monopile foundation. This economical evaluation leads to the conclusion that in the examined case, the application of a scour protection leads to the most economic solution. However, the difference is limited so it is suggested to make further inquiries. They do however acknowledge that some problems, e.g. the free spanning of the J-tubes, are not considered in their comparison.

3.1.2 Failure modes

In general it is always necessary to keep in mind the overall picture. All failure mechanisms should be considered when designing a scour protection. Figure 3-3 shows the relevant failure mechanisms for the scour protection around a monopile foundation (adapted from Hoffmans and Verheij (1997)). Comparable failure mechanisms are also listed by Chiew (1995) and Sumer and Fredsøe (2002):

- a) erosion of the top layer caused by the flow, possibly leading to scour near the structure;
- b) loss of subsoil through the scour protection, which may lead to sinking of the top layer in the bed. This can be an iterative process, eventually leading to scour holes near the construction;
- c) due to the edge scour, which originates from the abrupt change in roughness between the riprap and the bed, stones may disappear at the edge of the scour protection, leading to an undersized scour protection (horizontal dimensions);
- d) when the scour hole is too steep, flow slide may damage the scour protection from the edge:

Sumer and Fredsøe (2002) add liquefaction as another possible failure mechanism for scour protections. Due to liquefaction, the scour protection material may sink into the seabed.

In chapter 4, section 4.2 and 4.3, the main focus lies on the prevention of failure mechanism a) through the development of a design formula for the required stone size. Failure mechanism b) can be prevented by using a correctly designed and adequately placed filter. Although no additional research on filter design was done for this thesis, the fundamentals are given in Appendix I. Loss of material at the edges, leading to a so-called falling apron will be almost unavoidable. Also a possible flow slide at the edges is caused by the scour which exists at the edges. Chapter 4, section 4.4 examines the edge effects and their influence on the scour protection design in more detail.

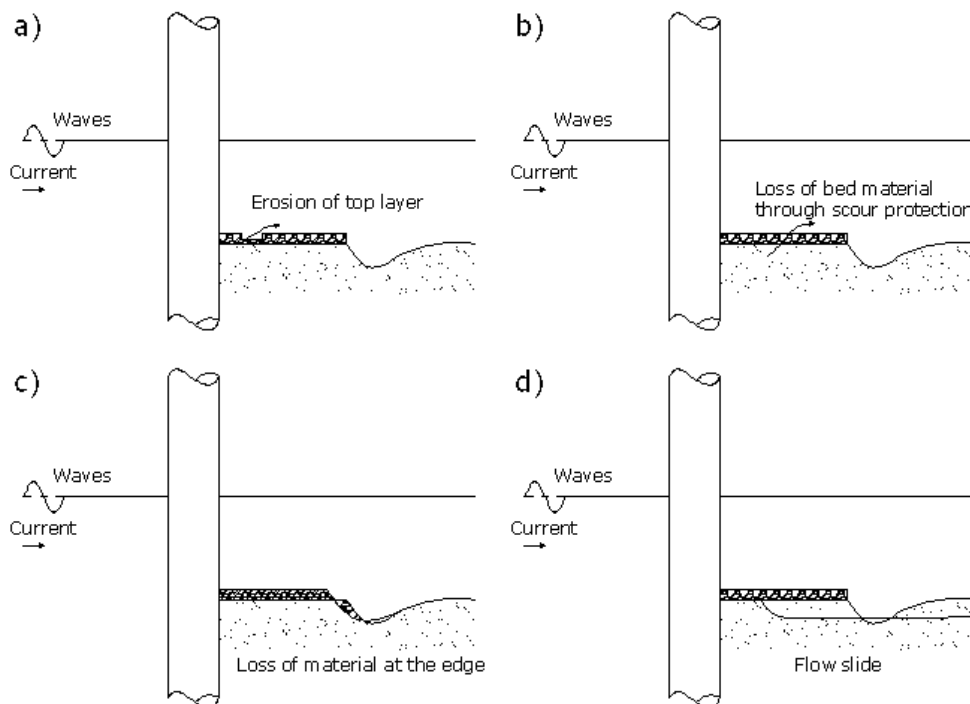


Figure 3-3: Failure mechanisms for scour protection around an offshore monopile foundation; after Hoffmans and Verheij (1997)

3.2 Environmental and structural parameters

In order to design a scour protection, both the environmental parameters and the structural parameters need to be specified. Figure 3-4 shows the basic outline of these parameters and how these influence the loads upon the structure and its strength. The environmental parameters (wave/current characteristics and water depth) together with the structural parameters (related to the foundation, e.g. pile shape and size; related to the scour protection, e.g. grain size) determine the load on the scour protection. The main resulting load parameters are the increased bed shear-stress and the turbulence which are caused by the structure (chapter 1). The structural parameters on the other hand, also determine the strength of the scour protection. Here, the main resulting parameters are the critical bed shear-stress and the settling velocity, which are both influenced by rock size and density.

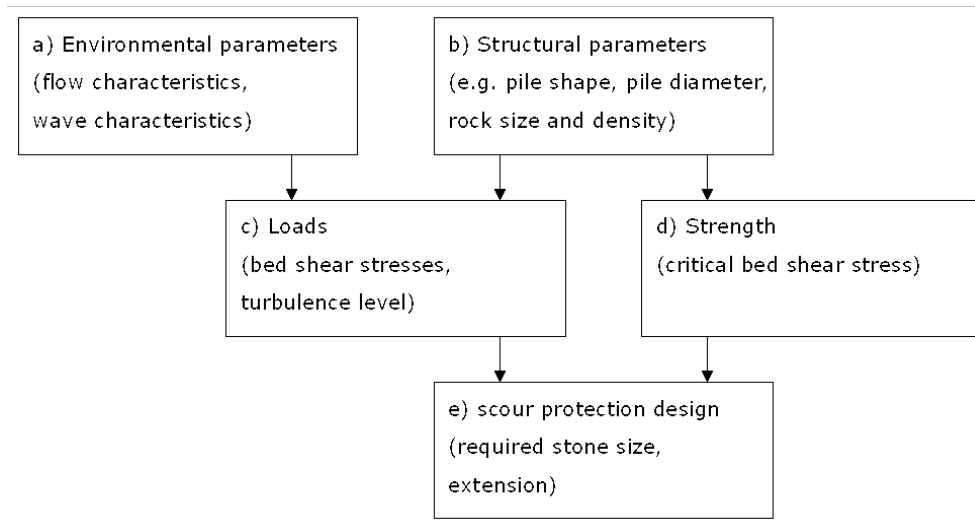


Figure 3-4: Basic outline of loading and response of a scour protection

3.2.1 Environmental parameters

The main environmental parameters that determine the scour protection design are the current velocity U_c , the wave characteristics (wave height, wave period) and the sediment properties. The wave characteristics and water depth d determine the horizontal component of the orbital velocity U_w at the bottom, which is needed to calculate the resulting bed shear stress.

3.2.1.1 Water depth

The water depth d has a significant influence on the load of the scour protection. On the one hand the water depth determines the wave length and the orbital velocity near the bottom. For the same wave characteristics (H and T_w) a larger water depth leads to a smaller bottom velocity. The water depth and flow rate also determine the current velocity: smaller water depths lead to higher current velocities for a constant flow rate. On the other hand, when the water depth limits the wave height and causes wave breaking (see section 3.2.1.2), larger water depths allow higher waves and thus possibly higher bottom velocities. It is therefore not known a priori which water depth will lead to the highest load on the scour protection.

3.2.1.2 Wave characteristics

The term waves is used to describe surface gravity waves, generated by winds. Estimates of wave conditions are needed in almost all coastal engineering studies, and the basics of wave mechanics are briefly described in this section for further reference.

Definition of wave parameters

A simple, periodic wave propagating over a horizontal bottom can be completely characterized by its wave height H , wavelength L and the water depth d .

As shown in Figure 3-5, the wave height is defined as the vertical distance between the highest point (crest) and the lowest point (trough). For linear or small-amplitude waves, the distance between wave crest and still-water level (SWL) and the distance between trough and SWL are each equal to the wave amplitude a . Therefore $a = H/2$ for linear waves. The wave period T_w is defined as the time interval between the passage of two successive wave crests or troughs at a given point. The wavelength L is the horizontal distance between two identical points on a successive wave (e.g. distance between two wave crests).

The most elementary wave theory is the small-amplitude or linear wave theory, which was developed by Airy (1845). It is easy to apply and gives a reasonable approximation of the wave characteristics for a wide range of wave parameters. Although there are limitations to its applicability, linear theory is still useful provided that the assumptions which are made are reasonably valid. Moreover, linear wave theory is even useful in many respects, when the requirements of linear theory are violated (Dean and Dalrymple (1991)).

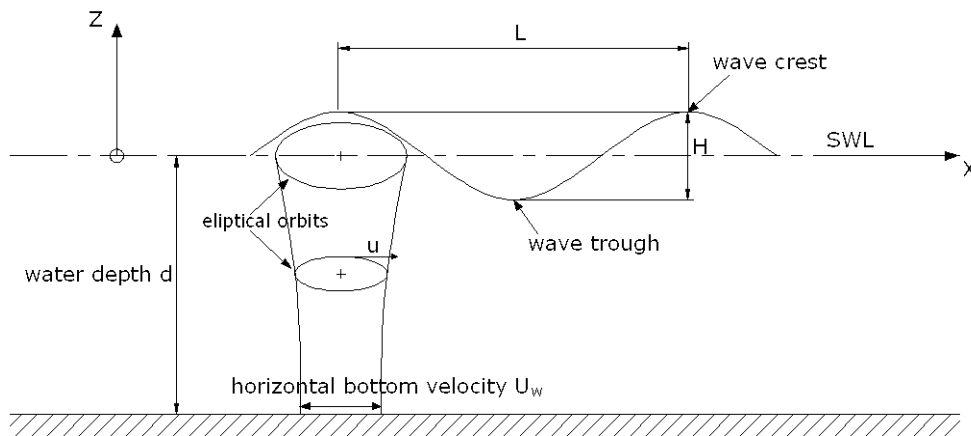


Figure 3-5: Definition of wave characteristics – regular linear wave

When using linear theory, the surface elevation at a given location x is represented by a cosine profile:

$$\eta(x,t) = \frac{H}{2} \cos(kx - \omega t - \phi) \quad (3.1)$$

in which $k = 2\pi/L$ is the wave number; ω is the angular frequency and ϕ is the phase shift.

The wave length L is determined from the wave period T_w and the water depth d using the dispersion relationship:

$$L = \frac{gT_w^2}{2\pi} \tanh\left(\frac{2\pi d}{L}\right) \quad (3.2)$$

in which $g = 9.81 \text{ m/s}^2$, the acceleration due to gravity. Equation (3.2) expresses the dispersive character of waves, indicating that waves with different periods travel with different speeds.

Figure 3-5 also shows the motion of a water particle in a finite water depth. Water particles move in elliptical orbits and a water particle's velocity is determined by a horizontal and a vertical component. When approaching the bottom, the ellipses are flattened and at the bottom, only a horizontal component remains.

As we are mainly interested in the bottom velocity, only the horizontal component is discussed here. Using linear wave theory, the amplitude of the horizontal velocity u can be calculated at any depth z as:

$$u = \frac{H}{2} \frac{gT_w}{L} \frac{\cosh\left[\frac{2\pi(z+d)}{L}\right]}{\cosh\left(\frac{2\pi d}{L}\right)} \quad (3.3)$$

leading to the amplitude of the horizontal velocity U_m at the bottom for $z = -d$:

$$U_m = u(z = -d) = \frac{H}{2} \frac{gT_w}{L} \frac{1}{\cosh\left(\frac{2\pi d}{L}\right)} \quad (3.4)$$

When using the dispersion relationship (3.2), this can be transformed to:

$$U_m = \frac{\pi H}{T_w} \frac{1}{\sinh\left(\frac{2\pi d}{L}\right)} \quad (3.5)$$

Non-linear waves

When the wave amplitude is no longer small compared to the water depth, the distance between SWL and wave crest is no longer equal to the distance between SWL and wave trough. Generally, the wave trough becomes less deep and wider, whereas the wave crest is higher and steeper. As this leads to a deviation from the cosine profile, linear wave theory is no longer able to describe the sea surface. A more complete theoretical description of the wave surface is advisable. This may be obtained by summing many successive approximations, where each additional term in the series is a correction to preceding terms.

When water depth becomes small or the wave steepness is too high, waves are better described by these higher-order theories, which are usually referred to as finite-amplitude wave theories (Dean and Dalrymple (1991)). Figure 3-6 shows the different wave theories and their validity range.

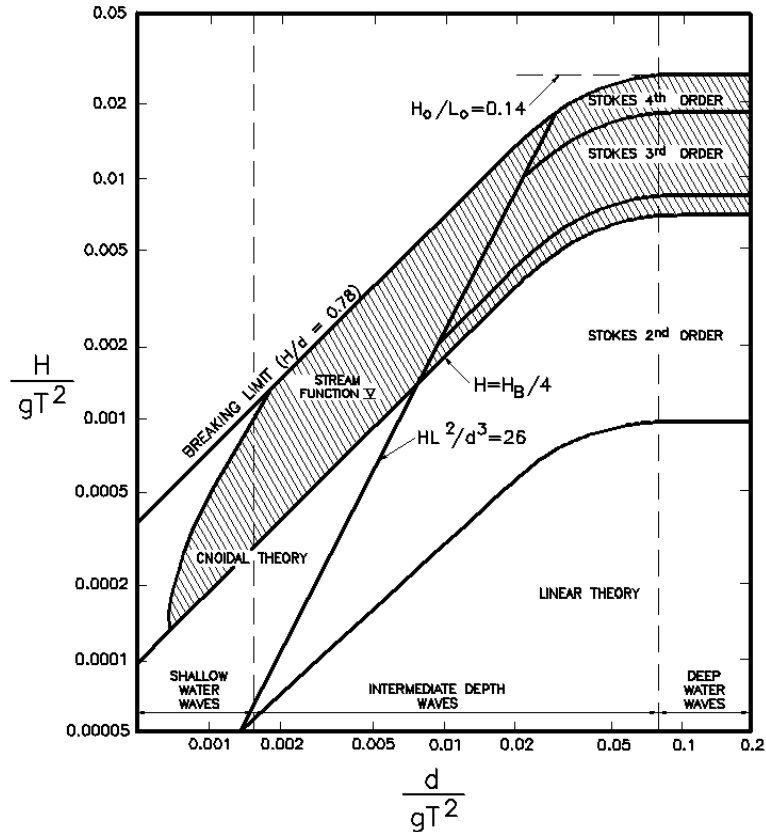


Figure 3-6: Validity regions for different wave theories; from US Army Corps of Engineers (2002)

Stokes' higher order theories are often applicable for larger wave heights in not too small water depths. The first and second order terms for elevation and horizontal velocity at a level z below the SWL are (Dean and Dalrymple (1991)):

$$\eta = \frac{H}{2} \cos(kx - \omega t) + k \frac{H^2}{16} \frac{\cosh(kd)}{\sinh^3(kd)} (2 + \cosh(2kd)) \cos(2(kx - \omega t)) \quad (3.6)$$

$$u = \frac{H}{2} \frac{gk}{\omega} \frac{\cosh(k(z+d))}{\cosh(kd)} \cos(kx - \omega t) + \frac{3kH^2 \omega}{16} \frac{\cosh(2k(z+d))}{\sinh^4(kd)} \cos(2(kx - \omega t)) \quad (3.7)$$

For the horizontal velocity, the non-linear effect mainly has an influence on the upper third of the water depth (Troch (2000)). This means that the second order term of the velocity near the bottom (equation (3.7)) is small compared to the first order term, and it can be neglected.

A fairly recent theory, called Fenton's Fourier series theory (Fenton (1988)), describes oceanic waves better than all previous similar theories for all water depths. Any periodic function can be approximated by a Fourier series. Fenton uses a numerical solution for the coefficients of the Fourier series. The method gives an accurate solution (when sufficient terms are used) while being independent of the water depth. For coastal applications, the formulae have been included in the ACES program (Coastal Engineering Research Center (1992)) up till 25 terms. Figure 3-7 shows an application of Fenton's theory with 18 terms.

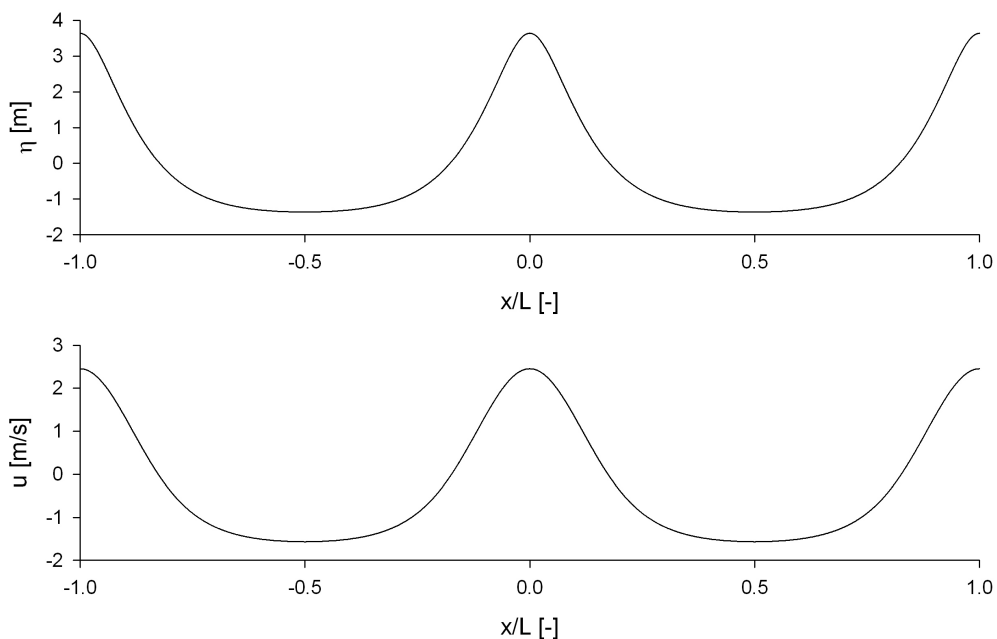


Figure 3-7: Example of the use of Fenton's Fourier series: wave elevation and horizontal bottom velocity for $d = 10\text{m}$, $H = 5\text{m}$, $T_w = 10\text{s}$ as a function of x/L

Figure 3-7 shows that, although the velocity in the trough is smaller than in the crest, the trough velocity persists much longer than the crest velocity. During one wave period, the horizontal velocity in this example (water depth $d = 10\text{m}$, wave height $H = 5\text{m}$, wave period $T_w = 10\text{s}$) is higher than 1m/s during 2.24s , while it is lower than -1m/s during 4.72s . This can be important regarding the development of the horseshoe vortex as it only develops for waves when the velocity persists long enough (see chapter 1, section 1.2).

A wave is physically limited in height by the water depth and its wavelength. In deep water, waves break when they become too steep. The upper limit or

breaking wave height H_b in deep water is a function of the wavelength only. Breaking wave height in deep water is given by Michell (1893) as:

$$\frac{H_b}{L} = 0.142 \quad (3.8)$$

In transitional and shallow water depths, waves break when the wave height becomes too high compared to the water depth or when they are too steep. The upper limit depends in this case both on the wave length and water depth. A simple, first estimate of the breaking wave height in limited water depth is given by (US Army Corps of Engineers (2002)):

$$\left(\frac{H_b}{d}\right)_{\max} = 0.78 \quad (3.9)$$

Fenton and McKee (1990) give a more elaborate equation to determine the breaking wave height:

$$\frac{H_b}{d} = \frac{0.141063 \frac{L}{d} + 0.0095721 \left(\frac{L}{d}\right)^2 + 0.0077829 \left(\frac{L}{d}\right)^3}{1.0 + 0.078834 \frac{L}{d} + 0.0317567 \left(\frac{L}{d}\right)^2 + 0.0093407 \left(\frac{L}{d}\right)^3} \quad (3.10)$$

Laboratory studies have shown that equation (3.9) gives a good estimate for oscillatory waves and that the nearshore slope has a substantial effect on this ratio (US Army Corps of Engineers (2002)).

Some higher order theories (e.g. Fenton's theory) can be used to describe the wave kinematics over the entire range of wave heights, and even obtain realistic solutions for waves near breaking.

Irregular waves

In reality, the sea surface is composed of waves of varying heights and periods and in addition to this waves move in different directions. Measurements of the sea surface at one single point result in a graph like Figure 3-8, which shows a wave measurement with duration T_0 .

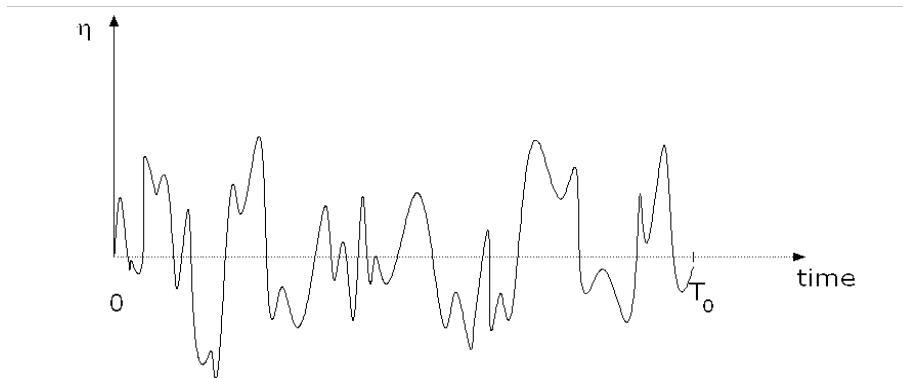


Figure 3-8: Typical example of an irregular wave train

Two different approaches exist for treating irregular waves: a spectral method and a wave-by-wave (wave train) analysis. Spectral approaches are based on a Fourier transformation of the measured wave train. The wave-by-wave analysis on the other hand uses the time-history of the sea surface at one point: the undulations are identified as waves and statistics of the registered values are developed. The main drawback to the wave-by-wave analysis is that it does not give information on the direction of the waves. Disadvantage of the spectral approach is the fact that it is linear and thus can distort the representation of nonlinear waves. As it is important to know which method and which assumptions are used for the wave analysis both methods are described below.

For the wave-by wave analysis the average position of the water surface is determined as the still-water level. The zero down-crossing or zero up-crossing method is used to identify individual waves. Both methods yield statistically similar mean values of wave parameters, but the zero down-crossing method is preferred (IAHR (1986)). In the zero down-crossing method, a wave is determined by two consecutive zero crossings on a downward flank of the elevation. The wave height is determined as the distance between the lowest point and the consecutive highest point between the two zero crossings. The wave period is defined as the time between the two zero crossings.

The main goal of the analysis is to describe an irregular sea state by means of a limited number of simple parameters. The sea state can roughly be characterized by two parameters, a characteristic wave height H and characteristic wave period T_w .

The characteristic wave height may be defined in different ways, e.g. the mean wave height H_m , the root-mean-square wave height H_{rms} or the mean height of the highest one-third of all waves known as the significant wave height H_s or $H_{1/3}$. The largest wave height in the record is called H_{max} . Similar to the significant wave height, the average height of $1/n$ highest waves is called $H_{1/n}$, where $H_{1/100}$ or $H_{1/10}$ are often used for the design of coastal engineering structures. The characteristic wave period could be the mean zero crossing wave period T_z , which is the mean value of all measured wave periods.

The significant wave height H_s is also sometimes described as the wave height which is visually estimated by an experienced observer and is the wave height which is most commonly used (US Army Corps of Engineers (2002)).

From statistical theory, it can be shown that if the individual components are statistically independent and a large number of waves is used, the probability that a wave height in a time series, characterized by H_{rms} exceeds a given wave height H_d , is given by (Dean and Dalrymple (1991)):

$$P(H \geq H_d) = e^{-(H_d/H_{rms})} \quad (3.11)$$

with the root-mean-square wave height H_{rms} defined as:

$$H_{rms} = \sqrt{\frac{1}{N} \sum_{i=1}^N H_i^2} \quad (3.12)$$

Distribution (3.11) is called the Rayleigh distribution and it is valid for deep water waves. For waves in limited water depth, the Rayleigh distribution tends to overestimate the larger wave heights.

The introduction of the Rayleigh distribution allows relating H_{rms} to the other characteristic wave heights:

$$\begin{aligned} H_m &= 0.886H_{rms} \\ H_s &= 1.416H_{rms} \\ H_{1/10} &= 1.80H_{rms} \\ H_{1/100} &= 2.359H_{rms} \\ H_{max} &= 2.63H_{rms} \end{aligned} \quad (3.13)$$

In the spectral approach, an irregular wave train is considered to be a superposition of a number of regular waves (cf. equation (3.1)), with respective wave heights H_i , wave periods T_i , ...:

$$\eta(x, t) = \sum_i \eta_i(x, t) = \sum_i \frac{H_i}{2} \cos(k_i x - \omega_i t - \phi_i) \quad (3.14)$$

or, when x is considered to be 0 at the measurement location:

$$\eta(t) = \sum_i \frac{H_i}{2} \cos(\omega_i t + \phi_i) \quad (3.15)$$

This information can be represented in the frequency domain by an amplitude spectrum and phase spectrum using a Fourier transformation. Typically, only the

amplitude spectrum is used and for each frequency $f_i = 1/T_i$, the amplitude a or energy (proportionate to a^2) is plotted. The energy spectral density or variance spectral density $S(f)$ is mostly used and $S(f)$ is plotted against f :

$$S(f) = \frac{1}{2} \frac{a^2}{\Delta f} \quad (3.16)$$

Figure 3-9 shows an example of the energy spectral density of an irregular wave train. Although the Fourier transformation yields a double, symmetrical spectrum around the nyquist frequency $f_{nyquist} = f_s/2$, with f_s the sampling frequency, normally only the first half of the spectrum is used. One should make sure that the irregular waves contain no frequencies above $f_{nyquist}$ to avoid aliasing. In this case, only the left part of the frequency spectrum represents the true energy of the wave field. The frequency band width Δf depends on the duration of the measurement T_0 :

$$\Delta f = \frac{1}{T_0} \quad (3.17)$$

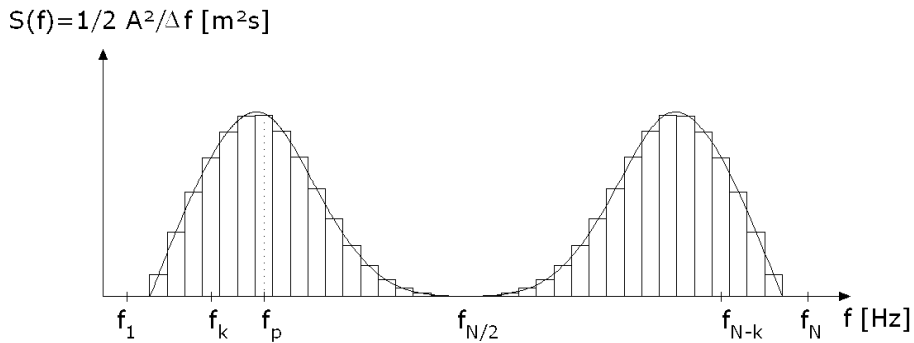


Figure 3-9: The energy spectral density

For the theoretical calculation of the wave spectrum based on a Fourier analysis of the measured time series, a reference is made to Troch (2000) or Brorsen et al. (2003).

The energy of the irregular wave train is represented by the moment m_0 :

$$m_0 = \int_0^{+\infty} S(f) df \quad (3.18)$$

When using spectral analysis the significant wave height H_{m0} is generally used:

$$H_{m0} = 4.004 \sqrt{m_0} \quad (3.19)$$

H_{m0} is approximately equal to H_s , derived from the wave train analysis, except for small water depths or for very steep waves (Massel (1996)) and it is often used as a substitute of H_s .

The characteristic wave periods, resulting from the spectral analysis are the peak period T_p corresponding to the peak frequency f_p (see Figure 3-9) and the wave periods based on the moments of the wave spectrum:

$$T_{m-1,0} = T_e = \frac{m_{-1}}{m_0} \quad (3.20)$$

$$T_{m0,2} = \sqrt{\frac{m_0}{m_2}} \quad (3.21)$$

$$T_{m0,1} = \frac{m_0}{m_1} \quad (3.22)$$

with the n^{th} moment of the spectral density m_n defined as:

$$m_n = \int_0^{\infty} f^n S(f) df \quad (3.23)$$

with f the frequency and $S(f)$ the spectral density.

The use of periods based on the spectral moments is sometimes preferred above the use of T_p , as the magnitude of the peak period can differ, depending on the choice of the frequency band width Δf (cf. equation (3.17)).

Different theoretical spectra exist, which define a wave spectrum, based on the wind speed. The best known ones are the Pierson-Moskowitz (PM) spectrum and the Jonswap spectrum (Massel (1996)). The parameterized spectra determine the shape of the wave spectrum, based on the known value of H_{m0} , T_p (or f_p) and for the Jonswap spectrum, a value for γ . The Jonswap spectrum and the Pierson Moskowitz spectrum coincide for $\gamma = 1$. The parameterized spectra can be written as (Goda (2000)):

$$S_{PM}(f) = \frac{5}{16} H_{m0}^2 f_p^4 f^{-5} \exp\left(-\frac{5}{4} \left(\frac{f_p}{f}\right)^4\right) \quad (3.24)$$

$$S_{JON}(f) = \alpha H_s^2 f_p^4 f^{-5} \gamma^\beta \exp\left(-\frac{5}{4} \left(\frac{f_p}{f}\right)^4\right) \quad (3.25)$$

$$\text{with } \alpha = \frac{0.0624}{0.230 + 0.0336\gamma - \left(\frac{0.185}{1.9 + \gamma}\right)}$$

$$\beta = \exp\left(-\frac{(f - f_p)^2}{2\sigma^2 f_p^2}\right)$$

$$\sigma = 0.07 \quad f \leq f_p$$

$$\sigma = 0.09 \quad f > f_p$$

A Jonswap spectrum with $\gamma = 3.3$ is the most representative for the North Sea (Goda (2000)). In this case ($\gamma = 3.3$), the following relationships can be found between the peak period and the n^{th} moment spectral periods:

$$\begin{aligned} T_p &= 1.286T_{m0,2} \\ T_p &= 1.1986T_{m0,1} \\ T_p &= 1.107T_{m-1,0} \end{aligned} \quad (3.26)$$

Design wave characteristics

When designing an offshore structure, one must decide which environmental conditions the structure must be able to withstand. Regarding the wave characteristics, the design wave height is often considered the most important parameter. The selection of the design wave height is described in terms of the return period and the encounter probability (Massel (1996)). As the return period T_r usually is much longer than the time during which measurements have been made, extrapolations of wave probability distributions have to be performed.

We will not pursue this matter in more detail here, but it is important for the reader to know that, once a design wave height H_d is selected, the exceeding probability of H_d should be calculated as follows (Troch (2007)):

$$P(H \geq H_d) = \sum_i P(H > H_d)_{H_{si}} \cdot P(H_{si}) \quad (3.27)$$

with $P(H > H_d)_{H_{si}}$ the exceeding probability of the wave height H_d in a storm characterised by the significant wave height H_{si} , for example determined by the Rayleigh distribution (equation (3.11)), and $P(H_{si})$ the encounter probability of H_{si} .

Monopile foundations for offshore wind farms have a typical lifespan of approximately 20 years. Return periods of 50 to 100 years are typically chosen to design a scour protection.

Although the design wave height is very important, the wave period plays an important role in the loading on the scour protection as well. Less statistical relations exist for the wave period, compared to the wave height. Soulsby (1997) mentions that, when only H_s is known for a particular site, the following equation can be used to estimate the mean zero upcrossing wave period T_z as a function of the significant wave height H_s :

$$T_z = 11 \sqrt{\frac{H_s}{g}} \quad (3.28)$$

with $T_z = 0.781T_p$ for a JONSWAP spectrum with $\gamma = 3.3$. IMDC (2005) obtained the following relationship between H_{m0} and T_p for the period between 1995 and 2001:

$$T_p = 4.4 \sqrt{H_{m0}} \quad (3.29)$$

It is important to keep in mind that both equation (3.28) and equation (3.29) are site specific and care must be taken when using them outside the region for which they were intended.

Number of waves

When using regular waves in a model test the structure experiences the same force each time a wave passes. This leads to quick damage development. Random or irregular waves give a better representation of reality. When random waves are used in model tests, it takes a longer time for an equilibrium state to be reached and the number of waves, representing the duration of the storm, have a significant influence on stability tests (Van der Meer (1988), Schiereck (2001)). Van der Meer (1988) includes the number of waves in his design formulae. He concludes that 3000 waves are sufficient to obtain a profile close to the equilibrium profile in his physical model tests of rubble mound breakwaters. Further more, when random waves are used, the wave height (e.g. H_s) and period need to be characterised before comparison with regular waves is possible. This is done as is described above.

3.2.1.3 Flow characteristics

Sea currents are mainly driven by tides and ocean circulations, although locally, the outflow of a river might induce an extra current. In shallow water, a steady current can also be caused by breaking waves. The current velocity varies very slowly compared to the other loads which act on a wind turbines foundation (wind, waves) and both the current's magnitude and direction are therefore regarded as constant for design calculations.

The main flow characteristics are the averaged flow velocity U_{cr} , the flow direction and the velocity distribution over the water depth.

The current velocity is usually highest where large tidal differences occur or where local bathymetry causes an increase in the current velocity.

The velocity distribution of a current depends mainly on the boundary layer and is discussed in more detail in chapter 1 (section 1.1.1.1).

Another important aspect is the influence of the current on the wave characteristics. The interaction of wave and current boundary layers is described in chapter 1 (section 1.1.1.3), other interactions between waves and currents are described in Appendix III.

3.2.1.4 Sediment characteristics

The characteristics of the bed material are important when designing a scour protection and are therefore shortly described below. Only non-cohesive soils are considered here. For non-cohesive sediments the grain size and distribution are important for the filter design (Appendix I) and the angle of internal friction is important for the extent of the scour hole, both for the slope of the scour hole without scour protection (chapter 2) as for the extent of the scour at the edge of the scour protection (section 4.4). The settling velocity is important when examining the effects of the scaling of the bed material (further described in section 3.4).

Grain size and distribution

Non-cohesive grain diameters vary between 0.062mm and 2mm (van Rijn (1993)). The grain size distribution is often presented in a log-linear distribution plot (Figure 3-10). The diameter corresponding to the 50% value on the log-probability plot is called the geometric mean diameter d_{50} and is related to the sieve size (with square openings) through which 50% of the material (in weight) passes.

The grading of the grains is often characterized by the standard deviation σ_g :

$$\sigma_g = \frac{1}{2}(d_{84} - d_{15}) \quad (3.30)$$

or by the ratio of the grain size for which 85 % of the material is finer by weight d_{85} and the grain size for which 15 % of the material is finer by weight d_{15} :

$$\frac{d_{85}}{d_{15}} \quad (3.31)$$

Small values of the standard deviation indicate a narrow grading, while large values of the standard deviation indicate a wide grading.

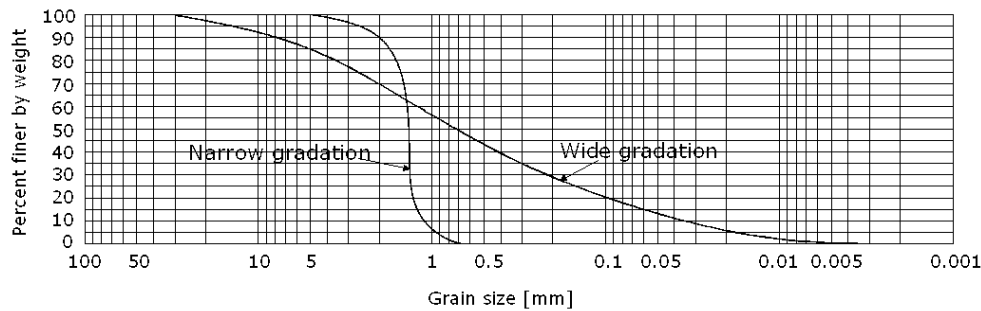


Figure 3-10: Log-probability plot of a wide and narrow grain size distribution

Angle of repose

The angle of (natural) repose or the angle of internal friction ϕ is the equilibrium slope grains have when they are piled up onto each other (van Rijn (1993)). Observations of the angle of repose for sand lie within the range $\phi = 30^\circ$ to 40° .

Settling velocity

The settling or fall velocity w_s of the sediment determines its transport mode. The settling or fall velocity of a sphere in a fluid can be obtained by expressing the balance between the fluid drag force and the gravitational force:

$$w_s = \sqrt{\frac{4g(s-1)d_s}{3C_D}} \quad (3.32)$$

in which $g = 9.81 \text{ m/s}^2$ represents the acceleration due to gravity; s is the relative density of the sphere (ρ_s/ρ_w); d_s is the sphere diameter and C_D is the drag coefficient. The drag coefficient for a sphere is a function of the Reynolds number $Re = w_s d_s / \nu$.

For a non-spherical particle, the shape of the particle also influences the Reynolds number. Many empirical formulae exist that give the fall velocity for non-spherical sediment particles. Only a few of the most used formulae are presented here.

van Rijn (1993) suggests the following formulae for non-spherical particles:

$$w_s = \frac{(s-1)gd_s^2}{18\nu} \quad \text{for } 1 < d_s \leq 100 \mu\text{m}$$

$$w_s = \frac{10\nu}{d} \left[\left(1 + \frac{0.01(s-1)gd_s^3}{\nu^2} \right)^{0.5} - 1 \right] \quad \text{for } 100 < d_s < 1000 \mu\text{m} \quad (3.33)$$

$$w_s = 1.1 \left[(s-1)gd_s \right]^{0.5} \quad \text{for } d_s \geq 1000 \mu\text{m}$$

with d_s the sieve diameter.

Soulsby (1997) gives the following empirical equation for the settling velocity of individual grains for all values of the dimensionless grain size D_* (equation (1.35)):

$$w_s = \frac{v}{d} \left[\left(10.36^2 + 1.049 D_*^3 \right)^{1/2} - 10.36 \right] \quad (3.34)$$

3.2.2 Structural parameters

On the one hand the structural parameters are related to the foundation characteristics and on the other hand to the scour protection's characteristics.

The structural parameters of a monopile foundation for an offshore wind turbine are limited to the pile diameter D and the foundation's shape. In an offshore environment, where the waves can come from different directions, a circular shape is mostly used to minimize the influence of the structure on the flow (Sumer and Fredsøe (1997)). The diameter of the pile is determined by the resistance against static and dynamic loading (chapter 2).

The structural parameters, related to the scour protection are stone density, stone size, stone grading, stone shape and settling velocity. They are shortly described below.

3.2.2.1 Density

The mass density of a stone ρ_s is defined as the mass m per unit volume V_s of a solid rock:

$$\rho_s = \frac{m}{V_s} \quad (3.35)$$

ρ_s plays an important role in the stability of stones. A high density might decrease the required stone weight to a large extent. Typical mass densities of rocks lie within the range of 2600 (e.g. granite) and 3100 kg/m³ (e.g. basalt). It is possible to make artificial blocks with a higher mass density than the one of stones.

The bulk density of the stones is defined as the mass of a volume of stones, divided by the volume they occupy:

$$\rho_d = \frac{m}{V_d} \quad (3.36)$$

The volume V_d includes the space between the particles. The bulk density of the stones depends on the mass density of the stones as well as on the porosity of the stones and is therefore somewhat more difficult to determine as the mass density. The bulk density is used to estimate the required weight of stones to

obtain the desired volume (determined by the thickness and extension) of the scour protection.

De Rouck (1991) measured the bulk density of several riprap gradations and found that it is very difficult to get a correct estimate of the bulk density, due to the difficulty to determine the volume of the stones. A porosity of 33% was found for the widest gradation (2-300kg), while a porosity of approximately 40% was found for most of the stone gradations which were used for the breakwaters at the port of Zeebrugge.

3.2.2.2 Individual stone size and weight

The individual stone size and weight is important in coastal engineering, as it is mainly the weight which prevents displacement of the stone. The relationship between stone size and weight is usually defined as the equivalent volume cube (with side D_n) or the equivalent volume sphere (with diameter D_s) (CIRIA/CUR (1991)):

$$D_n = \left(\frac{W}{\rho_s} \right)^{1/3} \quad (3.37)$$

$$D_s = 1.24 \left(\frac{W}{\rho_s} \right)^{1/3} \quad (3.38)$$

When discussing graded rock materials (section 3.2.2.3), size and weight refer to the medians. The nominal diameter D_{n50} is defined as the side of the equivalent cube with median weight W_{50} and is given by:

$$D_{n50} = \left(\frac{W_{50}}{\rho_s} \right)^{1/3} \quad (3.39)$$

In CIRIA/CUR (1991), a relation between D_{50} and D_{n50} is suggested:

$$D_{n50} / D_{50} = 0.84 \text{ or } D_{50} = 1.19 \left(\frac{W_{50}}{\rho_s} \right)^{1/3} \quad (3.40)$$

with D_{50} the side of the median sieve with square openings through which 50% of stones pass (by weight).

The size of the stones is not only important to determine the resistance against the loading condition, it also influences the bed shear-stress through its impact on the roughness, and thus influences the load on the stones as well.

3.2.2.3 Stone grading

Quarries produce crushed and broken stone in sizes ranging from small gravel to huge blocks that cannot be handled and transported without special equipment. For stones smaller than 1000mm, sieving techniques are used and the gradation of the rock material is determined the same way as for sediment (section 3.2.1.3). For large stones (sieve diameter > 250mm), direct measurement of the stone weight becomes more practical and the relationship between the size and weight (3.40) is used. The stone weight distribution is then presented in a percentage lighter by weight cumulative curve, where W_{50} represents the block weight for which 50% of the total sample weight exist of lighter blocks. Again, the steepness of the curve (comparable to that for sediments) indicates the grading width. For stones, the following grading widths are distinguished, based on the D_{85}/D_{15} ratio (CIRIA/CUR (1991)):

$D_{85} / D_{15} < 1.5$: narrow grading

$1.5 < D_{85} / D_{15} < 2.5$: wide grading

$2.5 < D_{85} / D_{15} < 5$: very wide or "quarry run" grading

Generally, when the required stone diameter (mostly representing D_{50}) is chosen, a standard rock grading which fulfills this requirement is chosen. Figure 3-11 (De Rouck (1999)) shows some standard grading curves which were used for the breakwaters of the Zeebrugge Harbour. Each time the upper and lower limit are given. To satisfy the requirements, the grading curve has to lie between these borders. Requirements and supplementary information for standard gradings are handed in CIRIA/CUR (1991).

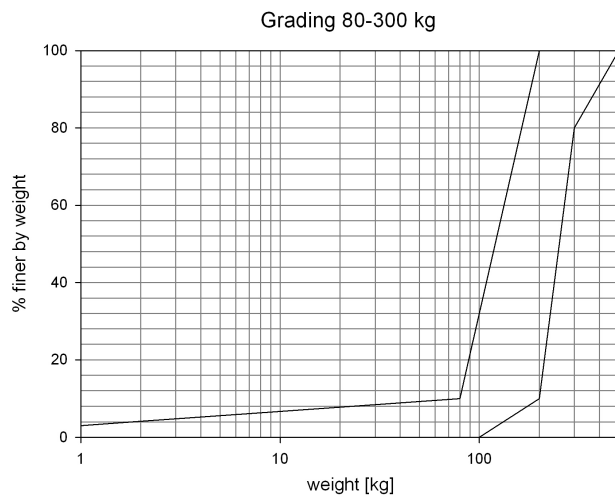
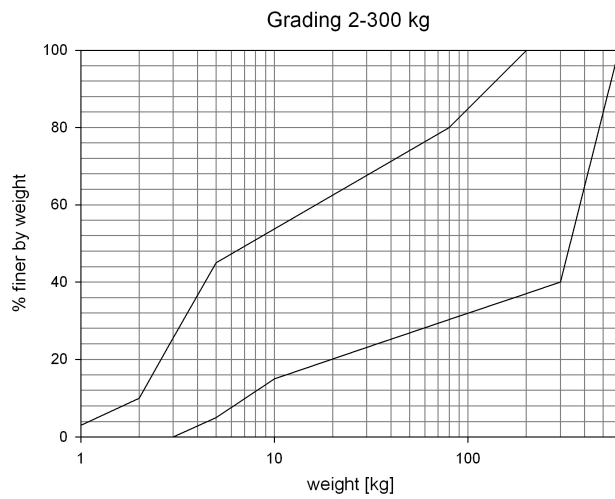
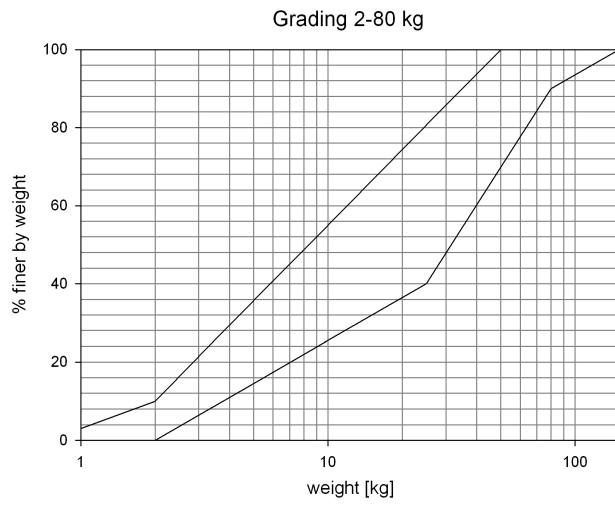


Figure 3-11: Upper and lower limits for standard grading curves for different weight categories: 2-80 kg, 2-300 kg and 80-300 kg

3.2.2.4 Stone shape

Not only the stone size but also the shape of the stone plays an important role in the entrainment of the stone. Ideally, all armor stones are blocky in shape and nearly uniform in size. A generally applied rule is that the largest stone dimension on an individual stone should be no more than three times the shortest dimension (US Army Corps of Engineers (2002)). CIRIA/CUR (1991) mentions as requirement that for the armour layer less than 5% in number of blocks can have a ratio of largest stone dimension on smallest stone dimension equal to or more than 3. For standard gradings it is likely to have approximately 20%, so some production losses due to shape rejection can be expected.

Furthermore, angular or blocky stones are preferred over rounded stones as they interlock better with adjacent stones (US Army Corps of Engineers (2002)). Quarry-produced stones are typically angular, whereas stones from glacial deposits and alluvial sources are usually rounded. Examples of stone shape and classification are given in CIRIA/CUR (1991).

3.2.2.5 Settling velocity

For the settling velocity, the same goes as for the settling velocity of sediment. Many empirical formulae exist, but equations (3.33) and (3.34) are withheld.

3.3 Existing design criteria for scour protections around cylindrical monopiles

When designing a scour protection, four questions need to be solved:

- 1) What is the required stone size for the armour layer to be stable?
- 2) What is the required horizontal extent of the scour protection?
- 3) What is the required thickness of the scour protection?
- 4) Are filter layers required in the design?

Aspects 1 to 3 are discussed in this section, applied to a monopile foundation. The necessity and design of a filter is discussed in Appendix 1. Special attention is given to the OPTI-PILE project (Optimisation of Monopile Foundations for Offshore Wind Turbines in Deep Water and North Sea Conditions). The OPTI-PILE objective was to develop an optimal monopile foundation for offshore wind turbines in deep water with North Sea characteristics. Their research included riprap scour protection design. At the end of this section, existing offshore wind parks and their applied scour protection are presented, as far as the information is available.

3.3.1 Required stone size

Empirical formulae exist for scour protections around bridge piers, i.e. the current alone case, but few design formulae exist for waves or combined waves and current. The typical design method and the empirical formulae for the steady current case are described in this section. Section 3.3.3 elaborates on the

OPTI-PILE project, which hands an empirical formula to determine the stone size around a vertical pile in a combined wave and current climate.

The general design method is to determine the amplified bed shear stress near the pile (chapter 1, section 1.1.1 and 1.2) and to use the Shields criterion (chapter 1, section 1.1.2) to establish the required stone size.

Most authors (Breusers and Raudkivi (1991), Hoffmans and Verheij (1997), Van Oord (2003)) state that the threshold of motion around a cylindrical vertical pile is reached when the amplified bed shear-stress, equal to 4 times the undisturbed bed shear-stress $\tau_{b,\infty}$ exceeds the critical bed shear-stress τ_{cr} determined with the Shields criterion. Or, when turning things around, in order to guarantee a stable scour protection, the following criterion needs to be fulfilled:

$$\tau_{cr} > 4\tau_{b,\infty} \text{ or } U_{cr} > 2U_c \quad (3.41)$$

with U_c the mean current velocity and U_{cr} the critical flow velocity. For sufficiently coarse bed material, the critical Shields parameter (determined from Figure 1-5 or equation (1.36)) approaches 0.055.

Breusers and Raudkivi (1991) obtain some simple equations based on equation (3.41) and an assumption for the critical Shields parameter. The following equation is obtained by applying a conservative value for $\theta_{cr} = 0.04$:

$$U_{cr} \cong 4.8\Delta^{1/2}D_r^{1/3}d^{1/6} \quad (3.42)$$

in which $\Delta = (\rho_s - \rho_w)/\rho_w$, D_r is the stone diameter of the scour protection and d is the water depth.

Breusers and Raudkivi (1991) state furthermore that most empirical equations give the stone diameter proportional to U_{cr}^2 . The simplest equation is (when assuming a density ρ_s of 2600 kg/m³):

$$U_{cr} = 4.92\sqrt{D_s} \quad (3.43)$$

with D_s the diameter of the equivalent sphere in m in equation (3.38) and U_{cr} in m/s. Equation (3.43) in combination with equation (3.41) yields:

$$D_s > 0.165U_c^2 \quad (3.44)$$

Breusers and Raudkivi (1991) note also that the riprap should be composed of a well-graded mixture of rocks and the characteristic representative size of the riprap is approximately equal to D_{67} in weight.

In May et al. (2002) three empirical relationships are given to calculate the required stone size for riprap around a bridge pier (current alone). They mention that the results obtained may differ significantly, due to limitations in the extent of laboratory testing, over-simplification of the parameters that affect the stability and the use of different safety factors. They recommend to use all three formulae and to choose either the average solution as design stone size, or the largest solution depending on the consequences of failure. The three recommended formulae (3.45), (3.47), (3.48) are designed respectively by Escarameia and May in 1992, by Pilarczyk in 1990 and by Maynard in 1995. Each formula requires an estimate of the flow velocity and the degree of turbulence.

The formula from Escarameia and May is developed from laboratory tests on riprap, stone mattresses and gabion mattresses:

$$D_{n50} = C_I \frac{U_b^2}{2g(s-1)} \quad (3.45)$$

in which D_{n50} is the characteristic stone size according to equation (3.39); U_b is the current velocity at a height of $0.1d$ above the bottom $= 0.87U_c$ around a structure (May et al. (2002)); g is the gravitational force; $s = \rho_s/\rho_w$ is the relative density of the stone and

$$C_I = 12.3TI - 0.20 \quad (3.46)$$

with TI a parameter characterizing the turbulence intensity $= 0.35$ around structures such as piers.

The formula of Pilarczyk is based on work around the stability of riprap, stone mattresses and concrete block mattresses:

$$D_{n50} = \frac{\mu}{s-1} \frac{0.035}{\Psi_{cr}} \frac{K_T K_Y}{K_S} \frac{U_c^2}{2g} \quad (3.47)$$

in which D_{n50} again represents the characteristic stone size according to equation (3.39); μ a stability correction factor $= 0.75$ for a continuous protection and $= 1.0$ to 1.5 at edges and transitions; s the relative density of the stone; Ψ_{cr} a stability factor $= 0.035$ for riprap; K_T a turbulence factor $= 1.5$ to 2 for high turbulence like bridge piers; K_Y a depth factor, taking the value of $K_Y = (D_{n50}/d)^{0.2}$ for highly turbulent flows, with d the water depth; K_S a slope factor $= 1$ for a horizontal bottom; U_c the depth averaged velocity and g the acceleration due to gravity $= 9.81 \text{ m}^2/\text{s}$.

The third equation is used in the US Army Corps of Engineers and was developed and refined by Maynard using laboratory tests and full-scale trials:

$$D_{s30} = S_f C_s C_v d \left(\sqrt{\frac{1}{s-1}} \frac{U}{\sqrt{K_l g d}} \right)^{2.5} \quad (3.48)$$

in which D_{s30} is the characteristic size of an equivalent sphere of which 30% is finer by weight; S_f is a safety factor; C_s is a stability coefficient = 0.3 for angular rock and = 0.375 for rounded rock; C_v is a velocity distribution coefficient = 1 for a straight channel and = 1.25 downstream of a hydraulic structure; d is the water depth; s is the relative density of the stone; U is the depth averaged velocity; g is the acceleration due to gravity = 9.81 m²/s and K_l is a sideslope correction factor = 1 for a horizontal bottom.

Chiew (1995) discusses the mechanics of riprap failure at bridge piers. He finds that the threshold of scouring at a cylindrical bridge pier depends both on the pier size relative to the grain size D/D_{50} and on the water depth compared to the pier size d/D :

$$\frac{U_c}{U_{cr}} = \frac{0.3}{K\left(\frac{D}{D_{50}}\right) \cdot K\left(\frac{d}{D}\right)} \quad (3.49)$$

The minimum value of $U_c/U_{cr} = 0.3$. The value of the correction factors $K(D/D_{50})$ and $K(d/D)$ is:

$$K\left(\frac{D}{D_{50}}\right) = 0.398 \ln\left(\frac{D}{D_{50}}\right) - 0.034 \left[\ln\left(\frac{D}{D_{50}}\right) \right]^2, \quad 1 \leq \frac{D}{D_{50}} < 50 \quad (3.50)$$

$$K\left(\frac{D}{D_{50}}\right) = 1, \quad \frac{D}{D_{50}} \geq 50$$

$$K\left(\frac{d}{D}\right) = 0.783 \left(\frac{d}{D}\right)^{0.322} - 0.106, \quad 0 < \frac{d}{D} < 3 \quad (3.51)$$

$$K\left(\frac{d}{D}\right) = 1, \quad \frac{d}{D} \geq 3$$

Chiew (1995) suggests an iterative calculation for the required stone size, with a value of 0.3 for U_c/U_{cr} as a first estimate for the minimum size of the riprap stones:

$$D_{50} > \frac{1}{5.956\sqrt{d}} \frac{U_c^3}{\left((U_c/U_{cr})\sqrt{(s-1)g}\right)^3} \quad (3.52)$$

with D_{50} in m; U_c the depth averaged velocity in m/s; s the relative stone density and d the water depth in m. An adjustment should be made to U_c/U_{cr} in this equation according to equations (3.50) and (3.51) when the pile size to stone size ratio D/D_{50} is smaller than 50 or the water depth to pile size ratio d/D is smaller than 3.

Whitehouse (1998) discusses scour protections in a marine environment (both waves and currents). He mentions that the calculation of the bottom shear stress is complicated due to the fact that the shear stress acting on the protection layer is determined by the characteristics of the bed material, which are not known a priori. He suggests getting an initial estimate of the material that will be stable under the design current or wave action by implementing criteria (3.53) and (3.54), suggested by Soulsby (1997) for an undisturbed bed. An iterative approach, based on the calculation of the bed shear-stress should then be used to refine these estimates.

According to Soulsby (1997), an initial estimate for the critical stone diameter d_{cr} for a steady current is:

$$d_{cr} = \frac{0.25U_c^{2.8}}{h^{0.4} [g(s-1)]^{1.4}} \text{ for } d > 10\text{mm} \quad (3.53)$$

and for waves it is:

$$d_{cr} = \frac{97.9U_w^{3.08}}{T^{1.08} [g(s-1)]^{2.08}} \text{ for } d > 10\text{mm} \quad (3.54)$$

However Whitehouse (1998) does not propose which scour protection strategy is appropriate for the combined wave and current situation.

Most existing designs of scour protections are based on the method described above. They use the Shields criterion, where the amplified bed shear stress is estimated with equation (3.41) or calculated numerically (Kirkegaard et al. (1998)). The resulting design is then validated with a physical model study.

Disadvantages of this method (especially when estimating the amplified bed shear-stress) are:

- the variety of possibilities to calculate the wave-induced bed shear stress and the combined wave and current bed shear-stress (see chapter 1, section 1.1.1);
- the hydraulic roughness of the sand bed is smaller than that of the scour protection. This sudden increase in roughness gives rise to another non-

uniform flow, characteristic for bed protections (Hofland (2005), Whitehouse (1998)) This effect is not taken into consideration when calculating the bed shear-stress at the scour protection;

- different amplifications due to the presence of the pile are measured for waves and currents; Van Oord (2003) mentions that the amplification of the bed shear-stress due to the presence of the pile is limited to 2.25 for waves with a KC number smaller than 6, whereas it is 4 for a steady current. Others (see chapter 1, section 1.2) mention much higher values for the amplification in a steady current. The combined wave and current bed shear-stress on the other hand is not a linear composition of the separate bed shear-stress for waves and current. It is difficult to estimate the combined effect of these two phenomena on the final amplified bed shear-stress;
- all designs are conservative, in a way that they do not allow movement of a single stone within the scour protection.

Part of this study is the performance of physical model tests with combined wave and currents while looking for a relationship between loading and initiation of motion (Chapter 4, section 4.2). Another part is to see whether it is possible to allow some movement of the scour protection and the development of a dynamic profile, without threatening the stability of the structure.

3.3.2 Radial extent and thickness of the scour protection

Several suggestions are found in literature concerning the required extent of a scour protection around a vertical pile. Most of them are based on the current alone situation. The CEM, US Army Corps of Engineers (2002) notes that little is known on the required extent of a scour protection around a vertical pile in waves. An extent of 2 times the predicted scour depth is suggested. A review of the existing design recommendations is given in Figure 3-12 (compiled from Hjorth (1975), Breusers and Raudkivi (1991), Hoffmans and Verheij (1997), Schiereck (2001), May et al. (2002)).

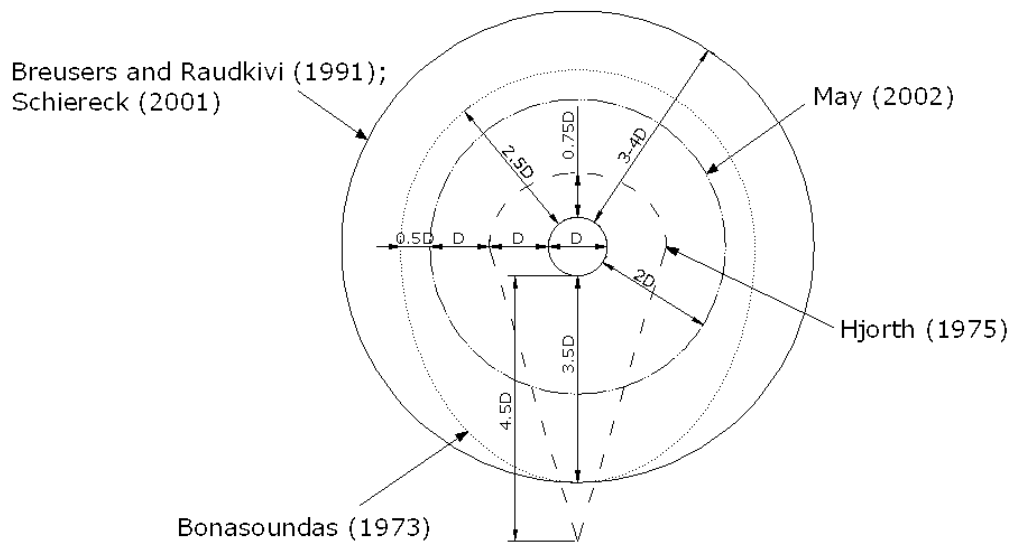


Figure 3-12: recommendations for the extent of a scour protection

Others (Carstens (1976), Sumer and Fredsøe (2002)) suggest to place the scour protection as far as the scour would reach, or:

$$L_s = F_s S_e \cot \phi \quad (3.55)$$

with L_s the distance from the pile to the edge of the scour protection (Figure 3-13), F_s a safety factor and ϕ the angle of repose. With a scour depth $S_e = 1.5D$ and an angle of repose of 30° , this would lead to a scour protection with a diameter of $6.2D$.

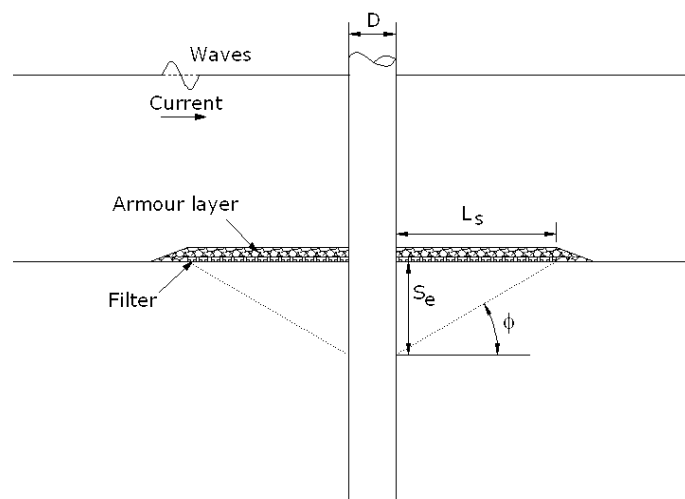


Figure 3-13: Definition of extent of scour protection L_s

As there is a large difference between the existing recommendations, we will elaborate on this subject in chapter 4, section 4.4.

Regarding the thickness of the scour protections, Breusers and Raudkivi (1991) recommend a thickness of at least two layers of riprap, which is suggested by other authors as well (Hoffmans and Verheij (1997), Whitehouse (1998)). May et al. (2002) recommend a thickness between $2.5D_{50,upper}$ and $1.5D_{100,upper}$ for a scour protection which is placed underwater, with $D_{50,upper}$ and $D_{100,upper}$ respectively the upper value of the gradation limits for D_{50} and for D_{100} . Chiew (1995) investigated the influence of the thickness of the rip-rap layer on the failure of the scour protection and found that an increased velocity could be withstood with increasing layer thickness. He used rather small stone sizes and the increase in resistance was mainly caused by the fact that for sufficiently thick layers, a redistribution of the scour protection material could re-armour possible gaps.

3.3.3 OPTI-PILE project

The OPTI-PILE project was funded by the European Commission (Fifth Research and Technological Development Framework Programme) and ran for two years from early 2002. It was coordinated by E-Connection Project BV, P.O.Box 101, 3980 CC Netherlands. Other partners were Vestas - Wind Systems (DK) and Germanischer Lloyd Windenergie (D).

The goal of the project was to optimise monopile foundations for offshore wind turbines in deep water and for North Sea conditions. OPTI-PILE was part of the engineering of the 120 MW Offshore wind park Q7-WP located 23 km off the Dutch coast at Ijmuiden in water with a depth varying from 20 to 25 meters. The results of the Q7 project are generalised towards other similar locations and the OPTI-PILE project is thus of relevance for many offshore areas with similar characteristics.

One part of the OPTI-PILE project aimed to improve the design for scour protections in combined waves and current. As it is one of the few projects, to the author's knowledge, describing the results of an experimental study on scour protections around offshore monopile foundations, more attention is given to it here.

A physical model study was performed on scale 1/47.25 at HR Wallingford, testing the following conditions (den Boon et al. (2004)):

- scour depth for an unprotected monopile foundation;
- damage to scour protection designs, supplied by van Oord ACZ for design waves and current

Froude scaling was applied for the structural and environmental parameters. Two types of scour protections were tested, a so-called static protection, which is designed according to the rules described in section 3.3, and a dynamic protection. For the dynamic protection, a scour hole was allowed to develop and was then backfilled with scour protection material (comparable to the scour

protection design for the Scroby Sands wind farm, described by Cefas (2006) and Hansen and Gislason (2005)).

The test conditions are described Table 3-1, which gives both prototype and model scale dimensions. The tests ran for one model hour and damage was determined using radial bed profiles, measured with a touch-sensitive bed profiler, and overhead photographs.

Table 3-1: test conditions for the OPTI-PILE project

Parameter	Symbol	Unit	Tested range (prototype)	Tested range (model scale)
Significant wave height	H_{m0}	[m]	6.5 – 8.5	0.138 – 0.180
Mean wave period	T_m	[s]	8.9 – 9.6	1.3 – 1.4
Current velocity in combined wave and current situation	U_c	[m/s]	1.01 -1.15	0.147 – 0.170
Current velocity in current alone situation	U_c	[m/s]	2.01 – 2.06	0.295 – 3.03
Water depth	D	[m]	24	0.508
Extension of the scour protection	L_s	[m]	15; 25; 35	0.32 – 0.53 – 0.74
Pile diameter	D	[m]	4.2	0.89
Median stone diameter for static protection	D_{50}	[m]	0.607; 0.396; 0.222	0.0115; 0.0075; 0.0042
Thickness of armour layer for static protection		[-]	$3D_{n50}$	$3D_{n50}$
Thickness of filter layer for static protection		[m]	0.5	0.01
Median stone diameter for dynamic protection	D_{50}	[m]	0.591; 0.396; 0.222; 0.121	0.0112; 0.0075; 0.0042; 0.0023
In-fill height of dynamic scour protection		[-]	1/3; 2/3; fully filled	1/3; 2/3; fully filled

The results from the tests were:

- in the situation without scour protection, a scour hole of up to 1.75 times the pile diameter D developed;
- both the static and the dynamic scour protections prevented erosion around the monopile;
- significantly smaller rock sizes could be used for the dynamic protection;
- a stability parameter $Stab$ is able to describe the damage state of the scour protection

In the OPTI-PILE project the tests were classified into three damage categories:

- no movement of rocks;
- some movement, but no failure;
- failure.

The scour protection is considered to have failed when the filter layer is exposed over a minimum area of four armour units ($4D_{50}^2$) or, when no filter is present

(in the dynamic scour protections) when a volume of rock has disappeared equal to the volume of rock required to cause failure for a scour protection with filter.

They define a stability parameter $Stab$ as:

$$Stab = \frac{\theta_{max}}{\theta_{cr}} \quad (3.56)$$

With θ_{max} the maximum Shields parameter according to equations (1.2) and (1.31) and θ_{cr} the critical Shields parameter = 0.056.

The value of the stability parameter $Stab$ is plotted against the damage categories (Figure 3-14) and two limits are found for the stability parameter, $Stab_{1,2}$ and $Stab_{2,3}$, which define the transition between the damage categories. For the tested range:

$$\begin{aligned} Stab_{1,2} &= 0.415 \\ Stab_{2,3} &= 0.460 \end{aligned} \quad (3.57)$$

In den Boon et al. (2004), the results are compared against two prototype wind farms, Horns Rev and Scroby Sands and they find that for Horns Rev, a smaller stone size could have been applied, whereas they expect some damage to the Scroby Sands scour protection, which was however designed as a non-maintenance free scour protection.

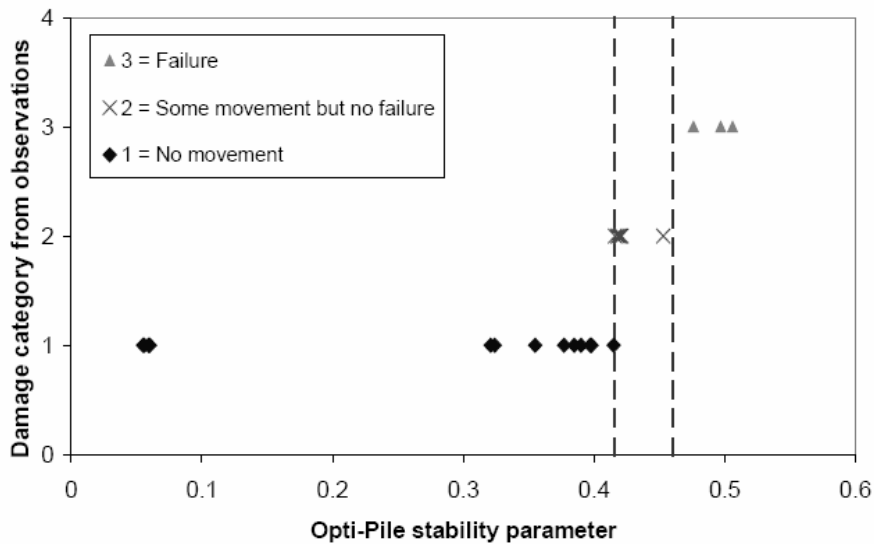


Figure 3-14: Damage categories against Stability parameter; from den Boon et al. (2004)

den Boon et al. (2004) comment that the choice of friction factor significantly affects the value of θ_{max} and thus the interpretation of the results. However, the friction factor they apply only gives a weak dependence of θ_{max} on the stone size D_{50} , which implies that the boundaries of stability can be less clear. They note that friction factor tuning is possible with physical model tests, but has yet to be investigated.

In Whitehouse et al. (2006) another test series is described, carried out for the Arklow Bank Wind Park, which is subject to strong currents and high waves. Tests were performed on scale 1/36. They use larger rock sizes, due to the high loads and define damage as the number of stones which are displaced by more than one diameter and subsequently calculate the damage for each quadrant. For smaller rock gradings, damage was assessed using bed profiling. When applying the OPTI-PILE stability parameter, Whitehouse et al. (2006) conclude that the stability parameter *Stab* is not closely related to the maximum damage and would need to be recalibrated for the specific circumstances of the Arklow Bank offshore wind park.

3.3.4 Existing offshore wind farms and their scour protection design

Since the building of the first offshore wind farm on Vindeby (Denmark) many projects have been built or are under development. The operational offshore wind parks are given in Table 0-1 and the location is shown in Figure 0-1. Mostly, a scour protection was placed around the base of the foundation, but only for two cases, the size and extent of the scour protection material are known. For the Horns Rev wind farm, a scour protection with a diameter of 25m is applied. The applied thickness was 0.8m, and stone sizes varied between 0.35 and 0.55m, with a D_{n50} of 0.4m. The underlying filter layer had a thickness of 0.5m, a diameter of 27m and consists of a stone grading with stone sizes varying between 0.03 and 0.2m. For the Scroby Sands wind farm, scour holes were allowed to develop and were backfilled with scour protection material. The stone sizes varied between 0.01 and 0.3m, with a D_{n50} of 0.15m. For each scour protection approximately 900m³ of stones were used.

3.4 Physical modelling of scour protection

In coastal engineering three complementary techniques are applied to deal with the complex flow regimes that often exist around coastal structures: laboratory/physical modelling, numerical modelling and field measurements. The main advantage of physical modelling compared to numerical modelling is that no simplifying assumptions need to be made concerning the governing physical processes. The main advantages compared to field measurements are the lower cost and the ability to control and adjust the separate loading conditions (Hughes (1993)). According to Hughes (2003), small-scale laboratory physical models remain the most reliable tool for designing and testing most types of coastal structures, despite the advances in numerical modelling. Ideally, the three techniques are combined to find an optimal solution for a problem.

Offshore vertical piles are a typical example of a structure with a complex flow regime (chapter 1). It becomes even more complex when considering the

combined effect of waves and current and a scour protection at the base of the structure, making physical modelling indispensable for the design (Whitehouse (1998)).

Although there are many advantages of using physical modelling as a means to investigate the stability of scour protections, there are some shortcomings. These are related to the laboratory environment and the use of different (smaller) scales compared to the actual prototype structure. These effects may lead to discrepancies between prototype and laboratory behaviour and are listed in Figure 3-15 (Sutherland and Whitehouse (1998), Whitehouse (1998), Kortenhaus et al. (2005), Whitehouse et al. (2006)). The sections below discuss the model and scale effects in more detail.

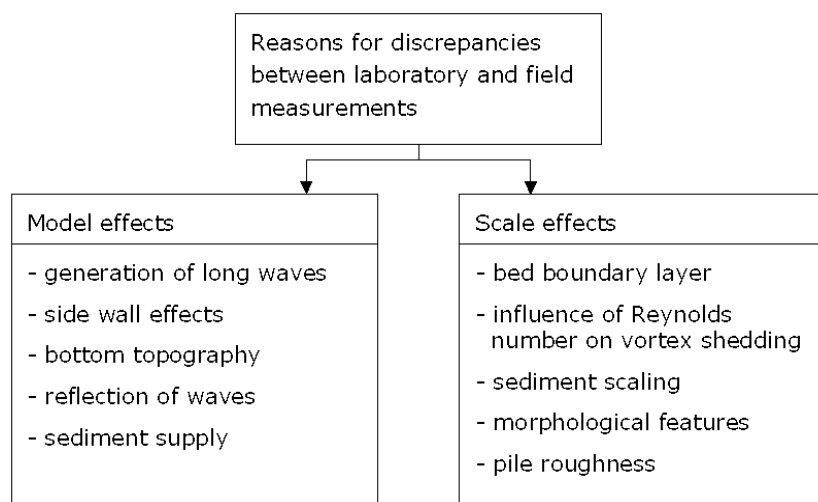


Figure 3-15: Overview of model and scale effects for scour protection design

3.4.1 Laboratory or model effects

Model or laboratory effects arise from the incorrect reproduction of the prototype situation, i.e. the model structure and generation of waves and currents, or due to the boundary conditions of a wave flume (side walls, finite length with reflection at the end of the flume). Significant progress is made in modeling techniques, but influences of model effects on physical model tests are inevitable.

The main model effects which exist when modelling a scour protection around a vertical pile in a two-dimensional wave flume are attributed to (Hughes (1993), Whitehouse (1998), Hughes (2003), Kortenhaus et al. (2005)):

- the generation of unintentional non-linear effects caused by the generation of waves and currents. Improvements are possible by generating higher order waves, but to date, problems still exist in eliminating these model effects.
- the generation of unidirectional waves. Not much can be done about this simplification of reality. It is up to the experimenter to decide whether

this is a reasonable approximation and to decide whether 3-dimensional tests are required.

- the reflection and re-reflection of waves in a wave flume. This effect is dealt with by using energy dissipating beaches at the end of the flume and/or the use of active wave absorption by the wave paddle.
- the influence of the side walls on the waves (damping of waves). This is usually minimal and to date no influence on the results is found when the reference waves are the waves measured in front of the structure.
- the obstruction of the model in the flume (blockage). This effect is avoided when the ratio of the model area to the flume area satisfies the following condition:

$$\frac{\text{Area (model)}}{\text{Area (flume)}} \leq \frac{1}{6}.$$

- the differences regarding bottom topography, i.e. typically a local platform is made to create a sand bottom in the flume. The slope which is used to obtain the elevation will inevitably influence the wave characteristics. This effect is dealt with by measuring the wave characteristics at the location of the structure.

It is sometimes difficult to distinguish between model and scale effects and according to Kortenhuis et al. (2005), more attention is given to scale effects, as they are believed to have more influence on the results as compared to model effects. It is therefore not possible to quantify the model effects, but one should be aware of their existence.

3.4.2 Scale effects

For the scaling of waves and currents in laboratory studies, both the Froude number and Reynolds number should be preserved. The Froude number Fr and Reynolds number Re are defined as:

$$Fr = \frac{U}{\sqrt{gd}} \quad (3.58)$$

$$Re = \frac{UD}{\nu} \quad (3.59)$$

With U the flow speed, g the acceleration due to gravity, d the water depth, D the pile diameter and ν the kinematic viscosity.

When the geometric length scale is preserved, both Froude and Reynolds number can not be correctly scaled down at the same time. Scaling for hydraulic models is usually done according to the Froude model law (prototype Froude number = model Froude number) (Hughes (1993)). The Reynolds number is however important when considering viscous effects (boundary layer). Hughes (1993) suggests that viscous effects can be disregarded when $Re \geq 1.10^4$.

Sutherland and Whitehouse (1998) give a complete review of the scale effects in the physical modelling of scour around coastal and offshore structures. They note that Froude scaling will adequately scale the wave height and period, provided that the scale is sufficiently large for viscosity to be ignored. The non-linearity of waves, often described by the Ursell parameter Ur is also important and the Ursell parameter should be maintained in the model:

$$Ur = \frac{HL^2}{d^3} \quad (3.60)$$

With H the wave height, L the wave length and d the water depth. All terms scale geometrically, thus Froude scaling preserves the non-linearity.

The formation of the vortices around a pile is important for the amplification of the bed shear stress (chapter 1, section 1.2). The vortex shedding depends on the pile Reynolds number for a steady current and on the KC number for waves. The KC number ($U_m T_w / D$) scales geometrically. The pile Reynolds number however does not scale down correctly and Sutherland and Whitehouse (1998) note that Re is important up to values of $2 \cdot 10^5$ for flow around piles. The vortex shedding may also be influenced by the pile roughness, which is usually not scaled down correctly. Sumer et al. (1992) state that for wave scour, the KC number mainly determines the scour process and the Reynolds number and the roughness of the pile are only of secondary importance, leading to the conclusion that scale effects for wave flow around a pile are limited. The data on which they base this statement has Reynolds numbers varying between 10^3 and 10^5 .

Sutherland and Whitehouse (1998) state that rough turbulent boundary layers in model and prototype will be dynamically similar. It is therefore important to pursue a turbulent boundary layer in the scale model. According to section 1.1.1.3, the wave friction factor f_w is determining for a combined wave and current climate. Whitehouse et al. (2006) state that a turbulent boundary layer is reached when the rough flow wave friction factor and the smooth flow wave friction factor are equal. According to Soulsby (1997), this is obtained when (equations (1.23) and (1.24)):

$$1.39 \left(\frac{A}{z_0} \right)^{-0.52} = 0.0521 Re_A^{-0.187} \quad (3.61)$$

with

$$A = \frac{U_m T_w}{2\pi}$$

$$z_0 = \frac{k_s}{30}$$

$$Re_A = \frac{U_m A}{\nu}$$

and U_m the horizontal wave velocity amplitude at the bottom; T_w the wave period; k_s the bottom roughness = $2.5D_{50}$ and ν the kinematic viscosity. When re-arranging, this leads to a lower limit for the stone diameter D_{50} :

$$D_{50} = \left[\frac{0.0521}{1.39} \left(\frac{U_m^2 T_w}{2\pi\nu} \right)^{-0.187} \left(\frac{6U_m T_w}{\pi} \right)^{0.52} \right]^{1/0.52} \quad (3.62)$$

When using equations (1.12) or (1.15) and (1.18), suggested by Fredsøe and Deigaard (1992), this leads to:

$$0.04 \left(\frac{A}{k_s} \right)^{-1/4} = 0.035 \text{Re}_A^{-0.16}, \quad \frac{A}{k_s} > 50 \quad (3.63)$$

$$0.4 \left(\frac{A}{k_s} \right)^{-0.75} = 0.035 \text{Re}_A^{-0.16}, \quad \frac{A}{k_s} \leq 50 \quad (3.64)$$

Again, this can be re-arranged in terms of the stone diameter D_{50} , when assuming the bottom roughness $k_s = 2.5D_{50}$ to obtain a lower limit for D_{50} :

$$D_{50} = \left[\frac{0.035}{0.04} \cdot \left(\frac{U_m^2 T_w}{2\pi\nu} \right)^{-0.16} \cdot \left(\frac{6U_m T_w}{\pi} \right)^{1/4} \right]^4, \quad \frac{A}{k_s} > 50 \quad (3.65)$$

$$D_{50} = \left[\frac{0.035}{0.4} \cdot \left(\frac{U_m^2 T_w}{2\pi\nu} \right)^{-0.16} \cdot \left(\frac{6U_m T_w}{\pi} \right)^{0.75} \right]^{4/3}, \quad \frac{A}{k_s} \leq 50 \quad (3.66)$$

Furthermore, bed roughness should be scaled by geometric length scale Sutherland and Whitehouse (1998). As the bed roughness is generally determined by the diameter of the bed material, this is not a problem for the rock material, which is scaled down correctly, but it does create difficulties for the sediment. The scaling of sediment according to the geometric length scale often leads to unacceptably small diameters and the sediment is not scaled geometrically. Moreover, when ripples are formed, the bed roughness is determined by the ripple height, which is also not scaled geometrically.

Sutherland and Whitehouse (1998) note that, when scaling sediment transport, it is important to maintain the Shields parameter (equation (1.2)). As the exact scour depth depends less on the Shields parameter for live-bed scour (section 1.3.1.3, Sumer et al. (1992)), live bed scour will be produced with more accuracy than clear-water scour. Oumeraci (1994) states that sediment characteristics should be scaled according to the dominant form of sediment

transport. According to Oumeraci (1994), the sediment fall velocity w_s is the main parameter that determines the type of transport and he concludes that the fall velocity should be scaled according to the Froude velocity scale ($=\sqrt{\text{length}}$ scale). As explained in section 3.2.1.4, many different formulae exist to quantify the settling velocity. As this determines the scaling of the sediment, different values for the sediment size can be obtained.

Regarding the time scale of sediment transport, Sutherland and Whitehouse (1998) note that it is important to report the duration of the test. It is not guaranteed that the time scale of scour is maintained in the model.

3.5 Conclusions

When designing a scour protection, a distinction can be made between the environmental and the structural parameters, both of which are described extensively in this chapter. The environmental parameters describe the water motion near the bed, while the structural parameters characterize the structure, i.e. the foundation and the scour protection. The main environmental parameters are the current velocity, the wave characteristics, the water depth and the sediment properties. The main structural parameters are the pile diameter D and the density, size and grading of the stones. Together they determine the load which acts upon the scour protection, while the structural parameters also determine the resistance of the scour protection to the load.

A review of the scour protection design formulae is given in this chapter. The existing design criteria are mainly based on the Shields criterion for initiation of motion, which is described in chapter 1. In almost all cases the required stone size represents the stone which is large enough not to be moved by the amplified bed shear stress. Quite some empirical formulae exist to determine the required stone size in case of a current alone situation, but limited research exists on the combined influence of a steady current and waves. Only in the OPTI-PILE project an attempt was made to account for both waves and current. Furthermore, the OPTI-PILE project investigated the influence on the design when allowing limited movement of the stones in the top layer of the scour protection. They found that the ratio of the Shields parameter and the critical Shields parameter could be used to determine both the initiation of motion and the damage development. Their results are further used in chapter 4.

Due to the complicated flow conditions and stone entrainment mechanism, a theoretical description of the process is difficult and empirical research is mostly used to quantify the required stone size. The difficulties of scaling down the physical properties and the challenges in performing a physical model study are discussed at the end of this chapter.

References

- Airy, G.B., 1845. Tides and Waves. *Encycl. Metropolitana*: 241–396.
- Ballast Nedam and Oud, J.C., 2002. Foundation Design Monopile - Comparison extra steel consumption versus scour protection - 3.6 & 6.0 MW wind turbines, DOWEC, Amstelveen.
- Breusers, H.N.C. and Raudkivi, A.J., 1991. Scouring. Balkema.
- Brorsen, M., Hald, T. and Frigaard, P., 2003. Experimental and Numerical Wave Generation and Analysis. Aalborg University, Aalborg, Denmark.
- Carstens, T., 1976. Seabed scour by currents near platforms, 3th Conference on port and ocean engineering under arctic conditions, University of Alaska, pp. 991-1006.
- Cefas, 2006. Scroby Sands Offshore Wind Farm – Coastal Processes Monitoring. Final Report for the Department of Trade and Industry. Contract AE0262, Cefas Lowestoft Laboratory, Suffolk.
- Chiew, Y.M., 1995. Mechanics of Riprap Failure at Bridge Piers. *Journal of Hydraulic Engineering*, 121(9): 635-643.
- CIRIA/CUR, 1991. Manual on the use of rock in coastal and shoreline engineering. CUR 154.
- Coastal Engineering Research Center, 1992. ACES, Automated Coastal Engineering System. Department of the army, Mississippi.
- De Rouck, J., 1991. De stabiliteit van stortsteengolfbrekers. Algemeen glijdingsevenwicht. Een nieuw deklaagelement. PhD Thesis, KUL, Leuven, België.
- De Rouck, J., 1999. Rivieren en kanalen, Lecture notes. Ghent University, Department of Civil Engineering, Belgium.
- Dean, R.G. and Dalrymple, R.A., 1991. *Water Wave Mechanics for Engineers and Scientists*. World Scientific.
- den Boon, J.H., Sutherland, J., Whitehouse, R., Soulsby, R., Stam, C.J.M., Verhoeven, K., Høgedal, M. and Hald, T., 2004. Scour Behaviour and Scour Protection for Monopile Foundations of Offshore Wind Turbines, European Wind Energy Conference & exhibition (EWEC), London, UK.
- E-Connection, Vestas Wind Systems, D.K. and Germanischer Lloyd Windenergie, D., 2002-2004. OPTI-PILE, Fifth Research and Technological Development Framework Programme.
- Fenton, J.D., 1988. The numerical solution of steady water wave problems. *Computers & Geosciences*, 14(3): 357-368.
- Fenton, J.D. and McKee, W.D., 1990. On calculating the length of water waves. *Coastal Engineering*, 14: 499–513.
- Fredsøe, J. and Deigaard, R., 1992. *Mechanics of Coastal Sediment Transport*. Advanced series on Ocean Engineering, Vol. 3. World Scientific.
- Goda, Y., 2000. *Random seas and design of maritime structures*. Advanced series on ocean engineering. World scientific, Singapore, 443 pp.
- Grune, J., Sparboom, U., Schmidt-Koppenhagen, R., Wang, Z. and Oumeraci, H., 2006. Stability Tests of Geotextile Sand Containers for Monopile

- Scour Protection, International Conference on Coastal Engineering, San Diego, pp. 5093.
- Hansen, N.-E.O. and Gislason, K., 2005. Movable scour protection on highly erodible sea bottom, International Coastal Symposium.
- Herman, S.A., Kooijman, H.J.T., Hendriks, H.B., van de Brug, E., Nedam, B., op den Velde, W., Van Oord, A.C.Z., van den Berg, R. and Holland, L.M.G., 2003. Variations on a 500 MW offshore wind farm design, Offshore Wind Energy in the Mediterranean and other European Seas Naples, Italy.
- Hjorth, P., 1975. Studies on the nature of local scour. Institute of Technology, Dept. of Water Resources Engineering.
- Hoffmans, G.J.C.M. and Verheij, H.J., 1997. Scour manual. A.A. Balkema, Rotterdam, Netherlands ; Brookfield, VT, xv, 205 p. pp.
- Hofland, B., 2005. Rock & Roll: Turbulence-induced Damage to Granular Bed Protections. Department of Civil Engineering and Geosciences, Delft University of Technology.
- Hughes, S.A., 1993. Physical Models and Laboratory Techniques in Coastal Engineering. Advanced series on ocean engineering, 7. World Scientific Pub Co Inc, 568 pp.
- Hughes, S.A., 2003. Physical modeling considerations for coastal structures. In: R.K. Mohan, O. Magoon and M. Pirrello (Editors), Advances in coastal structure design.
- IAHR, 1986. List of sea state parameters. Supplement to Bulletin No. 52, Ass. for Hydraulic Research/Permanent Intern. Ass. of Navigation Congresses., Brussels.
- IMDC, 2005. Hydraulisch randvoorwaardenboek Vlaamse Kust, Ministerie van de Vlaamse Gemeenschap, Departement Leefmilieu en Infrastructuur, Administratie Waterwegen en Zeewezen, Afdeling Waterwegen Kust.
- Kirkegaard, L., Hebsgaard, M. and Jensen, O.J., 1998. Design of Scour Protection for the Bridge Piers of the Øresund Link, International Conference on Coastal Engineering, Copenhagen, Denmark, pp. 3634-3642.
- Kortenhaus, A., Van der Meer, J.W., Burcharth, H.F., Geeraerts, J., Pullen, T., Ingram, D. and Troch, P., 2005. Report on conclusions of scale effects. Report D40, CLASH project.
- Massel, S.R., 1996. Ocean Surface Waves: Their Physics and Prediction. World Scientific Pub Co Inc.
- May, R.W.P., Ackers, J.C. and Kirby, A.M., 2002. Manual on Scour at Bridges and Other Hydraulic Structures. CIRIA.
- Michell, J.H., 1893. The highest waves in water. *Phil. Mag*, 36(5): 430-437.
- Oumeraci, H., 1994. Scour in front of vertical breakwaters - review of problems, International workshop on Wave Barriers in Deepwaters, Port and Harbour Research Institute, Yokosuka, Japan, pp. 281-307.
- Schiereck, G.J., 2001. Introduction to Bed, Bank and Shore Protection. Delft University Press.
- Soulsby, R., 1997. Dynamics of Marine Sands: A Manual for Practical Applications. Thomas Telford.

- Sumer, B.M. and Fredsøe, J., 1997. Hydrodynamics around cylindrical structures. Advanced series on ocean engineering. World Scientific, Singapore ; River Edge, NJ, xviii, 530 p. pp.
- Sumer, B.M. and Fredsøe, J., 2002. The mechanics of scour in the marine environment. Advanced series on ocean engineering. World Scientific, River Edge, N.J., 536 pp.
- Sumer, B.M., Fredsøe, J. and Christiansen, N., 1992. Scour Around Vertical Pile in Waves. Journal of Waterway, Port, Coastal and Ocean Engineering, 118(1): 15-31.
- Sutherland, J. and Whitehouse, R.J.S., 1998. Scale effects in the physical modelling of seabed scour, HR Wallingford.
- Troch, P., 2000. Experimentele studie en numerieke modellering van golfinteractie met stortsteengolfbrekers. PhD Thesis, Ghent University, Ghent.
- Troch, P., 2007. Offshore Constructions, lecture notes. Ghent University, Department of Civil Engineering, Belgium.
- US Army Corps of Engineers, 2002. Coastal Engineering Manual. Engineer Manual 1110-2-1100, Washington, D.C. .
- Van der Meer, J.W., 1988. Rock Slopes and Gravel Beaches Under Wave Attack. Delft Hydraulics.
- Van Oord, A.C.Z., 2003. Scour protection for 6 MW OWEC with monopile foundation in North Sea, Gorinchem.
- van Rijn, L.C., 1993. Principles of Sediment Transport in Rivers, Estuaries and Coastal Seas. Aqua Publications.
- Whitehouse, R., 1998. Scour at marine structures : a manual for practical applications. Thomas Telford, London, xix, 198 pp.
- Whitehouse, R.J.S., Sutherland, J. and O'Brien, D., 2006. Seabed scour assessment for offshore windfarm, International Conference on scour and erosion, Nanyang University, Nanyang, Singapore.
- Zaaijer, M.B. and Van der Tempel, J., 2004. Scour protection: a necessity or a waste of money?, 43rd IEA Topical Expert Meeting–Critical Issues Regarding Offshore Technology and Deployment, Skaerbaek, Denmark, pp. 43-51.

Chapter 4. Experimental research on scour protection design around a monopile foundation

4.0. Introduction

Within the framework of this study, an extensive experimental test-series was carried out to investigate damage development for a scour protection around a monopile foundation in a combined wave and current climate. A total of 40 regular wave tests and 75 irregular wave tests were performed. The main focus lies on the design of the required stone size. Two different approaches are considered: a statically stable scour protection, for which no movement of individual stones is allowed and a dynamically stable scour protection, for which the development of a dynamic profile is permitted. This chapter describes the set-up, analysis and results of the tests. At the end of this chapter, special attention is given to the scour at the edge of the foundation.

4.1. Experimental set-up

4.1.1. General description of set-up and model

All experiments are conducted at the department of Civil engineering of Ghent University. Figure 4-1 shows a sketch of the set-up in the wave flume. The dimensions of the flume are 30m in length, 1m in width and 1.2m in height. One of the flumes' side walls is partially made of glass to facilitate visual observations. A piston type wave paddle is used to generate waves, suitable for shallow water wave generation. An exterior pump-circuit can generate currents in both directions, permitting a current following or opposing the waves. The installation of the current circuit was done as a part of this study and is described in more detail in appendix II.

Part of the floor was lifted to create a movable bed in the middle of the flume and the transition from the bottom of the flume to the sand bed was made with a gentle slope of 1/20. Very fine, uniform sand with a diameter of 100 μm was used for the movable bed to minimize scale effects (see below). A model of a monopile is built in the middle of the wave flume, centrally in the 4 m long sandbox. The monopile was placed centrally between the two current inlets to minimize the differences in the flow pattern when the current is reversed. The length of the sandbox is chosen large enough to avoid influence of edge effects on the results (as there is no feeding of the sediment, edge effects may exist at the edges of the sandbox). The height of the sandbox (0.3 m) is chosen large enough for any expected scour to develop without influences of the bottom.

An absorption beach with slope 1/5 was installed at the end of the flume, to reduce reflections. The gravel beach developed its own profile, reducing reflection till less than 15%. Considering the small reflection, no active wave absorption was used.

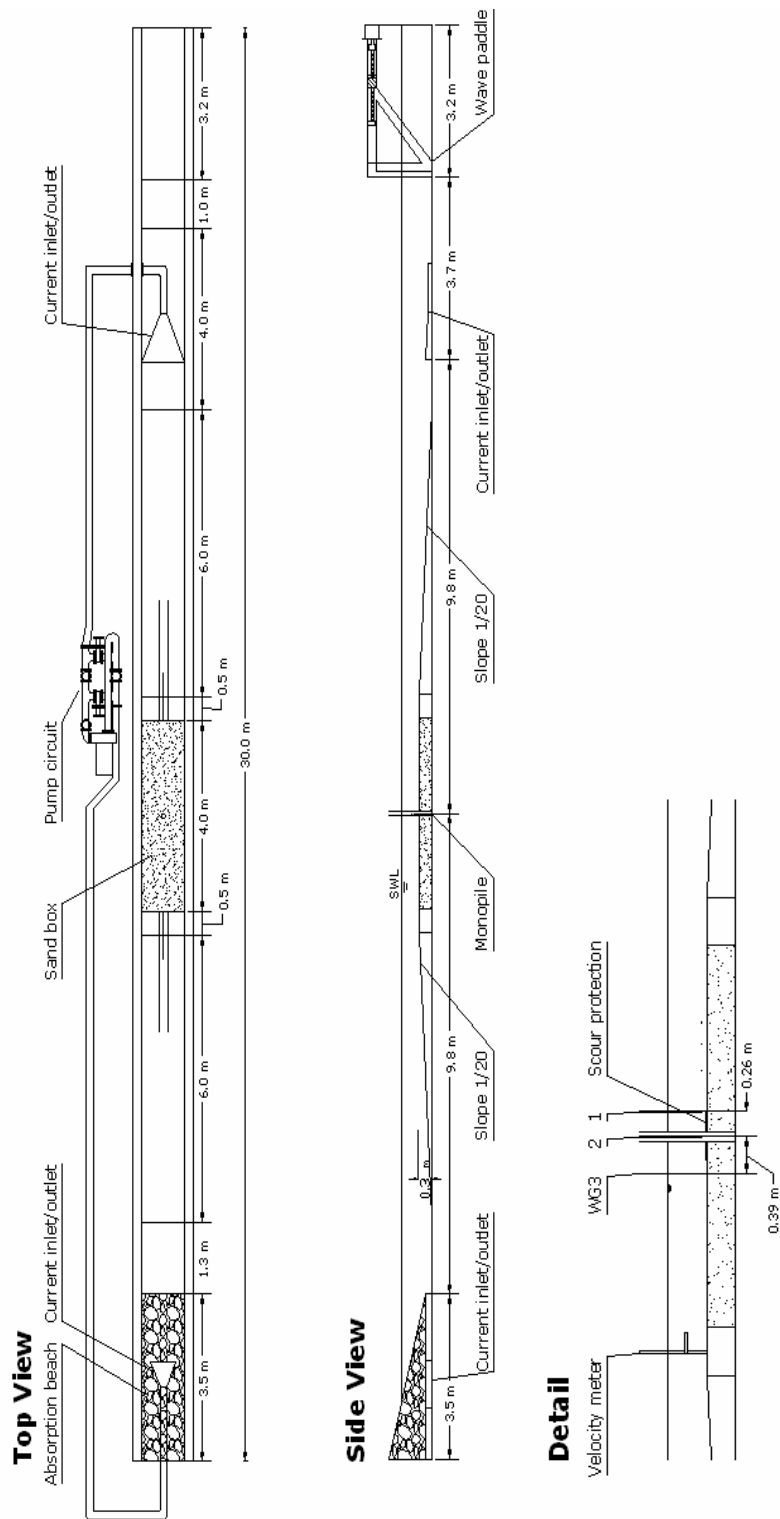


Figure 4-1: Experimental set-up in the wave flume

The diameter of the monopile is 0.1m and represents a typical monopile foundation for offshore wind turbines in the north sea, on scale 1/50. A scour protection made of loose stones is placed around the monopile foundation. Stones are painted in different colours to allow visual observation of the amount and direction of displacement. The coloured stones are placed in concentric circles around the pile, as shown in Figure 4-2 and each ring has a width equal to the piles' radius. The diameter of the applied scour protection is 5 times the pile diameter. 10% extra material was used for the outer ring, to make sure some material was also placed beside the geotextile without decreasing the height of the outer ring. Except for two tests, the thickness of the scour protection layer is $2.5D_{n50}$.

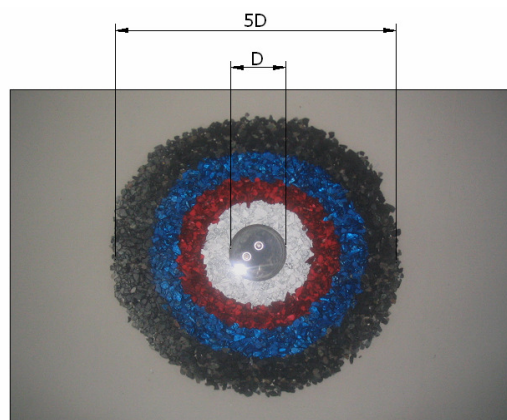


Figure 4-2: Top view of a scour protection, before loading (note that the pile was removed for making measurements and for taking pictures)

Before each test, the sand was flattened to ensure that for each test the scour protection had the same level and that test conditions were equal. The filter was then installed on top of the sand. Most often a geotextile filter was used. Figure 4-3 shows the construction sequence of the scour protection. The concentric circles are placed one after the other and were flattened by hand to obtain a leveled scour protection. The construction was done under water.

Although it is sometimes advised to place the top of the scour protection at the same level of the surrounding bed (Melville and Coleman (2000)), this is not done here for several reasons. Firstly, the scour protection is placed on top of the sand bed because Ballast Nedam and Oud (2002) showed that this is the most economical solution (compared to dredging and leveling the scour protection with the bed). The second reason is that the increase in wave load due to the higher location of the scour protection is very limited. The influence is mainly restricted to edge effects, which are disregarded here. Finally, when the scour protection is placed level with the sea bed, a global lowering of the sea bed due to overall sand transport will cause the same situation as described above. When large variations of the seabed are expected, a scour protection as applied at the Scroby Sands wind farm offers a better solution (Hansen and Gislason (2005), Cefas (2006)).

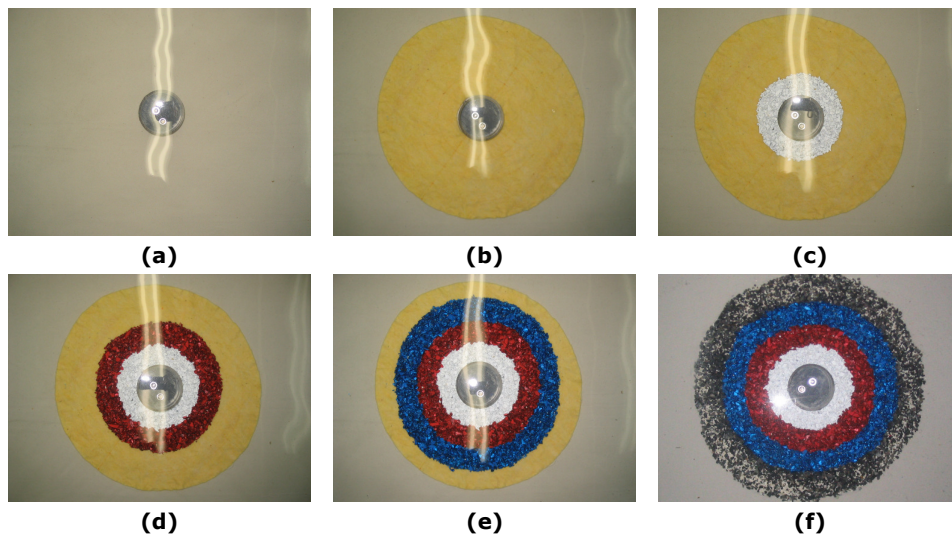


Figure 4-3: Construction of the scour protection: (a) leveled sand bed; (b) placement of the filter; (c), (d), (e) and (f): consecutive placement of the top layer in concentric circles

4.1.2. Hydraulic conditions

Table 4-1 lists the range of wave and current conditions at the monopile. The target spectrum of the irregular waves is a JONSWAP spectrum, with a peak enhancement factor γ of 3.3. All test series are run before the installation of the pile, to determine the undisturbed wave field at the location of the pile. The waves are measured with three resistance type wave gauges (Figure 4-1), allowing to determine the incident wave field with the method of Mansard and Funke (1980). When it was found that the total wave height, obtained by the analysis of the elevations at one location and thus resulting in a combination of incident and reflected wave field, yields better results (section 4.3), the wave gauge at the centre of the pile was used for the wave analysis.

For each test, a continuous velocity measurement is made with an electromagnetic velocity meter. At the beginning and end of each test, the pump circuit is respectively slowly started up and halted, to avoid the generation of a wave in the flume. When the desired flow speed is reached, stabilization of the current is awaited. This was possible because the current itself was too weak to initiate movement (both of the stones besides the model and of the sand further away from the pile), so this stabilization period did not influence the test itself. The current velocity, determined for each test, is deduced from this initial period, when no waves are present yet. The velocity profile over the height and width of the flume were determined for the different flow velocities, leading to the conclusion that a logarithmic velocity profile could be fit to the data and that the average velocity was measured at approximately 0.4 time the water depth. Velocities during the tests are therefore measured at a distance of $0.4d$ from the bed. So as not to disturb the flow at the location of the pile, the velocity measurement was done behind the pile, inevitably leading to a velocity

measurement which is influenced by the presence of the pile. A calibration was done for the ratio of the velocity which was measured at the location of the pile, without presence of the pile and the velocity which was measured behind the pile, with presence of the pile, leading to a correction factor which was applied to the measurements made during the tests. The velocity profiles over depth and width of the flume and the derivation of the correction factor for the flow velocity are described in appendix II. Variations in the velocity measurement are due to variations in the velocity (e.g. due to the turbulence, caused by the pile) and variations in the measurement device due to electrical noise. For each measurement, the average value, the standard deviation and minimum and maximum velocities are determined.

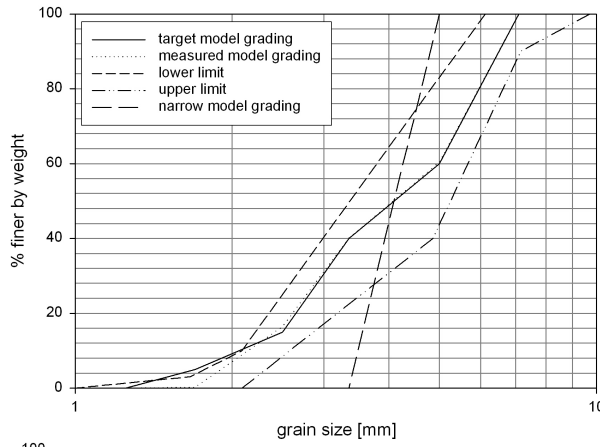
Table 4-1: Hydraulic conditions at the pile: wave and current characteristics

Parameter	Symbol	Range
Significant wave height [m]	H_s	0.05-0.168
Peak wave period [s]	T_p	1.13-1.7
Wave steepness [-]	s	0.02-0.065
Water depth [m]	d	0.2-0.4
Current velocity [m/s]	U_s	0-0.30
Keulegan Carpenter number [-]	KC	0.8-3.6
Pile Reynolds number [-]	Re_D	1.5-4.3 (10^4)

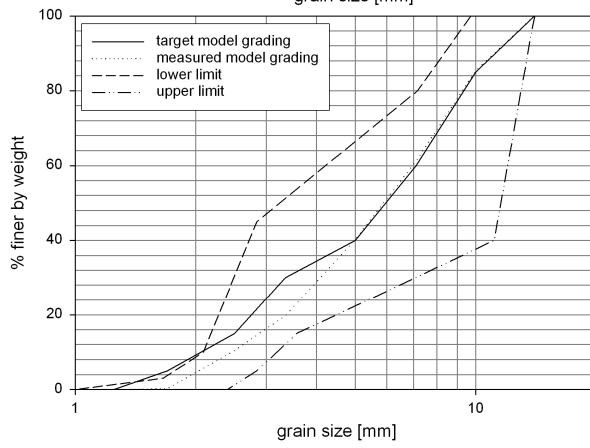
4.1.3. Scour protection characteristics

Four different rock armour gradings are used throughout the tests. The prototype gradings which were used are: 2-80 kg, 10-30 kg; 2-300 kg and 80-300 kg (prototype values). The first two gradings yield the same median grain size D_{50} . The resulting median grain sizes D_{50} are 4.1 mm, 6.0 mm and 8.5 mm, leading to a D_{n50} of 3.5 mm, 5.0 mm and 7.2 mm (with equation (3.40)). The gradings and their respective standard grading limits are shown in Figure 4-4. The full line represents the target grading which were used, while the dotted line represents the measured grading. Target and measured grading coincide almost perfectly. The value of D_{85}/D_{15} , which represents the grading width according to CIRIA/CUR (1991) is shown in Table 4-2, together with the other scour protection characteristics.

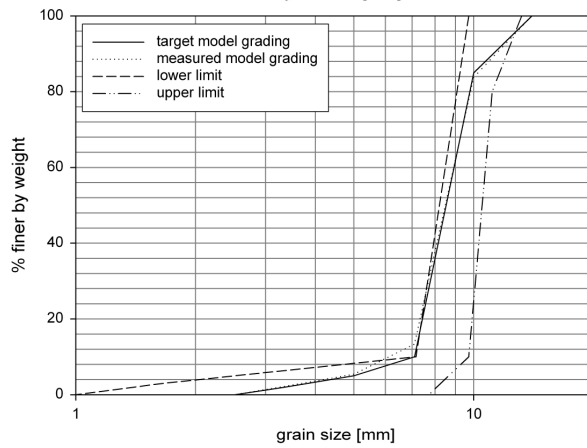
The stones of the scour protection existed of angular rocks. Two different mass densities were used for the scour protection material: $\rho_s = 2650 \text{ kg/m}^3$ and $\rho_s = 3200 \text{ kg/m}^3$. The latter stones were actually steel slag. Steel slag aggregates are highly angular in shape and have rough surface texture. They have high bulk densities and moderate water absorption (Federal Highway Administration (2008)), which makes them ideal as high density stones. The stone densities were determined in the lab, by pulverizing the stones and using a pycnometer. The bulk density of the stones was determined several times by measuring the weight of stones that fit into a volume of approximately 1 dm^3 and was found to lie in between 1.45 and 1.5, which indicates that the porosity of the scour protection lies between 43-46%. To calculate the required weight of stones, a porosity of 40% was assumed.



Grading 2-80 kg;
Grading 10-30 kg



Grading 2-300 kg



Grading 80-300 kg

**Figure 4-4: tested rock gradings (model scale):
(a) 2-80 kg and 10-30 kg; (b) 2-300 kg; (c) 80-300 kg.**

Table 4-2: Scour protection characteristics

Prototype grading	Model value of D_{50} [mm]	Model value of D_{n50} [mm]	D_{85}/D_{15} [-]	$D_{67.5}$ [mm]	Mass density ρ_s [kg/m³]
2-80 kg	4.1	3.5	2.48	5.4	2650 – 3300
10-30 kg	4.1	3.5	1.32	4.4	2650
2-300 kg	6.0	5.0	4.00	7.9	2650 – 3300
80-300 kg	8.5	7.2	1.39	9.1	2650

Washing out of fine bed material through the rocks might cause failure of the scour protection. This is avoided by applying a filter layer. For offshore situations it is common to use one or two granular filters. However, during the tests a geotextile was mostly used as a filter for the sake of convenience and because the main interest of the experiments is the stability of and the damage to the scour protection layer. To see whether the filter has an influence on the stability of the top layer, two alternatives for the geotextile are considered:

- Scour protection without filter
- Scour protection with a granular filter, with the following characteristics (derived according to appendix I): $d_{f15} = 0.6\text{mm}$, $d_{f50} = 1.5\text{mm}$ and $d_{f85} = 1.8\text{mm}$. One filter layer was sufficient and satisfied the filter criteria for all top layers.

4.1.4. Bed profiling

A remote controlled profiler (Figure 4-5) is used to measure the surface (sand bottom, armour layer) and track changes due to erosion and accretion. The profiler was purchased at Aalborg University. The profiler operates in a non-contact manner using a laser to make the measurements and is able to operate even if the target is under water. The profiler has three degrees of freedom: forward/backward; left/right and up/down and each of the axes is controlled by high precision step-motors, capable of a movement resolution less than 0.1 mm, enabling the profiler to position the laser very accurately.

When the water is clear enough, the working range of the laser is larger under water. The working range of the currently used laser is as following:

- Above still water level: 55 – 256mm
- Below still water level: 76 – 343mm

It was noticed that accuracy is also higher for measurements under water. For the present tests, all measurements are made under water, optimizing both the testing time (as the water did not need to be removed) and the accuracy.

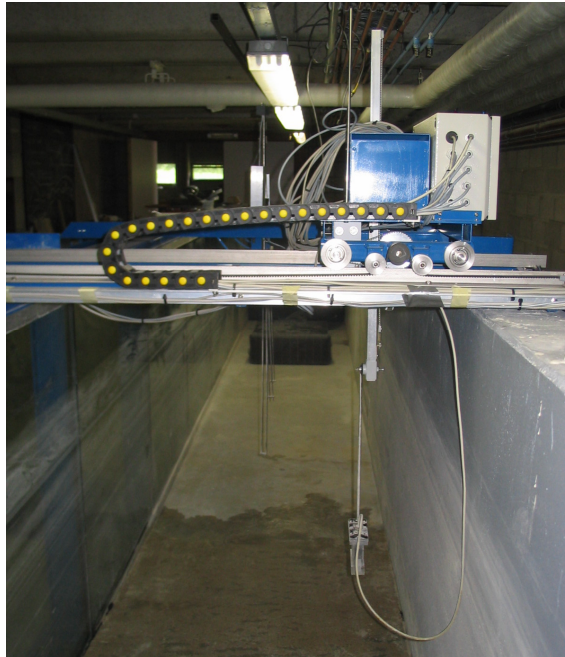


Figure 4-5: Non-contact profiler

The profiler is controlled by the program EPro. Both profiler and software program were developed by Aalborg University. The program enables multiple measurements of a well-defined target area. Afterwards the profiled surface can be presented visually, profiles can be compared and damage calculation between two profiles can be done.

For the present test set-up, the profiler measures a square surface of 0.6m (width) x 0.7m (length) around the pile. This surface is overlaid with a grid of 5mm x 5mm, which is slightly larger than the smallest value of D_{50} which was tested. Van der Meer (1988) used a comparable grid and measured with steps of 0.04m for stones with a $D_{n50} = 0.036$ m. A sensitivity analysis was performed to find the best grid density. For one test, the profiles were measured with 3 different grids, with a density of 2mm x 2mm, 5mm x 5mm and 10mm x 10mm. The measurements for the dense grid (2 x 2mm) lasted more than 4 times the profiling time needed for the grid of 5 x 5mm and many wrong measurements were made. Due to these large error readings, no good result was obtained for the last three profiles. The difference between the 5mm x 5mm grid and the 10mm x 10mm grid increased for smaller damages. The difference between the 2mm x 2mm grid and the 5mm x 5mm grid is limited, even for the small damage value. Table 4-3 gives the difference between the damage measured for the zone with the highest damage number. The 5mm x 5mm grid is used as a reference. This shows that the grid of 10mm x 10mm tends to underestimate the damage, while the difference between the 5mm x 5mm grid and the 2mm x 2mm grid is limited.

Table 4-3: Influence of grid density on damage

Number of waves	Damage grid 2mm x 2mm	Damage grid 5mm x 5mm	Damage grid 10mm x 10mm
1000	240 (+5%)	229	158 (-31%)
3000	-	815	690 (-15%)
5000	-	1118	1004 (-11%)
6000	-	1160	1081 (-7%)

Furthermore, the accuracy of the profiling plays an important role in the precision of the measured damage. The accuracy of the profiling is not determined by the accuracy of the positioning, as this is within 0.1mm both for the horizontal and vertical plane, but rather by the following two aspects:

- Although a fixed grid is used, the profiler does not stop at every grid point, yet runs continuously along the width of the flume. The speed of the profiler is determined by the measuring frequency, which should be higher than the profiler speed divided by the grid resolution
- the measurement with the laser has limited accuracy

Due to the continuous speed of the profiler, it is likely that a measurement is not made at the exact location of a grid point. In that case a weighted average of the surrounding measurements is used. The second aspect means that the accuracy of a measurement depends on the accuracy of the laser. The guidelines, offered by Aalborg university, stipulate that the accuracy of the laser lies within 1 to 2 mm. Both effects lead to the difficulty of measuring small damages with the profiler. This will be discussed further during the analysis of the damage for the dynamic stability criterion (section 4.3.3).

A few scour tests were performed to establish the maximum scour depth which develops under the loading conditions, described in Table 4-1. The tests were clear-water scour tests and are described in Appendix III. The maximum scour depth was measured for a current velocity $U_c = 0.298$ m/s and was equal to $S/D = 1.1$.

4.1.5. Model and scale effects

As mentioned in section 3.4, it is important to know what possible model or scale effects are and to minimize them as far as possible when performing small scale tests. Figure 3-15 is repeated here (Figure 4-6), and the potential laboratory and scale effects are shortly discussed below.

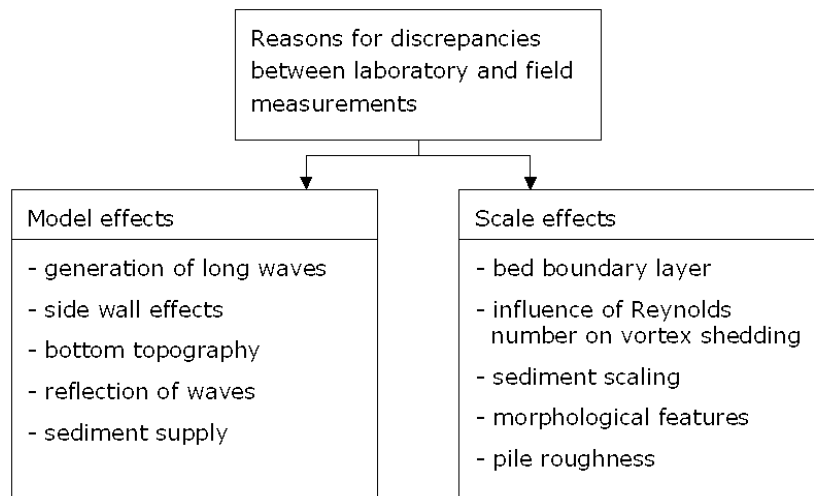


Figure 4-6: Overview of model and scale effects for scour protection design

Model effects

- generation of long waves: the steady current is slowly started up at the beginning and end of each test, to avoid the generation of a wave in the flume. Due to the presence of bounded long waves and different absorption characteristics of the absorbing beach, a standing wave generally exists when creating waves in a laboratory flume. So far little to no solutions exist to avoid this problem;
- side wall effects: the damping of waves can be disregarded here, as the waves are measured at the location of the monopile foundation. Due to the limited width of the flume, the flow will be slightly accelerated at the location of the pile. According to Whitehouse (1998), the ratio pile diameter to flume width should be less than 1/6 to avoid artificially high blockage in the laboratory model. In our model this ratio is 1/10.
- bottom topography: the gentle slope of 1/20 influences the generated waves. As the wave characteristics at the location of monopile are used, this does not influence the outcome of the research;
- reflection of waves: an absorption beach at the end of the wave flume reduces the reflection down to 15% or less, so reflection can be neglected. The total wave height will prove to give the best result for the damage analysis;
- sediment supply: no artificial sediment feeding was present during the tests. The sandbox was made large enough to avoid influences of the deficit in sediment supply. Furthermore, some of the sediment in suspension is transported by the pump and quite some sediment rested on the foreshore slope, providing some means of sediment supply.

Scale effects

- bed boundary layer: to have a rough boundary layer in all circumstances, the stone diameter should be larger than 0.05mm, according to equation (3.61) (Soulsby (1997)) and it should be larger than 3.5 mm, according to equations (3.64) and (3.65) (Fredsoe and

Deigaard (1992)). This requirement is fulfilled for all values of D_{50} of the scour protection;

- influence of Reynolds number on vortex shedding: as mentioned in chapter 3, the pile Reynolds number has an influence on the vortex shedding when it is smaller than $2 \cdot 10^5$. Table 4-1 shows that the pile Reynolds number in the model tests lies between $1.5 \cdot 10^4$ and $4.3 \cdot 10^4$, indicating that the pile Reynolds number might have an influence on the test results. For the performed test series, the prototype value of the pile Reynolds number lies between $54 \cdot 10^5$ and $153 \cdot 10^5$. Figure 1-15 and Figure 1-16 illustrate that this difference in Reynolds number implies that a different flow shedding regime exists in the model and in the prototype situation. In the model, a laminar boundary layer exists, whereas a fully turbulent boundary layer exists in prototype. This problem is acknowledged by Sumer et al. (1992), but no further information on the consequences for the scour protection were found. When looking at Figure 1-20 (which is limited to the range $10 \cdot 10^5$), it can be seen that for low KC numbers, the pile Reynolds number has little effect on the vortex shedding regime, which was also noted by Sumer et al. (1992);
- sediment scaling (sand): no specific prototype situation was modelled, but when upscaling the sediment diameter to a prototype value, we obtain a sediment diameter of 5mm, which represents fine gravel. Usually smaller sediment is present at the site. In chapter 3, the fall velocity is mentioned as the most important parameter regarding sediment transport. The fall velocity of the model sediment (diameter $d_s = 100 \mu\text{m}$) is calculated according to equations (3.33) and (3.34) and equals 0.009 m/s according to van Rijn (1993), while it is equal to 0.008 according to Soulsby (1997). When scaling the settling velocity to prototype scale, this leads to a fall velocity of approximately 0.06 m/s ($= \sqrt{50} w_{s,model}$), which corresponds to a sediment with a diameter of approximately 0.5mm (sand).
- morphological features: the ripples which are formed in a laboratory experiment differ from the ripples on prototype scale (Whitehouse (1998)). The bed roughness near the pile is however determined by the stone diameter, which is scaled geometrically, which means that the bed roughness is scaled correctly;
- pile roughness: the pile which was used for the tests had a smooth surface. In a marine environment it is likely for fouling to occur, making the pile rougher near the SWL. As the roughness might influence the vortex shedding, this may have an influence on the results, but has not been taken into account.

4.2. Development of static stability criterion

As explained in chapter 3, most scour protections are designed according to a static stability criterion, which states that stones have to remain stable under the maximum load. This is obtained by stating that the amplified bed shear stress has to be smaller than the critical bed shear-stress, determined with the

Shields criterion. As mentioned several times, it is difficult to assess the correct amplified bed shear-stress because of the complexity of the combination waves-current-pile-scour protection. This leads to a possibly overly conservative design of statically stable scour protections.

The presented test series was performed to assess which formula could lead to a more economical design, while still pursuing static stability (no movement). In order to do this, combined (regular) wave and current tests were performed to obtain the load at which movement initiated. The bed shear-stresses related to the tests are calculated with the different formulae given in chapter 1, section 1.1.1. The traditional Shields criterion is maintained. A transition from the regular wave results to an irregular sea state is suggested in section 4.2.3.2.

4.2.1. Test conditions

Tests were carried out with increasing current velocities (target velocities of 0 to 0.28m/s, in steps of 0.07m/s). Regular waves were superimposed on the current: for a certain wave period and current velocity, wave height was increased until movement initiated. For a given steady current velocity, the test was performed with different wave periods. The complete test program is given in Table 4-4, together with the wave height required to initiate movement.

Initiation of movement is visually established and is regarded as the displacement of at least one stone over a distance of at least two times the median stone size D_{50} .

It is possible that, just after installation, some stones are displaced almost immediately due to an unstable position (Hofland (2005)). To avoid underestimation of the wave height that initiates movement due to this "water working", tests which were carried out on a newly placed scour protection were repeated at the end of the test series.

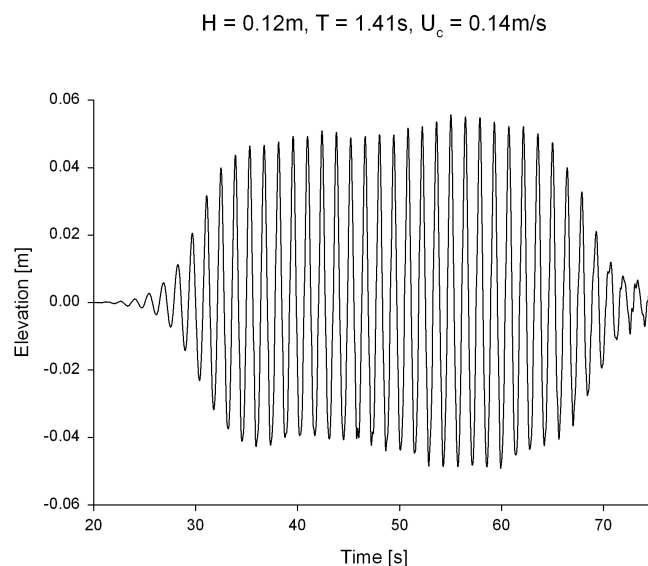


Figure 4-7: Regular wave record for wave gauge 2; static stability test n°6

The records of regular waves contain approximately 50 waves. Small variations in the wave height occur, due to the reflection at the end of the wave flume. The wave height used for the analysis is the maximum wave height, measured at the location of the pile and determined with the zero down-crossing method. An example of a wave record is given in Figure 4-7, which also shows the cosine shape build-up of the wave height, which is used to avoid the creation of a long wave due to a too sudden wave generation.

These tests were only carried out with the stones with a mass density ρ_s equal to 2650 kg/m³.

Table 4-4: Experimental conditions for static stability tests

Test n°	d	D _{n50}	U _c	T _w	H
[-]	[m]	[mm]	[m/s]	[s]	[m]
1	0.4	3.5	0.000	1.13	> 0.120
2	0.4	3.5	0.000	1.41	0.105
3	0.4	3.5	0.000	1.7	0.099
4	0.4	3.5	0.072	1.41	0.111
5	0.4	3.5	0.072	1.7	0.099
6	0.4	3.5	0.160	1.41	0.106
7	0.4	3.5	0.160	1.7	0.097
8	0.4	3.5	0.220	1.13	0.074
9	0.4	3.5	0.220	1.41	0.044
10	0.4	3.5	0.220	1.7	0.033
11	0.2	3.5	0.302	1.41	0.011
12	0.2	3.5	0.302	1.7	0.008
13	0.4	3.5	-0.067	1.41	0.112
14	0.4	3.5	-0.067	1.7	0.093
15	0.4	3.5	-0.142	1.41	0.099
16	0.4	3.5	-0.142	1.7	0.072
17	0.4	5.0	0.000	1.41	0.159
18	0.4	5.0	0.000	1.7	0.129
19	0.4	5.0	0.076	1.41	0.132
20	0.4	5.0	0.076	1.7	0.130
21	0.4	5.0	0.158	1.41	0.136
22	0.4	5.0	0.158	1.7	0.135
23	0.4	5.0	0.228	1.41	0.124
24	0.4	5.0	0.228	1.7	0.075
25	0.2	5.0	0.300	1.41	0.025
26	0.2	5.0	0.300	1.7	0.030
27	0.4	5.0	-0.137	1.41	0.134
28	0.4	5.0	-0.137	1.7	0.127
29	0.4	7.2	0.000	1.41	0.151
30	0.4	7.2	0.000	1.7	0.133
31	0.4	7.2	0.074	1.41	0.152
32	0.4	7.2	0.074	1.7	0.162
33	0.4	7.2	0.148	1.41	0.120
34	0.4	7.2	0.148	1.7	0.125
35	0.4	7.2	0.223	1.41	0.104
36	0.4	7.2	0.223	1.7	0.093
37	0.2	7.2	0.297	1.41	0.030
38	0.2	7.2	0.297	1.7	0.030
39	0.4	7.2	-0.134	1.41	0.118
40	0.4	7.2	-0.134	1.7	0.128

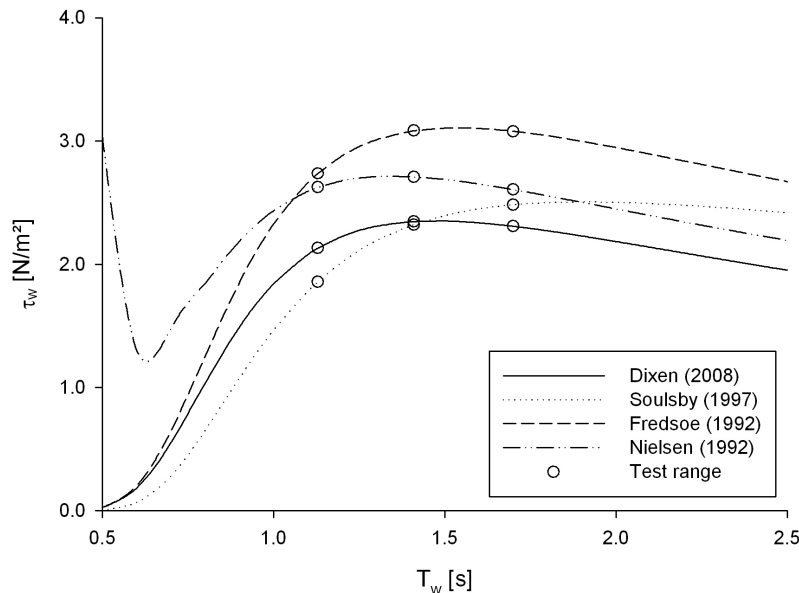
4.2.2. Analysis

The measured wave height and wave period are used to calculate the orbital velocities at the top of the scour protection with equation (3.3). The orbital velocity and the measured current velocity are used, first as a predictor variable to estimate the critical stone size, then to calculate the undisturbed bed shear stresses at the top of the scour protection. Undisturbed implies that we assume no pile is present. Equation (1.3) is used to calculate the bottom shear-stress, caused by a current, while equations (1.11) – (1.12) (Fredsoe and Deigaard (1992)); equations (1.16) (Dixen et al. (2008)); equation (1.21) (Nielsen (1992)) or equation (1.23) (Soulsby (1997)) are used to calculate the wave induced bed shear-stress.

The critical Shields parameter for initiation of movement is computed in two ways:

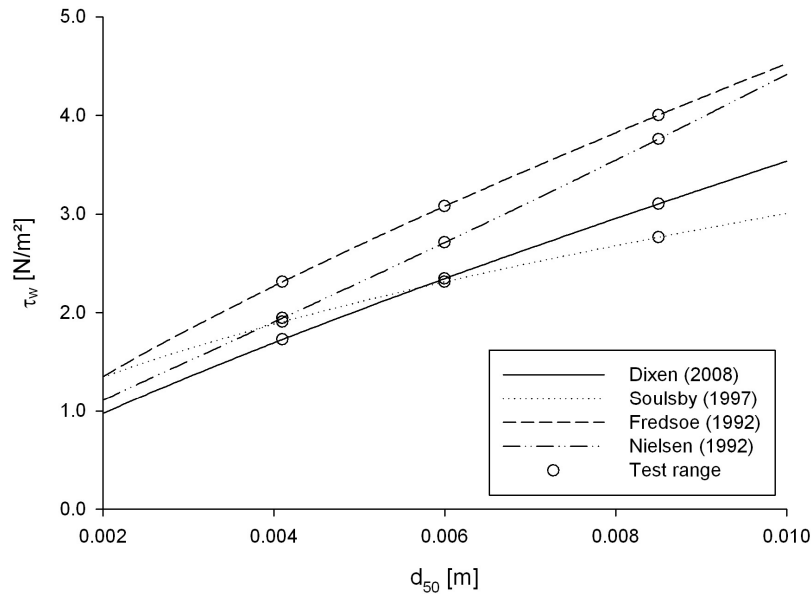
- according to equations (1.33) and (1.36) and (1.2), which yields θ_{cr} and thus τ_{cr} as a function of D_*
- according to Figure 1-7, which shows that the critical Shields parameter tends to 0.03 - 0.035 for large enough values of D_* when particle movement at a specific location is considered (curve 1 – 2). The value of D_* exceeds 100 for the smallest stone size, permitting us to use one critical Shields value for all investigated scour protections.

The wave height which initiates movement for the different combinations of U_{cr} , T_w and D_{n50} is shown in Table 4-4. Before performing the regression analysis, the differences between the alternative formulae to calculate the wave related bed shear-stress are demonstrated in Figure 4-8 and Figure 4-9. The range of the parameters for the tests are marked in the figures.



**Figure 4-8: Wave related bed shear-stress as a function of wave period:
d = 0.4m; H = 0.1m; d₅₀ = 6mm**

As can be seen in Figure 4-8 equation (1.21), suggested by Nielsen (1992) results in unexpected values of the wave induced bed shear stress for small values of the wave period. It is therefore advised to be careful when using this equation. It is in any case advised to restrict the use of the regression formulae, suggested in section 4.2.3.1 and section 4.2.3.2, to the region of the tested parameters.



**Figure 4-9: Wave related bed shear-stress as a function of stone size:
d = 0.4m; H = 0.1m; $T_w = 1.4s$**

4.2.3. Derivation of new prediction tool for statically stable scour protection around monopile foundations

4.2.3.1. Regular waves

A regression analysis is performed to determine whether the load which initiates movement can be estimated from the data set at hand. At first, a direct relation was sought between stone size and flow velocity (both wave and current), as suggested by equations (3.42) till (3.54) in chapter 3. These all in some way suggest a relationship between critical stone size and U^2 or U^3 . No adequate direct relationship was found between these parameters and regression analysis was used to find a better solution.

As mentioned above, the undisturbed bed shear-stress related to waves, currents and combined waves and currents was calculated according to Fredsøe and Deigaard (1992), Nielsen (1992), Soulsby (1997) and Dixen et al. (2008). The critical bed shear stress was also calculated in two ways. Several linear and non-linear relations were explored between the different values of the critical bed shear stress τ_{cr} and the undisturbed bed shear stress caused by the current

τ_{cr} , the waves τ_w , the mean combined current and wave bed shear stress τ_m , the maximum combined bed shear stress τ_{max} and combinations of these parameters. The best result (see below) was obtained by using a combination of τ_{cr} determined according to Liu (2001) (equations (1.3) – (1.4)) and τ_w , calculated with Diken et al. (2008) (equations (1.11) and (1.16)) to estimate the critical bed shear-stress which is on the threshold of motion. A value of 0.035 is withheld for the critical Shields parameter θ_{cr} . As θ_{cr} also tends to a constant value for sufficiently large values of D_{50} in equation (1.36), the difference between the two methods is only noticeable in a difference in the constants. In chapter 7, the methodology and final equations are grouped. As it is more intuitive to visualize the analysis, an example on how to interpret the results with only one predictor variable is presented in Figure 4-10.

In an undisturbed condition, where the scour protection is covering the entire bed and the flow is not disturbed by a structure (Figure 4-11 (a)), the expectation is that movement is initiated when the bed shear-stress equals the critical bed shear-stress. The Shields criterion is used to determine the critical bed shear stress. When the loading exceeds the resistance, stones will be moved by the flow. Whenever the resistance is larger than the load, the stones will stay in place. In the case a pile is present (Figure 4-11 (b)), the disturbance of the flow will cause the stones to move at a lower undisturbed load than would be expected in situation (a). An example of a regression fit on the measured data points (average value and 95% prediction interval) is shown in Figure 4-10.

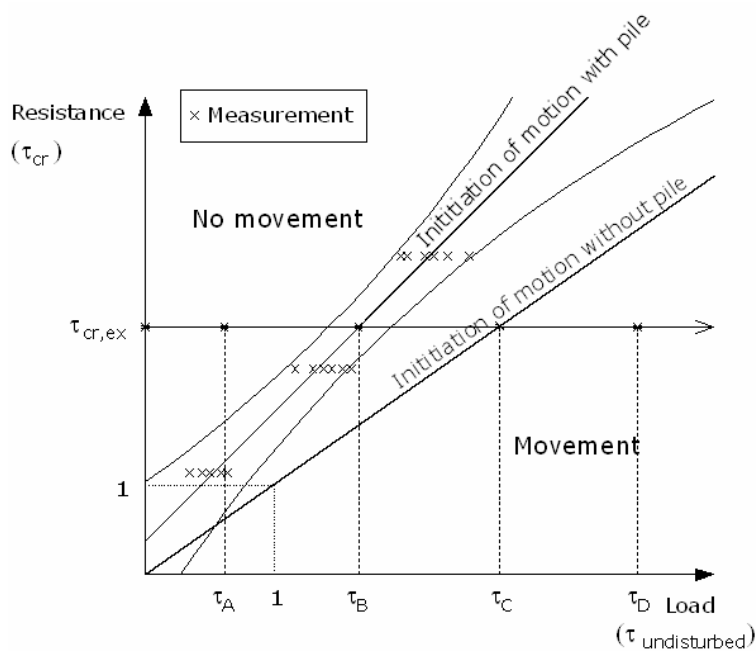


Figure 4-10: Relation between undisturbed bed shear-stress (load) and critical bed shear-stress (resistance)

When implementing this in an example (Figure 4-10), this means that for a value of the critical bed shear stress $\tau_{cr,exr}$ the following situations occur for increasing bed load:

- τ_A : the critical bed shear stress is large enough to avoid motion of the stones
- τ_B : motion is initiated in the case a pile is present. The undisturbed load τ_B is however smaller than the load τ_C at which movement is initiated without presence of the pile
- τ_C : initiation of motion takes place in the undisturbed case. In case a pile is present, several stones will already be displaced
- τ_D : movement of stones takes place both with and without pile

The loading conditions (τ_c and τ_w) are calculated in undisturbed conditions.

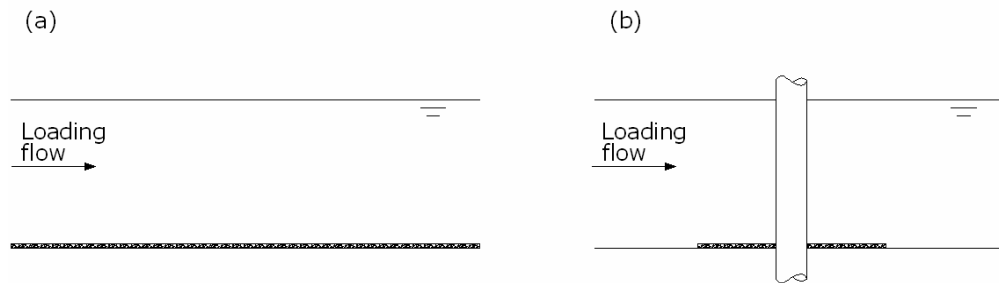


Figure 4-11: Bed protection without (left) and with (right) presence of a pile

When regressing τ_w (Dixen et al. (2008)) against τ_{cr} , the following relation is found:

$$\tau_{cr,pred} = 2.048 + 0.720\tau_w \quad (4.1)$$

The r^2 value, representing the coefficient of determination, equals 0.537 for equation (4.1). The measure r^2 can be interpreted as the proportionate reduction of the total variation associated with the use of the predictor variable τ_w (Neter et al. (1996)). The value of τ_{cr} is determined by assuming $\theta_{cr} = 0.035$:

$$\theta_{cr} = 0.035 = \frac{\tau_{cr}}{\rho_w g (s-1) D_{50}}$$

A large improvement is achieved when including the current induced bed shear-stress in the regression:

$$\tau_{cr,pred} = 0.868 + 3.511\tau_c + 1.039\tau_w \quad (4.2)$$

The r^2 value in this case amounts to 0.866, which indicates a large improvement of the fitted regression. The estimated value, obtained from the regression equation (4.2) is plotted in Figure 4-12 against the values of τ_{cr} , determined

from the tested stone sizes. From this figure, it can be seen that a certain dependency remains.

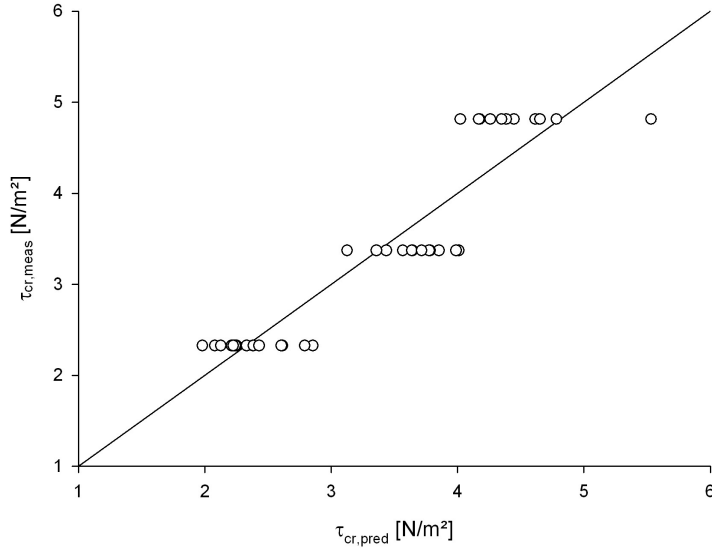


Figure 4-12: Estimated against measured value of τ_{cr} , regression (4.2)

While looking for an explanation for this remaining dependency, the stone grading seems to play a role. When the value of D_{85}/D_{15} is plotted against the residual in Figure 4-13, we can clearly see a trend as a function of the stone's grading. The values of D_{85}/D_{15} for the different gradings is listed in Table 4-2. The residual or error represents the difference between the observed value and the corresponding fitted value. The magnitude of the residual e_i is represented by the vertical deviation of the observation Y_i from the corresponding point on the estimated regression function \hat{Y}_i :

$$e_i = Y_i - \hat{Y}_i \quad (4.3)$$

This implies that positive values of the error term indicate an underestimation of the fitted value compared to the observed value, or that we are on the unsafe side. Figure 4-13 shows that this means that stones in a scour protection with a smaller grading will tend to move faster than those in a scour protection with a wide grading. This could be due to the fact that in widely graded material, smaller stones find a better shelter thanks to the larger stones.

Only one test gives a negative value of the error term for the most narrow scour protection material. It is Test n° 32 (Table 4-4). We will consider it to be an outlier and remove it from the data set. This leads to:

$$\tau_{cr,pred} = 0.773 + 3.582\tau_c + 1.096\tau_w \quad (4.4)$$

with an r^2 value of 0.875. Figure 4-14 shows that the same trend as a function of the grading remains.

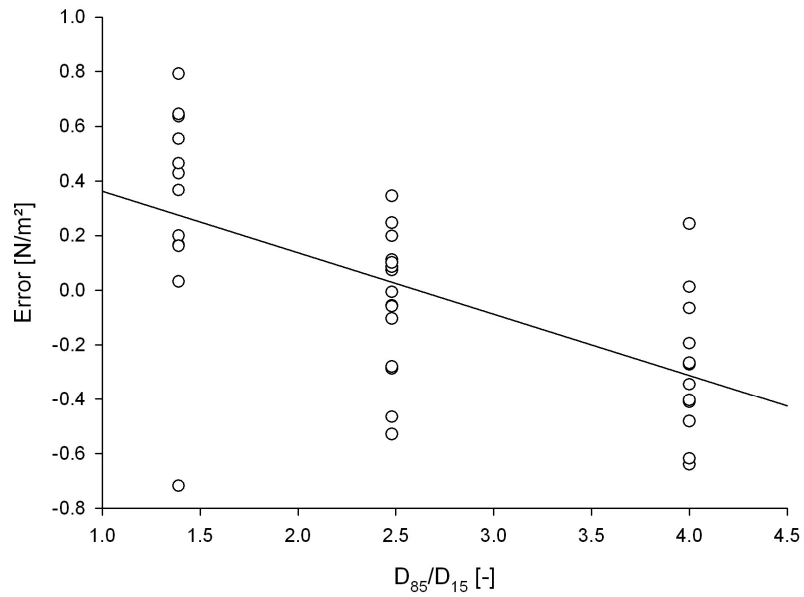


Figure 4-13: Residual as a function of D_{85}/D_{15} , regression (4.2)

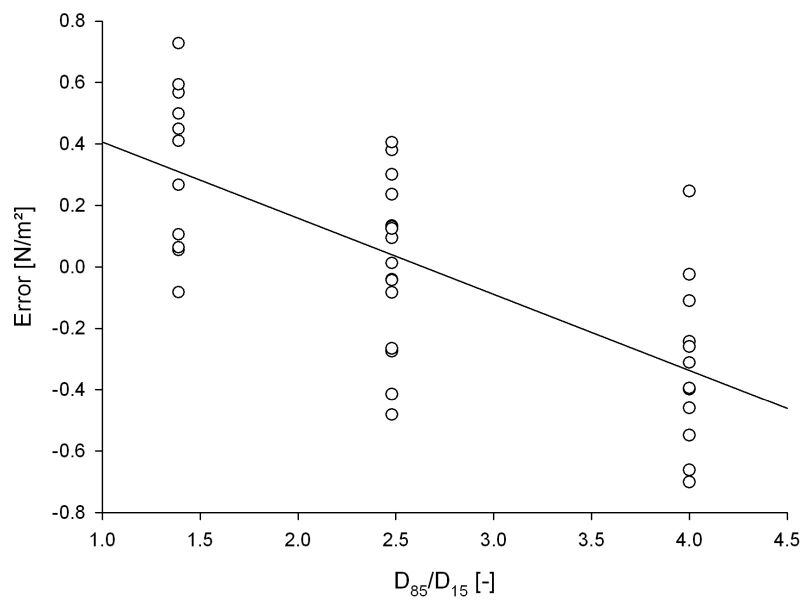


Figure 4-14: Residual as a function of D_{85}/D_{15} , regression (4.4)

A possibility is to say that the critical value for stone entrainment does not depend on the value of D_{50} , but on a larger stone size from the grading. This might offer a solution, as for wide gradings, a higher % stone size will be significantly larger than the value of D_{50} , whereas in narrow gradings, it will not. The value of $\tau_{cr,pred}$ is now obtained by using the value $D_{67.5}$ (Table 4-2) to calculate the critical bed shear stress τ_{cr} for the different scour protections, the following equation is obtained:

$$\tau_{cr,pred} = 1.720 + 3.303\tau_c + 1.015\tau_w \quad (4.5)$$

with an r^2 value of 0.926. Note that to calculate the bed shear stresses caused by waves and current, the value of D_{50} is still used to calculate the bottom roughness.

The predicted value of τ_{cr} is plotted against the measured value of τ_{cr} in Figure 4-15, showing that the influence of the stone size on the result is no longer present.

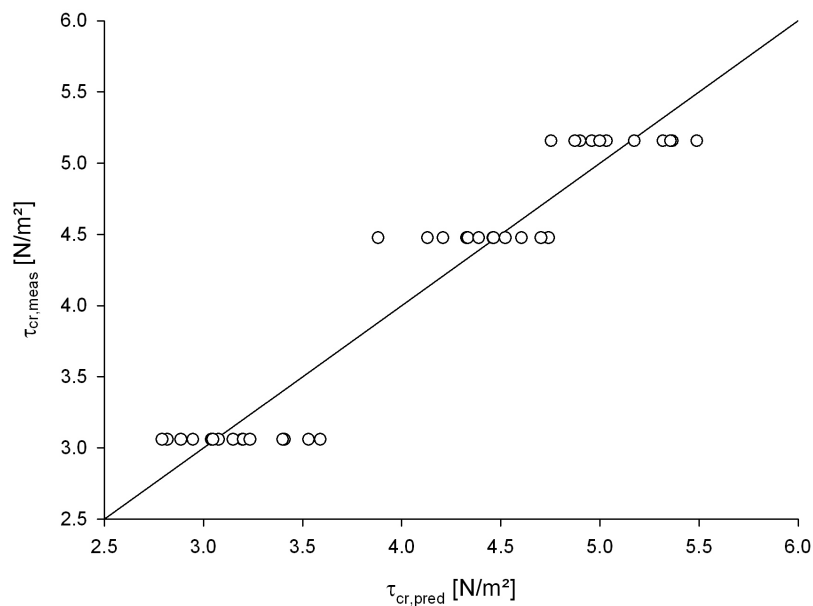


Figure 4-15: Estimated against measured value of τ_{cr} regression (4.5)

Figure 4-16 plots the predicted $\tau_{cr,pred}$, determined with equation (4.5) as a function of the wave induced bed shear stress τ_w together with the 90% confidence band for the regression line, for two values of the current induced bed shear stress τ_c , covering the range of values which were tested.

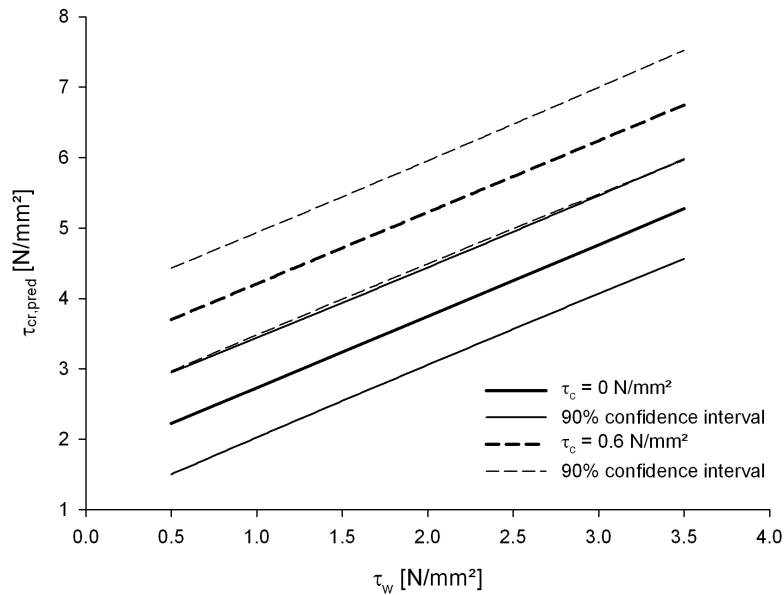


Figure 4-16: Regression lines and confidence interval as a function of τ_w

As it might be difficult to assess what the 90% confidence interval for the bed shear stress means when it is related to the prediction of the stone size, Table 4- 5 gives some examples of loading characteristics and resulting mean stone size, together with the lower and upper limit of the 90% confidence interval, showing that the required stone size for the statically stable scour protection can be rather well predicted with equation (4.5).

Table 4- 5: Required stone size and 90% prediction limits

τ_c	τ_w	$\tau_{cr, pred}$	$d_{67.5, lower limit}$	$d_{67.5, mean}$	$d_{67.5, upper limit}$
[N/mm ²]	[N/mm ²]	[N/mm ²]	[mm]	[mm]	[mm]
0	0.5	2.228	3.1	3.9	4.8
0	2	3.750	5.8	6.6	7.4
0	3.5	5.273	8.5	9.3	10.1
0.2	0.5	2.888	4.3	5.1	5.9
0.2	2	4.411	7.0	7.8	8.6
0.2	3.5	5.933	9.7	10.5	11.3
0.4	0.5	3.549	5.5	6.3	7.1
0.4	2	5.071	8.2	9.0	9.8
0.4	3.5	6.594	10.8	11.6	12.5
0.6	0.5	4.209	6.6	7.4	8.3
0.6	2	5.732	9.3	10.1	11.0
0.6	3.5	7.254	11.9	12.8	13.7

The problem with equations (4.1) to (4.5) is that they are not dimensionless, which causes problems when using a different scale. One solution could be to convert the bed shear stress to the Shields parameter. However, in this case, the critical Shields parameter is the same for all tests (θ_{cr} is assumed to be 0.035), which means that no statistical fitting can be done to the test results. To account for this problem, the bed shear stress is divided by $\rho_w \Delta g D$, with ρ_w the density of water, Δ the relative density of the stones (= 1.65), g the gravitational acceleration and D the pile diameter. As these parameters were not varied during the tests, this results in:

$$\frac{\tau_{cr}}{\rho_w \Delta g D} = 0.001 + 3.303 \frac{\tau_c}{\rho_w \Delta g D} + 1.015 \frac{\tau_w}{\rho_w \Delta g D} \quad (4.6)$$

While the r^2 value remains 0.926 and the prediction intervals, given in Figure 4-16 and Table 4- 5 remain unaltered.

4.2.3.2. Adjustment for irregular waves

Equation (4.5) is derived for regular waves, which means that the same load is experienced near the scour protection every time a wave passes. In reality however, a sea state consists of irregular waves with varying wave height and period, leading to varying loads on the scour protection material.

Two design approaches can be used to determine the initiation of stone entrainment in irregular wave conditions, a probabilistic or a deterministic approach (CIRIA/CUR (1991)). With a probabilistic approach the probability of stone entrainment is assessed by taking the probability distribution of both the load (wave and current characteristics) and the stone entrainment which belongs to each particular load into account. A deterministic approach on the other hand uses a characteristic value of the loading and a characteristic strength value to determine whether stone entrainment will take place.

We opt for the use of the traditional design method, the deterministic approach, which allows for an easy calculation of the required stone size. Thus a representative value for the wave load in equation (4.5) needs to be found. The wave load on the bottom can be represented by the bottom shear stress, which is mainly influenced by the orbital bottom velocity. Characteristic values of the bottom orbital velocities which are often used to describe irregular wave orbital velocities are the root mean square value U_{rms} , the "significant" velocity amplitude U_s and the velocity U_m , determined from the orbital velocity spectrum as (Sumer and Fredsøe (2002)):

$$U_{rms} = \sigma_U \quad (4.7)$$

$$U_s = 2\sigma_U \quad (4.8)$$

$$U_m = \sqrt{2}\sigma_U \quad (4.9)$$

with σ_U the r.m.s. value of the orbital velocity at the bed:

$$\sigma_U^2 = \int_0^\infty S_U(f) df \quad (4.10)$$

$S_U(f)$ is the power spectrum of the bottom velocity U_m which can be determined as:

$$S_U(f) = \left(\frac{2\pi}{T \sinh(kd)} \right)^2 S(f) \quad (4.11)$$

with $S(f)$ the variance spectral density of the wave climate according to equation (3.16) and f the wave frequency.

The larger bottom velocities are more likely to cause the stones to move. The question is which value of the bottom velocity will best represent the wave shear-stress and how this value can be retrieved from the spectrum.

For wave heights, the Rayleigh distribution can be used to assess the exceeding probability of a wave height for a storm characterised by H_{rms} (see chapter 3, section 3.2.1.2). Based on Figure 4-17, it was decided to use the Rayleigh distribution for the orbital velocities as well. The exceeding probability of a given amplitude of the bottom velocity U_d is determined as:

$$P(U > U_d) = \exp \left[- \left(\frac{U_d}{U_m} \right)^2 \right] = \exp \left[- \frac{1}{2} \left(\frac{U_d}{U_{rms}} \right)^2 \right] \quad (4.12)$$

in which U_m is determined according to equation (4.9) and U_{rms} according to equation (4.7).

Figure 4-17 shows a comparison of wave height distribution and orbital bottom velocity distribution for two irregular wave trains. This graph was made, based on a time series analysis of wave elevations and bottom velocities. The time series was generated from a theoretical JONSWAP spectrum, $\gamma = 3.3$ ($T_0 = 3000s$) by using the same (random) phase spectrum for both the elevations and the orbital velocities near the bottom. Time series analysis was then used to calculate the corresponding distributions. This intricate method was used because it is not possible to directly translate an irregular sea surface to the corresponding orbital velocities at the bottom.

The irregular wave test results (see section 4.3) are used to assess which value of the bottom velocity is best used to calculate the wave induced bed shear stress in equation (4.5). It appears that $U_{10\%}$ (the orbital velocity amplitude which is exceeded by 10% of the waves) gives the best result for the irregular wave test results, predicting when stones will or will not move. From equation (4.12), the relationship between $U_{10\%}$ and U_m can be calculated as:

$$U_{10\%} = 1.52U_m \quad (4.13)$$

An overview of all irregular wave tests is given in section 4.3. Damage is assessed visually and a damage level "1" corresponds with a visual interpretation that the scour protection's stones did not move when comparing before and after images of the scour protection. In Table 4-7, the visual damage level for the different tests is shown. Only 5 tests achieve a damage level 1. Even for these tests, movement was visually observed during 4 out of 5 tests (rocking or small back and forth displacements of the stones). The behaviour is well predicted by using the average value of the predicted critical bed shear stress with equation (4.6) and $U_{10\%r}$ as defined in (4.13).

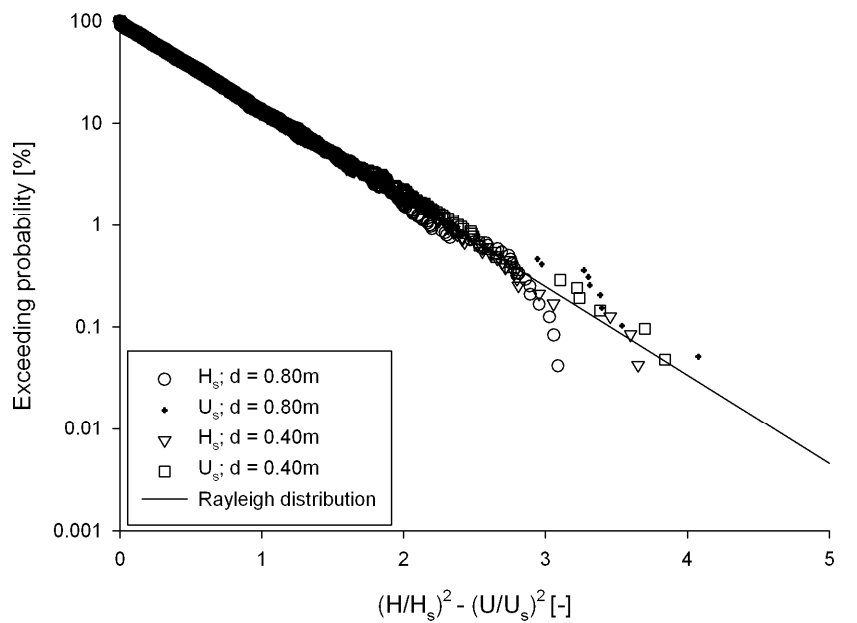


Figure 4-17: Appropriateness of the Rayleigh distribution to describe the orbital velocities.

4.2.4. Comparison and validation of formula and results

A comparison of the stone size obtained with equation (4.6) and the stone sizes obtained with the traditional method is made in section 4.3.5.2.

For the OPTI-PILE project, described in section 3.3.3, a comparable approach was used as in section 4.2.3. In the project, a parameter $Stab$ was defined as:

$$Stab = \frac{\theta_{max}}{\theta_{cr}} \quad (3.56)$$

with θ_{cr} the critical Shields parameter = 0.056 and θ_{max} the maximum Shields parameter, defined as:

$$\theta_{\max} = \frac{\tau_{\max}}{\rho_w g (s-1) D_{50}} \quad (4.14)$$

and τ_{\max} as defined in equation (1.31).

It was found that initiation of stone movement occurs when $Stab$ exceeds the value 0.415. Although the results are based on irregular wave tests, the possibility exists to calculate the value of $Stab$ for regular waves as well with the OPTI-PILE DESIGN TOOL V2.4 (HR Wallingford Ltd for E-Connection Project BV). The parameter was calculated by HR Wallingford for the test series given in Table 4-4.

Figure 4-18 plots the values of $Stab$ against the test n^o (Table 4-4). The limits, which are defined in the OPTI-PILE projects as the transition between no movement and movement without failure ($Stab = 0.415$) and the transition between movement without failure and failure ($Stab = 0.46$) are also plotted in the figure. As all tests represent initiation of movement, it can be decided that the parameter $Stab$, as calculated for the regular wave tests, can not be used to represent the initiation of movement. However, the tests which were performed (regular waves, only approx. 50 waves were generated) differ significantly from a significantly longer test with an irregular wave train, in which many waves exceed the value of H_{m0} which is used in the OPTI-PILE tool.

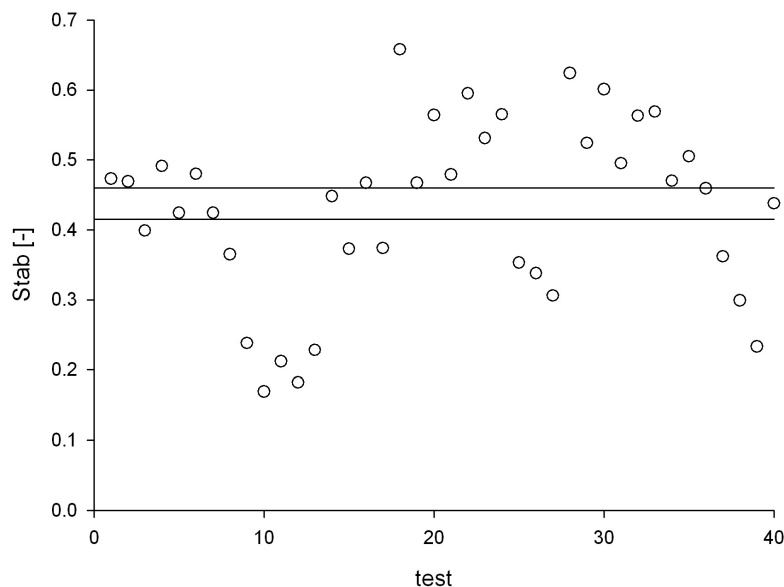


Figure 4-18: OPTI-PILE parameter $Stab$ (HR Wallingford Ltd for E-Connection Project BV) for the data set at hand

As mentioned above, the use of the OPTI-PILE parameter is actually comparable to the parameters which were used in this analysis, that is τ_w and τ_c . To compare the OPTI-PILE parameter with the results obtained in this thesis with

equation (4.6), the value of τ_{max} (equation (4.14)) is plotted in Figure 4-19 against the value of τ_{cr} , determined with equation (1.33). The data points from Figure 4-15, in which the values of $\tau_{cr,pred}$ (with equation (4.6)) are plotted against the values of $\tau_{cr,meas}$ are added to Figure 4-19. The difference between the values of $\tau_{cr,meas}$ which are used for the OPTI-PILE points and the values of $\tau_{cr,meas}$, which are used throughout this study is that a value of 0.056 is assumed for θ_{cr} in Optipile, while a value of 0.035 is assumed in this thesis. This however only results in a difference by a constant factor. Furthermore, the value of $D_{67.5}$ is used in this thesis to calculate $\tau_{cr,meas}$, while D_{50} is used for the OPTI-PILE parameter.

From Figure 4-19, it can be seen that the spreading around the value of τ_{max} is higher than the spreading around the predicted value, obtained with equation (4.6). When a linear regression is used, which goes through the points, as shown in Figure 4-19, a serious deviation is obtained from the data points.

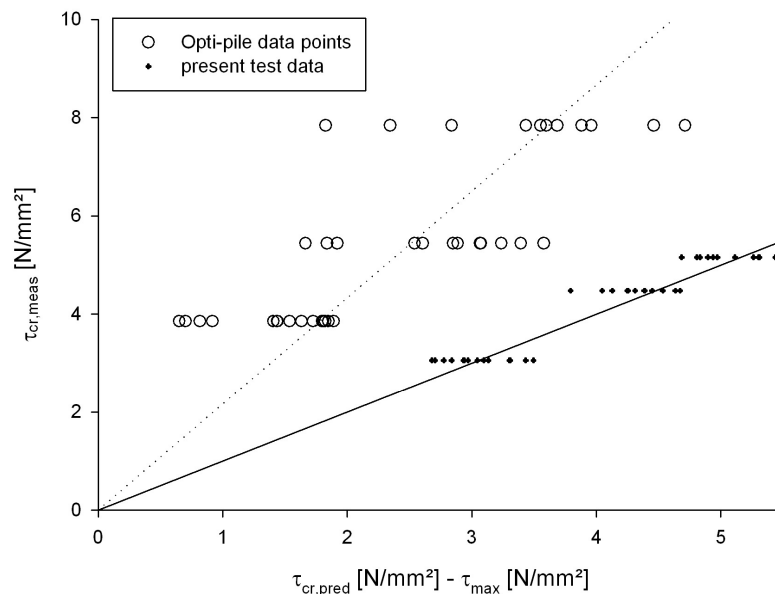


Figure 4-19: Comparison of OPTI-PILE calculation (HR Wallingford Ltd for E-Connection Project BV) with present data set

When plotting the value of $Stab$ against the median stone size D_{50} , it can indeed be seen that the same trend can be distinguished as noted before, that is that a higher load can be withstood for the wide gradation ($D_{50} = 0.006m$) (Figure 4-20).

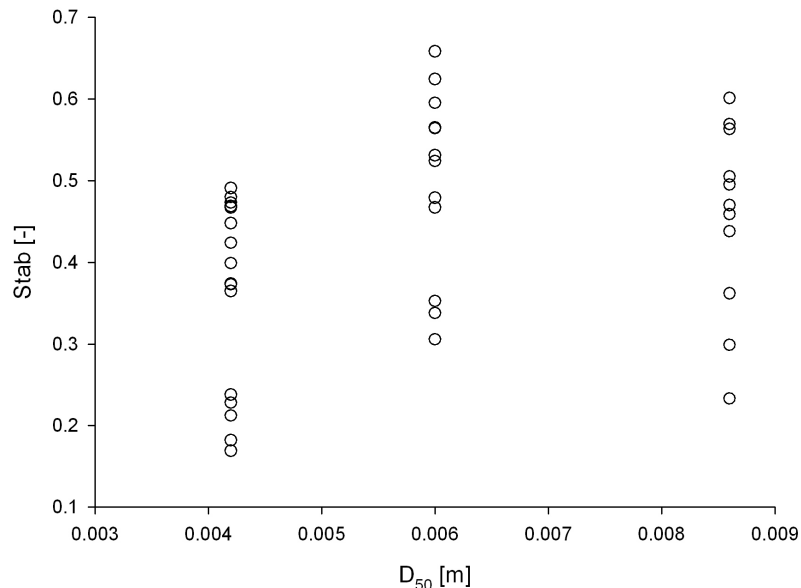


Figure 4-20: OPTI-PILE parameter Stab versus median stone size $D_{67.5}$

4.3. Including damage number in the stability criterion

4.3.1. Accepting local damage

When designing a statically stable scour protection, in principle no or only limited damage is allowed, damage being defined as the displacement of top layer stones. Such a design might lead to an overly conservative stone size and a high cost of the scour protection. As the design life time of offshore wind turbines is only 20 years (den Boon et al. (2003)), it is important to decrease the costs of a wind turbine as much as possible. An opportunity to do this can be found in using significantly smaller rock sizes for the scour protection. The use of smaller rock sizes may decrease the basic cost, but potentially leads to an additional decrease of the cost by reducing the number of filter layers. This can be the case when two filter layers are required, again reducing the costs of the scour protection.

A more economical solution may be building a protection with smaller elements, allowing movement of individual stones without failure of the protection. Under these conditions it is important:

- to clearly define damage;
- to formulate an acceptable damage criterion;
- to add damage as a parameter in the stability formula;
- to account for damage development over time as an important element in the design of scour protections.

Going even one step further, Van der Meer (1988) investigated breakwaters with significantly smaller stone sizes than ordinarily used for a statically stable design. He came to the conclusion that such breakwaters develop a dynamically stable profile, for breakwater damage as a function of time reaches an equilibrium state. The same could go for bottom protections as is shown in Figure 4-21 (CIRIA/CUR (1991)), which shows that damage development for a bottom protection also develops towards an equilibrium state. This is in stark contrast with a progressive failure mechanism in which damage increases exponentially. The similar decrease in damage rate for bed protections and breakwaters leads to the expectation that a dynamically stable profile will develop when the stone size of the scour protection is decreased. On this subject, Chiew (1995) investigated the stability of a riprap layer around a cylindrical bridge pier. He found that partial damage of a riprap layer led to rearmouring by the coarse riprap stones, which could effectively prevent a total disintegration of the riprap layer.

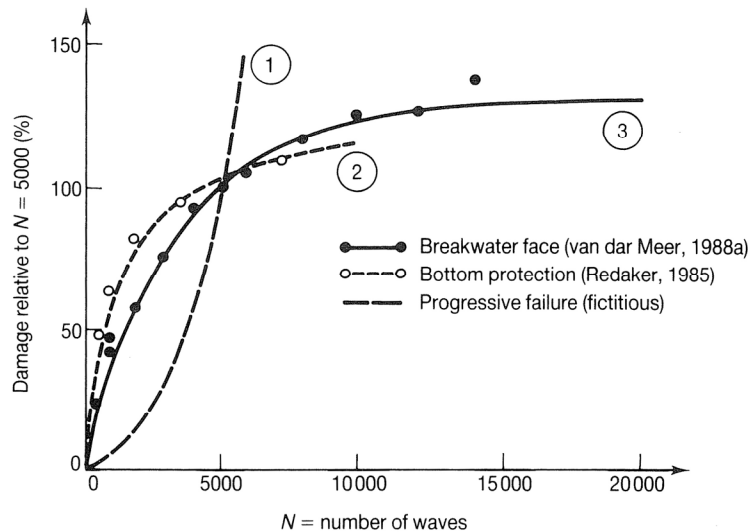


Figure 4-21: Damage evolution as a function of time; from CIRIA/CUR (1991)

This leads to the assumption that dynamically stable scour protections might be feasible, resulting in a more economical scour protection design as compared to those currently in use. When aspiring dynamically stable profiles, it is important to know whether the developed profile remains stable or whether damage will accumulate and ultimately lead to the scour protection's failure.

Even when a statically stable scour protection is wanted, damage might develop when the design criteria are exceeded. In this case, information on the development of the damage in time and the amount of damage which can be expected is important regarding the maintenance of the scour protection. Exceeding design criteria can be related to the limited life cycle of offshore wind turbines (approximately 20 years). As scour protection failure hardly ever leads to potentially lethal situations, a relatively short return period is often used for

its design. Moreover, scour protection failure does not immediately imply failure of the wind turbine's foundation as it is mostly designed for withstanding fatigue. Typically a return period of 50 years is considered acceptable (compare this to the return period used for the protection of the Belgian coasts, which is 1000 years or more). Chances of encountering higher loads than the design loads are therefore significant. Furthermore den Boon et al. (2003) suggest that the life time of a wind turbine might be considerably increased by a low-cost load-monitoring of the foundation. Measuring the effective load can instigate the idea of keeping the wind turbine operational for a longer period of time, leading to an even higher possibility of exceeding the design criteria.

To further investigate the possibility of allowing limited local damage, an extensive series of model scale tests was performed.

4.3.2. Tests conditions

Irregular wave tests were carried out for a range of wave heights and wave periods, combined with different steady current velocities following or opposing the waves. Two different water depths were used throughout the tests. For each test, characterised by a combination of the loading parameters, three consecutive wave trains were generated. Generally, an initial wave train of 1000 waves is followed by two wave trains of 2000 waves. When the scour protection was completely destructed after 3000 waves, the second wave train of 2000 waves was not generated. Before each test and after each wave train, a 3D profile of the scour protection was made.

The complete test program is given in Table 4-6, depicting the total number of waves N , the water depth d , the nominal stone diameter D_{n50} of the scour protection, the relative stone density $s (= \rho_s/\rho_w)$, the steady current velocity U_c , the significant wave height H_{m0} , the peak wave period T_p , the applied filter, the thickness of the scour protection t_s and the value of D_{85}/D_{15} which characterises the stone's grading. The test numbers with marked with an asterisk ("*") were repeated 1 or 2 times to assess the repeatability of the tests.

The target spectrum of the irregular waves is a JONSWAP spectrum, with a peak enhancement factor $\gamma = 3.3$. The different test series were carried out without the pile in the wave flume and wave characteristics were measured at the location of the pile to determine the undisturbed wave field. As a low-reflection absorption beach is installed at the end of the flume, it is assumed that reflection is small enough to be neglected (no active wave absorption was used throughout the tests). Reflection amounts to approximately 15%, which permits this method of working.

For the wave analysis, the spectral approach is used. The wave elevations are measured at a rate of 40Hz. To determine the bandwidth of the spectral window, a compromise needs to be found between an acceptable variance and enough detail in the spectrum (Troch (2000)). A spectral window with 1024 elements (25.6s) and 20% overlap is used to calculate the smoothed spectral estimate. An example of a measured spectrum and the corresponding theoretical JONSWAP spectrum is given in Figure 4-22.

Table 4-6: Experimental conditions for dynamic stability tests (measured characteristics)

Test n°	N	d	D _{n50}	s	U _c	H _{m0}	T _p	Filter	t _s	D ₈₅ /D ₁₅
[-]	[-]	[m]	[mm]	[-]	[m/s]	[m]	[s]	[-]	[times D _{n50}]	[-]
1	5000	0.4	3.5	2.65	0	0.139	1.45	geotextile	2.5	2.48
2	5000	0.4	3.5	2.65	0	0.125	1.71	geotextile	2.5	2.48
3	5000	0.4	3.5	2.65	0	0.141	1.71	geotextile	2.5	2.48
4	5000	0.4	3.5	2.65	0	0.156	1.71	geotextile	2.5	2.48
5	5000	0.4	3.5	2.65	0.077	0.120	1.16	geotextile	2.5	2.48
6	5000	0.4	3.5	2.65	0.080	0.135	1.42	geotextile	2.5	2.48
7	5000	0.4	3.5	2.65	0.077	0.120	1.71	geotextile	2.5	2.48
8	5000	0.4	3.5	2.65	0.081	0.136	1.71	geotextile	2.5	2.48
10	0	0.4	3.5	2.65	0.140	-	-	geotextile	2.5	2.48
11	5000	0.4	3.5	2.65	0.164	0.118	1.20	geotextile	2.5	2.48
12	1000	0.4	3.5	2.65	0.147	0.050	1.42	geotextile	2.5	2.48
13	3000	0.4	3.5	2.65	0.150	0.069	1.42	geotextile	2.5	2.48
14	5000	0.4	3.5	2.65	0.164	0.088	1.42	geotextile	2.5	2.48
15*	5000	0.4	3.5	2.65	0.159	0.114	1.42	geotextile	2.5	2.48
16	5000	0.4	3.5	2.65	0.165	0.129	1.42	geotextile	2.5	2.48
17	5000	0.4	3.5	2.65	0.161	0.140	1.40	geotextile	2.5	2.48
18	5000	0.4	3.5	2.65	0.164	0.115	1.71	geotextile	2.5	2.48
19	5000	0.4	3.5	2.65	0.163	0.130	1.71	geotextile	2.5	2.48
20*	5000	0.4	3.5	2.65	0.160	0.145	1.71	geotextile	2.5	2.48
21	0	0.4	3.5	2.65	0.205	-	-	geotextile	2.5	2.48
22	3000	0.4	3.5	2.65	0.230	0.083	1.42	geotextile	2.5	2.48
23	0	0.4	3.5	2.65	0.253	-	-	geotextile	2.5	2.48
24	5000	0.4	3.5	2.65	-0.067	0.146	1.71	geotextile	2.5	2.48
25	5000	0.4	3.5	2.65	-0.142	0.099	1.42	geotextile	2.5	2.48
26	5000	0.4	3.5	2.65	-0.138	0.117	1.42	geotextile	2.5	2.48
27	5000	0.4	3.5	2.65	-0.137	0.134	1.37	geotextile	2.5	2.48
28	5000	0.4	3.5	2.65	0	0.139	1.45	geotextile	2.5	1.32
29	5000	0.4	3.5	2.65	0	0.141	1.71	geotextile	2.5	1.32
30	5000	0.4	3.5	2.65	0	0.156	1.71	geotextile	2.5	1.32
31	5000	0.4	3.5	2.65	0.166	0.114	1.42	geotextile	2.5	1.32
32	5000	0.4	3.5	2.65	0.164	0.115	1.71	geotextile	2.5	1.32
33	3000	0.4	3.5	2.65	0.161	0.145	1.71	geotextile	2.5	1.32
34	5000	0.4	3.5	2.65	0.212	0.083	1.42	geotextile	2.5	1.32
35	3000	0.4	3.5	2.65	0.233	0.109	1.71	geotextile	2.5	1.32
36	3000	0.4	3.5	2.65	-0.147	0.134	1.71	geotextile	2.5	1.32
37	5000	0.4	3.5	2.65	0.154	0.115	1.71	no	2.5	2.48
38*	5000	0.4	3.5	2.65	0.164	0.145	1.71	no	2.5	2.48
39	5000	0.4	3.5	2.65	0.169	0.115	1.71	no	3	2.48

Test n°	N	d	D _{n50}	s	U _c	H _{m0}	T _p	filter	t _s	D ₈₅ /D ₁₅
[-]	[-]	[m]	[mm]	[-]	[m/s]	[m]	[s]	[-]	[times D _{n50}]	[-]
40	5000	0.4	3.5	2.65	0.156	0.145	1.71	no	3	2.48
41	5000	0.4	3.5	2.65	0.151	0.145	1.71	granular	2.5	2.48
41a	0	0.2	3.5	2.65	0.317	-	-	granular	2.5	2.48
42	5000	0.4	3.5	2.65	+0.159 -0.150	0.115	1.71	geotextile	2.5	2.48
43	3000	0.2	3.5	2.65	0.172	0.080	1.79	geotextile	2.5	2.48
44	5000	0.4	5	2.65	0	0.156	1.71	geotextile	2.5	4
45	5000	0.4	5	2.65	0.077	0.152	1.71	geotextile	2.5	4
46	5000	0.4	5	2.65	0.164	0.129	1.42	geotextile	2.5	4
47	5000	0.4	5	2.65	0.165	0.140	1.40	geotextile	2.5	4
48	5000	0.4	5	2.65	0.163	0.130	1.71	geotextile	2.5	4
49	5000	0.4	5	2.65	0.158	0.145	1.71	geotextile	2.5	4
50	5000	0.4	5	2.65	0.224	0.109	1.71	geotextile	2.5	4
51	5000	0.4	5	2.65	0.227	0.140	1.71	geotextile	2.5	4
52	3000	0.2	5	2.65	0.315	0.058	1.71	geotextile	2.5	4
53	5000	0.4	7.2	2.65	0.156	0.145	1.71	geotextile	2.5	1.39
54	5000	0.4	7.2	2.65	0.221	0.121	1.42	geotextile	2.5	1.39
55	5000	0.4	7.2	2.65	0.221	0.140	1.71	geotextile	2.5	1.39
56	5000	0.2	7.2	2.65	0.168	0.080	1.79	geotextile	2.5	1.39
57	3000	0.2	7.2	2.65	0.299	0.086	1.71	geotextile	2.5	1.39
58	5000	0.4	7.2	2.65	-0.142	0.163	1.71	geotextile	2.5	1.39
59	5000	0.4	7.2	2.65	0.236	0.140	1.71	no	2.5	1.39
60	5000	0.4	-	-	0.147	-	-	-	-	scour
61	5000	0.4	-	-	0.203	-	-	-	-	scour
62	5000	0.2	-	-	0.298	-	-	-	-	scour
71	3000	0.4	3.5	3.2	0	0.168	1.71	geotextile	2.5	2.48
72	3000	0.4	3.5	3.2	0	0.155	1.71	geotextile	2.5	2.48
73	3000	0.4	3.5	3.2	0.066	0.151	1.71	geotextile	2.5	2.48
74	3000	0.4	3.5	3.2	0.143	0.128	1.42	geotextile	2.5	2.48
75	3000	0.4	3.5	3.2	0.146	0.139	1.35	geotextile	2.5	2.48
76	3000	0.4	3.5	3.2	0.141	0.146	1.71	geotextile	2.5	2.48
77	3000	0.4	3.5	3.2	0.203	0.122	1.42	geotextile	2.5	2.48
78	3000	0.4	3.5	3.2	0.195	0.107	1.42	geotextile	2.5	2.48
81	3000	0.4	5	3.2	0	0.168	1.71	geotextile	2.5	4
82	3000	0.4	5	3.2	0	0.146	1.71	geotextile	2.5	4
83	3000	0.4	5	3.2	0.202	0.124	1.71	geotextile	2.5	4
84	3000	0.4	5	3.2	0.214	0.135	1.42	geotextile	2.5	4
85	3000	0.4	5	3.2	0.212	0.139	1.71	geotextile	2.5	4

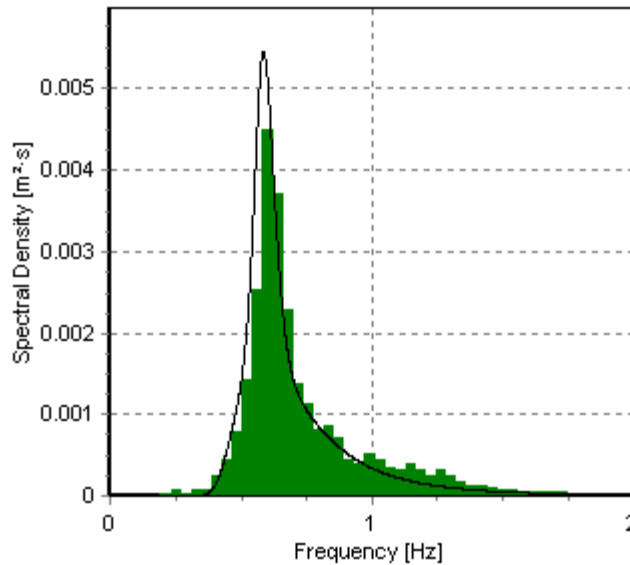


Figure 4-22: Smoothed measured spectrum and theoretical JONSWAP spectrum, test 19, 48: $U_{c,target} = 0.14\text{m/s}$, $H_{m0,target} = 0.14\text{m}$, $T_{p,target} = 1.7\text{s}$

As 3 successive wave trains are generated for each test, the characteristic values of a test are determined as a weighted average of the wave trains. In Table 4-6, the characteristics of the first 3000 waves are written down (as 3000 waves are used for the main damage analysis). For the wave height H_{m0} , the value after 3000 waves is calculated as:

$$H_{m0} = \frac{1}{3} (H_{m0,1000} + 2H_{m0,2000}) \quad (4.15)$$

with $H_{m0,1000}$ the significant wave height of the test series with 1000 waves and $H_{m0,2000}$ the significant wave height of the first test series with 2000 waves. For the wave height after 5000 waves, the same method was used to obtain a weighted average for H_{m0} .

The other characteristics (both steady current velocity and wave characteristics) are treated the same way.

4.3.3. Analysis

The analysis of the damage is based both on visual observations (top view pictures are taken before each test and after each wave series) and the 3D profiler measurements. The profiler measurements are given in Appendix V and pictures of all tests are shown in Appendix VI. Both are included on the enclosed DVD.

4.3.3.1. Damage definition

For the visual damage analysis, four damage levels are distinguished (Figure 4-23):

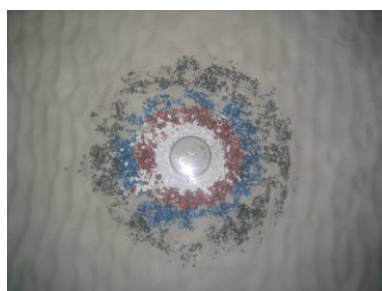
- damage level 1: no movement of the stones
- damage level 2: very limited movement of stones
- damage level 3: significant movement of stones, without failure of the protection
- damage level 4: failure of the protection



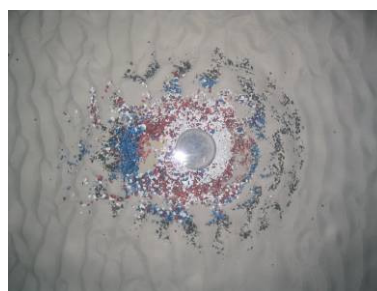
Damage level 1



Damage level 2



Damage level 3



Damage level 4

Figure 4-23: Example of visual damage levels

The scour protection is considered to have failed when the filter is exposed over a minimum area of four armour units ($4D_{50}^2$). This is the failure definition which is used for statically stable scour protections (den Boon et al. (2004)).

For the analysis of the profiler measurements, only the area which is covered by the scour protection (ring with outer diameter $5D$ and inner diameter D) is considered. The scour protection is divided into sub-areas to quantify the damage.

The division into sub-areas is done as shown in Figure 4-24. The scour protection area is divided into 4 rings, corresponding with the 4 coloured rings in the set-up (Figure 4-2). Each ring has a width of 0.05m , corresponding to the radius of the pile. These rings are then further divided into different sub areas, with a size equal to the pile's area. The orientation of the zones is chosen to optimally represent the damage location and is therefore mainly based on the current direction: when considering the direction of the current, damage is located downstream of the pile (see section 4.3.3.5 for a detailed description of the location of the damage).

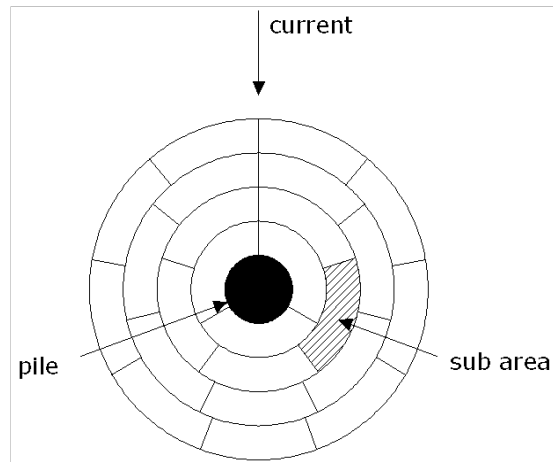


Figure 4-24: Division of the scour protection into sub areas

Dividing the scour protection into different zones of equal surface has several advantages. It facilitates the analysis of the results, as the damage can be located. Secondly the resulting damage becomes independent of the radial extent of the scour protection, as it is the sub area with the highest damage which is withheld to define the damage number. Another main advantage is that it significantly improves the accuracy of the damage number.

When talking about scour protection stability, a clear damage definition is required. Damage after a storm (or test) can be measured by either counting the number of displaced stones, or by comparing the initial profile with the profile after the event. For breakwaters, the two-dimensional damage is quantified by Van der Meer (1988) as $S = A_e/D_{n50}^2$, with A_e the eroded cross-sectional area of the profile and D_{n50} the nominal stone diameter. This implies that the damage S is equal to the number of squares with side D_{n50} which fit into the eroded area A_e . Similar to this definition, the three-dimensional damage of a scour protection can be defined as:

$$S_{3D} = \frac{V_e}{D_{n50}^3} \quad (4.16)$$

with V_e the eroded volume, S_{3D} equals the number of cubes with side D_{n50} which fit into V_e . As the applied stones are small, another definition is used for the quantitative analysis of the damage. The three dimensional damage number $S_{3D,sub}$ is defined per sub area as the ratio of eroded volume V_e and the surface of the sub area times the stone diameter:

$$S_{3D,sub} = \frac{V_e}{D_{n50} \cdot \pi \frac{D^2}{4}} \quad (4.17)$$

It represents the average height which has disappeared over the considered sub area, expressed as a function of the nominal stone diameter D_{n50} (when $S_{3D,sub} = 1$, this implies that the height of the scour protection has decreased over this sub area over a distance equal to $1D_{n50}$). The damage is calculated for each sub area (Figure 4-24) according to equation (4.17) and the damage number S_{3D} is defined as the highest damage which is obtained by considering all the sub areas:

$$S_{3D} = \max(S_{3D,sub}) \quad (4.18)$$

Table 4-7 shows the visual damage level and the damage number for the different tests after 3000 waves, determined with (4.18) and as described above. A visual estimate of the damage can only be made when coloured stones are used. For some tests, this was not the case, leading to missing visual damage levels in Table 4-7. For 1 test (test n° 26), the measurement of the initial profile failed and as a result no measured damage number is available for this test. Figure 4-25 graphically represents the data in Table 4-7, showing that there is a clear relationship between visual damage and measured damage number, defined with equation (4.18). As noted before, it is difficult to measure small damages, leading to an overestimation of the damage number when no movement can be established visually.

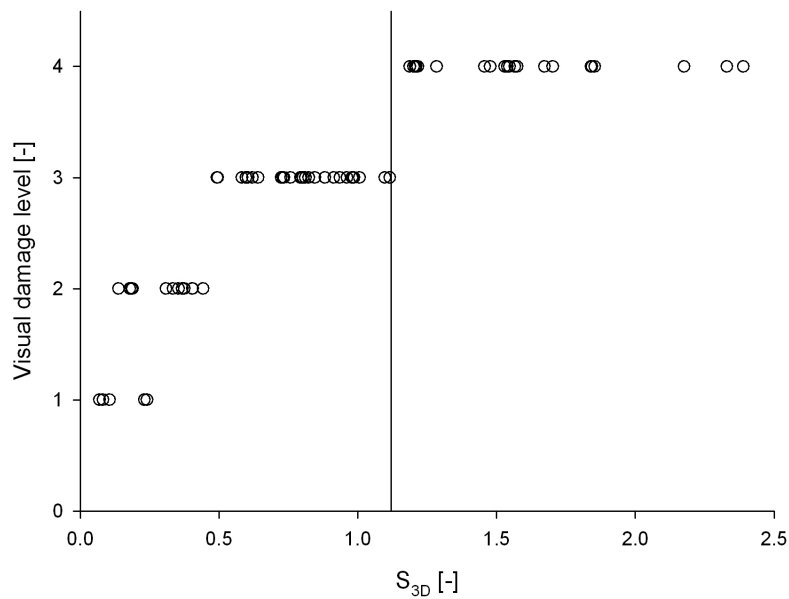


Figure 4-25: Visual damage versus damage number

Table 4-7: Visual damage and damage number for all irregular wave tests

Test n°	S_{3D}	Visual damage level	Test n°	S_{3D}	Visual damage level
[-]	[-]	[-]	[-]	[-]	[-]
1	0.81	3	37	0.73	-
2	0.96	3	38	1.83	4
3	1.21	4	38*	1.66	-
4	1.67	4	39	0.78	-
5	0.11	1	40	1.42	-
6	0.60	3	41	2.19	4
7	0.80	3	43	1.57	4
8	1.12	3	44	0.99	3
11	0.08	1	45	0.88	3
13	0.07	1	46	0.23	1
14	0.24	1	47	0.33	2
15	0.37	2	48	0.49	3
15*	0.31	2	49	0.85	3
15**	0.38	2	50	0.64	3
16	0.73	3	51	1.22	4
17	0.82	3	52	1.21	4
18	1.99	4	53	0.35	2
19	0.94	3	54	0.19	2
20	1.84	4	55	0.58	3
20*	1.53	4	56	0.18	2
20**	1.55	4	58	0.91	3
22	1.28	4	59	0.78	3
24	1.85	4	71	1.57	-
25	0.18	2	72	1.10	-
26	-	4	73	0.98	-
27	1.20	4	74	0.40	-
28	0.72	3	75	0.62	-
29	1.19	4	76	0.98	-
30	1.54	4	77	0.99	-
31	0.14	2	78	0.60	-
32	0.76	3	81	0.73	-
33	1.48	4	82	0.50	-
34	0.44	2	83	0.41	-
35	2.33	4	84	0.40	-
36	2.39	4	85	0.73	-

4.3.3.2. Repeatability

When carrying out model tests to develop a prediction formula, repeatability of the tests is of the utmost importance. Both the reproducibility of the loading conditions (waves and current) and of the damage are essential.

Some tests were repeated (once or twice) to get a view of the repeatability of the tests. These were tests 15, 20 and 38.

In repeating the tests, we aspired to reproduce the wave characteristics of the tests exactly by using the same time series for the elevations. In Figure 4-26, part of the measured elevations during test 15, which was performed three times, are presented. The wave elevations are reproduced very well, even though a small difference in the applied flow velocities was present. The wave characteristics used for the tests are equal for all three tests and were taken to be the wave characteristics at the location of the pile, when the pile was not present in the flume.

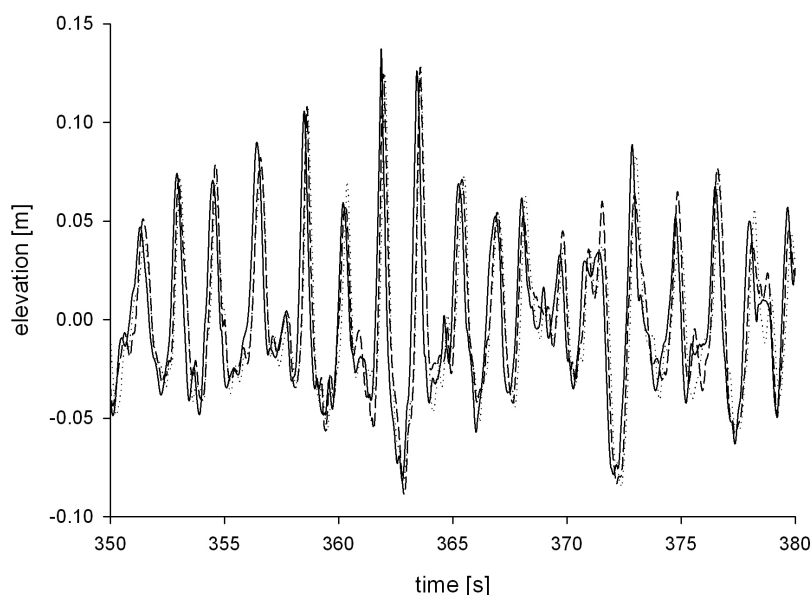


Figure 4-26: Fraction of time series elevations for test 15

As mentioned above, the repeatability of the steady flow velocity is not perfect. Therefore, the flow velocity which was measured during the test is used for the analysis. However a small difference in flow velocity does not influence the wave characteristics (H_{m0} and T_p).

For the reproducibility of the damage, two aspects need to be discerned. Both the stone movement due to flow action and damage measurement should not be prone to large variations. To assess the latter, the measurement of the bed profile after 1000 waves for test 29 can be used. Due to problems with the profiler, the measurement of the bed profile had to be repeated three times. Each time, the zero settings of the profiler were changed, possibly resulting in small horizontal and vertical offsets. The ensuing reproducibility estimate of the profiler's damage measurements therefore underestimates the accuracy, as in

most cases, no offset differences (certainly horizontal) are to be expected. Figure 4-27 shows a cross section perpendicular to the flow (left) and parallel with the flow (right). The damage number for the three repetitions (according to equation (4.18)) is $S_{3D} = 0.92, 0.95$ and 0.85 , which leads to an average value for the damage of 0.907 . As mentioned in section 4.2, the accuracy of the profiler measurement is limited due to the continuous measurements along the width of the wave flume. The accuracy of the measurement lies within the expectations of the accuracy of the profiler, although better results are to be expected if the zero settings were to remain unaltered.

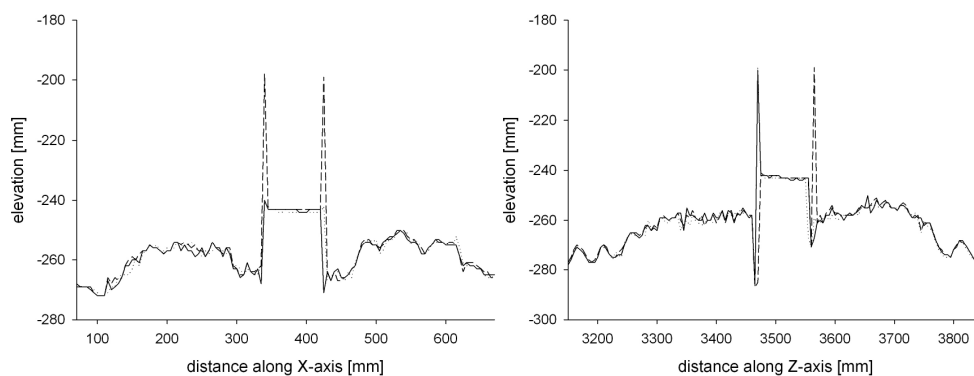


Figure 4-27: Repetition of profiler measurement for test 29, cross sections after 1000 waves

Considering the reproducibility of the damage, Figure 4-28 and Figure 4-29 show the pictures of the repeated tests 15 and 20 after 3000 waves. The damage numbers are, for test 15: $S_{3D} = 0.42, 0.37$ and 0.42 , when no filter is applied to the measurements. For test 20, the respective damage numbers are $S_{3D} = 1.84, 1.57$ and 1.57 .

For test 15, the damage seems very reproducible (visual damage level 2), and the difference in damage number is limited. For test 20 (visual damage level 4), the damage development differs more. It can indeed be seen from Figure 4-29 that the damage is considerably higher for the first test. No explanation for the high damage was found, as the flow velocity which was measured is not higher than it is for the other tests. Also during the analysis, the highest damage number seems to form some kind of outlier compared to all the other results. Possibly something went wrong during the placement of the material (e.g. the grading was not well mixed, the layer was placed too thin locally...). All tests do however categorize under damage level 4, as the geotextile filter is clearly visible in all cases. The repeatability of tests with high damage numbers is considered to be less good compared to damage for small damage numbers.

Test 38 was repeated to investigate the repeatability of the tests in absence of a filter. The test was repeated with uncoloured stones, so a visual comparison of the tests is not possible. The damage numbers for the two tests are $S_{3D} = 1.84$ and 1.74 , or an average of 1.79 , with a standard deviation of 0.05 . This lies

within the accuracy of the profiler measurements and the test is thus considered to be reproducible.

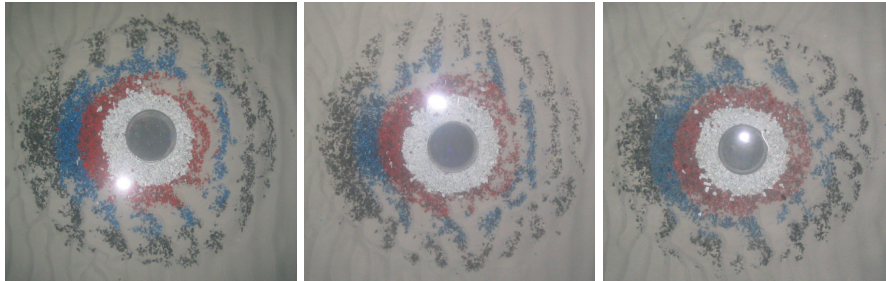


Figure 4-28: Damage after 3000 waves for repeated test 15

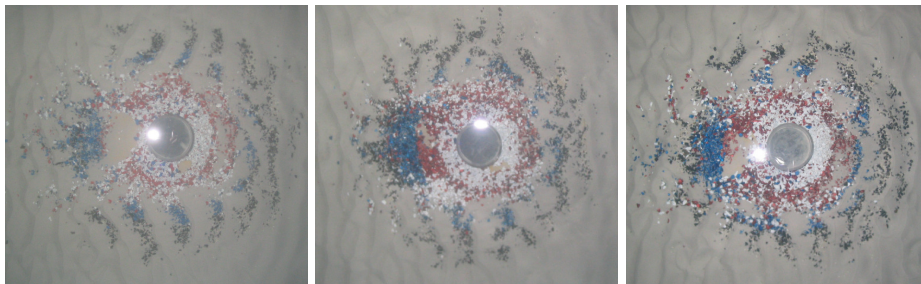


Figure 4-29: Damage after 3000 waves for repeated test 20

4.3.3.3. Acceptable damage criterion

For a statically stable scour protection, the scour protection is considered to have failed when the filter is exposed over a minimum area of four armour units ($4D_{50}^2$). When no filter is applied, it is assumed that the scour protection has failed when the same volume of stones is removed, required to disappear for failure of the statically stable scour protection.

From Figure 4-25, it can be deduced that the damage number S_{3D} at which the transition between damage level 3 (movement, but no failure) and damage level 4 (failure) is noticed is 1.12. One could say that for damage numbers higher than 1.1, damage is no longer acceptable. However, the acceptable damage level will also depend on the accuracy of the predicted damage and is further discussed in section 4.3.4.

When a dynamically stable profile is aspired, a higher damage number could be acceptable. Of main importance is that damage does not progress over time. The term "failure" which is used to describe damage level 4 is no longer applicable, but a representative profile should be described (Van der Meer (1988)). The damage development as a function of the number of waves (section 4.3.3.4.1) indeed leads to the suspicion that such a profile would develop: damage initially develops quite fast and the damage rate decreases with the number of waves. However, the geotextile filter is a fixed boundary and does not allow sand to be removed from the exposed area, which means that

the maximum damage is achieved when all stones from one sub area are removed. The maximum damage number in this case is equal to the thickness of the scour protection (expressed as times the nominal stone size). When on the other hand no filter or a granular filter is applied, it is likely that bed material will be removed at the location where no armour material is left. This has been investigated by extending some of the tests without filter or a granular filter. For test 41, in which a granular filter was used, a large current velocity was applied after the last test. A flow velocity $U_c = 0.32$ m/s (water depth $d = 0.2$ m) was maintained during 3 hours. At the end of test 41, the damage at the side of the pile was found to have increased significantly. Although the damaged area behind the pile was backfilled during the 3 hour test with large steady current, a significant scour hole developed beside the pile. The depth of the scour hole was approximately 3cm deep, leading to a value of $S/D = 0.3$. The damage after the high flow velocity increased from $S_{3D} = 2.39$ (damage number after 5000 waves) up to $S_{3D} = 3.25$.

Also test 38, in which no filter was used, was extended with an additional test to investigate the stability of the developed profile. First a flow velocity of 0.28 m/s was applied. This did not alter the developed profile. When waves were added to the maintained steady current velocity, a significant scour hole developed both in front of and beside the pile (significant wave height $H_{m0} = 0.12$ m and peak wave period $T_p = 1.7$ s). Figure 4-30 shows the measured sections parallel with the flow (right) and perpendicular to the flow (left) which go through the point with maximum scour depth. The initial profile, the final profile and the profile after the additional test are plotted, showing clearly that scour occurred. The damage after 500 additional waves increased from $S_{3D} = 1.70$ (damage number after 5000 waves) up to $S_{3D} = 5.23$.

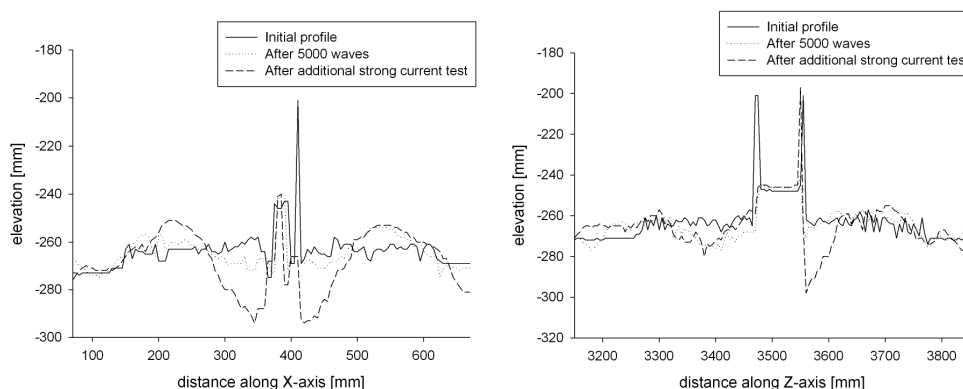


Figure 4-30: Cross-sectional plane for test 38 (initial profile, profile after 5000 waves and profile after additional test). left: perpendicular to the flow, right: parallel with the flow

A high flow velocity (0.3m/s) was also imposed on the scour protection after test 37, which had limited damage after 5000 waves. Visually, no difference could be seen before and after the high flow velocity was applied (no clear scour pattern developed). The profile was therefore not measured after the high flow velocity.

The tests described above show that for large current velocities, damage increases and a scour hole develops when the armour layer has initially failed. It was found that this situation is not acceptable as it could lead to the progressive failure of the scour protection. A damage level "4" is therefore not acceptable and the development of a dynamically stable profile is not possible for the applied scour protection with thickness $2.5D_{n50}$.

The development of a dynamically stable profile might be possible when a thicker scour protection armour layer is used and when the filter or bed material is not exposed during the formation of the profile. In section 4.3.3.4.2 the influence of an increased thickness is discussed. This topic requires more research before any conclusions can be drawn.

4.3.3.4. Influence of governing variables

Generally, governing variables can be classified into variables related to environmental conditions and variables related to the structure's characteristics (chapter 3, section 3.2).

Table 4-8 and Table 4-9 list the governing environmental and structural variables for this test series and it is indicated whether the variables are varied during the tests or not. The influence (both of the varied and unvaried parameters) on the damage development is described in this section.

Table 4-8: Environmental parameters

Parameter	Dimension	Description	Variation
U_c	m/s	average flow velocity	Yes
d	M	water depth	Yes
H_s	M	significant wave height	Yes
T_p	S	peak period	Yes
N	-	number of waves	Yes
ρ_w	kg/m ³	water density	No
ν	m ² /s	kinematic viscosity	No
G	m/s ²	acceleration due to gravity	No
α	°	Angle of wave attack: following waves (0°) or opposing waves (180°)	Yes
	-	spectral shape	No
	-	groupiness of waves	No

Table 4-9: Structural parameters

Parameter	Dimension	Description	Variation
D	M	pile diameter	No
D_{n50}	M	Median stone diameter of scour protection top layer	Yes
D_{85}/D_{15}	-	Ratio of 85% stone diameter to 15% stone diameter of scour protection	Yes
ρ_s	kg/m ³	stone density	Yes
t_s	M	thickness of armour layer	Yes
E	M	extension of scour protection	No
Type of foundation	-	monopile, tripod, gravity based...	No
Construction method	-	scour protection placed on top of the original bed or placed in a pit	No
Filter type	-	bed material characteristics	No
	-	geotextile, granular filter, no filter	Yes
	-	shape of stones	No
	-	Mechanical strength of stones	No

4.3.3.4.1. Influence of environmental parameters

Influence of flow velocity

The average flow velocity U_c in the tests was varied between 0m/s and 0.315m/s. When assuming a length scale of 1/50 and Froude scaling, this leads to a maximum prototype velocity of 2.23 m/s. The target average velocities were 0m/s (no current), 0.07 m/s, 0.14 m/s, 0.21 m/s and 0.28 m/s.

The influence of the average flow velocity on the damage depends both on the magnitude of the flow velocity and on the stone size:

- For the smallest stone size ($D_{n50} = 3.5\text{mm}$) large current velocities appear to significantly influence the damage level (target $U_c > 0.21$ m/s). Figure 4-31 compares test 14 and test 22, which have the same target wave characteristics but a different average flow velocity (0.164 m/s and 0.230 m/s). The pictures show that, whereas almost no movement can be seen for test 14, the scour protection failed for test 22.
- For the two larger stone sizes, the influence of large average current velocities on the damage is less pronounced, though still present. Figure 4-32 shows the damage after 3000 waves for test 53 and 55, which again have the same target wave conditions, but a differing average current velocity (0.156 m/s and 0.221 m/s). The pictures do show some influence of the flow velocity on the damage level, albeit less than for the smallest stone size.

For all stone sizes, relatively small current velocities (target $U_c = 0.07$ m/s and 0.14 m/s) do not significantly affect the damage. Figure 4-33 compares the pictures taken at the end of test 1 and test 6, which have the same target wave

conditions. Test 1 is a wave alone case, whereas test 6 has an average current velocity of 0.080m/s.

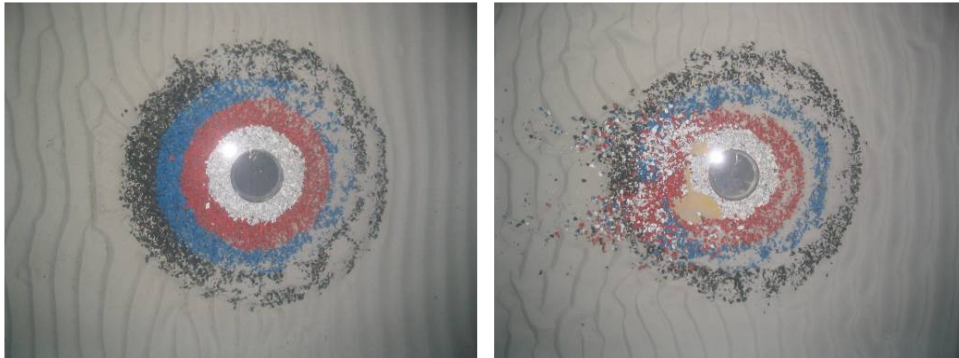


Figure 4-31: Influence of large current velocities on the damage after 3000 waves: $D_{n50} = 3.5\text{mm}$, $d = 0.40\text{m}$: test 14 ($U_c = 0.164 \text{ m/s}$, $H_s = 0.088\text{m}$, $T_p = 1.42\text{s}$) versus test 22 ($U_c = 0.23 \text{ m/s}$, $H_s = 0.083\text{m}$, $T_p = 1.42\text{s}$)

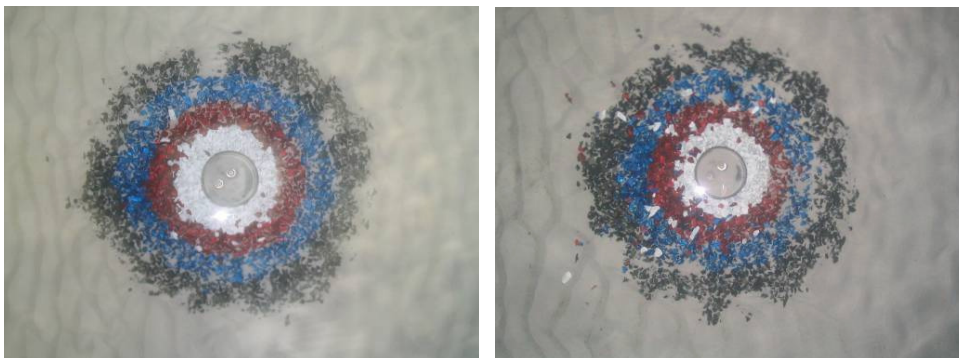


Figure 4-32: Influence of large current velocities on the damage after 3000 waves: $D_{n50} = 7.2\text{mm}$, $d = 0.40\text{m}$: test 53 ($U_c = 0.156 \text{ m/s}$, $H_s = 0.145\text{m}$, $T_p = 1.71\text{s}$) versus test 55 ($U_c = 0.221 \text{ m/s}$, $H_s = 0.140\text{m}$, $T_p = 1.71\text{s}$)

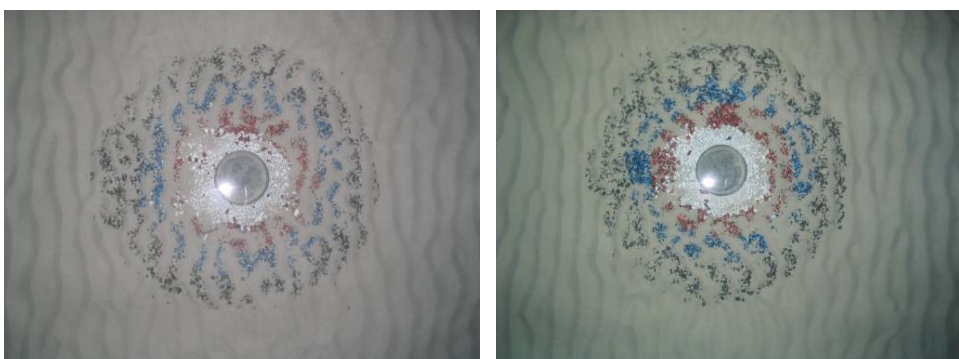


Figure 4-33: Influence of small current velocities on the damage after 3000 waves: $D_{n50} = 3.5\text{mm}$, $d = 0.40\text{m}$: test 3 ($U_c = 0\text{m/s}$, $H_s = 0.139\text{m}$, $T_p = 1.45\text{s}$) versus test 8 ($U_c = 0.080\text{m/s}$, $H_s = 0.135\text{m}$, $T_p = 1.42\text{s}$)

Figure 4-34 plots the damage number as a function of the flow velocity for a few comparable situations (same wave characteristics and stone gradings), demonstrating again the results described above. When two tests with a different flow velocity have the same target wave characteristics, the measured wave height will always be lower for a larger current velocity (see appendix IV). In case of test 3 - 8 - 19, this even leads to a lower damage for the highest current velocity ($U_{c,target} = 0.14$ m/s), possibly due to the significant decrease in wave height. In all cases, the damage is even slightly smaller when a small current is superimposed on a certain wave train. Although this could be due to the small decrease in wave height, the difference lies within the accuracy of the measurements.

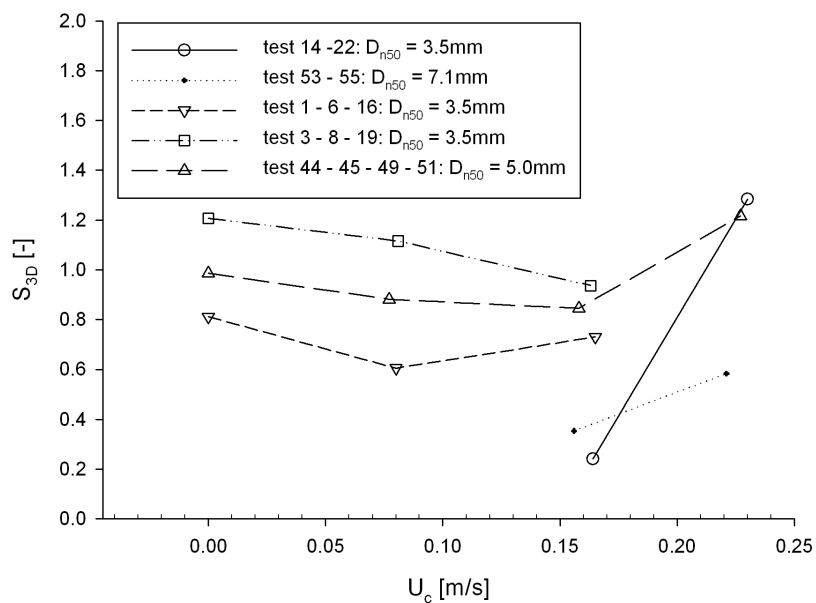


Figure 4-34: Influence of large current velocities on damage number

Influence of wave height

The tested range of wave heights lies between 0.050m and 0.168m (2.5m and 8.4m on prototype scale). The wave height has a significant influence on the damage, whereby increasing wave height leads to increasing damage, when the other variables (water depth, current velocity, wave period and stone size) are kept constant. Figure 4-35 and Figure 4-36 show some pictures of the damage after 3000 waves, comparing tests with increasing wave height for scour protections with a median stone diameter of respectively $D_{n50} = 3.5$ mm and $D_{n50} = 5.0$ mm.

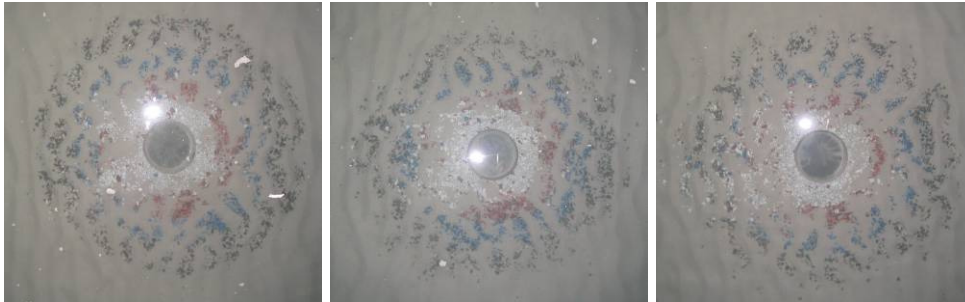


Figure 4-35: Influence of wave height on the damage after 3000 waves, $D_{n50} = 3.5\text{mm}$, $U_c = 0\text{m/s}$, $T_p = 1.71\text{s}$, $d = 0.40\text{m}$: test 2 (left, $H_s = 0.125\text{m}$), test 3 (centre, $H_s = 0.141\text{m}$) and test 4 (right, $H_s = 0.156\text{m}$)

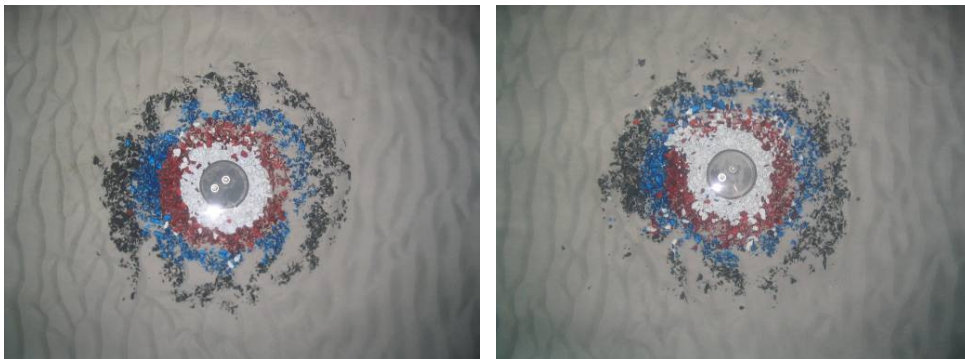


Figure 4-36: Influence of wave height on the damage after 3000 waves, $D_{n50} = 5.0\text{mm}$, $U_c = 0.16\text{m/s}$, $T_p = 1.71$, $d = 0.40\text{m}$: test 48 (left, $H_s = 0.130\text{m}$) versus test 4 (right, $H_s = 0.145\text{m}$),

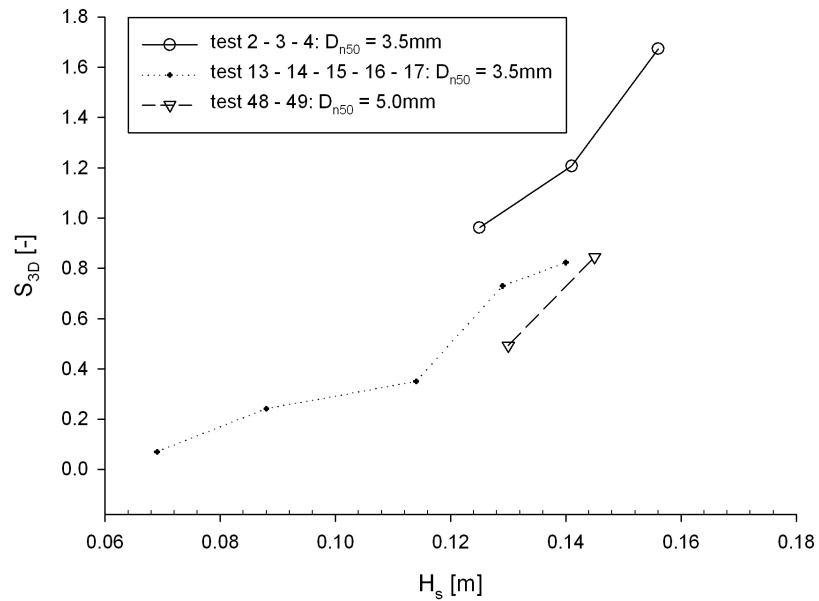


Figure 4-37: Influence of significant wave height on damage number

Figure 4-37 plots the damage number as a function of the significant wave height H_s for three different situations. For all cases, the measured damage increases as a function of the significant wave height.

Influence of wave period

The peak wave period which was used throughout the tests varied between 1.16s and 1.79s (8.2s and 12.65s on prototype scale). Most tests were performed with a peak wave period of 1.42s or 1.71s. Analogous to the wave height, damage increases for increasing peak wave periods. Figure 4-38 and Figure 4-39 compare the damage after 3000 waves for two tests which only differ through the applied peak wave period. Both for the test with $D_{n50} = 3.5\text{mm}$ (Figure 4-38) and $D_{n50} = 5\text{mm}$ (Figure 4-39), the damage increases significantly with the applied wave period, for the same significant wave height.

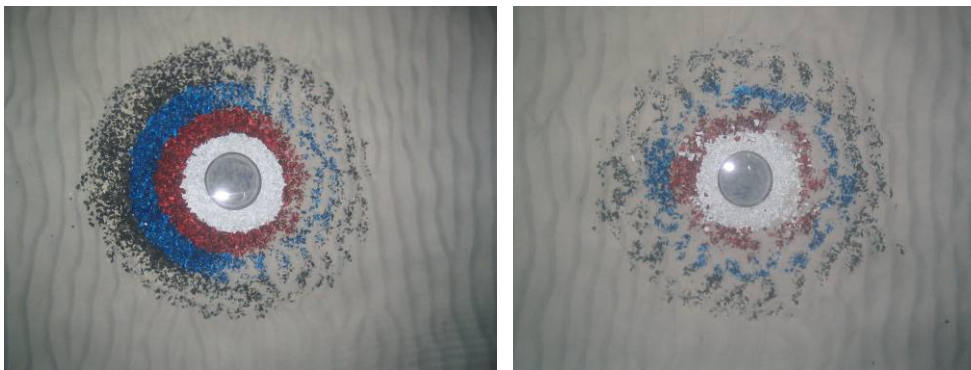


Figure 4-38: Influence of wave period on the damage after 3000 waves, $D_{n50} = 3.5\text{mm}$, $U_c = 0.077\text{m/s}$, $H_s = 0.120\text{m}$, $d = 0.4\text{m}$: test 5 (left, $T_p = 1.16\text{s}$) versus test 7 (right, $T_p = 1.71\text{s}$)

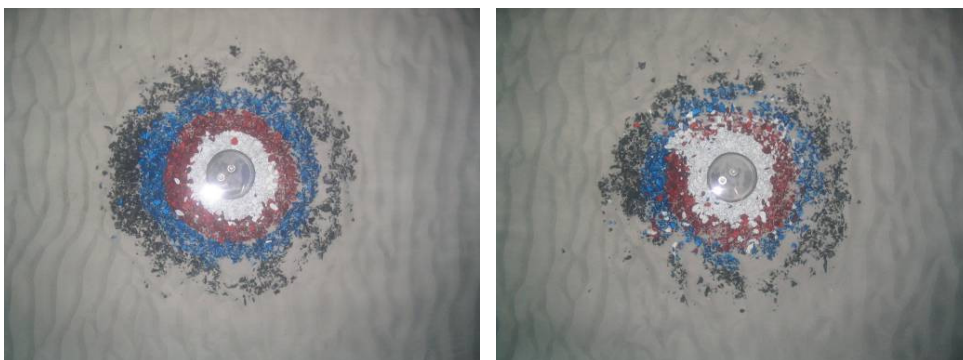


Figure 4-39: Influence of wave period on the damage after 3000 waves, $D_{n50} = 5.0\text{mm}$, $U_{c, target} = 0.14\text{m/s}$, $d = 0.4\text{m}$: test 47 (left, $T_p = 1.40\text{s}$, $H_s = 0.140\text{m}$) versus test 49 (right, $T_p = 1.71\text{s}$, $H_s = 0.145\text{m}$)

Figure 4-40 plots the damage number as a function of the peak wave period T_p for three different situations. For all cases, the measured damage increases as a function of the peak wave period.

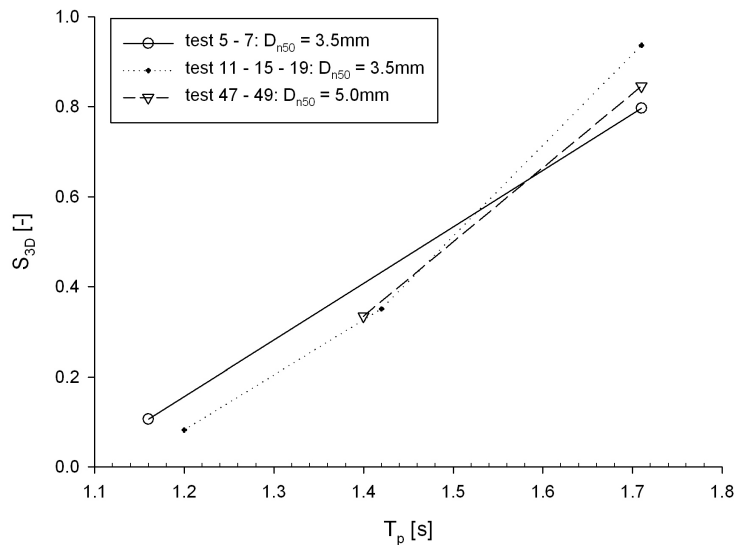


Figure 4-40: Influence of peak wave period on damage number

Influence of water depth

A water depth of 0.40m was used throughout most of the tests (20m in prototype situation). A few tests were performed with a smaller water depth of 0.20m, mostly to generate higher flow velocities. The water depth has a significant influence on the damage development of the scour protection. Damage increases with decreasing water depth. Figure 4-41 shows the increase in damage when the water depth changes from 0.4m to 0.2m, while flow velocity and wave period are approximately equal. The increase in the damage is attributed to several causes. First of all, orbital velocity is a function of water depth so that when given a certain wave height and period the orbital velocity at the bottom will be smaller for larger water depths. The converse of this implies that the orbital velocity near the bottom increases for smaller water depths. Secondly, the bed shear stress which is caused by the flow velocity increases for decreasing water depths (chapter 1).

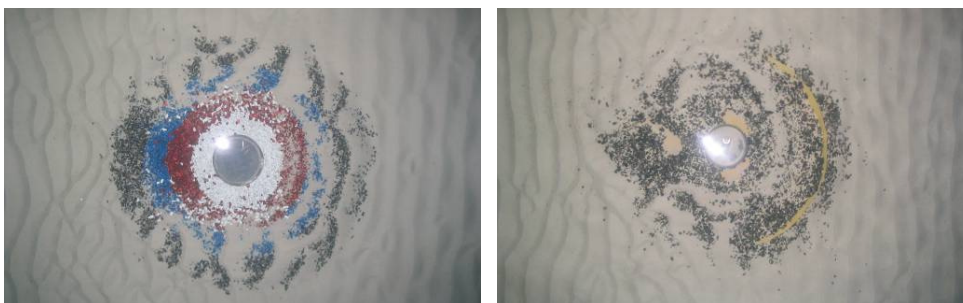


Figure 4-41: Influence of water depth on the damage after 3000 waves, $D_{n50} = 3.5\text{mm}$, $U_{c, target} = 0.14\text{m/s}$, $T_p = 1.71\text{s}$: test 32 (left, $d = 0.4\text{m}$; $H_s = 0.111\text{m}$) versus test 43 (right, $d = 0.2\text{m}$; $H_s = 0.080\text{m}$)

Influence of wave induced bottom velocity

The influence of wave height, wave period and water depth can be translated into an influence on the orbital velocity. Figure 4-42, Figure 4-43 and Figure 4-44 compare different tests which have the same orbital velocity near the bottom, though wave period (and/or) water depth vary. The pictures show that a slight influence of the wave period remains, while the water depth seems to have a large residual influence on the damage.

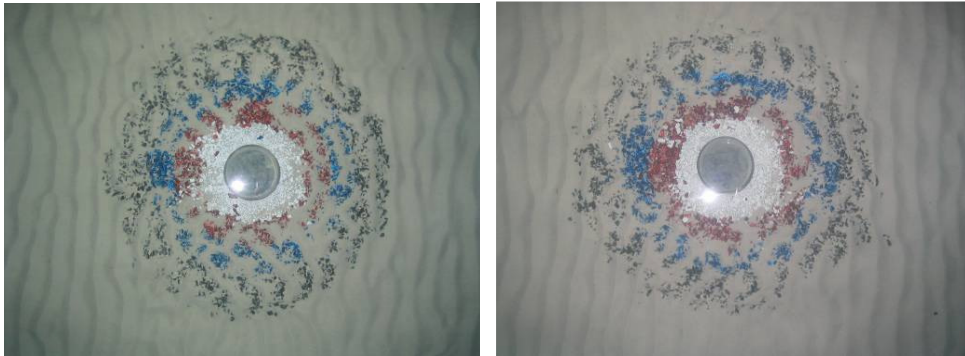


Figure 4-42: Influence of orbital velocity on the damage after 3000 waves, $D_{n50} = 3.5\text{mm}$, $U_{c, \text{target}} = 0.07 \text{ m/s}$, $d = 0.4\text{m}$: test 6 (left; $H_s = 0.135\text{m}$; $T_p = 1.42\text{s}$; $U_m = 0.151$) versus test 7 (right; $H_s = 0.120\text{m}$; $T_p = 1.71\text{s}$; $U_m = 0.146$)

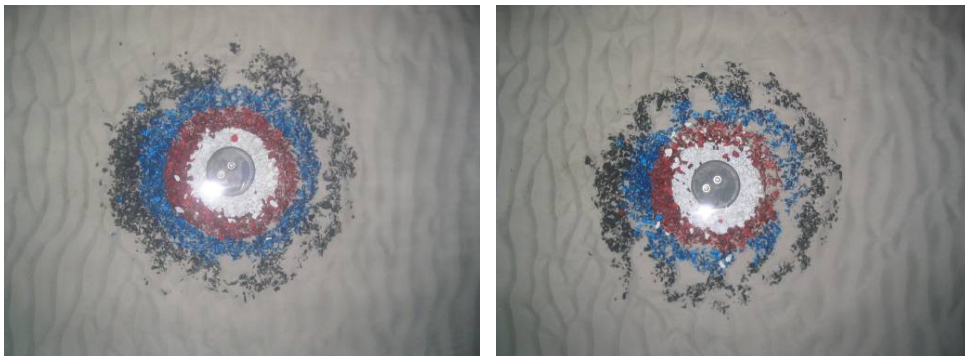


Figure 4-43: Influence of orbital velocity on the damage after 3000 waves, $D_{n50} = 5\text{mm}$, $U_{c, \text{target}} = 0.14 \text{ m/s}$, $d = 0.4\text{m}$: test 47 (left; $H_s = 0.140\text{m}$; $T_p = 1.40\text{s}$; $U_m = 0.160$) versus test 48 (right; $H_s = 0.130\text{m}$; $T_p = 1.71\text{s}$; $U_m = 0.161$)

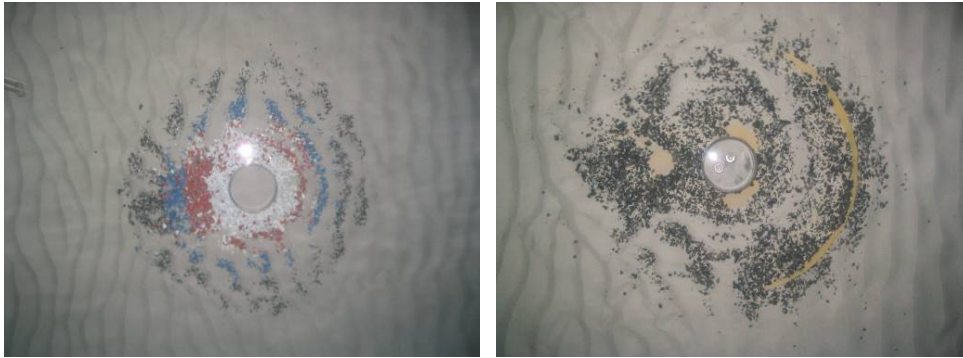


Figure 4-44: Influence of orbital velocity on the damage after 3000 waves, $D_{n50} = 3.5\text{mm}$: test 17 (left; $U_c = 0.161\text{m/s}$; $H_s = 0.140\text{m}$; $T_p = 1.40\text{s}$; $d = 0.4\text{m}$; $U_m = 0.160$) versus test 43 (right; $U_c = 0.172\text{ m/s}$; $H_s = 0.080\text{m}$; $T_p = 1.79\text{s}$, $d = 0.2\text{m}$; $U_m = 0.159$)

Figure 4-45 shows the increase in damage number as a function of increasing orbital velocity for tests with the same target flow velocity and stone diameter. The plot shows a more than linear increase in damage number with increasing orbital velocity.

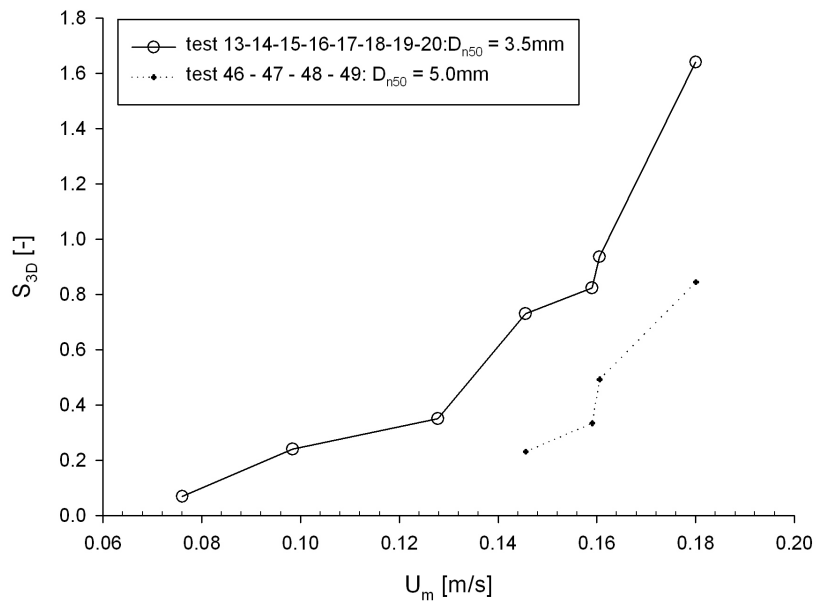


Figure 4-45: Influence of near bottom orbital velocity on damage number

Influence of flow direction

As the tests were performed in a wave flume, only two flow directions can be tested, a flow following or opposing the waves. The test results show a significant influence of the flow direction on the damage development, with considerably higher damage when the flow opposes the waves (Figure 4-46 to

Figure 4-48). This is against the expectations, as one would expect the same damage in both situations for linear waves (as the orbital velocity is the same in both directions) or a higher damage for a current following the waves in case of non-linear waves, as in this case the orbital velocity under the wave peak is higher than under the wave trough.

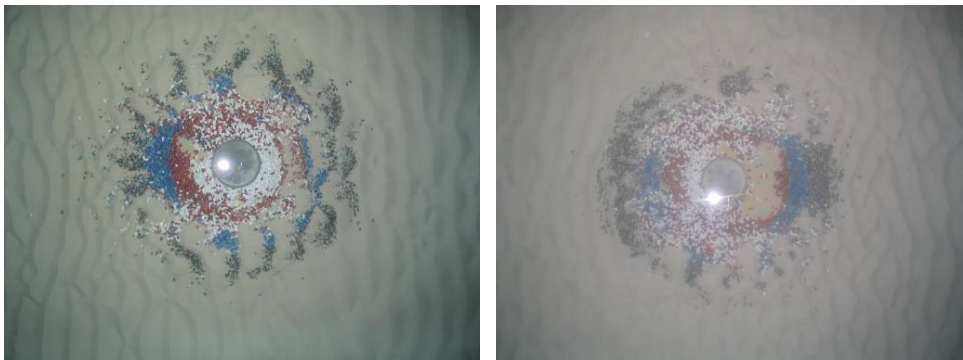


Figure 4-46: Influence of flow direction on the damage after 3000 waves, $D_{n50} = 3.5\text{mm}$, $d = 0.4\text{m}$: test 33 (left; $U_c = 0.161\text{m/s}$; $H_s = 0.145\text{m}$; $T_p = 1.71\text{s}$) versus test 36 (right; $U_c = -0.147\text{ m/s}$; $H_s = 0.134\text{m}$; $T_p = 1.71\text{s}$)

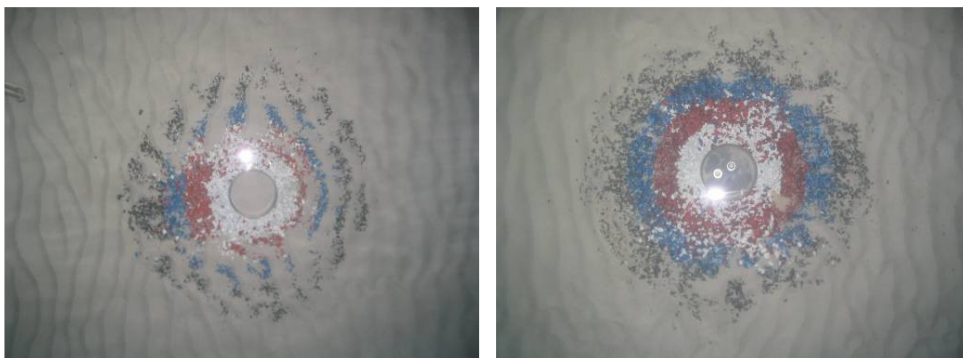


Figure 4-47: Influence of flow direction on the damage after 3000 waves, $D_{n50} = 3.5\text{mm}$, $d = 0.4\text{m}$: test 17 (left; $U_c = 0.161\text{m/s}$; $H_s = 0.140\text{m}$; $T_p = 1.40\text{s}$) versus test 27 (right; $U_c = -0.137\text{ m/s}$; $H_s = 0.134\text{m}$; $T_p = 1.37\text{s}$)

Figure 4-48 shows the influence of the flow direction in three cases. For relatively small waves (test 15 and 25), the flow direction has virtually no influence (note that the load is somewhat smaller in test 25, leading to a slightly smaller damage number). For the two other cases, the magnitude of the influence of the flow direction seems to depend on the wave period, with an increasing influence for an increasing wave period. In both cases however, the damage number is larger for waves opposing the current. When looking at Figure 3-6, one can see that for the same wave height, waves will sooner be non-linear for larger wave periods or smaller water depths. Wave non-linearity can therefore be the cause of this unexpected influence of the flow direction. Figure 3-7 shows how it is possible that damage is larger for an opposing current. When waves follow a current, the orbital velocity under the wave crest

has the same direction as the flow velocity, whereas for a flow opposing the waves, it is the orbital velocity under the wave trough which has the same direction as the flow. When using non-linear wave theories, the orbital velocity is higher under the wave crest, but it's duration is much shorter than the orbital velocity near the wave trough. As mentioned above, when considering the orbital velocity, the wave period has an important influence on the damage development, with increasing damage for an increasing wave period. This is also discussed in chapter 1, where it is noted that the KC number (and thus the wave period) determines whether vortex shedding occurs or not. Figure 1-11, reproduced from Sumer and Fredsøe (2002), shows that indeed, a larger vortex is formed under the wave trough than under the wave peak. Sumer and Fredsøe (2002) ascribe this phenomenon to the asymmetry between the two half periods of the waves.

Another unexpected aspect is that the flow velocity does seem to have an influence on the damage development when the flow is opposing the waves, even for a target flow velocity of 0.14 m/s (in contrast to the flow following the waves). An explanation could be similar to what Sumer and Fredsøe (2001) found for scour development. They found that when a current was superimposed on waves, scour increased, while the increase depended both on the KC number as well as on the relative importance of the flow velocity. As KC numbers are limited in our tests (varying between 1 and 3.6) it is possible that the influence of the flow is only noted when or the KC number or the flow velocity is sufficiently large. Due to the non-linearity, discussed above, it is possible that KC numbers are higher under the wave trough than under the wave crest, leading to an influence of the flow velocity for smaller absolute values of the flow speed. This topic however requires more research. Its importance is stressed again, as for tidal currents, waves following the current will oppose the current when the tide is reversed.

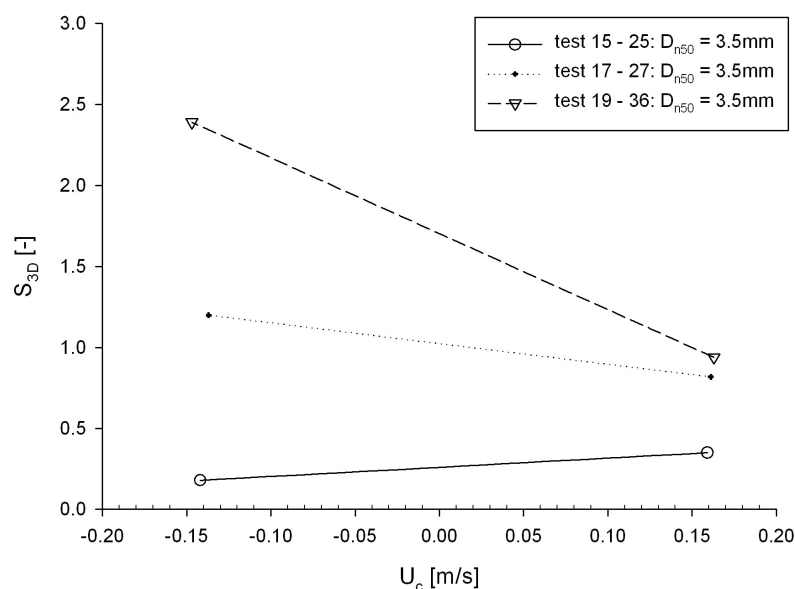


Figure 4-48: Influence of flow direction on damage number

Influence of number of waves

Profiles were measured after 1000 waves, 3000 waves and 5000 waves. The relative damage number is plotted in Figure 4-49 against the number of waves, for all tests with damage number larger than 0.5 (60% of the tests). The relative damage is obtained by dividing the damage number by the damage after 3000 waves. The plot shows both the average values as spreading on the results ($\pm\sigma$). Figure 4-49 shows that the damage increases rapidly in the beginning, while the increase slows down after 3000 waves. The relationship between damage number, S_{3D} and number of waves, N can be described as a power function when N is between 1000 and 5000 waves:

$$S_{3D}(N)/S_{3D}(3000) = aN^b \quad (4.19)$$

in which a and b are curve fitting coefficients. Based on the data of Figure 4-49, the coefficients are found to be 0.129 and 0.254 respectively.

With this function, damage does not reach an equilibrium. Long duration tests should be carried out to find whether a stable damage profile develops and when the damage limit (equilibrium) is reached. Another fit might then be used to assess the influence of the number of waves.

Equation (4.19) leads to a value of 1.12 for average ratio of the damage after 5000 waves and the damage after 3000 waves:

$$S_{3D}(5000)/S_{3D}(3000) = 0.129(5000)^{0.254} = 1.12 \quad (4.20)$$

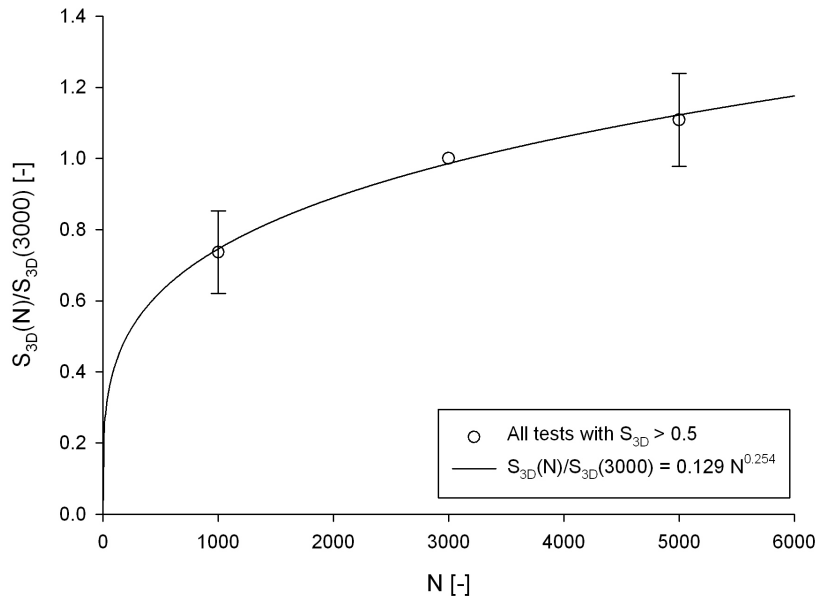


Figure 4-49: Influence of number of waves on damage number

Influence of unvaried environmental parameters

Parameters which are not varied throughout the tests are basically the parameters which are characteristic for the used liquid (water) and parameters typical for the spectral shape or groupiness of the waves. The influence of these parameters could be investigated further, although it is assumed that they have less influence.

4.3.3.4.2. Influence of structural parameters

Influence of stone size

Four different gradings are used throughout the tests, with three different nominal stone diameters D_{n50} . The values of D_{n50} are 3.5mm, 5mm and 7.2mm, and the gradings correspond respectively with the following prototype gradings: 2-80kg, 2-300kg and 80-300kg.

Figure 4-50 compares two tests which differ only through the applied stone size. As can be seen from this figure, the influence of the stone size on the damage is significant.

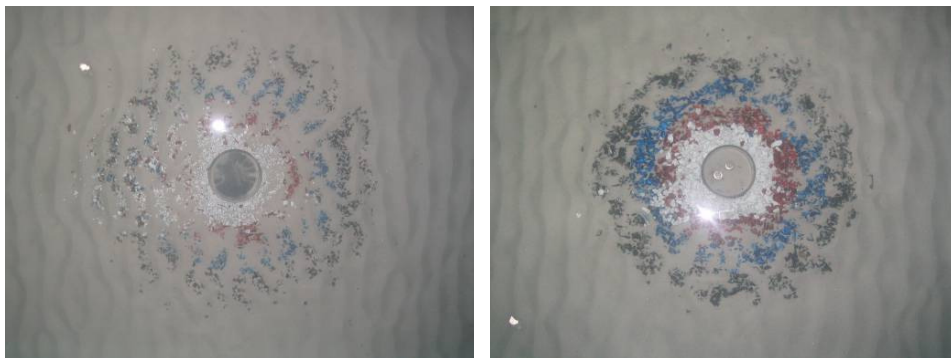


Figure 4-50: Influence of stone size on the damage after 3000 waves, $U_c = 0$ m/s, $H_s = 0.156$ m, $T_p = 1.71$ s, $d = 0.4$ m: test 4 (left; $D_{n50} = 3.5$ mm) versus test 44 (right; $D_{n50} = 5$ mm)

Figure 4-51 shows the damage number as a function of stone size. It shows that for the presented cases damage is inversely proportional to stone size. It can again be noted that for high flow velocities (test 35 and 50), the influence of the stone size is larger than for smaller flow velocities.

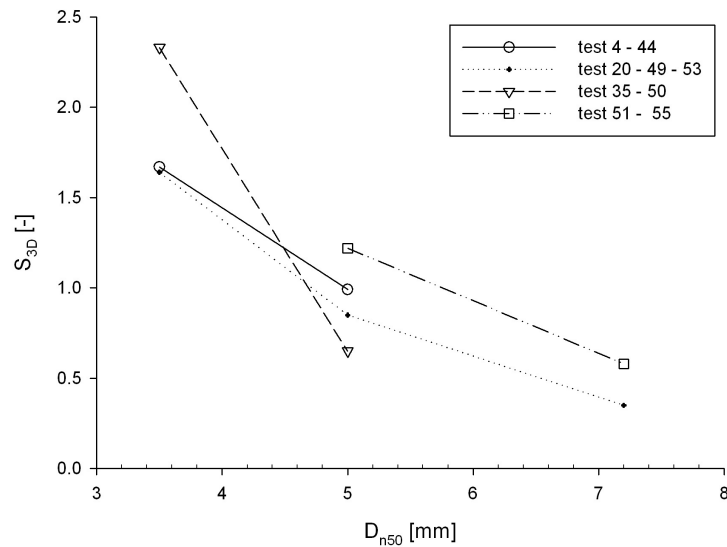
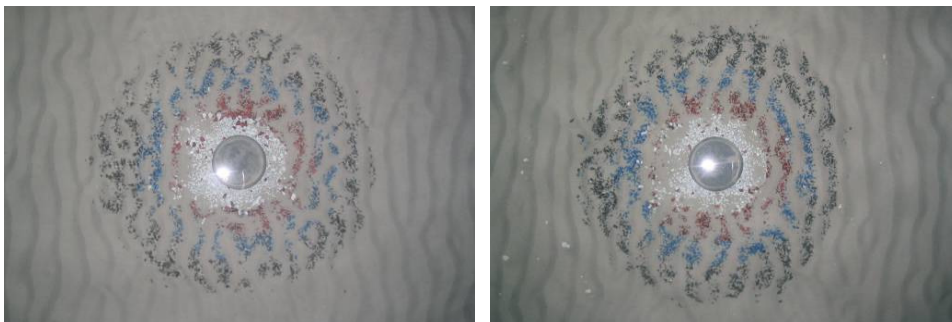


Figure 4-51: Influence of stone size on damage number

Influence of armour layer grading

For the smallest stone size ($D_{n50} = 3.5\text{mm}$), several tests were carried out with two different stone gradings: a wide stone grading ($D_{85}/D_{15} = 2.48$) and a very narrow stone grading ($D_{85}/D_{15} = 1.32$). Figure 4-52 presents the pictures which were taken after 3000 waves for test 1 and test 28. Both tests only differ in the applied stone grading. The visual damage assessment leads to the conclusion that the stone grading does not influence the damage. Figure 4-53 shows the damage numbers for the different tests which were performed under the same conditions. Unlike the initiation of motion, the damage is found to be practically uninfluenced by the stone grading and variations in damage number lie within the measuring accuracy of the profiler. It can therefore be concluded that the grading of the armour layer has no influence on the damage development and that, within the tested range, the armour layer can be described by its nominal diameter D_{n50} .



**Figure 4-52: Influence of stone grading on the damage after 3000 waves,
 $U_c = 0 \text{ m/s}$, $H_s = 0.139\text{m}$, $T_p = 1.45\text{s}$, $d = 0.4\text{m}$, $D_{n50} = 3.5\text{mm}$:
 test 1 (left; $D_{85}/D_{15} = 2.48$) versus test 28 (right; $D_{85}/D_{15} = 1.32$)**

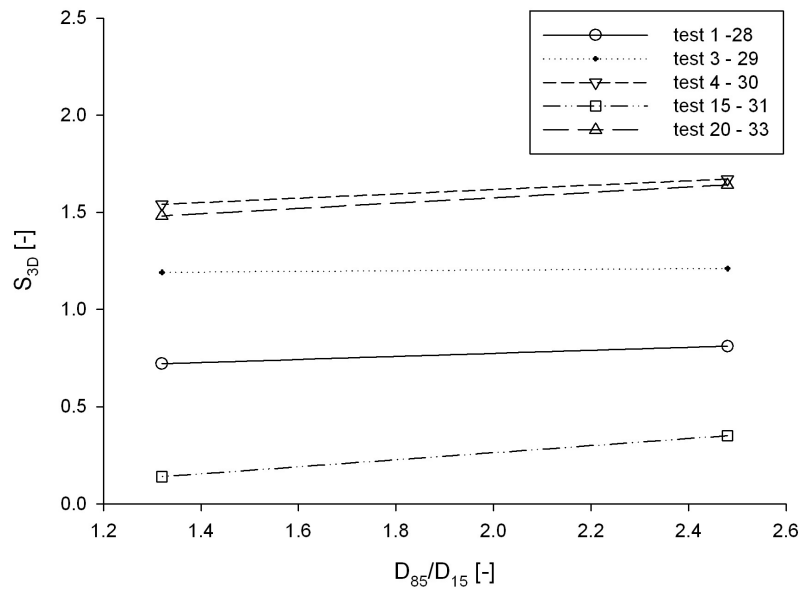


Figure 4-53: Influence of stone grading on damage number, $D_{n50} = 3.5\text{mm}$

Influence of stone density

The tests were performed with stones with two different stone densities. "Normal" stones, which had a density $\rho_s = 2650 \text{ kg/m}^3$ and heavy stones (steel slag) with a density $\rho_s = 3200 \text{ kg/m}^3$. Figure 4-54 shows that damage is in all cases significantly lower for the high density stones.

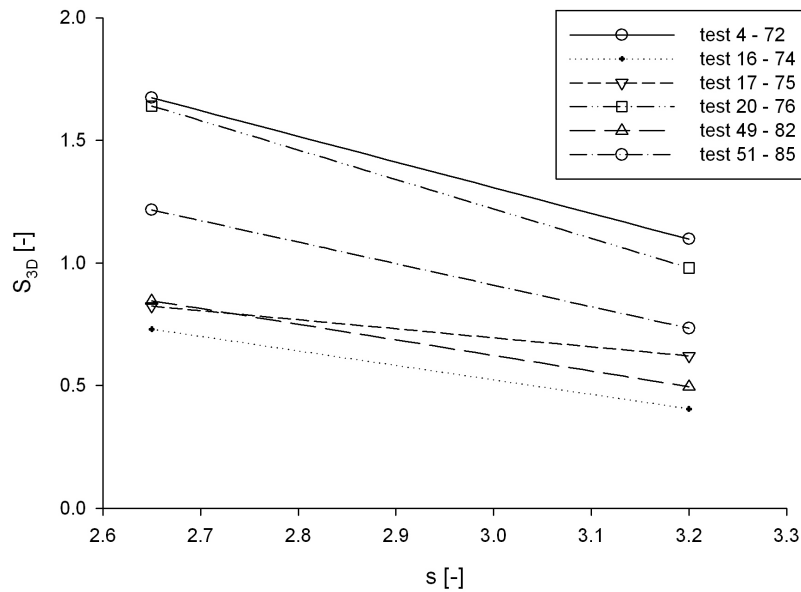


Figure 4-54: Influence of stone density on damage number

Influence of thickness of scour protection

Two tests were repeated with a different thickness for the scour protection. In almost all tests, the thickness of the scour protection was approximately $2.5D_{n50}$. For these two particular tests, the thickness was increased to $3D_{n50}$. As it is likely that the thickness of the armour layer has a larger influence on the damage for a scour protection without a filter as compared to with a geotextile filter, the two tests were performed without filter, where the bed material can disappear once it is exposed by the loss of armour material. The tests with thicker scour protection armour layer are test 39 and 40, which should be compared with test 37 and 38 respectively. The tests are compared in Figure 4-55, which shows that the thickness of the armour layer does not influence the damage for small damage numbers. This could be expected, as the bed material will not be displaced independent of the thickness of the scour protection. When the damage is higher however (and the protection has failed), the damage is significantly reduced for a thicker scour protection, even when the difference in thickness is limited. A more detailed investigation of the influence of the thickness of the scour protection is an interesting topic for further research.

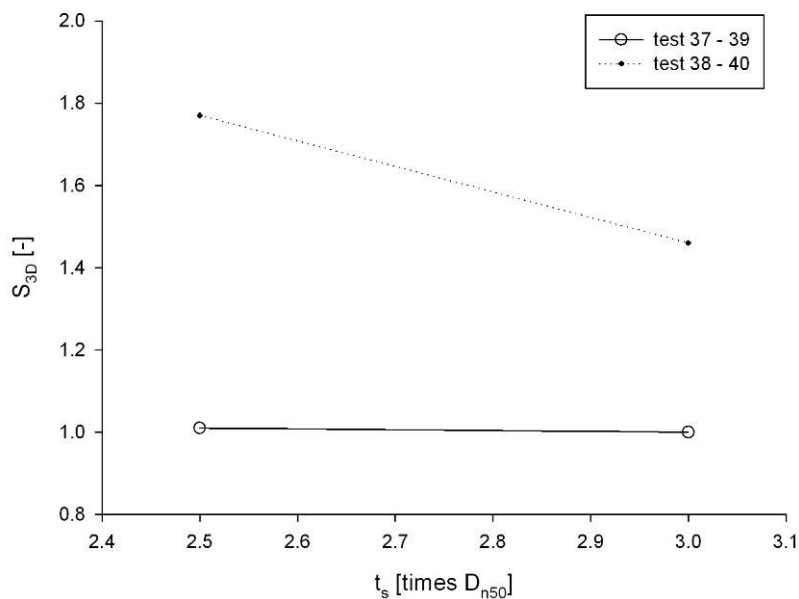


Figure 4-55: Influence of thickness of scour protection on damage number

Influence of filter type

A geotextile filter was used throughout most of the tests. Even though the aim of this test series was not to investigate filter design, the alternative of using no filter or a granular filter was tested. Figure 4-56 shows the influence of the filter type on the damage. As could be expected, the difference in damage number for tests with or without filter and a small damage number lies within the accuracy range and therefore does not differ significantly. This was expected, as the filter avoids bed material to be transported. Due to the difference in scaling of the bed

material, no bed material is lost through the armour layer in case no filter is used. This does however not represent the prototype situation! This means that for the model tests, bed material will only be transported once the armour layer disappears and therefore the filter type does not influence the damage for small amounts of damage.

A significant increase in the damage number is found for test 41, in which a granular filter was applied. The increase in damage number is most likely caused by the higher location of the armour material above the bed, as the filter, which was placed on top of the bed, had a thickness of 1cm. The higher location increases the disturbance of the flow and brings on higher orbital velocities at the top off the scour protection. The increase in damage is also caused by the loss of bed material at the location where the filter (and even bed material) is exposed. It was already noted in section 4.3.3.3 that more research is needed when dynamically stable profiles (in which larger amounts of displacement are allowed) are to be investigated.

An aspect that may influence the damage number when using geotextile filters, is that, when the filter is exposed, the remaining armour stones lie on top of a "smooth" surface and will be more easily displaced, quickly leading to larger exposed areas of the filter. When comparing test 20, with geotextile filter, and test 38, without filter, it appears that for this particular tests, the loss of material due to the exposed bed material in test 38 is approximately of the same magnitude as the increased damage in test 20, caused by the use of a "smooth" geotextile.

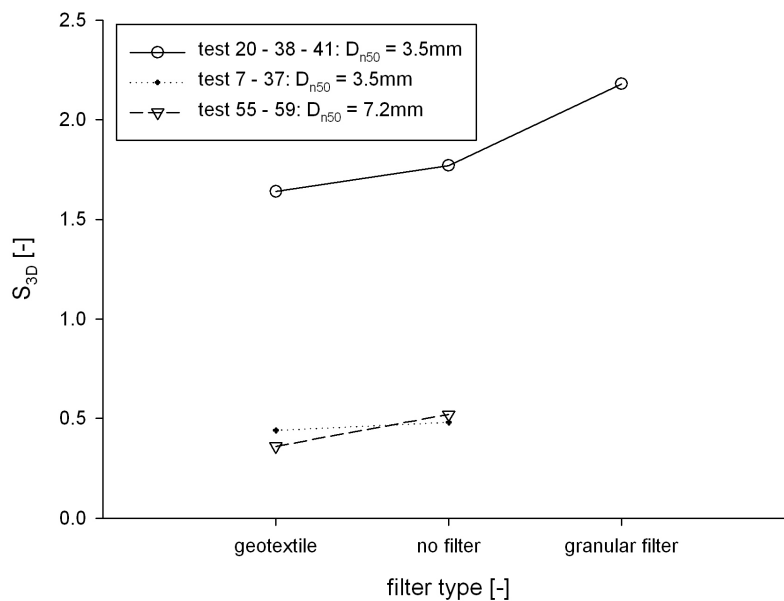


Figure 4-56: Influence of filter type on damage number

Influence of unvaried structural parameters

Structural parameters which are not varied and which most likely will influence the damage development are:

- the pile diameter: Sumer and Fredsøe (1997) show that the pile's diameter has an influence on the disturbance of the flow in case of waves (see chapter 1). It is therefore likely that the diameter of the pile has an influence on the damage development. Further research is required to determine the correct influence of the pile diameter. The formulae derived in 4.2 and 4.3.4 are only valid for pile diameters which do not differ significantly from the tested pile size.
- the type of foundation: the shape of the foundation (monopile, tripod, gravity foundation) significantly influences the disturbance of the flow and it can therefore be expected that it will influence the damage development. More research (physical model tests) would be needed to investigate the influence of this parameter.
- the construction method of the scour protection: the test with the granular filter material showed that the elevation of the bed material may have an influence on the damage development. It is possible that the damage would decrease if the scour protection is placed level with the surrounding seabed. An economical comparison should be made between the additional costs for the dredging of the bed material and the decrease in damage. It is also important to consider the global lowering of the sea bed as it might influence the damage development. Further research on this topic is required.

Unvaried parameters which are not likely to influence the damage number are:

- the scour protections extension: damage to the scour protection is mostly limited to a distance of 1 time the pile diameter from the pile's surface. The largest damage number is always measured in the ring closest to the pile (white ring) or the ring between $0.5D$ and $1D$ from the pile's wall. It is unlikely that the damage of the scour protection close to the pile would be influenced by the radial extension of the scour protection, unless it is made much smaller. The radial extension of the scour protection will however influence the effect of the edge scour on the foundation. Section 4.4 elaborates on this subject.
- the bed material characteristics: as long as the filter works properly, the bed material does not influence the damage to the top armour layer of the scour protection.
- Filter material characteristics: Thompson and Shuttler (Van der Meer (1988)) tested different ratios of the D_{50} of the armour layer and the D_{50} of the filter for the stability of breakwaters. They concluded that it had little influence on the stability of the armour material.
- the strength of the armour material: although the mechanical strength of the armour layer can be important for the material which is used in the prototype situation, the tests are too short to encounter an influence of the mechanical strength of the rock material.

A parameter for which it is unsure whether it would influence the damage is:

- the shape of the armour material: it is possible that the shape of the stones in the armour layer influence the damage number. Specific tests should be performed to pursue this matter.

4.3.3.5. Location of damage

The location of the damage was investigated to assess whether a distinctive profile could be distinguished. It was found that the location of the damage mainly depends on the flow characteristics, leading to the three typical damage profiles shown in Figure 4-57, which represents the damage at the scour protection obtained by subtracting the initial bed profile from the bed profile after a test series. The pile, scour protection and sand ripples can be recognised. The lighter areas indicate erosion of the armour material (i.e. damage), while the darker areas indicate no change or deposition (of sand or scour protection material). Waves are always travelling from bottom to top.

The three different loading cases (waves only, waves following a current and waves opposing a current) clearly lead to three different damage profiles:

- waves only: Figure 4-57 (a) represents a typical wave alone case: damage is present at the sides of the pile, while a less deep lowering is also found in front of the pile. The scour protection is damaged up to a distance of approximately $0.5D$ from the pile. The damage number for the wave alone cases varied between 0.50 (test 82) and 1.67 (test 4), but the same profile was found for all tests. The same damage profile is found in case that a small current is superimposed on the waves, showing that a small steady current does not influence the location of the damage.
- Waves following a current: Figure 4-57 (b) represents a typical damage profile for waves following a significant current: an area behind the pile experiences erosion of the scour protection material and some damage is still found at the edges of the pile. In Figure 4-57 (b), the test with the largest extension of the damage is shown (test 20). The damage extends over a distance of $1.35D$ behind the pile and the eroded area is somewhat wider than the pile diameter. In some cases (test 51, 55 and 59), the damage behind the pile is not located immediately behind the pile, but some spacing exists between the pile and the damage.
- Wave opposing a current: Figure 4-57 (c) represents a typical damage profile for waves opposing a current: the damage is now located in front of the pile (when looking in the travelling direction of the waves). Some damage is also found at the edges of the pile, but never extends further than approximately $0.5D$ from the pile. As for waves following a current, the damaged area in front of the pile is somewhat wider than the pile diameter.

When the flow is sufficiently large, damage shifts from the side region of the pile to the area behind downstream of the pile. This can be attributed to the vortex

shedding which occurs in the case of a steady current. When movement of the stones occurs, stones can be displaced over a longer distance when the combination of flow velocity and orbital velocity is sufficiently large to transport the stones.

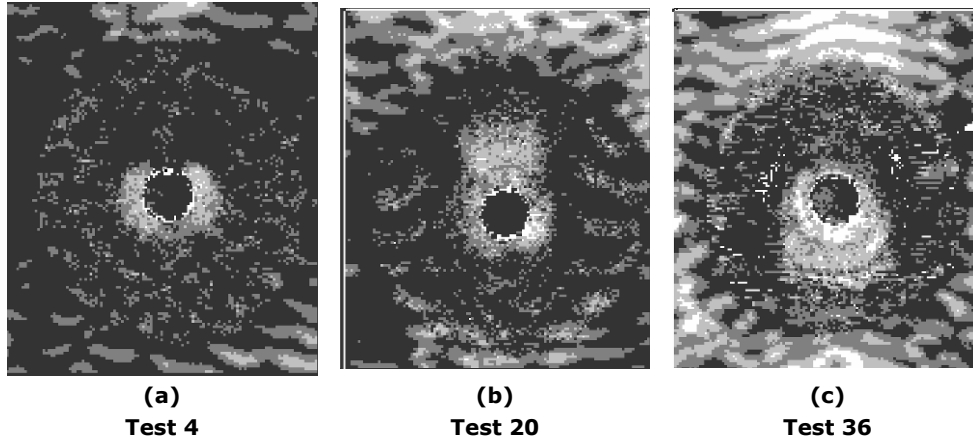


Figure 4-57: Location of damage in a scour protection around a vertical pile.
Measured elevations [mm] (erosion (< 0) and deposition (> 0)) from the bed profiles: ■ : +20 < elevation ≤ 0; ▒ : 0 < elevation ≤ -5; □ : -5 < elevation ≤ -10; □ : -10 < elevation

4.3.4. Derivation of new prediction tool for scour protections around monopile foundations

Most existing design formulae for a statically stable scour protection give the required stone size as a power function of flow velocity or orbital velocity. Equation (4.21) is used in case of a steady current and equation (4.22) in case of waves only (see chapter 3, section 3.3.1).

$$D_s = a \frac{U_c^b}{(\Delta g d)^{b/2}} \quad (4.21)$$

$$D_s = \frac{U_w^c}{T^e (g \Delta)^f} \quad (4.22)$$

with D_s a representative value for the stone size (e.g. the nominal diameter D_{n50}); U_c the steady current velocity; U_w the bottom orbital velocity caused by the waves; g the gravitational acceleration; Δ the relative density of the stones and d the water depth. The constants b and c which are used as a power of the velocity, are equal to 2 or 3, while the parameter e is approximately equal to 1.

The main goal of the prediction formula is to include the damage number and to combine the influence of waves and currents into one equation. The number of

waves N are also incorporated at the end. In this way, a more economical design (stone size) is aspired. An acceptable level for the damage number is already shortly discussed in section 4.3.3.3 and a recommendation will be given, depending on the accuracy by which predictions can be made.

In the Optipile project (E-Connection et al. (2002-2004)), the parameter $Stab$ was used to assess the damage level of the scour protection. This parameter is defined as:

$$Stab = \frac{\theta_{max}}{\theta_{cr}} \quad (3.56)$$

with θ_{max} the Shields parameter for the combined wave and current flow field, determined according to equations (1.31) and (1.2) and θ_{cr} the critical Shields parameter, assumed to be equal to 0.056 (den Boon et al. (2004)). This parameter, calculated for the performed tests is plotted against the visually observed damage in Figure 4-58. In den Boon et al. (2004) the limit $Stab = 0.4155$ is defined as the transition between no movement and movement without failure and the limit $Stab = 0.46$ as the transition between movement without failure and failure. Both limits are included in Figure 4-58. Although some trend can be observed, it seems that the parameter $Stab$ fails to correctly predict the observed damage levels for the new test series. In Whitehouse et al. (2006) it was noted that for another test series, the limits for the parameter $Stab$ should be adjusted.

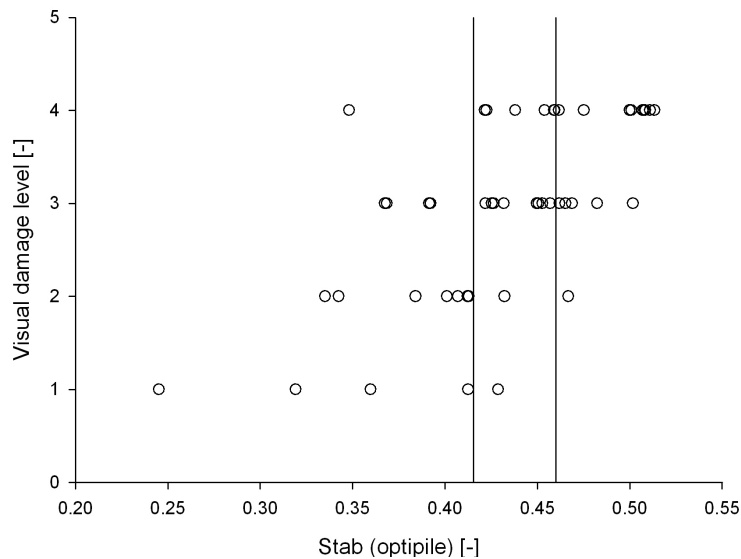


Figure 4-58: Optipile parameter $Stab$ against observed visual damage levels

When looking more closely at the data, it appears that damage is (sometimes severely) underestimated by the use of the parameter $Stab$ for:

- larger current velocities ($U_c > 0.2$ m/s, on scale 1/50)

- larger wave periods for the smallest stone size ($T_p = 1.7s$, scale 1/50)
- somewhat smaller wave heights
- high density stones
- reverse currents

The damage is sometimes overestimated for the larger stone sizes, mainly for the peak wave period $T_p = 1.4s$.

For this reason, the parameter *Stab* is found to be inadequate to predict the test results of this study and a different approach is used. The damage level is incorporated in an adjusted stability equation.

The different parameters which have an influence on the damage level and which are discussed in section 4.3.3.4 are included one after the other. As much as possible, it is aspired to maintain the traditional shape of the equation. The best fit for the data points was investigated for one parameter after the other. To obtain the best fit for a parameter, both the r^2 value as the residuals as a function of the parameter were investigated. The best fit was chosen to be for a high value of r^2 and no remaining influence of the inserted parameter when plotted against the standardised error.

Orbital velocity

One of the main parameters influencing the damage is the orbital velocity U_m . In Figure 4-59, the damage number S_{3D} (equation (4.18)) is plotted against the orbital velocity for all tests with a target steady velocity $U_{c,target} = 0.14m/s$, a nominal diameter $D_{n50} = 3.5mm$ and a relative density $s = 2.65$. For very small values, the damage number approaches zero. The best fit is found by applying a third degree function.

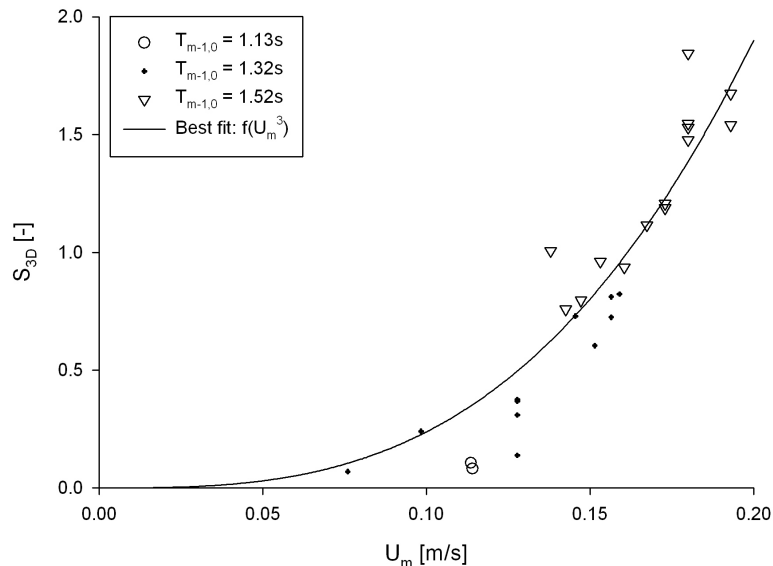


Figure 4-59: Damage number S_{3D} as a function of orbital velocity U_m ; $D_{n50} = 3.5mm, s = 2.65$

Wave period

In Figure 4-59, a distinction is made between different values of the wave period $T_{m-1,0}$. The value of $T_{m-1,0}$ is used instead of the peak period T_p , as the latter is a less stable measure of wave period than $T_{m-1,0}$, which is based on the integrated wave field (Wiberg and Sherwood (2008)) and given by equation (3.20). Although lower values of $T_{m-1,0}$ result in lower values of U_m , there remains an influence of $T_{m-1,0}$, which can be noted in Figure 4-59. Lower values of $T_{m-1,0}$ result in lower damages than predicted according to the fit. In Figure 4-60, the damage number is plotted against $U_m T_{m-1,0}^{2/3}$, accounting for the influence of $T_{m-1,0}$.

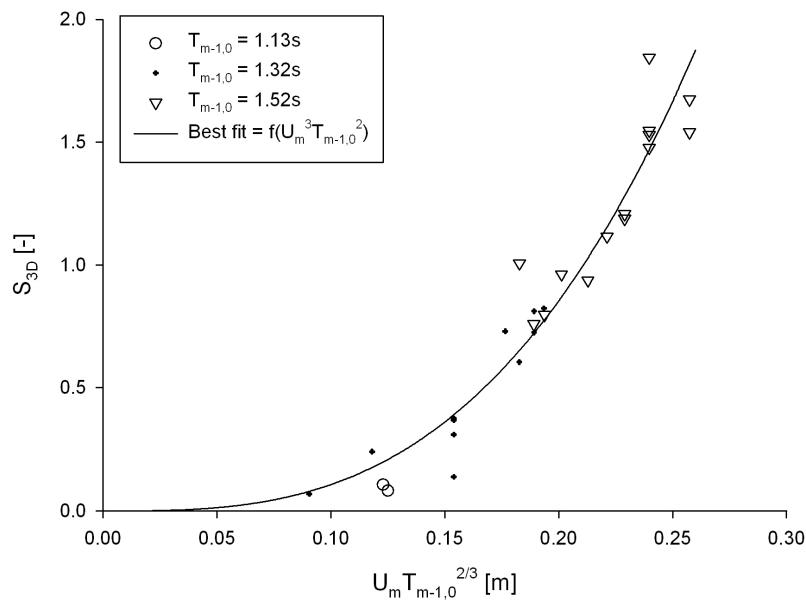


Figure 4-60: Damage number S_{3D} as a function of $U_m T_{m-1,0}^{2/3}$; $D_{n50} = 3.5\text{mm}$, $s = 2.65$

Stone size

In Figure 4-61, the value of $U_m T_{m-1,0}^{2/3}$ is plotted for all scour protections with D_{n50} respectively equal to 3.5mm, 5.0mm and 7.2mm. All tests in Figure 4-61 have a relative density $s = 2.65$.

The plot in Figure 4-61 clearly shows the influence of the stone size. In Figure 4-62 the influence of the stone diameter is accounted for by dividing the prediction variable by $D_{n50}^{2/3}$, which yields the best fit for the data at hand.

Stone density

The influence of the stone density on the damage number is shown in Figure 4-63.

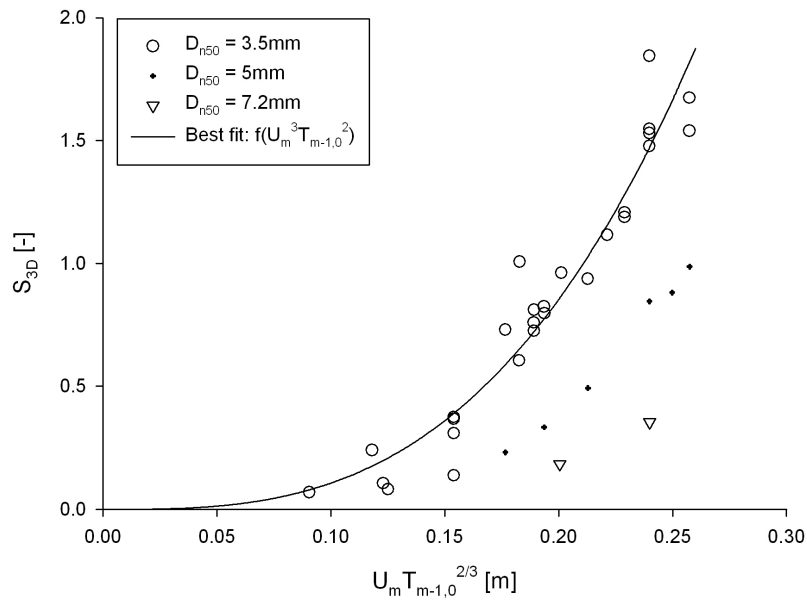


Figure 4-61: Damage number S_{3D} as a function of $U_m T_{m-1,0}^{2/3}$ for all values of D_{n50} ; $s = 2.65$

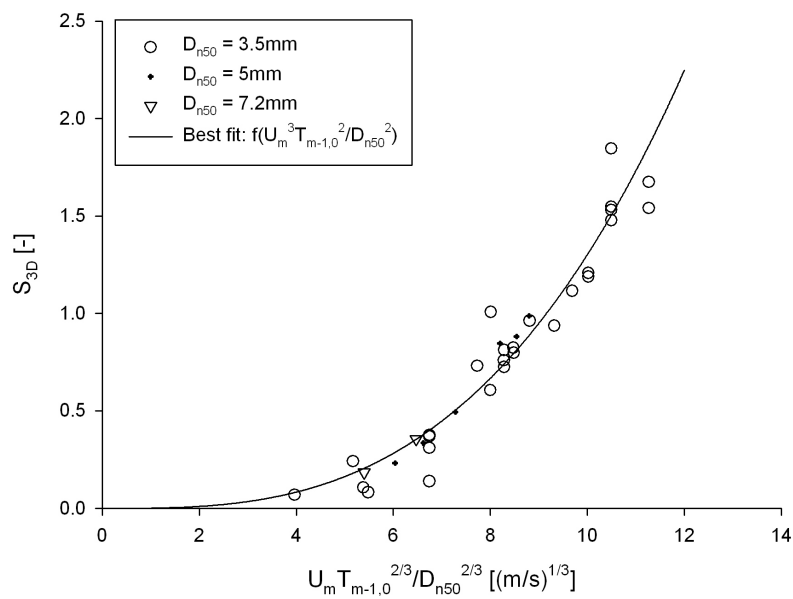


Figure 4-62: Damage number S_{3D} as a function of $U_m T_{m-1,0}^{2/3} / D_{n50}^{2/3}$; $s = 2.65$

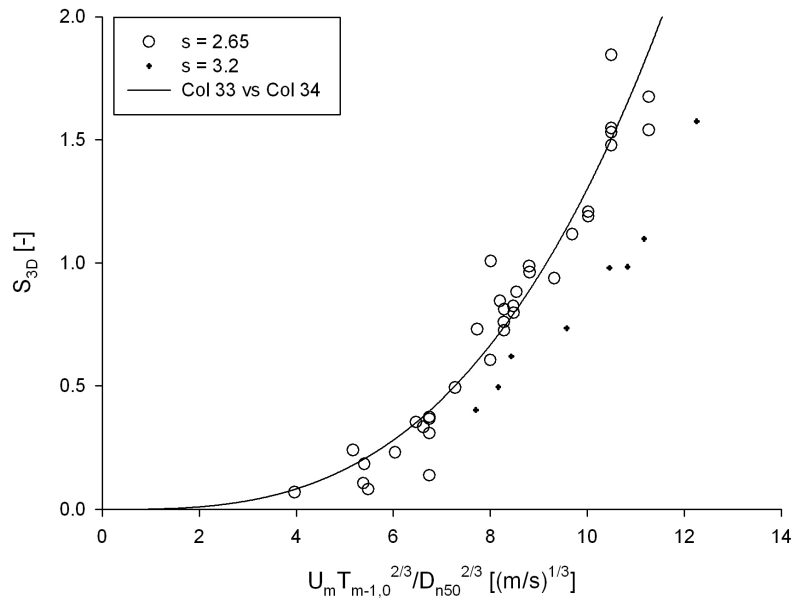


Figure 4-63: Damage number S_{3D} as a function of $U_m T_{m-1,0}^{2/3} / D_{n50}^{2/3}$ for all densities

The influence of stone density can be taken into account by dividing $U_m T_{m-1,0}^{2/3} / D_{n50}^{2/3}$ by $\sqrt{s-1}$, as shown in Figure 4-64. Again, this represents the typical expressions, used to determine the stable stone size, discussed in chapter 3, section 3.3.1.

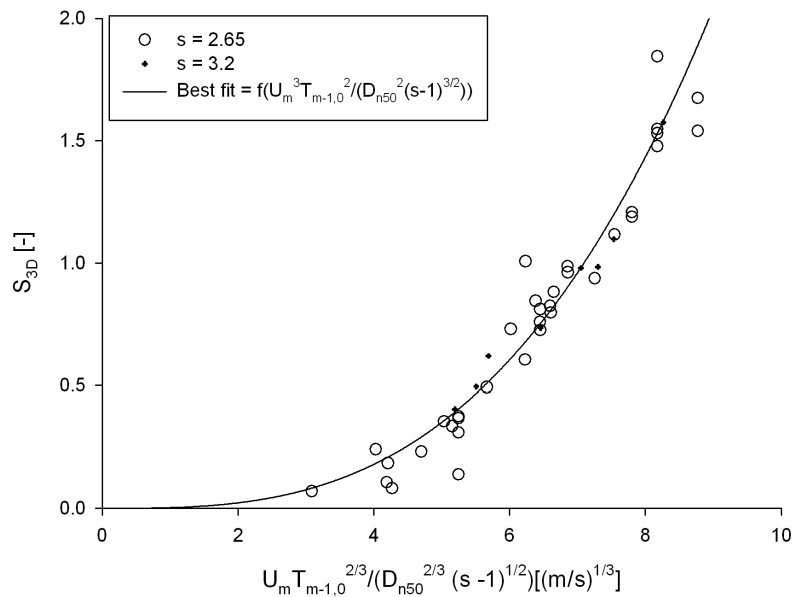


Figure 4-64: Damage number S_{3D} as a function of $U_m T_{m-1,0}^{2/3} / (D_{n50}^{2/3} (s-1)^{1/2})$

Water depth

The influence of the water depth is hard to distinguish, as only two tests were performed with a smaller water depth ($d = 0.2\text{m}$ instead of 0.4m) and a limited flow velocity. The influence of the water depth is already included in the parameter U_m , but it is found that a residual influence remains. Damage increases for smaller water depths. To incorporate this in the formula and to obtain a dimensionless parameter, the parameter $U_m T_{m-1,0}^{2/3} / D_{n50}^{2/3} \sqrt{s-1}$ is divided by $(gd)^{1/6}$ with g the gravitational acceleration and d the water depth. The resulting plot is shown in Figure 4-65. More tests with a different water depth are needed to validate this result. So far, the best fit for the data is:

$$S_{3D} = a \frac{U_m^3 T_{m-1,0}^2}{\sqrt{gd} (s-1)^{3/2} D_{n50}^2} \quad (4.23)$$

with $a = 0.0055$.

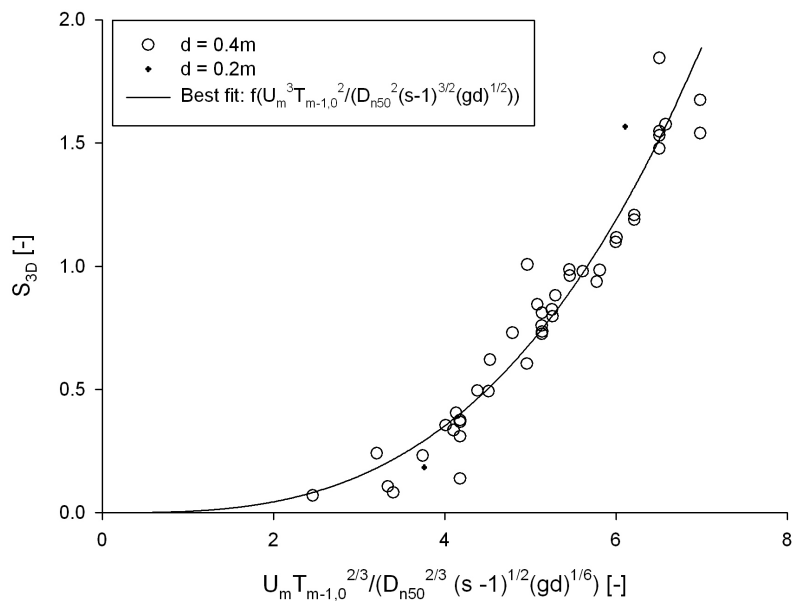


Figure 4-65: Damage number S_{3D} as a function of $U_m T_{m-1,0}^{2/3} / (D_{n50}^{2/3} (s-1)^{1/2} (gd)^{1/6})$

Flow velocity and flow direction

The influence of flow velocity is not as clear as it is for the other parameters that we have discussed so far. It was already noted above that the influence of the steady current depends both on flow velocity, stone size and flow direction. For small flow velocities, the steady current does not seem to influence the damage development, except for a current which opposes the waves. In Figure 4-66 the data with flow velocity $U_c > 0.21 \text{ m/s}$ and the data with an opposing current are

added to Figure 4-65. It is clear that the fit is not good enough for these data points. To investigate the missing influence, the difference (= error) between the measured damage number S_{3D} and the prediction of the damage number, obtained by using equation (4.23), with $a = 0.0055$ is considered. It was found that the following parameters have an influence on the increase in damage development:

- U_d/w_s : the ratio of the flow velocity to the settling velocity. It was further noted that the flow velocity has an influence on the damage development once U_d/w_s exceeds the critical value 0.61, when the settling velocity w_s is calculated according to van Rijn (1993), equation (3.33). This can be explained by the fact that stones are displaced over a larger distance when the flow velocity increases compared to the settling velocity of the stones.
- $U_c + U_m$: the combination of steady current velocity and wave induced orbital velocity. Damage remains limited when small orbital velocities are superimposed on the flow velocity.
- D_{n50} : the nominal stone size. As for the orbital velocity, damage is significantly reduced for larger stone sizes.
- d : the water depth.

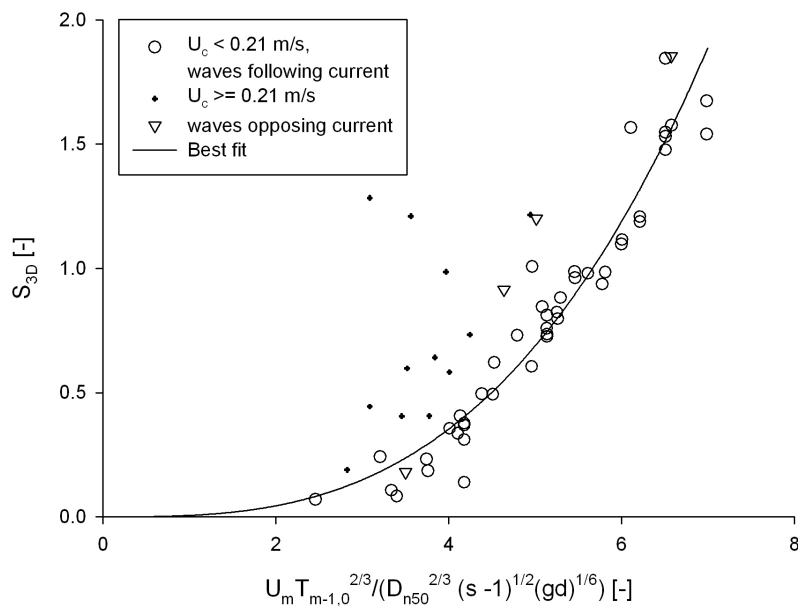


Figure 4-66: Damage number S_{3D} as a function of $U_m T_{m-1,0}^{2/3} / (D_{n50}^{2/3} (s-1)^{1/2} (gd)^{1/6})$ influence of flow velocity

The best linear fit for the error data is obtained by plotting it against the dimensionless parameter (Figure 4-67):

$$\frac{\left(\frac{U_c}{w_s}\right)^2 (U_c + bU_m)^2 \sqrt{d}}{gD_{n50}^{3/2}} \quad (4.24)$$

The parameter b is used only when the flow opposes the waves. In this case, the influence of the orbital velocity depends on the wave non-linearity. This is accounted for by including the Ursell number Ur (often used to describe wave non-linearity, (CEM, US Army Corps of Engineers (2002)) in the parameter b :

$$b = \frac{Ur}{6.4} \quad (4.25)$$

$$Ur = \frac{L^2 H}{d^3} \quad (4.26)$$

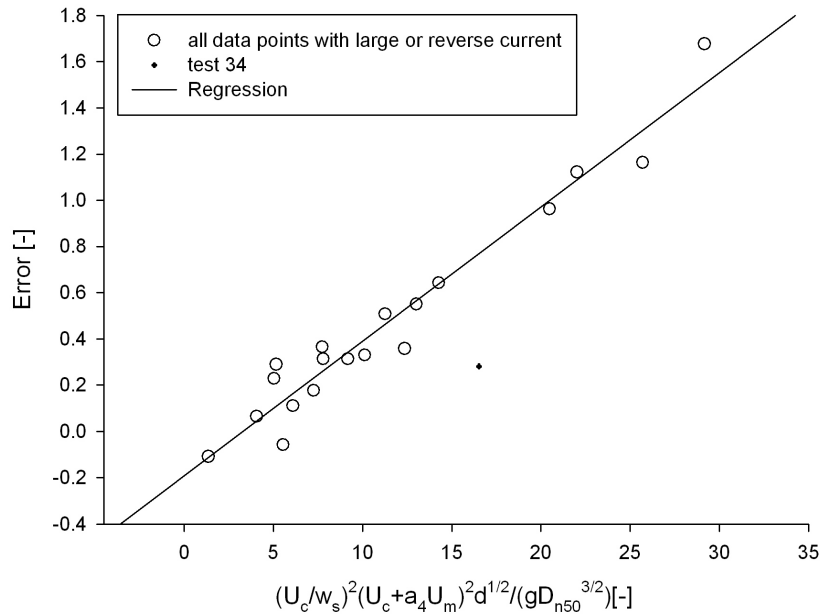


Figure 4-67: Residue of $(S_{3D} - 0.0055U_m T_{m-1,0}^{2/3} / (D_{n50}^{2/3} (s-1)^{1/2} (gd)^{1/6})$ as a function of $(U_c/w_s)^2 (U_c + a_4 U_m)^2 d^{1/2} / (gD_{n50}^{3/2})$

For one test (test 34), the damage is seriously overestimated when using the proposed fit (dot in Figure 4-67). On the other hand, the low damage number which was found for this particular test was unexpected. This test is therefore regarded as an outlier and is withheld from the fitting.

A linear regression of the remaining data points leads to the following equation:

$$S_{3D} = a_0 \frac{U_m^3 T_{m-1,0}^2}{\sqrt{gd} (s-1)^{3/2} D_{n50}^2} + a_1 \left(a_2 + a_3 \frac{\left(\frac{U_c}{w_s}\right)^2 (U_c + a_4 U_m)^2 \sqrt{d}}{g D_{n50}^{3/2}} \right) \quad (4.27)$$

in which the parameters a_0 , a_2 and a_3 are determined through regression and are respectively equal to 0.0055, -0.159 and 0.057. The parameters a_1 and a_4 depend on the ratio of flow velocity and stone size and on the flow direction and are to be determined as:

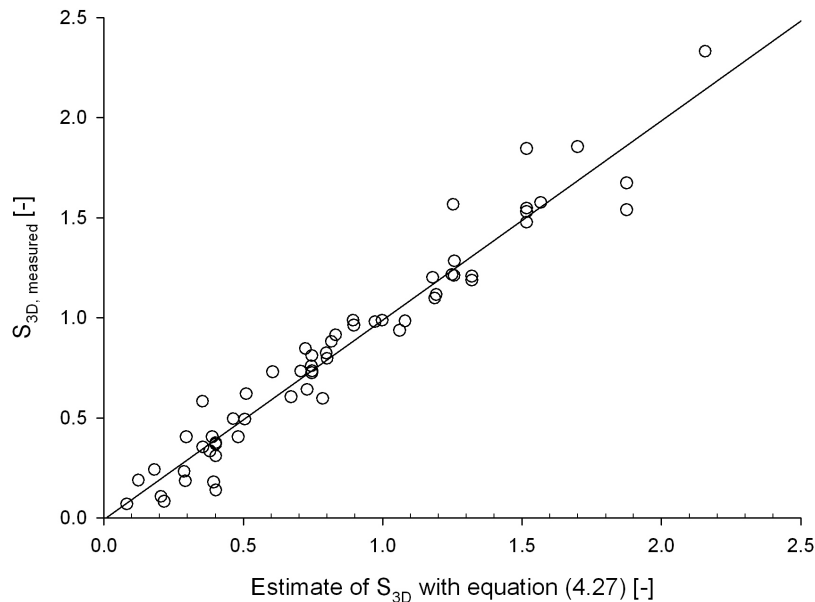
$$a_1 = 0 \quad \text{for } \frac{U_c}{\sqrt{g D_{n50}}} < 0.92 \text{ and waves following current} \quad (4.28)$$

$$a_1 = 1 \quad \text{for } \frac{U_c}{\sqrt{g D_{n50}}} \geq 0.92 \text{ or waves opposing current}$$

$$a_4 = 1 \quad \text{for waves following current} \quad (4.29)$$

$$a_4 = \frac{U_R}{6.4} \quad \text{for waves opposing current}$$

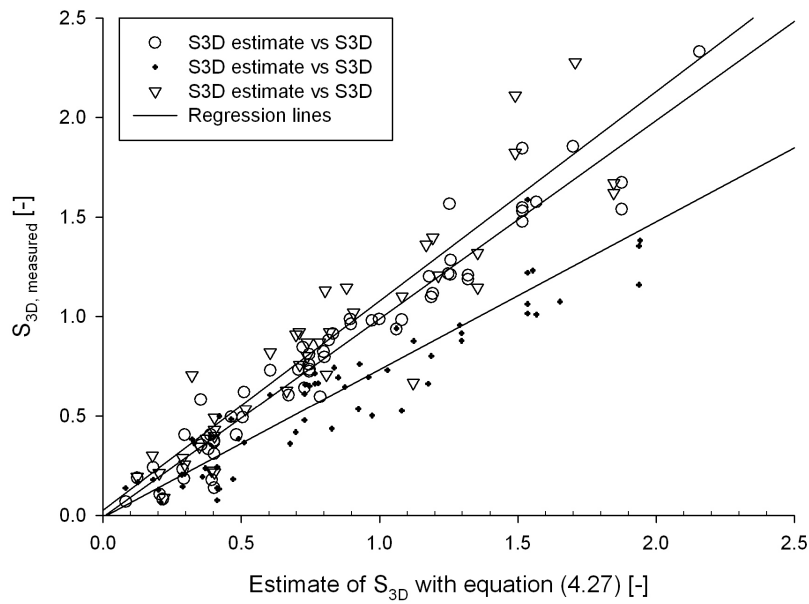
The fit is plotted in Figure 4-68. An r^2 value of 0.951 is obtained.



**Figure 4-68: Measured damage versus estimated damage with equation (4.27);
N = 3000**

Number of waves

To investigate the influence of the number of waves on the damage development, the estimated damage number with equation (4.27) is plotted against the measured damage number for $N = 1000, 3000$ and 5000 in Figure 4-69, with N the number of waves. The plot shows that the damage is significantly overrated for $N = 1000$, while it is slightly underestimated for $N = 5000$. This shows again that the damage for a constant loading develops towards some kind of equilibrium state. Another conclusion which can be drawn from this plot, is that damage develops quite quickly.



**Figure 4-69: Measured damage versus estimated damage with equation (4.27);
N = 1000, 3000 and 5000**

The number of waves can be accounted for in the damage formula by dividing the damage number S_{3D} by a power function of the number of waves N . The final equation becomes:

$$\frac{S_{3D}}{N^{b_0}} = a_0 \frac{U_m^3 T^{2m-1,0}}{\sqrt{gd} (s-1)^{3/2} D_{n50}^2} + a_1 \left(a_2 + a_3 \frac{\left(\frac{U_c}{w_s}\right)^2 (U_c + a_4 U_m)^2 \sqrt{d}}{g D_{n50}^{3/2}} \right) \quad (4.30)$$

in which the parameters b_0 , a_0 , a_2 and a_3 are determined through regression and are respectively equal to 0.243, 0.00076, -0.022 and 0.0079. The parameters a_1 and a_4 are to be determined with equations (4.28) and (4.29). The r^2 of the regression line is reduced to 0.907 by adding the data after 1000 and 5000 waves.

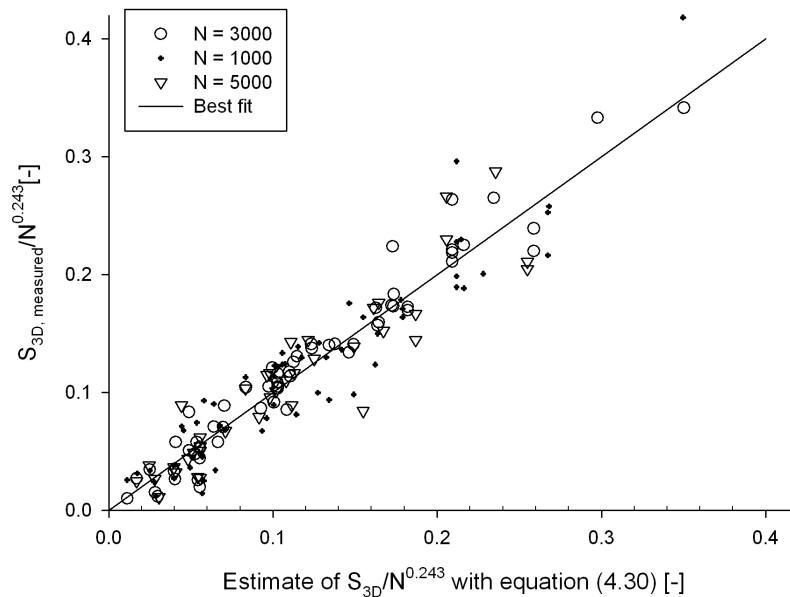


Figure 4-70: Measured damage versus estimated damage with equation (4.30)

Remaining influences

The parameters which haven't been or have been insufficiently tested and are therefore not included in the model are:

- filter type: for high damage numbers, damage is significantly larger in case no filter or a granular filter are used. As the acceptable damage number is limited, the filter type will most probably not influence the damage number for the accepted damage level. However, further investigation on the influence of differing filter types on the damage number should confirm this theorem;
- construction type of scour protection: as mentioned above, damage seems to be influenced by the protrusion of the scour protection above the bed;
- pile diameter: only one pile diameter was tested. The result is therefore only valid for pile diameters which do not vary too much from the tested pile size. As the pile diameter has an influence on the vortex shedding, it is likely that it will have an influence on the damage number;
- foundation type: other foundations, such as tripods or gravity based foundations have a different influence on the flow pattern. It is to be expected that the damage development will be influenced by the foundation type
- damage due to steady current alone: no tests were performed with flow velocities which are high enough to move the stones. Some expressions exist to calculate the required stone size for a statically stable stone size, but extra model tests are needed to include the damage number.

Further research is required to assess to what extent these parameters influence the damage number. Furthermore, more research is required to assess the influence of a reverse current, the influence of water depth and large flow velocities on the damage development.

Damage criterion

In Figure 4-71 the estimate of the damage is plotted against the visual damage level for $N = 3000$. The damage number gives a clear limit for the different damage levels. The limits which are established, based on these (model) data are:

- $S_{3D} < 0.25$: no to little movement
- $0.25 < S_{3D} < 1$: movement, but no failure
- $S_{3D} > 1$: failure

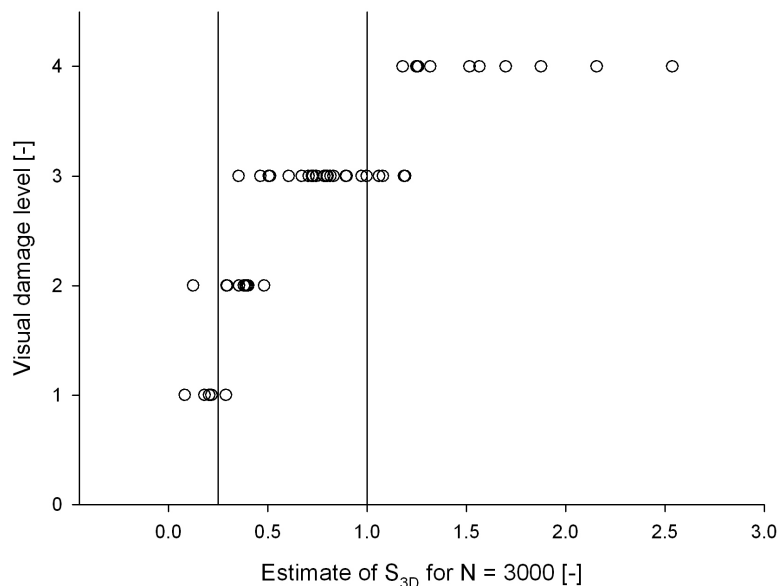


Figure 4-71: Estimated damage number (equation (4.27)) versus visual damage level; $N = 3000$

The steps which should be taken to calculate the required stone size for a statically stable scour protection in which some damage is allowed are given in chapter 7, section 7.2.

4.3.5. Comparison and validation of formula and results

Equation (4.30) can be used either to calculate the required stone size when the acceptable damage level is defined, or it can be used to assess whether an existing scour protection will fail or not.

4.3.5.1. Comparison with OPTI-PILE results

The OPTI-PILE project is described in chapter 3, section 3.3.3. Table 3.1 gives the range of parameters they tested. The model pile diameter had a diameter of 0.089m on model scale, while a scale 1/47.25 was used ($D = 4.2\text{m}$ on prototype scale) and differs therefore slightly from the pile diameter used in the current test series (prototype $D = 5\text{m}$). For the Optipile project a visual assessment of the damage was used and the following damage codes were used to classify the tests:

- Damage code 1: no movement of rocks;
- Damage code 2: some movement, but no failure;
- Damage code 3: failure of the scour protection.

These definitions are comparable to the visual damage assessment which was done for this test series. In Table 4-10, the OPTI-PILE test specifics are given, together with the result obtained from the prediction formula (4.30), resulting in an assessment of the visual damage level. The damage levels are derived from Figure 4-71 and a distinction is made between the following damage levels:

- Damage level 1: $S_{3D} < 0.25$: no movement of rocks;
- Damage level 3: $0.25 < S_{3D} < 1$: some movement, but no failure;
- Damage level 4: $S_{3D} > 1$: failure of the scour protection.

The wave period $T_{m-1,0}$ was obtained from the average wave period T_m by assuming that $T_{m-1,0} = 1.157 T_m$. The orbital velocity near the bottom was calculated from a theoretical Jonswap spectrum, with $\gamma = 3.3$ and the given wave characteristics.

Table 4-10 shows that, in spite of the difference in pile diameter, equation (4.30) correctly predicts almost all of the damage observations. The damage levels which are not correctly predicted are indicated in red in the last column of Table 4-10. For 1 case (OPTI-PILE test n° 14), no movement is predicted, while some stone movement was visible during the test. Figure 4-72 shows a picture of the scour protection before and after test n° 14, showing that movement was very limited. It can be noted that in this particular test, a developed scour hole was backfilled with scour protection material, resulting in a scour protection which is level with the bed. Even in this case, the damage is predicted rather well.

Table 4-10: comparison of prediction formula with OPTI-PILE results

Test n°	d [m]	U _c [m/s]	H _s [m]	T _{m-1,0} [s]	U _m [m/s]	s [-]	D _{n50} [mm]	visual damage assessment [-]	result code Opti-pile	S _{3D} [-]	resulting damage level
1	0.5	0.287	0	0	0.000	2.71	9.7	no movement	1	0.00	1
2	0.499	0.287	0	0	0.000	2.71	9.4	no movement	1	0.00	1
3	0.499	0.293	0	0	0.000	2.71	9.4	no movement	1	0.00	1
4	0.585	0.3	0	0	0.000	2.71	9.7	no movement	1	0.00	1
5	0.508	0.158	0.139	1.54	0.149	2.71	9.7	no movement	1	0.08	1
6	0.508	0.167	0.138	1.50	0.145	2.71	9.4	no movement	1	0.08	1
7	0.508	0.175	0.129	1.52	0.137	2.71	9.7	no movement	1	0.06	1
8	0.508	0.152	0.143	1.66	0.161	2.71	9.7	no movement	1	0.12	1
9	0.508	0.167	0.163	1.57	0.176	2.71	9.4	no movement	1	0.15	1
10	0.508	0.154	0.168	1.58	0.183	2.71	9.7	no movement	1	0.16	1
11	0.508	0.159	0.148	1.61	0.164	2.71	9.7	no movement	1	0.12	1
12	0.508	0.145	0.174	1.66	0.196	2.71	9.7	no movement	1	0.21	1
13	0.508	0.147	0.179	1.62	0.198	2.71	9.4	some movement, no failure	2	0.22	1
14	0.508	0.167	0.162	1.58	0.176	2.71	6.3	some movement, no failure	2	0.34	3
15	0.508	0.167	0.142	1.53	0.151	2.71	3.5	some movement, no failure	2	0.63	3
16	0.508	0.167	0.163	1.56	0.176	2.71	6.3	some movement, no failure	2	0.33	3
17	0.495	0.126	0.114	1.35	0.111	2.65	1.3	some movement, no failure	2	4.58	4
18	0.508	0.147	0.18	1.61	0.198	2.71	6.3	some movement, no failure	2	0.49	3
19	0.428	0.208	0.089	1.33	0.099	2.65	1.3	failure	3	14.01	4
20	0.508	0.167	0.14	1.52	0.148	2.71	1.9	failure	3	4.88	4
21	0.508	0.147	0.178	1.61	0.196	2.71	3.5	failure	3	1.53	4

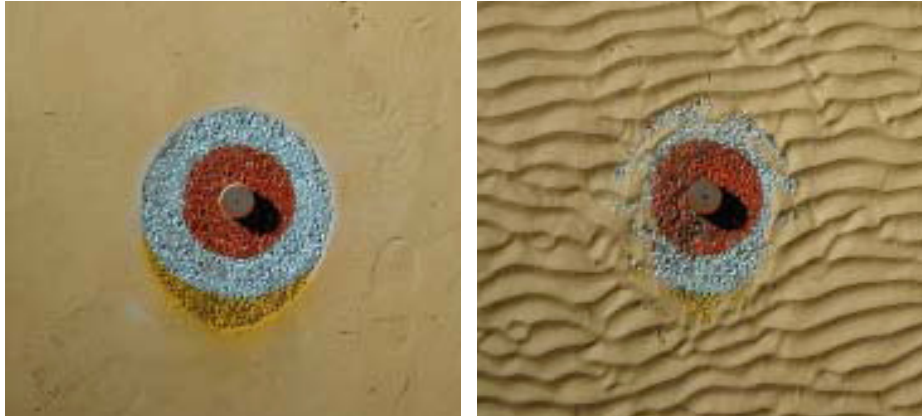


Figure 4-72: Overhead picture of OPTI-PILE test n° 14

Only for 1 case, the damage seems to be overrated. This is the case for OPTI-PILE test n° 18. When we look in detail to this case, we see that it concerns a test of the filter material, which had a much smaller stone size than tested in our test series. The damage number which is predicted is $S_{3D} = 4.58$, which means that a lowering of the bed of $4.58 \times D_{n50}$ (1.3 mm) = 6 mm can be expected over an area which is equal to the pile diameter. This is actually only a limited lowering of the filter layer. From the measurements made during the OPTI-PILE project, it can be seen that the maximum lowering of the bed which was measured was approximately 6.5 mm . Because no complete bed profile was measured, it is difficult to say in which amount the damage was overrated by our prediction model. Moreover, in OPTI-PILE test n° 20, the filter layer was tested without armour layer. Again, the very high damage number $S_{3D} = 14.01$ should be seen in the context of a very small stone diameter (actually coarse sand), leading to a lowering of the bed of 1.8 cm . Figure 4-73 shows an overhead picture of the filter at the end of the test. It can indeed be seen that a scour pattern develops near the pile, within a radial distance of $1D$ from the pile. The measurements of the profile shows that a maximum lowering of approximately 3 cm was found (from the top of the filter layer). When assuming a slope with an angle of 30° , this results in a scour hole with a radial distance of 5.2 cm from the pile, which is somewhat more than $0.5D$. The sub-areas which were used for the calculation of the damage number have a width of $0.5D$. A simple calculation leads to an average lowering of the bed of somewhat more than 1.5 cm . The prediction of the damage number can thus be considered to be remarkably well, even though such small stone sizes were not tested. It is however stressed that this cannot be taken as a proof that equation (4.30) can be used outside the tested range!!



Figure 4-73: Overhead picture of OPTI-PILE test n° 20

4.3.5.2. Comparison of required stone size with different formulae

A comparison is made between the stone size calculated with different methods for a typical situation in the North Sea. A monopile foundation is to be installed in a water depth of 20m. The pile diameter is 5m. The design wave conditions have a significant wave height $H_{m0} = 6.5\text{m}$. According to equation (3.29), the corresponding peak wave period $T_p = 4.4 \sqrt{H_{m0}} = 11.2\text{s}$. According to equation (3.26), the corresponding wave period $T_{m-1,0} = T_p/1.107 = 10.1\text{s}$. The tidal velocity has an average value $U_c = 1.5\text{m/s}$. The number of waves is taken to be 3000. In Table 4-11, the comparison is made between the required scour protection stone size for several calculation methods:

- the traditional approach, in which the amplified combined current and wave bed shear stress determine the critical bed shear stress. An amplification factor (equation (1.40)) $\alpha = 4$ is used to account for the influence of the pile. A value of $\theta_{cr} = 0.056$ is used for the critical Shields parameter. The combined maximum bed shear stress caused by the waves and the current, τ_{max} is calculated according to equations (1.29) or (1.31).
- the static scour protection approach for which initiation of motion is prevented derived in section 4.2: equation (4.6).
- the static scour protection approach in which a certain amount of damage is accepted (equation (4.30)). 2 damage levels are considered for the calculations which are listed in Table 4-11: $S_{3D} = 0.5$ and $S_{3D} = 1$

- the equations (3.53) and (3.54) given by Soulsby (1997), which calculate a critical stone size for the two separate loading conditions: wave loading and steady flow. No interaction between waves and current is considered. An amplification factor $\alpha = 3$ is assumed for the steady flow velocity and $\alpha = 1.75$ is assumed for the wave induced flow velocity.

The OPTIPILE parameter's calculation is bound to confidentiality and can therefore not be included in this calculation.

Table 4-11: Comparison between required stone size (D_{n50} [m]) according to different calculation methods: $d = 20\text{m}$, $H_{m0} = 6.5\text{m}$, $T_p = 11.2\text{s}$; $U_c = 1.5 \text{ m/s}$.

Wave direction	Traditional approach	Static scour protection without movement	Static protection, accepted damage $S_{3D} = 1$	Static protection, accepted damage $S_{3D} = 0.5$	Static protection, accepted damage $S_{3D} = 0.25$	Soulsby (1997), current	Soulsby (1997), waves
Following current	2.74	0.499	0.233	0.271	0.331	0.103	0.727
Opposing current	2.74	0.499	0.280	0.356	0.438	0.103	0.727

Table 4-11 shows that a significantly smaller stone size can be obtained when using equation (4.6) instead of the traditional approach. The additional decrease in stone size, obtained by allowing some movement (equation (4.30)), depends on the accepted damage level, but can be significant. Both for the traditional approach and the equations handed by Whitehouse (1998), the required stone size depends strongly on the assessment of the amplification factor.

It should be added that, for the traditional approach, much depends on the amplification factor and formulae which are used.

4.4. Radial extent of a scour protection

The existing design criteria to determine the radial extension of the scour protection are described in chapter 3, section 3.3.2. Figure 3-12 shows that the guidelines lead to a scour protection diameter which varies between 2.5 (Hjorth (1975)) and 8 (Breusers and Raudkivi (1991), Schiereck (2001)) times the pile diameter D , although a cone shaped scour protection was used in the former case, reaching up to $4.5D$ in the downstream direction.

When discussing the required extent of a scour protection, two aspects need to be taken into account. Firstly, it is important to know which area around the pile is influenced by the presence of the pile and has an amplification factor α higher than 1 (equation (1.40)). When the scour protection does not cover the complete area of amplified bed shear stress, scour will develop due to the disturbance of the flow caused by the pile at these locations. Secondly, the transition in bed roughness, caused by the transition from sea bed to scour protection, causes an increase in the bed shear stress downstream of this transition, both in a steady current and under waves (Whitehouse (1998)). The increase of the bed shear stress at the edges is augmented further when the

scour protection protrudes above the sea bed. Both aspects lead to scour at the edges of the scour protection.

Whitehouse (1998) notes that the bed protection should extend far enough to ensure that the foundation is not influenced by the edge scour and that the scouring at the edges should be minimised by the design of the scour protection.

In this section, we will first discuss the size of the area which is disturbed by the flow based on previous investigations, PIV measurements of the flow around the base of a monopile which were performed as a part of this study and the scour protection tests described in section 4.3. In section 4.4.2 the influence of the edge effects on a monopile foundation are investigated. The discussion will result in a recommendation for the radial extent of the scour protection around a monopile foundation.

4.4.1. Disturbance of the flow: impact area

In chapter 1, the impact of the pile's presence on the flow is discussed, showing that the pile has a local influence on the flow pattern. In this section, we will mainly focus on the distance to which the impact of the pile reaches.

4.4.1.1. Amplification

The local disturbance of the flow by the structure results in an increase in the flow velocity, which is expressed by an amplification factor. Generally an amplification factor α (equation (1.40)) is used for the bed shear stress while α_U represents the flow velocity amplification, with $\alpha_U = \sqrt{\alpha}$.

Hjorth (1975) investigated the amplification caused by a vertical cylindrical pile on the bed shear stress near the bed for a current alone situation. He used two pile diameters, two water depths and two current velocities. He measured the bed shear stress at the locations shown in Figure 4-74 and interpolated the measured values of the bed shear stress to obtain the results shown in Figure 4-75 and Figure 4-76. Bed shear stress was only measured up to a distance of 2.25cm from the pile surface, while the two pile diameters were respectively 5 and 7.5cm, leading to a limited investigated area.

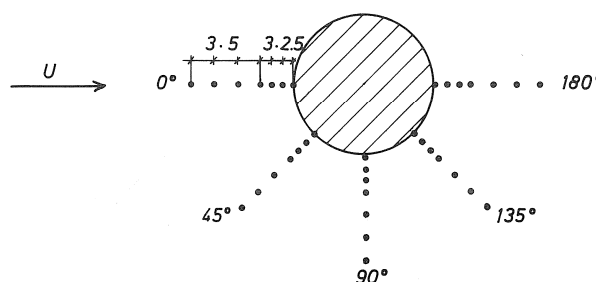


Figure 4-74: Location of observation points around vertical cylinder; from Hjorth (1975), distance in mm

Figure 4-75 shows that the amplification of the bed shear stress is reduced to approximately 1 at a distance of less than $0.5D$ from the pile's surface.

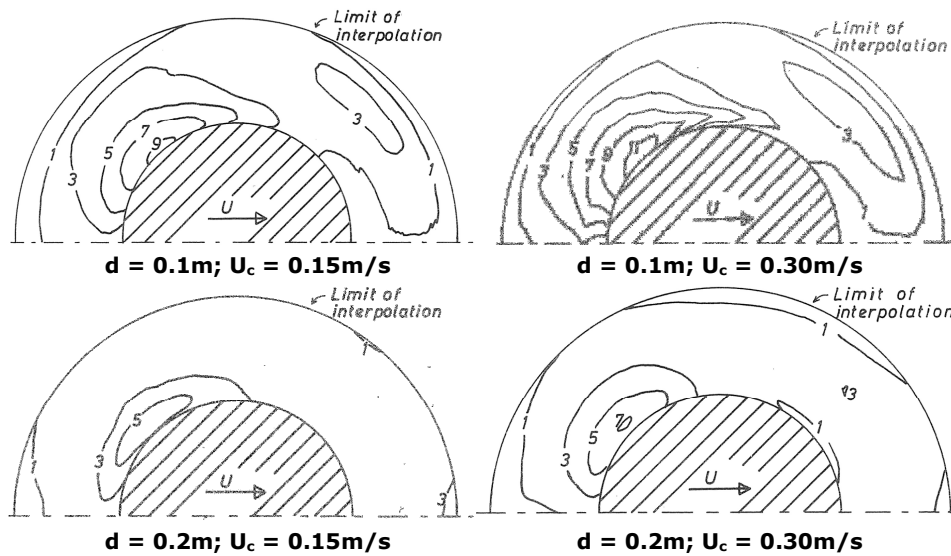


Figure 4-75: Results from Hjorth (1975): amplification of bed shear stress around a vertical pile for steady current, $D = 5\text{cm}$

Figure 4-76 shows that the amplification in the case of a larger cylinder can be somewhat larger. In this case, maximum values of 5 are found for the amplification of the bed shear stress at the edge of the interpolated region. However this region only covers a distance of $0.3D$ from the pile's surface.

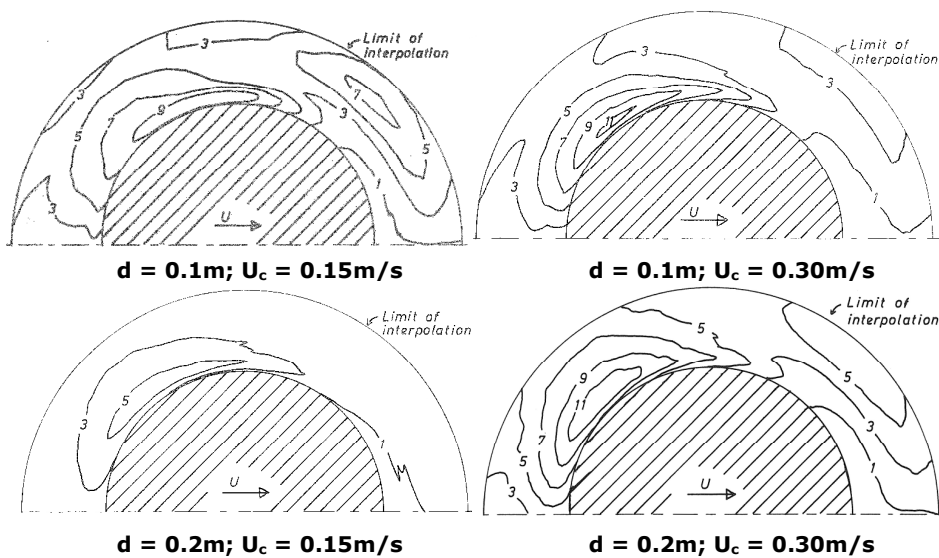


Figure 4-76: Results from Hjorth (1975): amplification of bed shear stress around a vertical pile for steady current, $D = 7.5\text{cm}$

The results from Hjorth (1975) were validated by the numerical study from Roulund, described in Sumer et al. (2001). A comparison for the pile diameter $D = 5\text{cm}$, water depth $d = 0.2\text{m}$ and current velocity $U_c = 0.3\text{m/s}$ is shown in Figure 4-77.

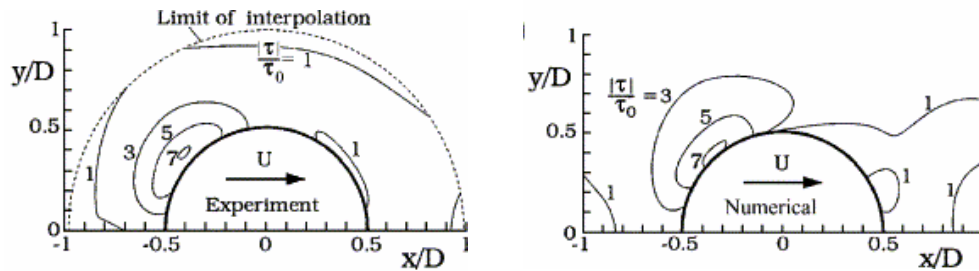


Figure 4-77: Comparison between experimental result from Hjorth (1975) and numerical result from Roulund; from Sumer et al. (2001)

As discussed in chapter 1, the amplification of the bed shear stress for waves is much smaller than it is for a steady current. Figure 1-22, reproduced from Sumer et al. (1997), shows the amplification of the bed shear stress at the base of a vertical cylinder for different values of the Keulegan Carpenter number KC . Their results show that in the case of waves, the amplification of the bed shear stress at a distance of $1D$ varies between 1.5 and 2.

4.4.1.2. PIV measurements

As a part of this study, Particle Image Velocimetry (PIV) was used to measure the flow field around a vertical cylindrical pile in a wave field (Smits (2005), Vansteenkiste (2007)). The experiments have been conducted in two wave flumes at Ghent University, Belgium. The small wave flume (SWF) has a length of 15m, a width of 0.35m and a depth of 0.60m. The large flume (LWF) has a length of 30m, a width of 1m and a depth of 1.2m. For both flumes, a piston-type wave paddle is used for wave generation.

Particle Image Velocimetry is a powerful measuring technique to obtain instant whole flow field measurements. Figure 4-78 shows the working principle of PIV. Seeding particles are added to the flow and reflects the laser light. A CCD camera takes two images of the flow field, illuminated by a double pulsed laser. With a cross correlation technique a velocity vector map is deduced from these two images.

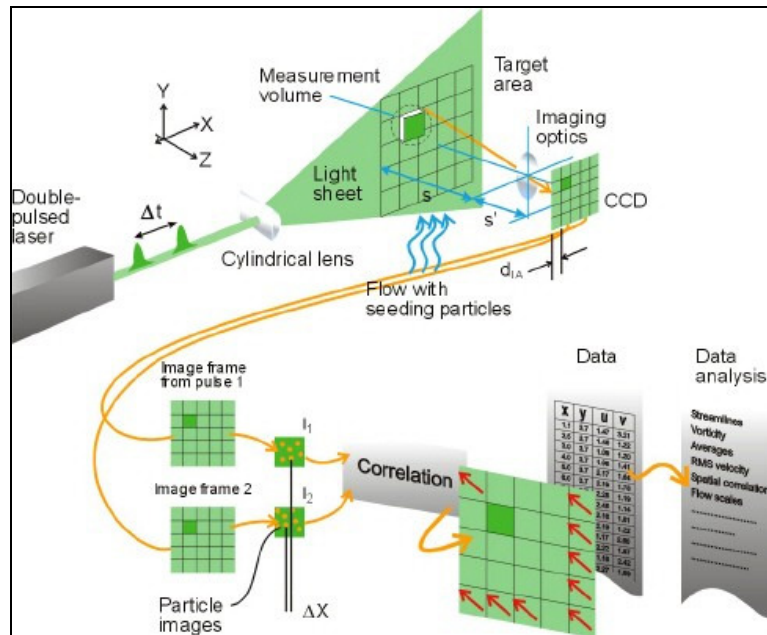


Figure 4-78: Particle Image Velocimetry, definition sketch; from Raffel et al. (1998)

Both the flow field in a horizontal plane, just above the bottom, and the flow field in the vertical plane through the centre of the pile are captured. The SWF has both plexiglass side walls and a plexiglass bottom. The experimental test set-up for the images of the horizontal flow field in the SWF is shown in Figure 4-79 (left): images are captured using a mirror, positioned underneath the wave flume. As the LWF only has a vertical glass wall a different set-up had to be used, with under water light sheet optics and a mirror, placed on the bottom of the wave flume, as shown in Figure 4-79 (right).

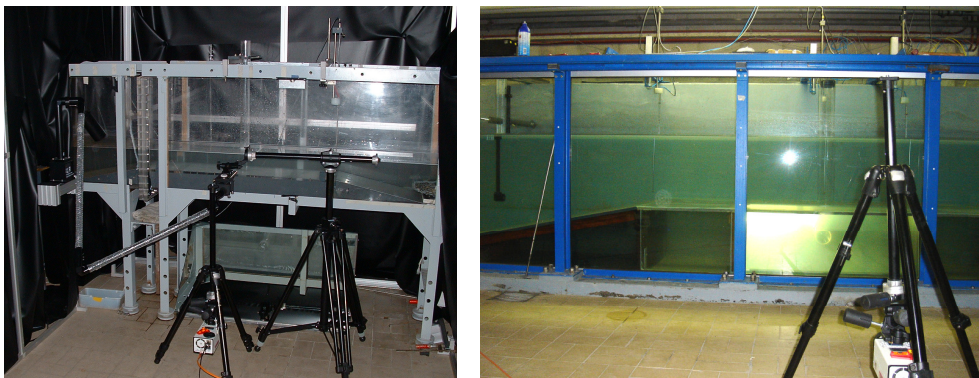


Figure 4-79: Experimental set-up for PIV tests, at scales 1/100 (Small Wave Flume, left) and 1/50 (Large Wave Flume, right).

Considering the dimensions of the wave flumes, tests were performed on two scales (1/100 en 1/50), using Froude scaling. Each test series comprised two

regular waves, one non-breaking and one breaking wave. The test characteristics are shown in Table 4-12. The two test set-ups and the PIV technique are described in more detail in Appendix VII.

Table 4-12: Test matrix for PIV tests

Scale [-]	Pile diameter D [m]	Water depth d [m]	Wave height H [m]	Wave period T [s]	KC number [-]	Pile Reynolds number Re_D [-10 ⁴]	Maximum bottom velocity U_m [m/s]
1/100	0.05	0.20	0.089	1.52	8.4	1.4	0.275
1/100	0.05	0.12	0.089	1.45	10.8	1.8	0.372
1/50	0.10	0.40	0.182	2.15	8.6	4.0	0.398
1/50	0.10	0.22	0.124	2.05	7.9	3.9	0.385

The first test series was performed on scale 1/100 and the main purpose was to investigate the influence of wave breaking on the amplification of the velocity near the pile. The second test series had as main objective to investigate possible scale effects.

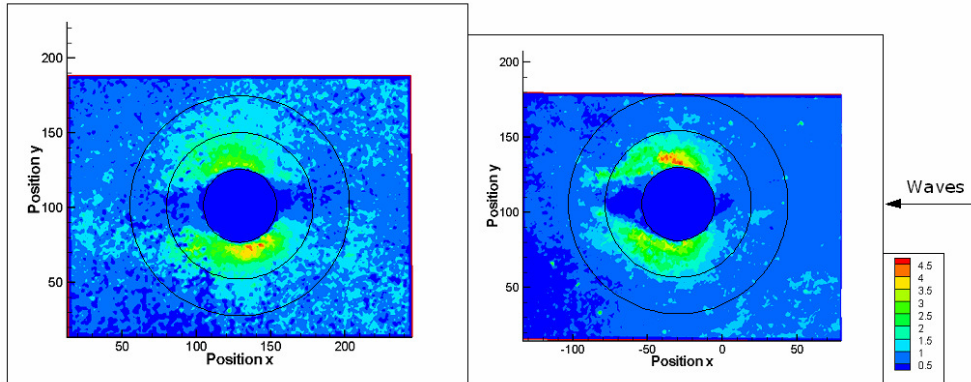
The PIV system is triggered when a specific wave elevation is exceeded at a specified location in front of the pile. Measurements of the flow field are made every 50ms. Due to the accuracy and high reproducibility of the tests, the images from the vertical flow field can be linked to the images in the horizontal flow field. This way, for each velocity field in the horizontal plane, the exact location of the wave crest in relation to the pile is known.

The amplification of the flow field around the pile is derived from the measured velocities by dividing the maximum measured total velocity at each grid point by the maximum horizontal velocity which is to be expected in absence of the pile. Figure 4-80 and Figure 4-81 show the amplification of the bed shear stress for the two test set-ups (determined as the amplification of the velocity squared).

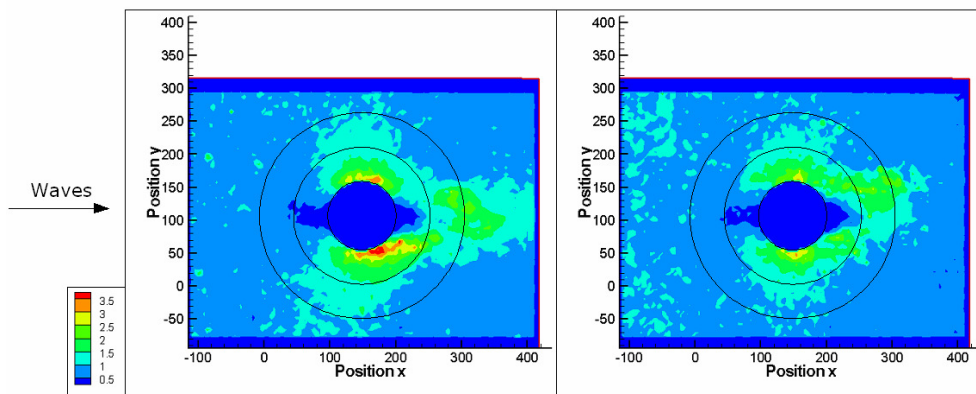
For the smallest scale, the waves travel from right to left on the velocity images, while in the large wave flume the waves travel from left to right. In reality it is the other way around, but the rotation is caused by the fact that the camera had to be put upside down to take the images (in both cases).

In both set-ups, the maximum amplification is measured just before the wave crest reaches the pile.

For the small scale tests (Figure 4-80), the test results show that the amplification of the bed shear stress for the breaking wave is slightly higher than for the non-breaking wave. The maximum amplification measured for the non-breaking wave is 4.85, while it increases to 5.53 for the breaking wave. This increase in amplification could be due to the wave breaking, but it could also be caused by the higher *KC* number. The results can be compared with Figure 1-24, reproduced from Sumer et al. (1997), who measured maximum amplification factors between 4 and 4.5 for *KC* values between 6.1 and 10.3. As these values are smaller than 5.53 measured for the breaking wave, this leads to the assumption that a slight increase in amplification can be expected for breaking waves.



$d = 0.20\text{m}$, $H = 0.089\text{m}$, $T = 1.52\text{s}$ $d = 0.12\text{m}$, $H = 0.089\text{m}$, $T = 1.48\text{s}$
Figure 4-80: Amplification of bed shear stress, scale 1/100, for non-breaking (left) and breaking (right) wave



$d = 0.40\text{m}$, $H = 0.182\text{m}$, $T = 2.15\text{s}$ $d = 0.22\text{m}$, $H = 0.124\text{m}$, $T = 2.05\text{s}$
Figure 4-81: Amplification of bed shear stress, scale 1/50, for non-breaking (left) and breaking (right) wave

For the larger scale tests (Figure 4-81), the amplification of the bed shear stress is somewhat higher for the non-breaking (3.97) wave than it is for the breaking wave (3.18). This might be due to the smaller KC number, but it could also be explained by the fact that the wave broke at some distance before the pile, resulting in a lower amplification around the pile.

The amplification for the smaller scale is somewhat higher than it is for the larger scale. In Vansteenkiste (2007) it was noted that, while vortex shedding occurs in the small scale, it did not in the large scale. Instead a pair of asymmetric vortices was formed. This can be explained by Figure 1-22, which shows that the vortex regime also depends on the Reynolds number. In our case, we are located at the edge of the formation of a pair of asymmetric vortices and vortex shedding. Relating the KC and Reynolds numbers of our test series to Figure 1-22 shows that they are located in the transition zone between

asymmetric vortices and vortex shedding. Moreover, in prototype scale, the Reynolds number increases to more than 10^6 , for which the vortex regime is not shown in Figure 1-20. One should therefore be careful with unexpected scale effects.

An important conclusion is that, at a distance of $0.5D$ from the pile, the amplification of the bed shear stress is reduced to a factor 2 in both cases, while at a distance of $1D$ from the pile's surface it is less than 1.5 on the smallest scale and less than 2 on the larger scale (behind the pile there is a location with a somewhat higher amplification, as can be seen in Figure 4-81). At a distance of $2D$ from the pile, the pile does not seem have an influence on the flow velocity.

4.4.1.3. Scour protection tests

For most scour protection tests, described in section 4.3, damage was limited to the zones closest to the pile (two inner circles of the scour protection, which extended to a distance of $1D$ from the pile's surface, white and red ring on Figure 4-2). The tests for which the damage extended the farthest were test 36 and test 20. In this case the damage extended up to a distance of 1.5 times the pile diameter from the pile's surface. This shows that the influence of the pile reaches up till approximately 1.5 times the pile diameter.

4.4.2. Edge scour

No specific references were found to calculate edge scour around scour protections for offshore monopiles. In Cefas (2006) a prototype measurement of the scour protection around one of the Scroby Sands wind turbine foundations is plotted. It shows significant edge scour around the scour protection, with a maximum depth of 3 to 4m.

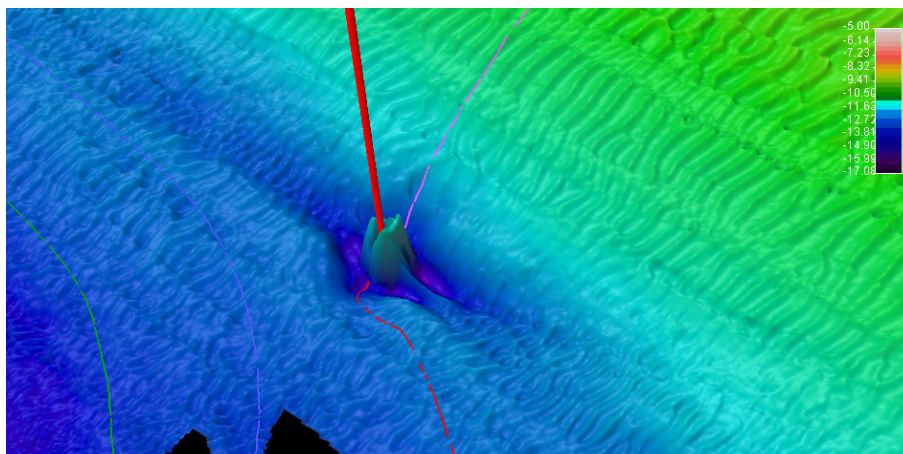


Figure 4-82: Fledermaus image showing the scour protection around the base of the monopile (red cylinder ~4.2 m diameter, WTG01), along with the secondary scour pits, Scroby Sands wind farm; from Cefas (2006)

Some general considerations on edge effects of other bed protections can however be extended for edge scour around monopile foundations' scour protection.

Schiereck (2001) notes that the amplification factor of the flow velocity at the edge of a scour protection is minimally equal to 1.5 – 2. Scour at the edge of a scour protection is therefore inevitable. The amplification factor increases both when the scour protection does not extend far enough to cover the area which is influenced by the structure or when smooth scour protections are applied. According to Schiereck (2001) the edge scour endangers the scour protections stability when the upstream slope of the edge scour is too steep in combination with a deep scour hole. In this case, a flow slide can be expected.

4.4.2.1. Dimensions of edge scour

The edge scour can be modelled as a triangular scour hole with a scour depth S_{edge} , an upstream slope $\tan(\beta_1)$ and a downstream slope $\tan(\beta_2)$ as shown in Figure 4-83.

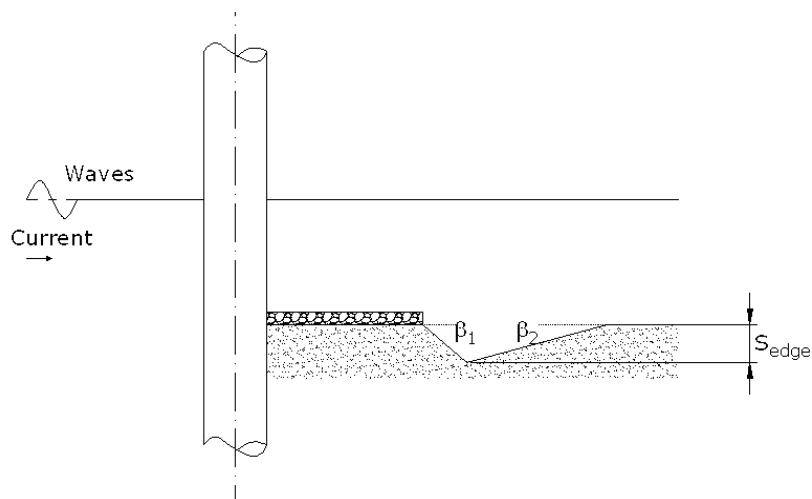


Figure 4-83: Edge scour: definition sketch

Comparable to the scour hole which develops around an unprotected pile, the scour depth at the edge of the scour protection will reach a maximum value in the clear-water situation, as there is no sediment supply from upstream. No formulae were found for the case of waves or combined waves and current, so it is assumed that, analogous with scour around a pile, the worst situation exists in a current alone situation.

For clear-water scour in a current alone situation, the scour depth at the edge of a scour protection can be calculated as (according to Schiereck (2001)):

$$S_{edge} = d \cdot \frac{0.5\alpha_U U_c - U_{cr}}{U_{cr}} \quad (4.31)$$

with d the water depth; α_U the amplification of the flow velocity at the edge of the scour protection; U_c the average flow velocity and U_{cr} the critical flow velocity. The factor 0.5 is used to account for the fact that the amplification at the bottom of the scour hole is measured at some distance from the edge of the scour protection.

A maximum scour depth is reached when $U_c = U_{cr}$. A value of 2.5 is recommended for α_U (Hoffmans and Verheij (1997), Van Oord (2003)), leading to a maximum scour depth of:

$$S_{edge} = 0.25d \quad (4.32)$$

When we bear in mind that the flow will generally cause a live bed situation (especially when waves are present) and that the amplification of the flow around a pile is limited to 1.23 at a distance of 1 time the pile diameter from the pile surface (see section 4.4.1), equation (4.32) will most possibly overestimate the scour depth.

According to May et al. (2002), the upstream slope $\tan(\beta_1)$ lies between 1/2 and 1/3 and is approximately twice as steep as the downstream slope, the latter thus varying between 1/4 and 1/6.

According to Hoffmans and Verheij (1997) and Schiereck (2001), the upstream scour angle β_1 can be calculated as:

$$\beta_1 = \arcsin \left(2.9 \cdot 10^{-4} \frac{U_c^2}{\Delta g d_{50}} + (0.11 + 0.75 r_0) f_c \right) \quad (4.33)$$

with U_c the depth averaged flow velocity; $\Delta = (\rho_s - \rho_w) / \rho_w$; ρ_s the sediment density; ρ_w the density of water; g the acceleration due to gravity = 9.81 m/s²; d_{50} the median sediment size; r_0 the relative turbulence intensity at the end of the scour protection:

$$r_0 = \frac{\alpha_U - 1.5}{5 f_c} \quad (4.34)$$

and f_c a roughness function = $C/40$ or = 1 for $C < 40$ with C the Chézy coefficient for the scour protection $\approx 18 \log(12d/k_s)$; d the water depth and k_s the bed roughness, assumed to be equal to $2.5d_{50}$. In the case of sand with a $d_{50} = 2\text{mm}$, $\beta_1 \approx 21.8^\circ$ for a water depth $d = 5\text{m}$, and $\beta_1 \approx 23.6^\circ$ for a water depth of 20m.

To counter possible flow slide, May et al. (2002) describe how a "falling apron" at the edge of the scour protection can be used to avoid that the upstream slope $\tan\beta_1$ of the edge scour becomes too steep. A falling apron consists of (additional)

loose material (rip-rap material can be used) that adapts to the shape of the scour hole which develops at the edge. Ideally, sufficient armour material should be present to cover the sloping face bearing in mind the largest expected scour depth. The deployment of the apron is obtained by material which rolls or slides into the developed scour hole. For this reason May et al. (2002) recommend to use a thicker protection at the edge of the main scour protection. They suggest that the material for the falling apron should amount to 1.5 times the required material for a normal engineering design of a scour protection, as some material will be lost during the formation of the falling apron. When a filter is applied for the main scour protection, the same filter should be used for the falling apron when similar rip-rap material is used for both falling apron and main scour protection. It is however recommended to use twice the normal underlayer thickness, for the same reason of loss of material. Another possibility is to use finer material at the edge, sufficiently large to withstand the flow load, but with enough fine material to fulfil the filter purpose. This can be possible, when considering that the large bed shear stress amplifications near the structure do not have to be taken into account at the edge of the scour protection. Both the limited scour depth and the deployment of a falling apron make sure that the combination of deep edge scour holes and steep upstream slopes are avoided. It therefore seems reasonable to assume that slope instability at the edges will not occur when steepening of the edges is avoided by using a falling apron at the edges.

4.4.2.2. Effect of edge scour on lateral bearing capacity

The edge scour will have an influence on the design of a monopile foundation whenever the scour protection does not cover the complete soil triangle which provides the lateral soil resistance of the pile. When using the same theory as in chapter 2, the soil triangle which should be protected is shown in Figure 4-84. This leads to an extent L_s of the scour protection, equal to:

$$L_s = t_0 \tan\left(\frac{\pi}{4} + \frac{\phi}{2}\right) \quad (4.35)$$

with t_0 the penetration depth of the pile and ϕ the angle of internal friction. When $\phi = 30^\circ$, equation (4.35) gives $L_s = 1.73t_0$, leading to very large scour protection extents. e.g. for a penetration depth t_0 of 15m this leads to a scour protection with a diameter of $11.28D$, when $D = 5m$.

The edge scour is modelled as shown in Figure 4-83. The volume of soil per unit width which is lost by the edge scour V_{eS} can be calculated as:

$$V_{eS} = \frac{S_{edge}^2}{2 \tan \beta_1} + \frac{S_{edge}^2}{2 \tan \beta_2} \quad (4.36)$$

with S_{edge} the depth of the edge scour hole and $\tan(\beta_1)$, $\tan(\beta_2)$ respectively the upstream and downstream slope of the scour hole.

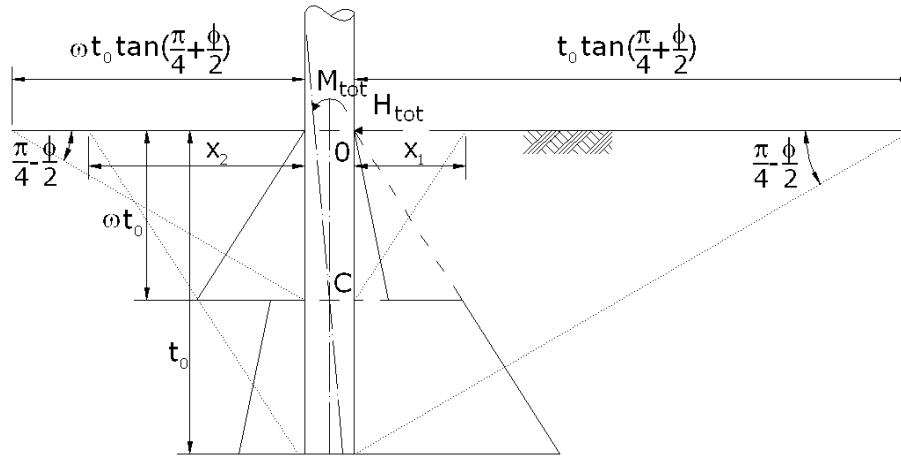


Figure 4-84: Soil triangle which provides the lateral bearing capacity of the pile

The method of Coulomb, which is used in Vandepitte (1979) to calculate the active and passive soil pressure, does not account for the exact location of the edge scour, as long as it fully lies within the soil triangle which generates the active and passive soil pressure.

To know whether the edge scour influences each of the contributing soil pressure parts, the distances x_1 and x_2 , $t_0 \tan\left(\frac{\pi}{4} + \frac{\phi}{2}\right)$ and $\omega t_0 \tan\left(\frac{\pi}{4} + \frac{\phi}{2}\right)$

(Figure 4-84) need to be calculated and compared with the radial extent of the scour protection L_S .

The distances x_1 and x_2 which determine the active soil triangle can be calculated as:

$$x_1 = \sqrt{\omega t_0 \tan(\phi + \psi) \cdot \left(\omega t_0 \tan\left(\frac{\pi}{2} - \phi\right) + \omega t_0 \tan(\phi + \psi) \right)} - \omega t_0 \tan(\phi + \psi) \quad (4.37)$$

$$x_2 = \sqrt{t_0 \tan(\phi + \psi) \cdot \left(t_0 \tan\left(\frac{\pi}{2} - \phi\right) + t_0 \tan(\phi + \psi) \right)} - t_0 \tan(\phi + \psi) \quad (4.38)$$

The method of Vandepitte (1979), used in chapter 2 to determine the pile penetration depth t_0 is adapted to account for the loss in bearing capacity due to the eroded volume at the edge. Both for the active and passive soil pressure, the depth at which the edge scour has no influence and the depth at which the total edge scour is felt are determined. This is illustrated for the active and passive soil pressure respectively on the left and on the right side of Figure 4-85 (note that this location does not coincide with the true location of active and passive soil pressure, which are located as in Figure 4-84).

At the depth t_1 , the passive soil pressure is not influenced by the edge scour and equals $\delta_p \gamma t_1$. At the depth t_2 , the passive soil pressure is decreased by the total loss of weight due to the edge scour and is equal to:

$$\delta_p \gamma \left(t_2 - \frac{V_{eS}}{(t_2 - t_1) \tan\left(\frac{\pi}{4} + \frac{\phi}{2}\right)} \right) \quad (4.39)$$

Equation (4.39) implies that the loss of weight due to the edge scour V_{eS} is spread out over the distance:

$$(t_2 - t_1) \tan\left(\frac{\pi}{4} + \frac{\phi}{2}\right) \quad (4.40)$$

Between t_1 and t_2 the passive soil pressure is linearly interpolated. When the depth t_2 is smaller than the pile penetration depth, the influence of the edge scour hole between t_2 and t_0 remains, albeit less than at the depth t_2 . This is accounted for by spreading the loss of weight due to the edge scour between t_2 and t_0 over the distance which has an influence on the passive soil pressure, equal to:

$$(t_0 - t_1) \tan\left(\frac{\pi}{4} + \frac{\phi}{2}\right) \quad (4.41)$$

Again, a linear interpolation is used between t_2 and t_0 .

The same goes for the active soil pressure and the depths t_3 and t_4 . The distances t_1 , t_2 , t_3 and t_4 shown in Figure 4-85 can be calculated as (Figure 4-83 and Figure 4-85):

$$t_1 = L_s \tan\left(\frac{\pi}{4} - \frac{\phi}{2}\right) \quad (4.42)$$

$$t_2 = \tan\left(\frac{\pi}{4} - \frac{\phi}{2}\right) \left(L_s + \frac{S_{edge}}{\tan \beta_1} + \frac{S_{edge}}{\tan \beta_2} \right) \quad (4.43)$$

$$t_3 = \frac{L_s}{\tan \alpha} \quad (4.44)$$

$$t_4 = \frac{L_s + \frac{S_{edge}}{\tan \beta_1} + \frac{S_{edge}}{\tan \beta_2}}{\tan \alpha} \quad (4.45)$$

with ϕ the angle of internal friction, L_s the effective length of the scour protection, s_{edge} the depth of the edge scour, $\tan(\beta_1)$ and $\tan(\beta_2)$ respectively the upstream and downstream slope of the scour hole and $\tan(\alpha)$:

$$\tan \alpha = \frac{x_2}{t_0} = \sqrt{\tan(\phi + \psi) \left(\tan\left(\frac{\pi}{2} - \phi\right) + \tan(\phi + \psi) \right) - \tan(\phi + \psi)} \quad (4.46)$$

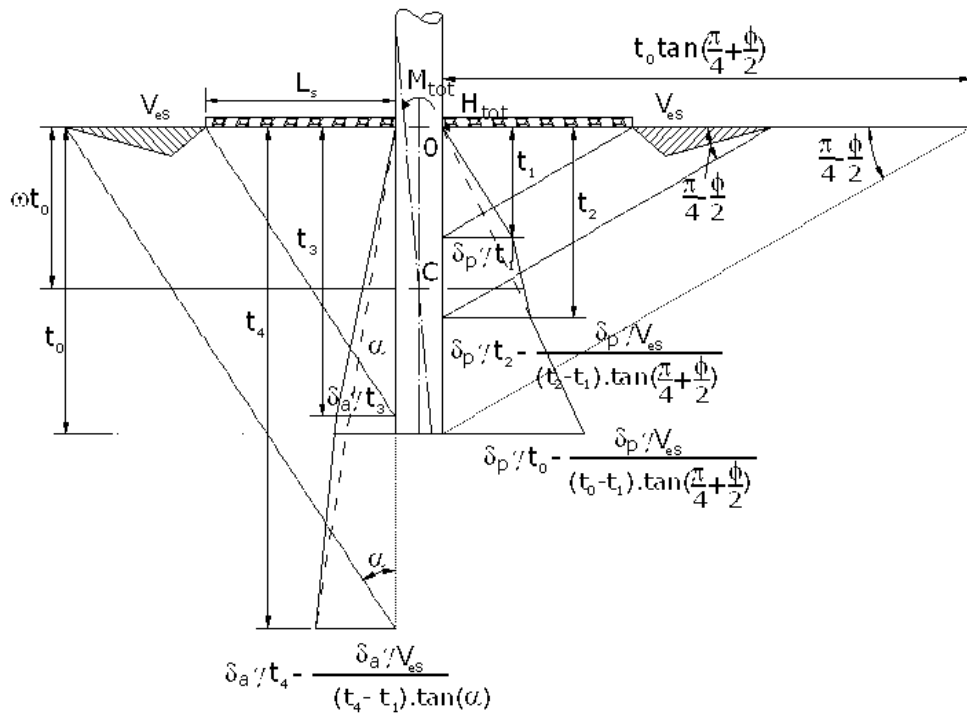


Figure 4-85: Influence of edge scour on lateral bearing capacity according to the method of Vandepitte (1979)

The influence on the lateral bearing capacity of the pile will depend on the location of t_1, t_2, t_3 and t_4 .

Contrary to the influence that scour has on the foundation design, the edge scour only influences the lateral bearing capacity and does not influence the horizontal load or moment (as the pile length remains unchanged).

The influence of the edge scour on the penetration is now computed for the example cases that were used in chapter 2 and the results are given in Table 4-14 and Table 4-15. The main characteristics of the two cases are repeated in Table 4-13. The radial extent of the scour protection L_s is varied from $1D$ to $4D$ with steps equal to the pile diameter and the edge scour depth is varied between 1m and 5m, with steps of 1m. The upstream and downstream slopes of the scour hole are assumed to be $1/2.5$ and $1/5$, according to May et al. (2002).

The formulae which are used to compute the pile penetration depth are written out for the case where $t_1 < \omega t_0$, $\omega t_0 < t_3 < t_0$, $t_2 > t_0$ and $t_4 > t_0$ (equations (4.47) to (4.51)), for example when $L_s = 2D$ and $S_e = 3m$. We refer to chapter 2, section 2.3.1. for the deduction of the original formulae. It is assumed that the neutral soil pressure and the passive soil pressure which acts on the side of the passive soil triangle are not influenced by the edge scour. The other cases are deduced in a similar way.

$$\begin{aligned}
H_u = & D\delta_p\gamma\left[\frac{t_1^2}{2} + t_1(\omega t_0 - t_1) + (E_1 - t_1)\frac{\omega t_0 - t_1}{2}\right] \\
& - D\delta_{pp}\gamma\left[E_1(t_0 - \omega t_0) + (E_2 - E_1)\frac{t_0 - \omega t_0}{2}\right] \\
& + D\delta_a\gamma\left[\omega t_0(t_3 - \omega t_0) + \frac{(t_3 - \omega t_0)^2}{2} + t_3(t_0 - t_3) + (E_3 - t_3)\frac{t_0 - t_3}{2}\right] \\
& - D\delta_a\gamma\frac{(\omega t_0)^2}{2} + D\lambda_n\gamma_0^2(2\omega^2 - 1)\tan\psi + \frac{1}{3}\omega^3\gamma_0^3\tan\phi\tan^3\left(\frac{\pi}{4} + \frac{\phi}{2}\right)
\end{aligned} \tag{4.47}$$

$$\begin{aligned}
M_u = & -D\delta_p\gamma\left[\frac{t_1^2}{3} + t_1(\omega t_0 - t_1)\left(t_1 + \frac{1}{2}(\omega t_0 - t_1)\right) + (E_1 - t_1)\frac{\omega t_0 - t_1}{2}\left(t_1 + \frac{2}{3}(\omega t_0 - t_1)\right)\right] \\
& + D\delta_{pp}\gamma\left[E_1(t_0 - \omega t_0)\left(\omega t_0 + \frac{1}{2}(t_0 - \omega t_0)\right) + (E_2 - E_1)\frac{t_0 - \omega t_0}{2}\left(\omega t_0 + \frac{2}{3}(t_0 - \omega t_0)\right)\right] \\
& - D\delta_a\gamma\left[\omega t_0(t_3 - \omega t_0)\left(\omega t_0 + \frac{1}{2}(t_3 - \omega t_0)\right) + \frac{(t_3 - \omega t_0)^2}{2}\left(\omega t_0 + \frac{2}{3}(t_3 - \omega t_0)\right)\right] \\
& + t_3(t_0 - t_3)\left(t_3 + \frac{1}{2}(t_0 - t_3)\right) + (E_3 - t_3)\frac{t_0 - t_3}{2}\left(t_3 + \frac{2}{3}(t_0 - t_3)\right) \\
& + D\delta_a\gamma\frac{(\omega t_0)^3}{3} + D\frac{2}{3}\lambda_n\gamma_0^3(1 - 2\omega^3)\tan\psi - \frac{1}{6}\omega^4\gamma_0^4\tan\phi\tan^3\left(\frac{\pi}{4} + \frac{\phi}{2}\right)
\end{aligned} \tag{4.48}$$

with t_1 , t_2 , t_3 and t_4 calculated as in equations (4.42) to (4.45) and:

$$E_1 = \left(\left(t_2 - \frac{V_{es}}{(t_2 - t_1)\tan\left(\frac{\pi}{4} + \frac{\phi}{2}\right)} - t_1 \right) \frac{\omega t_0 - t_1}{t_2 - t_1} \right) + t_1 \tag{4.49}$$

$$E_2 = \left(\left(t_2 - \frac{V_{eS}}{(t_2 - t_1) \tan\left(\frac{\pi}{4} + \frac{\phi}{2}\right)} - t_1 \right) \frac{t_0 - t_1}{t_2 - t_1} \right) + t_1 \quad (4.50)$$

$$E_3 = \left(\left(t_4 - \frac{V_{eS}}{(t_4 - t_1) \tan(\alpha)} - t_3 \right) \frac{t_0 - t_3}{t_4 - t_3} \right) + t_3 \quad (4.51)$$

Table 4-13: Characteristic parameters of the example cases

Parameter	Unit	Case 1	Case 2
Pile diameter D	[m]	4.5	4.5
Water depth d	[m]	5	20
Significant wave height H _s	[m/s]	3.7	8
Wave period T _p	[s]	9	12
Tidal current velocity U _c	[m/s]	1.5	1.5
Average wind speed V _w	[m/s]	8	8
Horizontal load H _{tot}	[kN]	1890	1960
Moment M _{tot}	[kNm]	48402	66200
Moment arm r _{tot}	[m]	25.61	33.78
Pile penetration depth without edge scour	[m]	14.4	15.8

Table 4-14: Adjusted penetration depth in case of edge scour for case 1

Pile penetration depth t ₀ [m]	L _s = 1D	L _s = 2D	L _s = 3D	L _s = 4D	L _s = 5D
S _{edge} = 1m	14.5	14.5	14.5	14.5	14.5
S _{edge} = 2m	14.7	14.7	14.6	14.5	14.5
S _{edge} = 3m	14.8	14.7	14.6	14.5	14.5
S _{edge} = 4m	14.8	14.7	14.6	14.5	14.5
S _{edge} = 5m	14.8	14.7	14.6	14.5	14.5

Table 4-15: Adjusted penetration depth in case of edge scour for case 2

Pile penetration depth t ₀ [m]	L _s = 1D	L _s = 2D	L _s = 3D	L _s = 4D	L _s = 5D
S _{edge} = 1m	15.9	15.9	15.9	15.8	15.8
S _{edge} = 2m	16.0	16.0	16.0	15.9	15.8
S _{edge} = 3m	16.1	16.0	16.0	15.9	15.8
S _{edge} = 4m	16.1	16.1	16.0	15.9	15.8
S _{edge} = 5m	16.2	16.1	16.0	15.9	15.8

The edge scour leads to a maximum increase of the required pile penetration depth of 2.1%, in the case that the extent of the scour protection is limited to a distance of $1D$ from the pile and a scour depth of 5m. When the extent $L_s = 2D$, the maximum increase in pile penetration depth is 1.3%, while it reduces to less than 1% once the extent L_s exceeds $3D$. Considering the fact that we did not account for the increase in pile bearing capacity by the extra weight of the scour protection itself, we can conclude that the influence of edge effects on the horizontal pile bearing capacity is limited, certainly when L_s exceeds $2D$, when assuming that a triangular shaped edge scour hole develops. To get a rough estimate of the influence of the shape of the scour hole, for 1 situation, the edge scour hole is assumed to be horizontal and the lowering of the bed is put equal to S_{edge} from the edge of the scour protection (Figure 4-86). When $L_s = 2D$ and $S_{edge} = 5m$, this results in an increase of the pile penetration depth t_0 to 17.2m instead of 16.1m, which is a significant increase, but still the increase of the pile penetration depth is less than 8.5% of the original pile penetration depth.

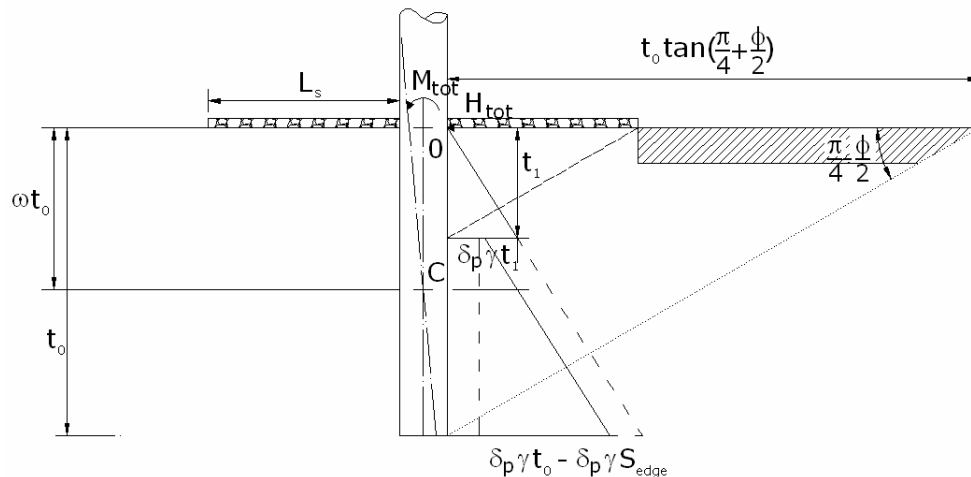


Figure 4-86: Influence of horizontal edge scour hole

4.4.3. Recommendations

All the above shows that the amplification of the flow velocity due to the presence of the pile is limited to a radial distance of 1 to 1.5 times the pile diameter from the pile's surface. It is therefore unlikely that the edge scour is influenced by the pile's presence once the scour protection diameter exceeds 4 times the pile diameter. This does not mean that no edge scour should be expected, but that the edge scour in this case is mainly caused by the transition from the bed to the scour protection and the elevation of the scour protection above the bed. The edge scour will then be limited, with a maximum scour depth of 0.25 times the water depth, according to Schiereck (2001).

Furthermore, the influence of the edge scour on the lateral bearing capacity of the pile is limited when a triangular shape is assumed for the edge scour hole.

Even when a horizontal lowering of the bed is assumed, the influence of the edge scour on the pile penetration depth remains limited when L_s exceeds $2D$. It is advisable to place some extra material at the edges, to form a falling apron and protect the slope of the edge scour closest to the scour protection. The extent of this extra material depends strongly on the expected edge scour depth.

When large uncertainty exists around the expected edge scour, monitoring of the scour protection and armouring of the side slopes of the edge scour might yield a possible alternative.

Based on the above, a scour protection with a minimum diameter of 5 times the pile diameter is recommended, which corresponds to the recommendations of May et al. (2002).

4.5. Conclusions

In this chapter, the experimental research which was performed to determine the required stone size for the top layer of a scour protection around a monopile foundation is discussed. Two approaches were used. In the first approach, the required stone size was determined as the stone size which is on the threshold of motion under the design loading conditions. The experimental results lead to the following equation which relates the required critical bed shear-stress τ_{cr} - representing the resistance of the stones to movement- to the current and wave induced bed shear-stresses τ_c and τ_w , which represent the load which acts on the scour protection:

$$\frac{\tau_{cr}}{\rho_w \Delta g D} = 0.001 + 3.303 \frac{\tau_c}{\rho_w \Delta g D} + 1.015 \frac{\tau_w}{\rho_w \Delta g D} \quad (4.6)$$

in which ρ_w is the density of water; Δ is the relative stone density; g is the gravitational acceleration and D is the pile diameter. The critical bed shear-stress τ_{cr} in this equation is related to the required $D_{67.5}$ of the scour protection. For irregular waves, $U_{10\%}$, which represents the orbital bottom velocity which is exceeded by 10% of the waves has to be used to calculate the wave induced bed shear-stress.

In the second approach, a more economical approach was aspired, in which smaller stone diameters are used and limited stone motion is allowed for top layer stones. A damage number was defined as the maximum damage measured over a sub area with surface equal to the pile's surface. It was found that the damage number depends strongly on the orbital velocity, caused by the waves. One of the most striking results is that the damage is larger when waves oppose the current, a phenomenon where the magnitude of this influence depends on the non-linearity of the waves. Another important conclusion is that the current velocity only influences the damage development when it exceeds a certain value.

The following formula was found to relate the damage number to the loading and resistance characteristics:

$$\frac{S_{3D}}{N^{b_0}} = a_0 \frac{U_m^3 T_{m-1,0}^2}{\sqrt{gd} (s-1)^{3/2} D_{n50}^2} + a_1 \left(a_2 + a_3 \frac{\left(\frac{U_c}{w_s}\right)^2 (U_c + a_4 U_m)^2 \sqrt{d}}{g D_{n50}^{3/2}} \right) \quad (4.30)$$

in which S_{3D} is the damage number; N is the number of waves; U_m is the horizontal orbital velocity at the bottom, caused by waves; $T_{m-1,0}$ is the characteristic wave period; g is the gravitational acceleration; d is the water depth; s is the relative stone density; D_{n50} is the nominal stone diameter; U_c is the current velocity averaged over the water depth and w_s is the fall velocity.

The parameters b_0 , a_0 , a_2 and a_3 were determined through fitting and are equal to 0.243, 0.00076, -0.022 en 0.0079 respectively. The parameters a_1 and a_4 depend on both the current velocity/stone diameter ratio and the current direction and are determined as:

$$a_1 = 0 \quad \text{for } \frac{U_c}{\sqrt{gD_{n50}}} < 0.92 \text{ and waves following current} \quad (4.28)$$

$$a_1 = 1 \quad \text{for } \frac{U_c}{\sqrt{gD_{n50}}} \geq 0.92 \text{ or waves opposing current}$$

$$a_4 = 1 \quad \text{for waves following current} \quad (4.29)$$

$$a_4 = \frac{U_R}{6.4} \quad \text{for waves opposing current}$$

In a last part of this chapter, emphasis was put on the required radial extension of the scour protection. Both the amplification of the bed shear-stress due to the presence of the pile and the effect of edge scour was considered. It was found that, although the amplification of the bed shear-stress is mainly restricted to a distance of 1 to 1.5 times the pile diameter D , the influence of edge effects is limited once the diameter of the scour protection exceeds $4D$.

References

- Ballast Nedam and Oud, J.C., 2002. Foundation Design Monopile - Comparison extra steel consumption versus scour protection - 3.6 & 6.0 MW wind turbines, DOWEC, Amstelveen.
- Breusers, H.N.C. and Raudkivi, A.J., 1991. Scouring. Balkema.
- Cefas, 2006. Scroby Sands Offshore Wind Farm – Coastal Processes Monitoring. Final Report for the Department of Trade and Industry. Contract AE0262, Cefas Lowestoft Laboratory, Suffolk.
- Chiew, Y.M., 1995. Mechanics of Riprap Failure at Bridge Piers. *Journal of Hydraulic Engineering*, 121(9): 635-643.
- CIRIA/CUR, 1991. Manual on the use of rock in coastal and shoreline engineering. CUR 154.
- den Boon, H., Hessels, J. and van Rooij, J., 2003. Cost Reduction of Offshore Wind Parks by Low Cost Load Monitoring of Pile Foundations, Offshore Wind Energy in Mediterranean and other European Seas (OWEMES), Napels, Italy.
- den Boon, J.H., Sutherland, J., Whitehouse, R., Soulsby, R., Stam, C.J.M., Verhoeven, K., Høgedal, M. and Hald, T., 2004. Scour Behaviour and Scour Protection for Monopile Foundations of Offshore Wind Turbines, European Wind Energy Conference & exhibition (EWEC), London, UK.
- Dixen, M., Hatipoglu, F., Sumer, B.M. and Fredsøe, J., 2008. Wave boundary layer over a stone-covered bed. *Coastal Engineering*, 55(1): 1-20.
- E-Connection, Vestas Wind Systems, D.K. and Germanischer Lloyd Windenergie, D., 2002-2004. OPTI-PILE, Fifth Research and Technological Development Framework Programme.
- Federal Highway Administration, 2008. use of waste and byproduct materials in pavement construction.
- Fredsøe, J. and Deigaard, R., 1992. *Mechanics of Coastal Sediment Transport*. Advanced series on Ocean Engineering, Vol. 3. World Scientific.
- Hansen, N.-E.O. and Gislason, K., 2005. Movable scour protection on highly erodible sea bottom, International Coastal Symposium.
- Hjorth, P., 1975. Studies on the nature of local scour. Institute of Technology, Dept. of Water Resources Engineering.
- Hoffmans, G.J.C.M. and Verheij, H.J., 1997. Scour manual. A.A. Balkema, Rotterdam, Netherlands ; Brookfield, VT, xv, 205 p. pp.
- Hofland, B., 2005. Rock & Roll: Turbulence-induced Damage to Granular Bed Protections. Department of Civil Engineering and Geosciences, Delft University of Technology.
- HR Wallingford Ltd for E-Connection Project BV, OPTI-PILE DESIGN TOOL V2.4
- Liu, Z., 2001. Sediment transport, Aalborg.
- Mansard, E.P.D. and Funke, E.R., 1980. The measurement of Incident and Reflected Spectra using a Least Square Method, 17th Coastal Engineering Conference, Sydney, Australia.
- May, R.W.P., Ackers, J.C. and Kirby, A.M., 2002. Manual on Scour at Bridges and Other Hydraulic Structures. CIRIA.
- Melville, B.W. and Coleman, S.E., 2000. Bridge scour. Water Resources Publications Highlands USA, 550 pp.
- Neter, J., Kutner, M.H., Nachtsheim, C.J. and Wasserman, W., 1996. Applied linear statistical models. Irwin Homewood, IL.
- Nielsen, P., 1992. Coastal Bottom Boundary Layers and Sediment Transport. Advanced Series on Ocean Engineering, Vol. 4. World Scientific.

- Raffel, M., Willert, C. and Kompenhans, J., 1998. Particle Image Velocimetry, a practical guide. Springer-Verlag Berlin Heidelberg.
- Schiereck, G.J., 2001. Introduction to Bed, Bank and Shore Protection. Delft University Press.
- Smits, J., 2005. Bepalen van het stromingsprofiel rond een paal bij golfwerking met behulp van Particle Image Velocimetry. MSc Thesis, Ghent University, Ghent, 157 pp.
- Soulsby, R., 1997. Dynamics of Marine Sands: A Manual for Practical Applications. Thomas Telford.
- Sumer, B.M., Christiansen, N. and Fredsøe, J., 1997. The horseshoe vortex and vortex shedding around a vertical wall-mounted cylinder exposed to waves. *Journal of Fluid Mechanics*, 332: 41-70.
- Sumer, B.M. and Fredsøe, J., 1997. Hydrodynamics around cylindrical structures. Advanced series on ocean engineering. World Scientific, Singapore ; River Edge, NJ, xviii, 530 p. pp.
- Sumer, B.M. and Fredsøe, J., 2001. Scour around a Pile in Combined Waves and Current. *Journal of Hydraulic Engineering*, 127(5): 403-411.
- Sumer, B.M. and Fredsøe, J., 2002. The mechanics of scour in the marine environment. Advanced series on ocean engineering. World Scientific, River Edge, N.J., 536 pp.
- Sumer, B.M., Fredsøe, J. and Christiansen, N., 1992. Scour Around Vertical Pile in Waves. *Journal of Waterway, Port, Coastal and Ocean Engineering*, 118(1): 15-31.
- Sumer, B.M., Whitehouse, R.J.S. and Torum, A., 2001. Scour around coastal structures: A summary of recent research. *Coastal Engineering*, 44(2): 153-190.
- US Army Corps of Engineers, 2002. Coastal Engineering Manual. Engineer Manual 1110-2-1100, Washington, D.C. .
- Van der Meer, J.W., 1988. Rock Slopes and Gravel Beaches Under Wave Attack. Delft Hydraulics.
- Van Oord, A.C.Z., 2003. Scour protection for 6 MW OWEC with monopile foundation in North Sea, Gorinchem.
- van Rijn, L.C., 1993. Principles of Sediment Transport in Rivers, Estuaries and Coastal Seas. Aqua Publications.
- Vandepitte, D., 1979. Berekening van constructies I. E. Story-Scientia, Gent, 614 pp.
- Vansteenkiste, T., 2007. Vergelijken van PIV (Particle Image Velocimetry) metingen van het stromingsprofiel rond een paal met golven op grote en kleine schaal. MSc Thesis, Ghent University, Ghent, 161 pp.
- Whitehouse, R., 1998. Scour at marine structures : a manual for practical applications. Thomas Telford, London, xix, 198 pp.
- Whitehouse, R.J.S., Sutherland, J. and O'Brien, D., 2006. Seabed scour assessment for offshore windfarm, International Conference on scour and erosion, Nanyang University, Nanyang, Singapore.
- Wiberg, P.L. and Sherwood, C.R., 2008. Calculating wave generated bottom orbital velocities from surface wave parameters. *Computers & Geosciences*.

PART III. WAVE RUN-UP

Chapter 5. State of the art in wave run-up on monopiles

5.0 Introduction

Besides the wind turbines' foundation, the wave run-up on the pile at the SWL create new challenges compared to onshore wind turbines: wave run-up and wave impacts cause unexpected damage to boat landing facilities and platforms of the existing offshore wind parks. Figure 5-1 shows two pictures of wave run-up on one of the wind turbine foundations of the Horns Rev wind mill farm. The conditions at which the pictures were taken are $H_s = 2.5\text{m}$, while the platform level is 9.0m above SWL. Actual run-up values are much higher than expected or accounted for in the design. A logical countermeasure against run-up could be to build the platforms on a higher level, where they cannot be reached. However, this brings along other problems. As the wind turbines have to be accessible under all conditions, safety requirements dictate that the distance between boat and platform has to be limited. If these requirements are not met, additional safety measures have to be taken. For example, intermediate platforms are needed when the main platform is placed on too high a level, leading to the initial design problem. Consequently, it is important to have an insight in run-up levels and forces caused by the run-up. To assess the forces due to wave run-up, the distribution of run-up around the pile and the maximum run-up height need to be known. This chapter and chapter 6 illustrate the wave run-up problem as it was discussed in De Vos et al. (2007).



Figure 5-1: Wave run-up on one of the towers of the Horns Rev wind mill farm; $H_s = 2.5\text{m}$, platform level = 9m above SWL; © *Elsam*.

De Vos et al. (2007) describe the existing run-up models and a new physical model study of the run-up heights and run-up distribution on two shapes of foundations for offshore wind turbines, including both regular and irregular waves. The article is almost entirely reproduced in these chapters. The influence of wave steepness, wave height and water depth on run-up is investigated. The measured run-up values are compared with applicable theories and previous experimental studies predicting run-up on a circular pile.

5.1 Analytical models for wave run-up

A review of applicable theories and previous experimental studies is presented to provide the reader with a clear perspective on how the new test results add to this knowledge base. The main perspective of the study is to present a clear and easy to use formula to predict wave run-up on wind turbine foundations and to give an estimate of the run-up distribution around the pile.

5.1.1 Velocity stagnation head calculations

Hallermeier (1976) suggests an estimate for run-up by considering the stagnation head at the wave crest as it strikes the cylinder. The assumption is that the water particles at the wave crest are forced to convert their kinetic energy into potential energy by rising a distance equal to $u^2/2g$ up the cylinder above the elevation of the crest. Thus, the run-up is predicted to be

$$R_u = \eta_{\max} + \frac{u^2}{2g} \quad (5.1)$$

where u = the water particle velocity at the wave crest η_{\max} , both evaluated using some appropriate wave theory.

5.1.2 Diffraction theory

Linear diffraction theory allows calculation of the wave field around a body of arbitrary shape. This theory is valid for sufficiently small wave heights so linear wave theory is applicable. The result for the elevation around a circular cylinder surface is (Sarpkaya and Isaacson (1981)):

$$\frac{\eta}{H} = \text{Re} \left[\left[\sum_{m=0}^{\infty} \frac{i\beta_m \cos(m\theta)}{\pi k a H_m^{(1)}(ka)} \right] \cdot e^{-i\omega t} \right] \quad (5.2)$$

where $H_m^{(1)}$ is a Hankel function of the first kind; $k = 2\pi/L$ is the wave number and

$$\begin{aligned} \beta_m &= 1, & m &= 0 \\ \beta_m &= 2(-1)^m i^m, & m &> 0 \end{aligned}$$

The run-up $R_u(\theta)$ around the cylinder is the maximum value of η . Extension of diffraction theory to the second order has been carried out by several other authors (Kriebel (1990), Martin et al. (2001)), using different approaches. These authors have shown that there is a large influence in using a second order theory to calculate run-up and it is not sufficient to attempt an extrapolation based on linear diffraction theory.

As no analytical solution for the maximum value of the expression for η exists, an approximation is used further on in the article. The approximate result for run-up on the up-wave side of a circular cylinder is

$$\frac{R_u}{\eta_{\max}} = \left[1 + \left(\frac{2\pi D}{L} \right)^2 \right]^{1/2} \quad (5.3)$$

for a cylinder with diameter D .

The threshold of linear diffraction is widely regarded as $D/L > 0.2$. In this range, linear diffraction theory suggests that scattered wave energy is negligibly small. However, this is not the case for steep waves. Experience shows that there are significant nonlinear contributions in the case of steep waves, leading to a considerable amplification of the surface elevation. Stansberg et al. (2005) found that second-order diffraction analysis compares reasonably well in many cases, although there are still some discrepancies in steep waves. Fully non-linear modelling is advised in the case of steep waves.

5.2 Previous experimental studies and semi-empirical run-up formulae

Some previous experimental studies related to the same subject of run-up on piles are shortly described below. If possible, the results of the present experiments are compared with these findings (chapter 6). In table 2 a comparative view of the dimensionless parameters used in these earlier studies on wave run-up are compared with the parameter range of the current tests.

5.2.1 Wave run-up and forces on a cylinder in regular and random waves

Niedzwecki and Duggal (1992) performed a small-scale experimental study to investigate wave run-up on rigid full-length and truncated circular cylinders under regular and random sea conditions.

They found that linear diffraction theory underestimates the wave run-up for all but very low wave steepness. When applying the velocity stagnation head theory to the regular wave results, Niedzwecki and Duggal used linear theory to calculate wave kinematics and found that run-up heights were under predicted. They employed a semi-empirical variation of the formula, using a coefficient m to be found by fitting a straight line to the data, given by

$$R_u = \frac{H}{2} + m \frac{u^2}{2g} \quad (5.4)$$

with H the (regular) wave height, determined as the average of 3 consecutive peaks and troughs. They found that on average, $m = 6.83$ for a full-length cylinder, while using the maximum horizontal velocity u at the still water level. They found no significant differences for the wave run-up on the truncated and full-length cylinders and conclude that for the considered draft ($d \approx 2D$) the wave run-up is not significantly influenced by the wave kinematics below a certain elevation.

Their experiments were conducted in a flume with dimensions $l \times w \times h = 37\text{m} \times 0.91\text{m} \times 1.22\text{m}$, with a pile diameter of 0.114m. They measured the wave elevation over one-half of the cylinder's circumference by five equally spaced resistance type wave gauges, placed directly on the cylinder surface.

In another paper, Niedzwecki and Huston (1992) allow a second coefficient to vary the linear fit, and arrive at

$$R_u = 0.56H + 6.52 \frac{u^2}{2g} \quad (5.5)$$

for a single cylinder.

Table 5-1: Comparison of experimental studies on wave run-up

Reference	scatter parameter ka [-]	Deep water wave steepness $\frac{H}{gT^2/2\pi}$ [-]	Relative water depth d/L [-]	research focus
Niedzwecki et al. 1992	0.11	0.010	0.28	full length and truncated monopiles; regular and irregular waves
	- 1.30	- 0.126	- 3.32	
Martin et al. 2001	0.12	0.040	0.28	monopile; regular waves
	- 0.32	- 0.126	- 3.32	
Mase et al. 2001	0.08	0.007	0.09	monopile; regular and irregular waves
	- 0.24	- 0.065	- 0.27	
Current study	0.064	0.016	0.085	monopile/ cone; regular and irregular waves
	- 1.50	- 0.10	- 1.99	

5.2.2 Wave run-up on columns due to regular waves

Martin et al. (2001) have investigated run-up on columns caused by steep, deep water regular waves. They have compared their experimental results with different theories, including the theories described above (see section 5.1) and conclude that most theories underestimate the run-up values. They found that linear diffraction theory is inadequate and used the superposition method of Kriebel (1992), which was still found inadequate for their regime of interest (Table 5-1), although it did give an improvement of linear diffraction theory. They concluded that the semi-empirical method, suggested by Niedzwecki and Huston overestimates the run-up in nearly all cases.

Their experiments were conducted in a very narrow flume with dimensions $l \times w \times h = 20\text{m} \times 0.4\text{m} \times 1\text{m}$, with a pile diameter of 0.11m. With a pile diameter to flume width ratio of 0.275, the influence of the side walls on the measurements might be significant. To avoid artificially high blockage in the laboratory model, the value of pile diameter to flume width ratio should be smaller than 0.167 Whitehouse (1998). They estimated the run-up with visual examination of video recordings.

5.2.3 Wave run-up of random waves on a small circular pier

Mase et al. (2001) investigated run-up heights of random waves on a small circular pier, installed on a uniform bottom slope, $\tan\beta$, varying between 1:40 to 1:10. They derived a prediction formula for the 2% excess run-up height, as well as the maximum and the one-third maximum run-up heights on a small diameter circular pier as a function of bottom slope $\tan\beta$, deep water wave height H_0 , deep water wave length L_0 and water depth d at the pile. They arrive at the following formula for the 2% run-up (with a correlation coefficient $r = 0.98$):

$$\frac{R_{u2\%}}{d} = \left(0.24 - \frac{0.004}{\tan\beta}\right) + \left(11.43 - \frac{0.20}{\tan\beta}\right) \cdot \exp\left[-\left(1.55 - 0.77 \exp\left\{-69.46\left(\frac{H_0}{L_0}\right)\right\}\right) \cdot \left(1.02 - \frac{0.015}{\tan\beta}\right) \cdot \left(\frac{d}{H_0}\right)\right] \quad (5.6)$$

They found a linear relationship between the maximum run-up $R_{u\max}$, the significant run-up R_{us} and the 2% excess run-up $R_{u2\%}$:

$$R_{u\max} = 1.22 \cdot R_{u2\%} \quad (5.7)$$

$$R_{us} = 0.61 R_{u2\%} \quad (5.8)$$

Both formulae are valid for the following conditions:

$$\frac{1}{40} \leq \tan \beta \leq \frac{1}{10}$$

$$0.004 < \frac{H_0}{L_0} < 0.05 \quad (5.9)$$

$$\frac{d}{H_0} < 6$$

Their experiments were conducted in a flume with dimensions $l \times w \times h = 40\text{m} \times 0.7\text{m} \times 0.75\text{m}$, with a pile diameter of 0.114m. They measured the run-up variation by means of a capacitance-type wave gauge, placed 3 mm in front of the structure.

Because the bottom slope at an offshore location of a wind turbine park is often very flat, the present study uses an offshore bottom slope of 1:100, which is much flatter than the bottom slope in the experiments of Mase et al. (2001). Although there is an overlap in most parameters, the comparison of the present test results with the equation (5.6) does not give good results, due to the difference in offshore bottom slope ($\tan\beta = 1:40$ to $1:10$ as compared to $\tan\beta = 1:100$ in this study). This shows that it is recommended to only use the formula of Mase et al. within the specified range.

References

- De Vos, L., Frigaard, P. and De Rouck, J., 2007. Wave run-up on cylindrical and cone shaped foundations for offshore wind turbines. *Coastal Engineering*, 54(1): 17-29.
- Hallermeier, R.J., 1976. Nonlinear Flow of Wave Crests Past a Thin Pile. *Journal of the Waterways, Harbors and Coastal Engineering Division*, 102(4): 365-377.
- Kriebel, D.L., 1990. Nonlinear wave interaction with a vertical circular cylinder. Part. 1: diffraction theory. *Ocean Engineering*, 17(4): 345-77.
- Kriebel, D.L., 1992. Nonlinear wave interaction with a vertical circular cylinder. II: Wave run-up. *Ocean engineering*, 19(1): 75-99.
- Martin, A.J., Easson, W.J. and Bruce, T., 2001. Runup on Columns in Steep, Deep Water Regular Waves. *Journal of Waterway, Port, Coastal and Ocean Engineering*, 127(1): 26-32.
- Mase, H., Kosho, K. and Nagahashi, S., 2001. Wave Runup of Random Waves on a Small Circular Pier on Sloping Seabed. *Journal of Waterway, Port, Coastal and Ocean Engineering*, 127(4): 192-199.
- Niedzwecki, J.M. and Duggal, S.D., 1992. Wave Run-up and Forces on Cylinders in Regular and Random Waves. *Journal of Waterway, Port, Coastal, and Ocean Engineering*, 118(6): 615-634.
- Niedzwecki, J.M. and Huston, J.R., 1992. Wave interaction with tension leg platforms. *Ocean Engineering*, 19(1): 21-37.
- Sarpkaya, T. and Isaacson, M., 1981. *Mechanics of wave forces on offshore structures*. Van Nostrand Reinhold Co., New York.
- Stansberg, C.T. et al., 2005. OTC 17487 Extreme Wave Amplification and Impact Loads on Offshore Structures, Offshore Technology Conference, Houston, TX, USA.
- Whitehouse, R., 1998. *Scour at marine structures : a manual for practical applications*. Thomas Telford, London, xix, 198 p. pp.

Chapter 6. Experimental research on wave run-up on a monopile foundation

6.0 Introduction

This chapter presents the results of a small-scale experimental study that examines wave run-up on two different types of pile foundations subject to both regular and random waves. As offshore platforms are placed under diverse conditions, different foundation types are used. It is reasonable to assume that the run-up is influenced by the shape of the foundation. The scale and parameters selected for this study reflect a range useful for understanding the run-up phenomenon on a wind turbine foundation, placed in relatively deep water conditions (17 m to 25 m).

6.1 Experimental set-up

6.1.1 Description of set-up and model

The run-up experiments are conducted in a wave flume with dimensions $l \times w \times h = 30\text{m} \times 1.5\text{ m} \times 1\text{ m}$ at Aalborg University, Denmark. Figure 6-1 shows the test set-up. A piston-type wave paddle generates waves at one end of the wave flume, where an absorbing beach is installed at the other end. Two models (Figure 6-2) are built in front of the absorbing beach. One model is a monopile foundation, whereas the second model is a cone shaped gravity type foundation. Both models have a pile diameter of 0.12 m. The water depth varies between 0.35 and 0.5 m at the location of the foundation. The offshore slope is fixed at 1:100.

Ten resistance-type wave gauges are mounted on the model to measure the wave run-up and to determine the variation of the run-up around the pile. Figure 6-3 shows the position of the wave gauges whereas Figure 6-4 shows a picture of the mounted wave gauges. The wave gauges on the pile are mounted approximately 2 mm from the pile surface. This way it is insured that the water is able to move freely up and down the wave gauges. Marking tapes are placed with a distance of 0.02 m and video recordings are made to allow visual inspection of the recorded run-up measurements.

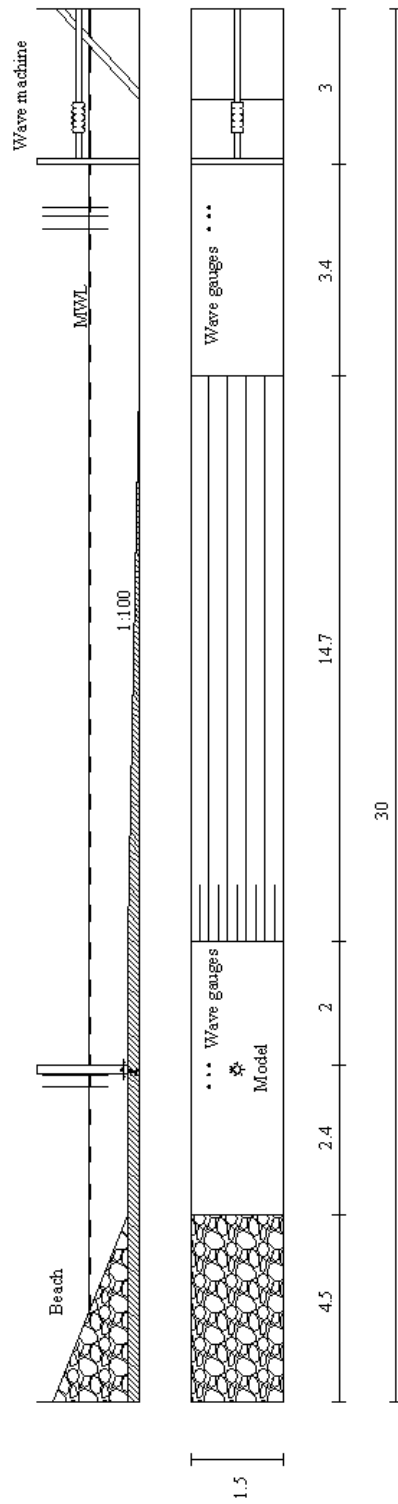


Figure 6-1: Test set-up, all values in meters

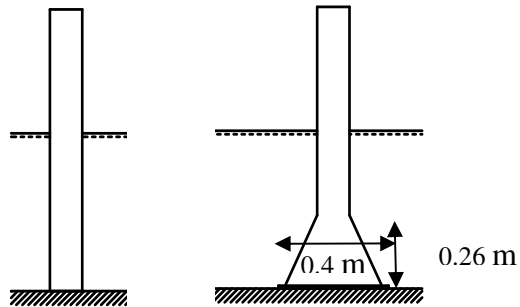


Figure 6-2: Model of monopile foundation and cone foundation

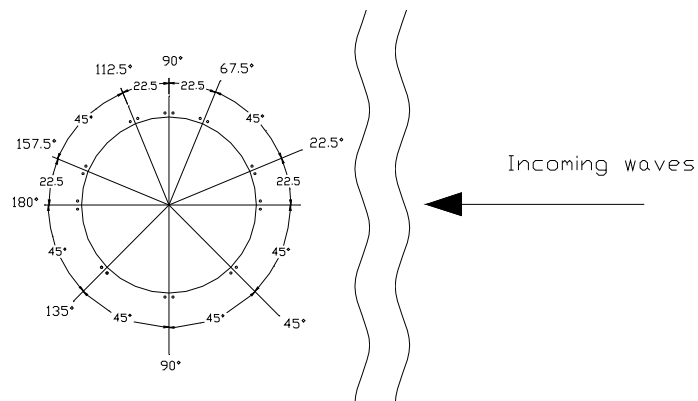


Figure 6-3: Position of wave gauges: 10 wave gauges installed 2 mm from the pile surface.



Figure 6-4: Mounted capacitance wave gauges on monopile and cone foundation.

6.1.2 Wave conditions

Two different wave types are tested, regular and irregular waves. The target spectrum of the irregular waves is a JONSWAP spectrum, with a peak enhancement factor γ of 3.3. A total of 60 regular and 36 irregular tests are carried out.

The water surface elevations are measured next to the model with two times three resistance wave gauges. Three gauges are used to separate the incoming and reflected waves by means of the method by Mansard and Funke (1980). Target wave conditions are generated satisfactorily, although slight deviations occur.

The records of irregular waves contain approximately 500 individual waves. The records of regular waves contain approximately 50 waves.

Table 6-1: Experimental conditions for irregular waves

d	H _s	T _p	$s_0 \left(\frac{2\pi H_s}{g T_p^2} \right)$	ka	d/L	models
[m]	[m]	[s]	[-]	[-]	[-]	
0.5	0.143	2.10	0.021	0.0877	0.11626	monopile
0.5	0.159	2.28	0.020	0.0799	0.10603	monopile cone
0.5	0.170	2.56	0.017	0.0701	0.09291	monopile cone
0.5	0.195	2.56	0.019	0.0701	0.09291	monopile cone
0.5	0.199	2.64	0.018	0.0676	0.08969	monopile
0.5	0.133	1.78	0.027	0.1069	0.14173	monopile cone
0.5	0.155	1.95	0.026	0.0957	0.12695	monopile cone
0.5	0.165	1.95	0.028	0.0957	0.12695	monopile cone
0.5	0.179	2.10	0.026	0.0877	0.11626	monopile cone
0.5	0.192	2.10	0.028	0.0877	0.11626	monopile cone
0.5	0.127	1.44	0.039	0.1413	0.18741	monopile
0.5	0.146	1.52	0.041	0.1313	0.17413	monopile
0.5	0.159	1.61	0.039	0.1218	0.16154	monopile
0.5	0.167	1.71	0.037	0.1127	0.14943	monopile
0.5	0.188	1.82	0.036	0.104	0.138	monopile
0.5	0.112	1.12	0.057	0.2047	0.27147	monopile
0.5	0.128	1.15	0.061	0.1956	0.25941	monopile cone
0.5	0.144	1.30	0.054	0.1629	0.21612	monopile cone
0.5	0.158	1.41	0.051	0.1448	0.19202	monopile cone
0.5	0.163	1.39	0.054	0.1483	0.19669	monopile
0.35	0.127	1.67	0.029	0.1328	0.1233	monopile
0.35	0.133	1.95	0.022	0.1112	0.10321	monopile
0.35	0.144	2.28	0.018	0.0936	0.0869	monopile
0.35	0.142	2.10	0.021	0.1022	0.09492	monopile
0.35	0.145	2.48	0.015	0.0852	0.07908	monopile

For the regular waves, wave heights vary between 0.01 m and 0.26 m, with a wave period varying between 0.40s and 2.78s, corresponding with a wave steepness varying between 0.02 and 0.12. For the irregular waves, only larger wave heights (H_s between 0.127 m and 0.224 m) are generated. Table 6-1 shows the most important parameters for the irregular wave tests. The deepwater steepness is defined as $s_0 = H_s / (gT_p^2/2\pi)$.

6.1.3 Definition of run-up

As shown in Figure 6-3, 10 resistance wave gauges are mounted on the monopile to measure the run-up distribution around the pile. Run-up is defined as the "green water" level on the surface of the pile. Splash is not taken into account as the wave gauges only measure the green water level. Splash is a phenomenon which occurs mostly with the largest waves. It is assumed that the largest forces on the structure are caused by the green water level.

As mentioned, video recordings were made during the tests. They show that the run-up levels are measured accurately. Only thin run-up layers, caused by the highest waves with very high run-up levels are underestimated slightly due to the distance of wave gauges to the pile (2 mm). The video images allow differentiating between the run-up caused by breaking waves and the run-up caused by non-breaking waves. They also allow to capture the splash height.

6.2 Analysis of wave run-up experiments

6.2.1 Dimensionless quantities

For the irregular waves, it is not obvious what statistical quantity should be used for design. The highest and largest waves cause the largest run-up values, but the thickness of the run-up layer is larger for smaller waves. It is therefore not sure that the highest waves cause the highest load on the deck.

The 2% excess run-up height $R_{u2\%}$ is often used in the studies of run-up on slopes. The use of $R_{u2\%}$ allows a safe design of coastal structures against wave overtopping. Mase et al. (2001) found that the R_{max} value only differs by a constant factor from the $R_{u2\%}$ value. They found that $R_{max} = 1.22 R_{u2\%}$. We found approximately the same value in the present study ($R_{max} = 1.23 R_{u2\%}$). For this reason only the $R_{u2\%}$ value is studied.

In most theories (valid for regular waves), the run-up is either normalised by the maximum elevation η_{max} or by the wave height H_{max} . When using linear theory this leads to $\eta_{max} = H_{max}/2$, but for a large range of waves (in particular for breaking waves), linear theory is not valid. Therefore beside linear wave theory, also higher order wave theories are used.

6.2.2 Regular wave test results

Wave height and run-up measurement data are only considered in the steady part of the wave train. Figure 6 shows an example of a steady part of the wave

train, including both the wave signal next to the pile and the simultaneous measurements on all 10 run-up gauges.

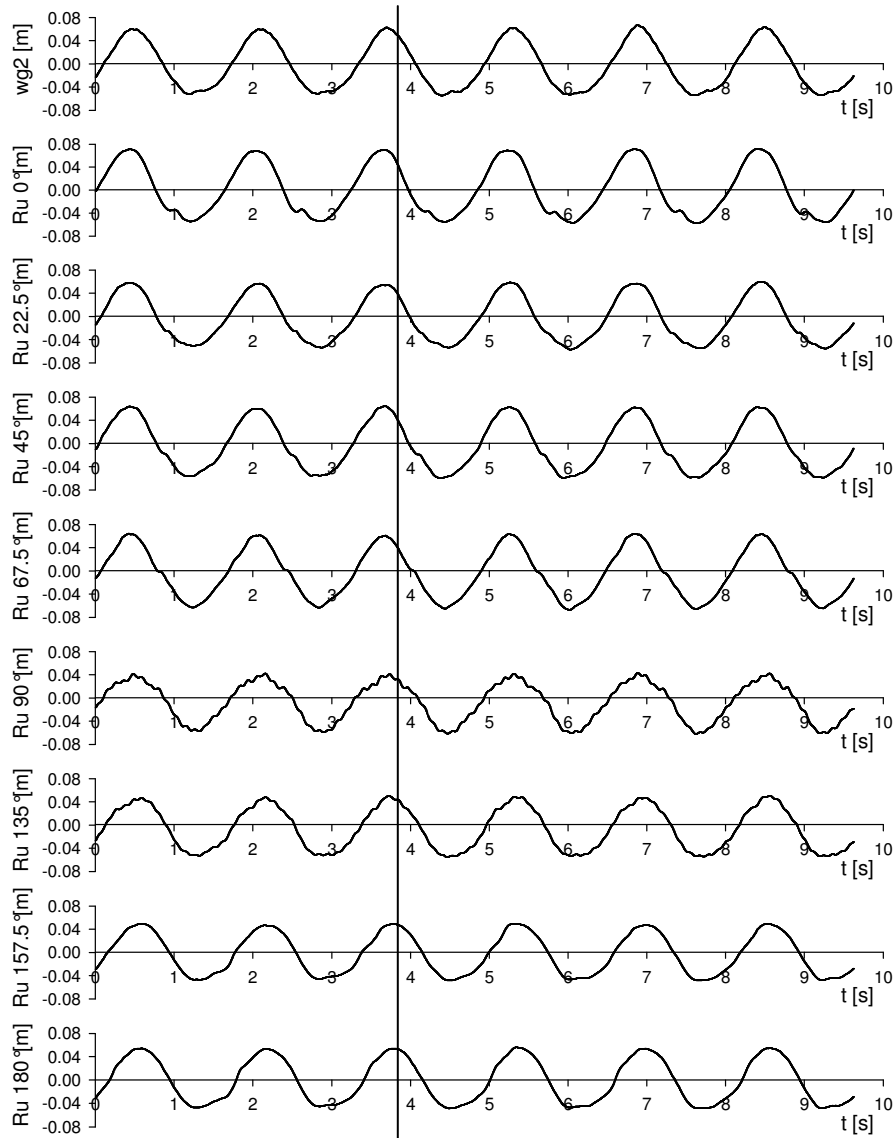


Figure 6-5: Steady part of regular wave train ($H = 0.12\text{m}$, $T = 1.6\text{s}$): wave signal next to the pile (wg2) and simultaneous measurements of run-up gauges.

Even when a steady wave train is reached, slight variations in the waves and in the run-up are observed. To accommodate for the variation, we average 20 consecutive peaks and troughs for the regular wave data. Averaging yields mean values of wave elevation, run-up and run-down. These mean values are plotted in Figure 6-6 to Figure 6-13.

Some electrical noise on the measured signal is observed. For small wave heights, this signal noise is of the same magnitude as the difference between

measured run-up and measured wave height, which might lead to values of $(R_u - H/2)$ smaller than 0. A wave height of 0.14m yields a noise ratio of less than 12%. For a wave height of 0.24m, the noise ratio is already smaller than 2%.

Figure 6-6 shows the measured $(R_u - H/2)$ - values on the front side of the pile as a function of wave height, for a target deep water wave steepness $s_0 = 0.03$ (measured deep water wave steepness s_0 varying between 0.24 and 0.34). Overlaid on this graph are three theories using linear wave kinematics and two theories using higher order wave kinematics. Linear theories include the velocity stagnation head theory as well as the suggestions from Niedzwecki and Duggal (1992) and Niedzwecki and Huston (1992). The applied higher order theories are the 2nd order Stokes theory and Fenton's Fourier approximation method.

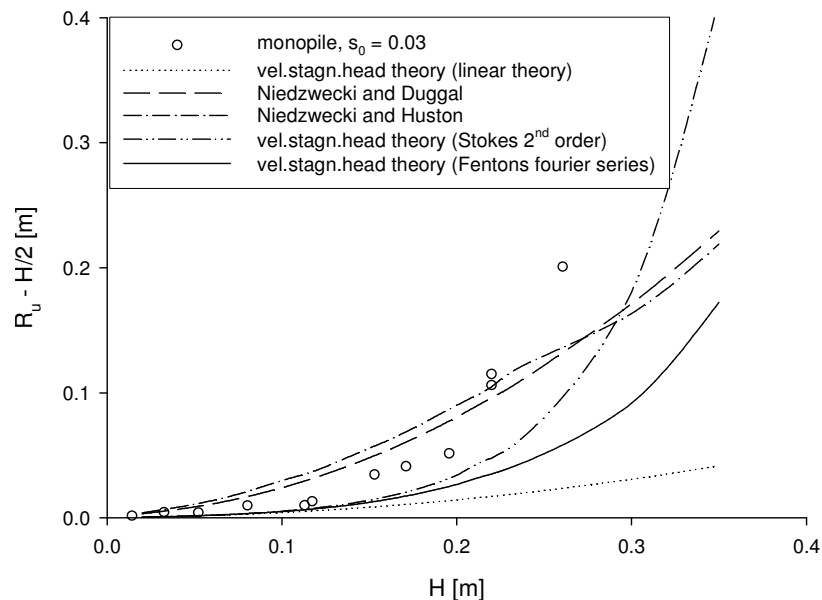


Figure 6-6: Run-up on cylindrical monopile for steepness $s_0 = 0.03$ (regular waves, $d = 0.5\text{m}$).

The graph shows that the velocity stagnation head theory seriously underestimates the run-up value (starting from $H = 0.16$ m) when linear theory is applied to calculate the wave kinematics in the crest. The suggestions made by Niedzwecki and Duggal (1992) and by Niedzwecki and Huston (1992) both overestimate the run-up for smaller wave heights, but for larger wave heights a substantial underprediction is observed. More so, the curve does not reproduce the test results. The occurrence of the measurement at $H = 0.26$ m indicates that both theories might seriously underestimate the wave run-up for very high wave heights. Better results are obtained when velocity stagnation head theory is calculated with higher order (non-linear) wave crest kinematics (assuming that $\eta_{max} = H_{max}/2$), as mentioned by other authors (Martin et al. (2001)). The applied non-linear theories are the 2nd order Stokes theory and Fenton's Fourier approximation method, with 20 Fourier components. The improvement lies

especially in the shape of the curve which follows the trend of the measurements more accurately. $H_{max}/2$ is used instead of η_{max} in this representation so that measured run-up values are located above the predictions made by the non-linear theories.

The second order Stokes theory seems to hand good results (bearing in mind that η_{max} is underestimated by using $H_{max}/2$ in the velocity stagnation head theory). A huge advantage is that this theory can be solved analytically, while the Fourier approximation method cannot. The implementation of Fenton's theory was done in the program ACES (1992).

In Figure 6-7, experimental results for different wave steepness are shown. It is difficult to identify from the figure whether the wave steepness has a big influence on the wave run-up, but the highest run-up values are measured for the lowest steepness and run-up values for the highest steepness ($s = 0.07$) are somewhat lower than for the other steepness. Linear theory predicts higher run-up values for higher steepness, as u increases when the steepness increases.

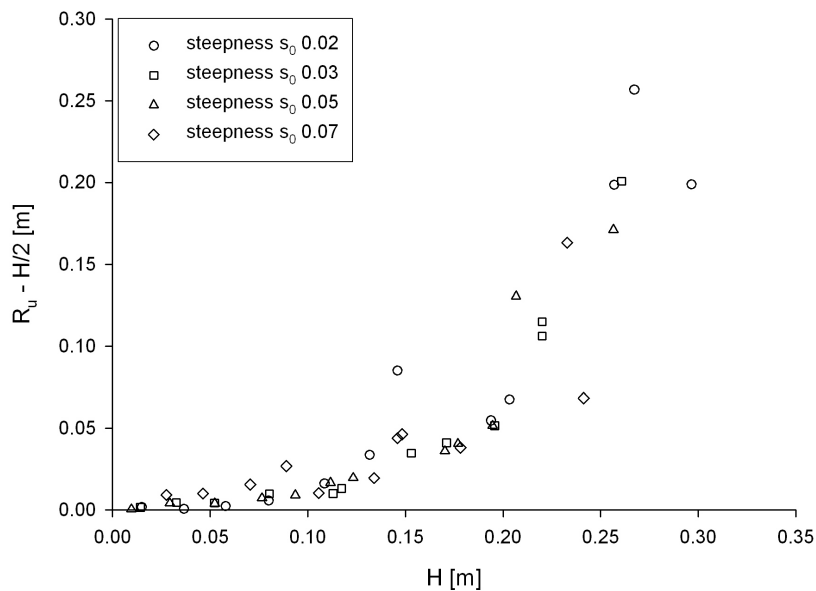


Figure 6-7: Run-up on monopile for different wave steepness (regular waves, d = 0.5m).

Figure 6-8 compares the wave run-up on a monopile with the run-up on a cone foundation for regular waves with the same wave steepness. Run-up values for the cone foundation are higher with increasing height of the incident waves.

In Figure 6-9 to Figure 6-13 the measured run-up is compared to the estimated run-up for all tests with regular waves, while using the theories which are described in chapter 5.

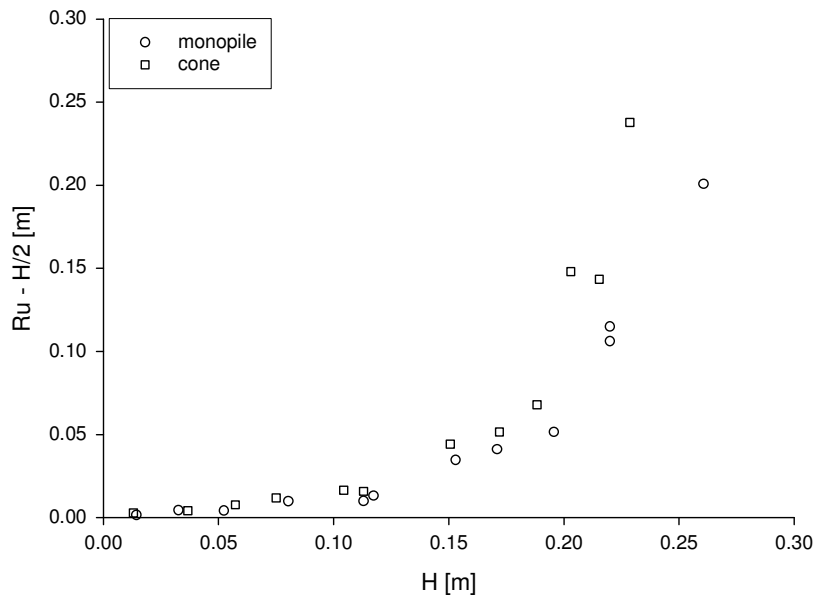


Figure 6-8: Run-up on cylindrical and cone shaped foundation for wave steepness $s_0 = 0.03$ (regular waves, $d = 0.5\text{m}$).

In Figure 6-9, the velocity stagnation head theory is represented, while linear theory is used to calculate the wave kinematics. Low run-up values are predicted very well, but high run-up values are clearly underestimated.

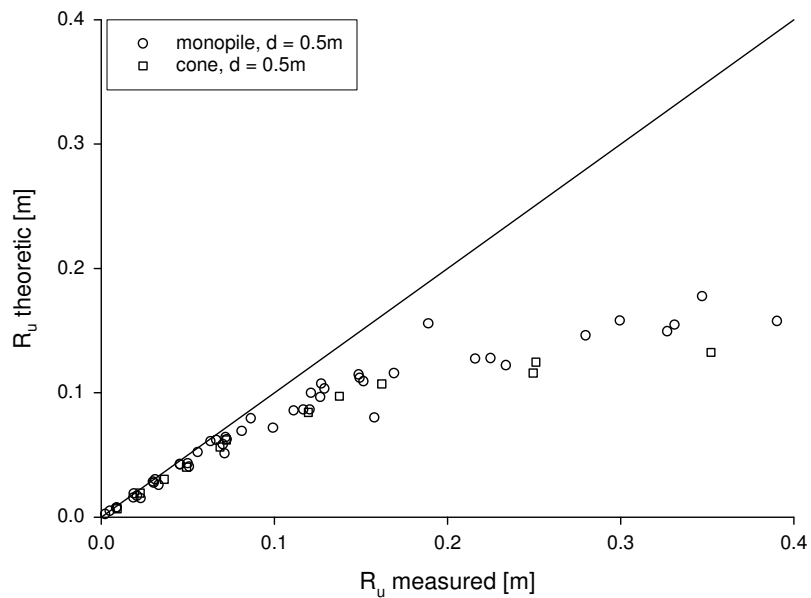


Figure 6-9: Comparison between measured and theoretical run-up. Theoretical run-up is calculated using the velocity stagnation head theory (equation (5.1)) with linear theory for wave kinematics (regular waves).

Figure 6-10 shows the prediction made by linear diffraction theory. The run-up prediction shows the same trend as for the velocity stagnation head theory; run-up is seriously underestimated for almost all measured run-up values.

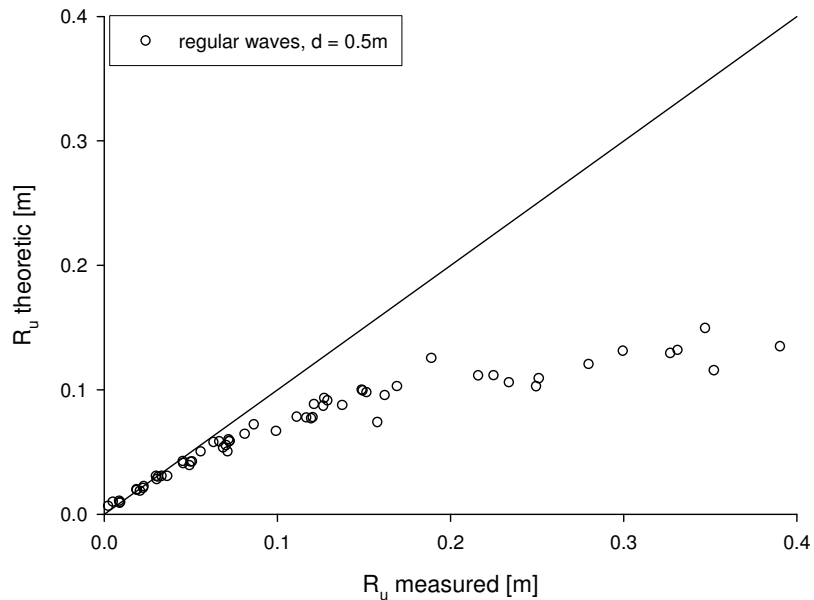


Figure 6-10: Comparison between measured (both cylindrical and cone shaped foundation) and theoretical run-up. Theoretical run-up is calculated using the diffraction theory (equation (5.3)) with linear theory for wave kinematics (regular waves).

In Figure 6-11, the adjustment made by Niedzwecki and Duggal (1992) is presented. In the study of Martin et al. (2001), all run-up values were overestimated by this formula. The present test results show an overestimation of low run-up values, while the high run-up values are underestimated. Furthermore, it is not possible to get a good estimate of the run-up by adjusting the value of the parameter m in equation (5.4) while using linear theory for the wave kinematics. Higher order wave theories offer a better solution.

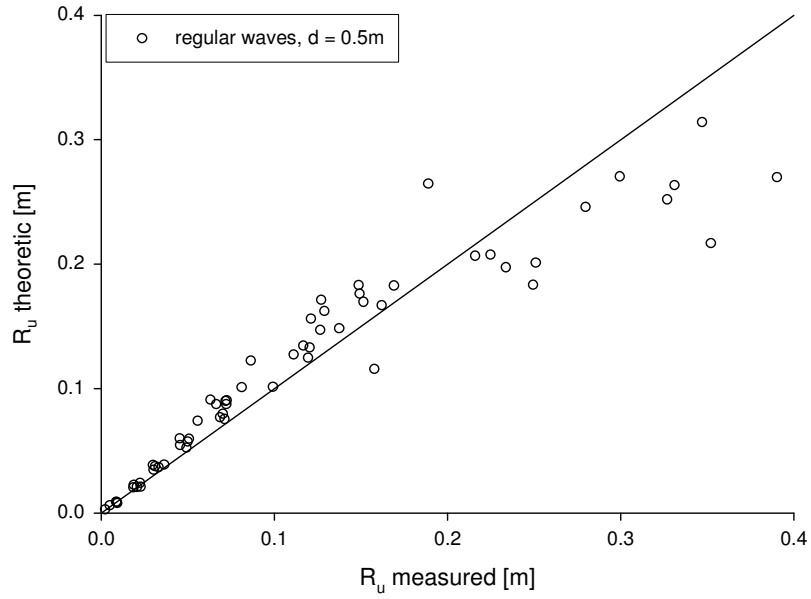


Figure 6-11: Comparison between measured (both cylindrical and cone shaped foundation) and theoretical run-up. Theoretical run-up is calculated using Niedzwecki and Duggal's adjustment for the velocity stagnation head theory (equation (5.4), with $m = 6.83$) (regular waves).

In Figure 6-12, the second order Stokes theory is used to calculate surface elevations:

$$\eta_{\max} = \frac{H}{2} + k \frac{H}{2} \frac{H}{8} \frac{\cosh(kd)}{\sinh^3(kd)} (2 + \cosh(2kd)) \quad (6.1)$$

and the horizontal particle velocity at the wave crest:

$$u_{\text{top}} = \frac{H}{2} \frac{gk}{\omega} \frac{\cosh(k(\eta_{\max} + d))}{\cosh(kd)} + \frac{3}{4} k \frac{H^2}{4} \omega \frac{\cosh(2k(\eta_{\max} + d))}{\sinh^4(kd)} \quad (6.2)$$

The prediction of the run-up on a monopile is very good, even for large run-up heights. Especially for the lower run-up there is a large improvement of the prediction compared to Niedzwecki and Duggal's prediction. For the cone foundation, run-up is underestimated for the larger wave heights.

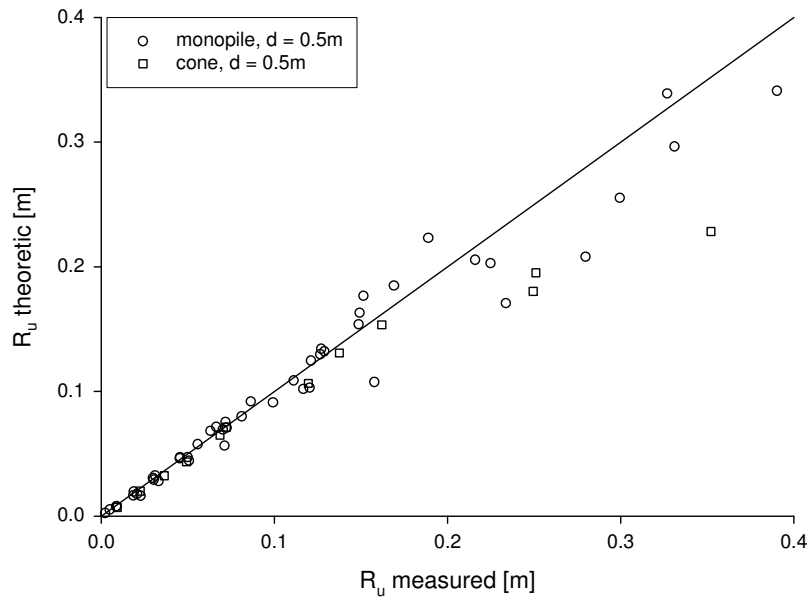


Figure 6-12: Comparison between measured and theoretical run-up. Theoretical run-up is calculated using the velocity stagnation head theory (equation (5.1)) with Stokes 2nd order theory for wave kinematics (equations (6.1) and (6.2)) (regular waves).

In Figure 6-13, Fenton's Fourier approximation method is used to calculate both η_{\max} and u .

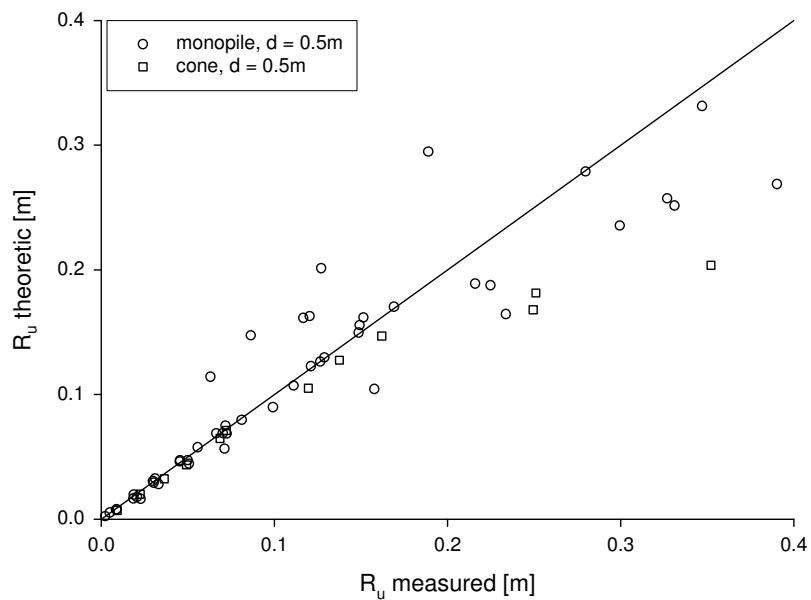


Figure 6-13: Comparison between measured and theoretical run-up. Theoretical run-up is calculated using the velocity stagnation head theory (equation (5.1)) with Fenton's Fourier series approximation for wave kinematics (regular waves).

The implementation of Fenton's theory was performed using the code ACES (1992). The run-up prediction is not improved by using this more complicated numerical wave theory.

As the velocity stagnation head theory with wave crest kinematics determined with second order Stokes theory gives the best results, it is further used for the irregular waves. The main goal for the irregular waves is to find a simple reliable formula to calculate the wave run-up.

6.2.3 Irregular wave experimental results

Although irregular/ random waves are often used in the design of offshore structures, there are no simple reliable formulas for irregular wave run-up. For this reason, the present study focuses on defining the wave run-up for irregular wave.

A typical part of an irregular wave train is shown in Figure 6-14, including both the wave signal next to the pile and the simultaneous measurements on all 10 run-up gauges.

The influence of the wave steepness on the 2% excess run-up is presented in Figure 6-15. The target deepwater steepness s_0 , presented in this figure, is calculated with H_s and T_p . The measured deepwater wave steepness may deviate slightly from the target value. Again, the difference for different wave steepness is limited, but the highest wave steepness (s_0) gives clearly lower run-up values and the highest run-up is measured for the lowest wave steepness.

Figure 6-16 shows the 2% excess run-up height as a function of the 2% excess wave height for a monopile in 2 water depths and for the cone foundation. All measurements shown in this figure have a deep water target wave steepness $s_0 = 0.03$. Run-up is significantly higher (15 to 35%) for the cone foundation. Due to the limited water depth, wave breaking occurs for $d = 0.35\text{m}$, leading to an equal $H_{2\%}$ value for each test. This implies that wave steepness decreases with increasing wave period. Again lower steepness leads to higher run-up values.

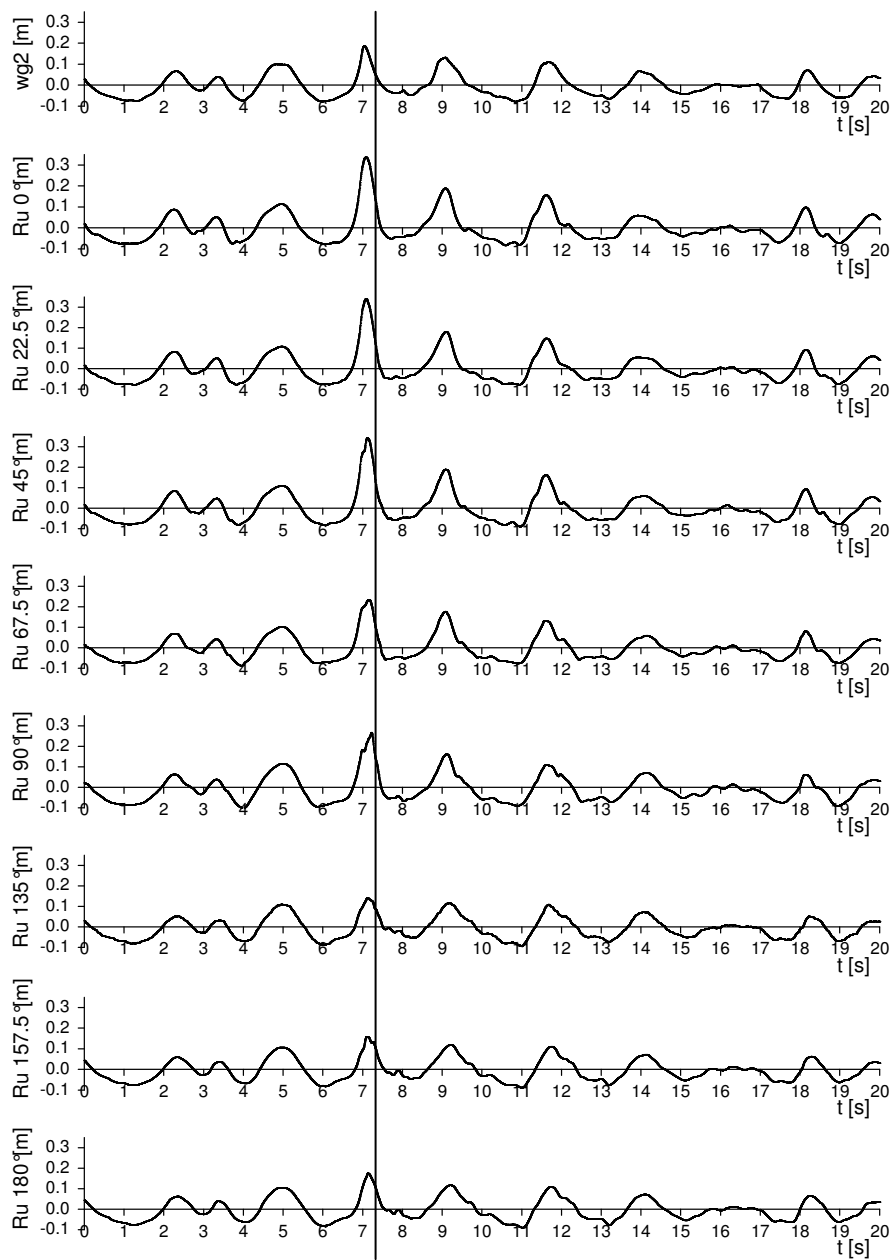


Figure 6-14: Irregular wave train ($H_s = 0.19\text{m}$, $T_p = 2.1\text{s}$): wave signal next to the pile (wg2) and simultaneous measurements of run-up gauges.

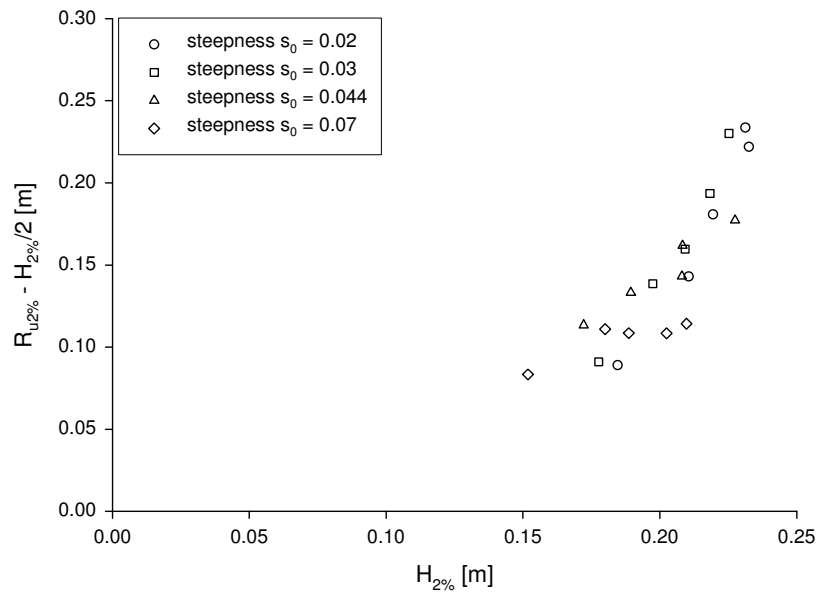


Figure 6-15: 2% Excess run-up on monopile for different wave steepness s_0 (irregular waves, $d = 0.5m$).

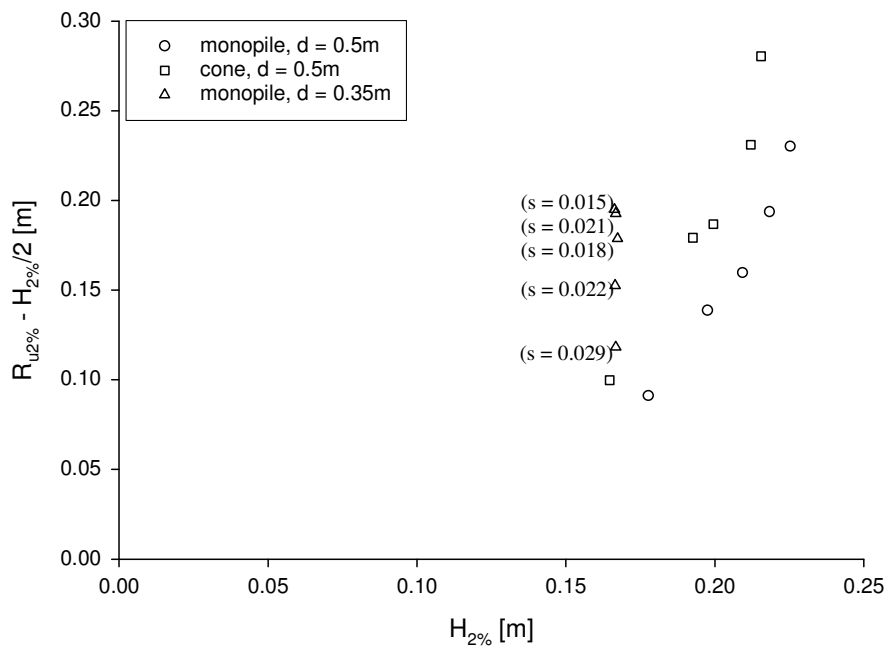


Figure 6-16: 2% Excess run-up on different foundations, target wave steepness $s_0 = 0.03$ (irregular waves).

For the irregular waves, a spectral analysis of both the run-up and the wave properties can be made (e.g. Niedzwecki and Duggal (1992)). Another possibility is to use linear random wave theory in the case of irregular waves to determine

the wave kinematics. The random wave theory decomposes the irregular wave spectrum into component waves and superposes the kinematics determined by linear extrapolation or with stretching techniques such as Wheeler stretching (Randall et al. (1993)). Another technique used for the prediction of irregular wave kinematics is to substitute an equivalent regular wave and treat it as a regular wave of equal height and frequency. The wave kinematics can then be computed using a high order non-linear wave theory, such as Stokes theory, and the resulting kinematics are assumed to be that of the irregular wave (Randall et al. (1993)). In this study the latter method is used for several reasons. First of all, a comparison between Figure 6-15 & Figure 6-16 and Figure 6-7 & Figure 6-8 reveals a similar behaviour for the wave run-up caused by regular and irregular waves. Secondly, Randall et al. (1993) show that Stokes second order theory gives comparable results to the Wheeler stretching technique for the velocities in the wave crest. They found that where Wheeler stretching under predicts the velocities in an irregular wave and linear extrapolation over predicts the velocities in an irregular wave, Stokes 2nd order theory tends to over predict the velocities under the SWL and slightly over predict the velocities above the SWL. The main reason why the technique of an equivalent regular wave is used, is that it makes it possible to obtain a simple formula.

Using $H_{2\%}$ as a characteristic wave height to predict the 2% run-up value might seem logical. Often however, only limited wave characteristics (e.g. H_s) are known. For this reason both the significant wave height H_s and the 2% excess wave height $H_{2\%}$ are used to predict wave run-up. T_p is used as a characteristic wave period.

In Figure 6-17, the result of using the velocity stagnation head theory is shown, applying Stokes second order equations to calculate the wave kinematics in the crest ((6.1) and (6.2)). The best fit is obtained for the regular waves. For the irregular waves, the theoretic run-up calculated with H_s and $H_{2\%}$ is compared to the measured 2% run-up value. When H_s is used to calculate $R_{u2\%}$, the run-up is seriously underestimated, due to the fact that a much smaller wave height than the one causing the run-up is used. When $H_{2\%}$ is used to calculate the run-up, the estimate is better, but still underestimating the 2% excess run-up.

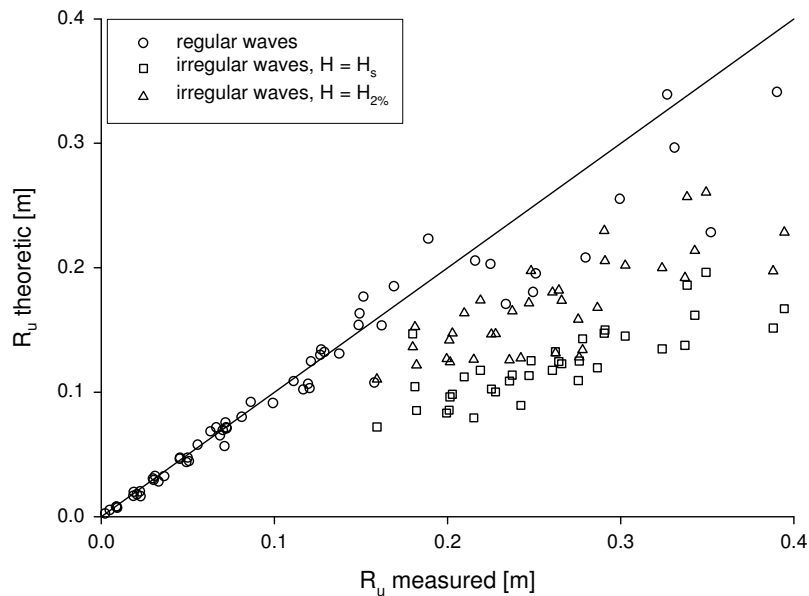


Figure 6-17: Comparison between measured and theoretical $R_{u2\%}$. Theoretical run-up is calculated using the velocity stagnation head theory (equation (5.1)) with Stokes 2nd order theory for the crest wave kinematics (equations (6.1) and (6.2)).

The velocity stagnation head theory is adjusted with a coefficient m in equation (5.4) as suggested by Niedzwecki and Duggal (1992) to improve the results, while using the second order Stokes theory for the wave kinematics. Equation (6.3) gives the best result when η_{max} is calculated with equation (6.1) and u is calculated with equation (6.2), both using $H = H_{2\%}$ and $T_w = T_p$. The results are presented in Figure 6-18. The value of m is determined by postulating $\overline{R_{u2\%, measured}} = \overline{R_{u2\%, theoretic}}$.

As higher run-up values were found for the cone foundation, a different coefficient m is found while trying to find the best fit. We find a value of $m = 4.45$ for the cone foundation, while $m = 2.71$ for the monopile. The difference indicates that the coefficient m is probably a function of the shape of the foundation and/or the pile diameter. It is however difficult to include this into the parameter m as only two different shapes are tested.

A standard deviation of 0.024 is obtained for all estimates of $R_{u2\%}$, being less than 10% of $\overline{R_{u2\%}} = 0.26\text{m}$.

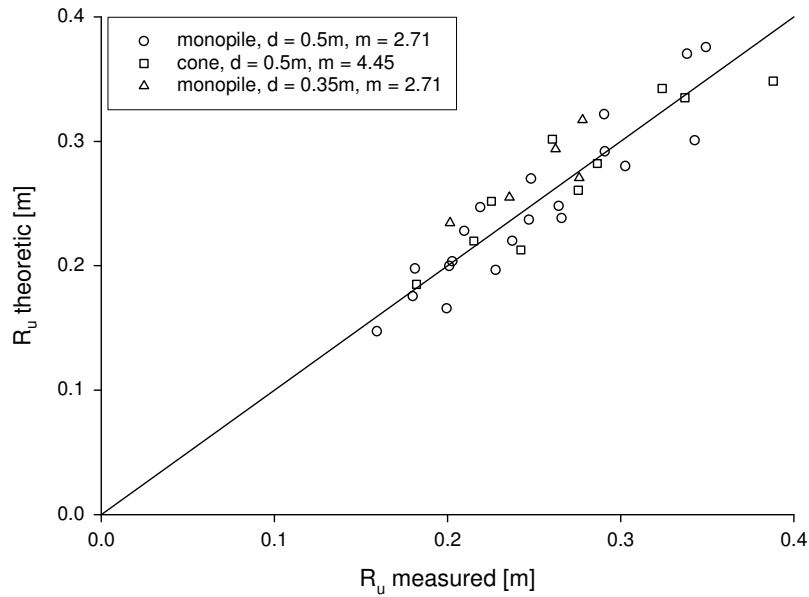


Figure 6-18: Comparison between measured and theoretical $R_{u2\%}$. Theoretical run-up is calculated using the adjusted velocity stagnation head theory with Stokes 2nd order theory for wave kinematics in the crest (equations (6.3) and (6.4)); (irregular waves, $H = H_{2\%}$, $T = T_p$).

Equation (6.3) is to be used to calculate $R_{u2\%}$:

$$R_{u2\%} = \eta_{\max} + m \frac{u^2}{2g} \quad (6.3)$$

with $m = 2.71$ for a monopile foundation and $m = 4.45$ for the specific case of a cone foundation

In this equation, $H_{2\%}$ and T_p are used to calculate the wave kinematics by means of equations (6.1) and (6.2). In most practical cases however, only H_s is known. When the waves are Rayleigh distributed, $H_{2\%}$ can be estimated by

$$H_{2\%} = 1.40H_s \quad (6.4)$$

One must however be careful to use equation (6.4). When H_s is on the limit of wave breaking, the run-up will be seriously overrated by using both equations (6.3) and (6.4).

In the present study, the smaller wave heights are Rayleigh distributed. For the larger significant wave heights, the distribution deviates quite a lot from the Rayleigh distribution due to wave breaking. In shallow water, Glukhovsky's distribution can be used (Glukhovsky (1966)). The distribution of the wave heights in the present study tends to be even steeper than Glukhovsky's distribution.

Generally, the Rayleigh distribution is adequate, except for near-coastal wave records in which it may overestimate the number of large waves. Investigations of shallow-water wave records from numerous studies indicate that the distribution deviates from the Rayleigh, and other distributions have been shown to fit individual observations better (US Army Corps of Engineers (1984)). The primary cause for the deviation is that the large waves suggested in the Rayleigh distribution break in shallow water. Unfortunately, there is no universally accepted distribution for waves in shallow water. As a result, the Rayleigh is frequently used with the knowledge that the large waves are not likely to occur (US Army Corps of Engineers (2002)).

6.2.4 Variation of run-up around the pile

The variation of the run-up around the pile for irregular waves was measured at nine different angles of the wave attack for four different wave steepness (0.020, 0.030, 0.044 and 0.070). Figure 6-19 to Figure 6-21 correspond with the measured R_{Us} , $R_{U2\%}$ and R_{Umax} values relative to the value of the run-up at the front side of the pile, for a wave steepness of 0.044. The relative run-up distribution along the pile is almost independent of the generated wave height. The further we are from the front line, the more the wave height affects the distribution of the run-up. At the back side of the pile, the relative significant run-up values tend to be smaller for higher waves (Figure 6-19). For the 2% run-up and the maximum run-up this is not the case: there seems to be no straight forward relation between the relative run-up at the back side of the pile and the wave height.

When looking at the significant wave height, the maximum run-up is found at the front of the pile. For the 2% and the maximum values, the maximum run-up is mostly found at an angle of 45°. At this location, the measured run-up values are 1% to 9% higher than those at the front side of the pile. The difference increases for the higher waves. This is probably due to the fact that the run-up tongue for very high waves is thinner at the front side of the pile than at an angle of 45°. Due to the distance of the wave gauges to the pile (2 mm), the very thin run-up tongues induced by very high waves are slightly underestimated.

Figure 6-20 shows that the lowest 2% run-up is not located on the leeside, as one might expect, but at an angle of approximately 135°. For the significant wave height, the lowest run-up is located at an angle of approximately 122.5°. The run-up at this position amounts to approximately 40% to 50% of the maximum run-up. As the location of the access facilities is optimal where maximum run-up is at its lowest, this information can be combined with information on wave directions to find an optimum location for the access facilities to the wind turbine.

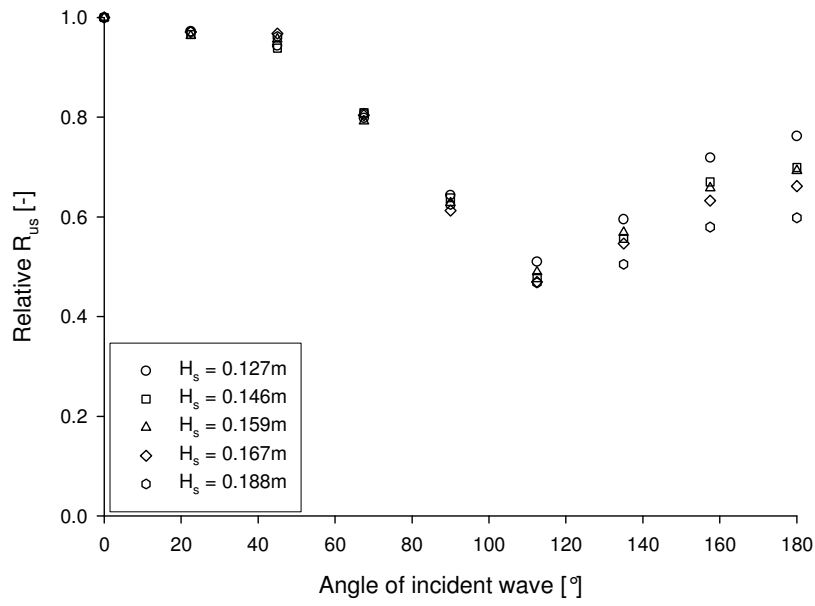


Figure 6-19: Variation of significant run-up along the monopile, $s_0 = 0.044$.

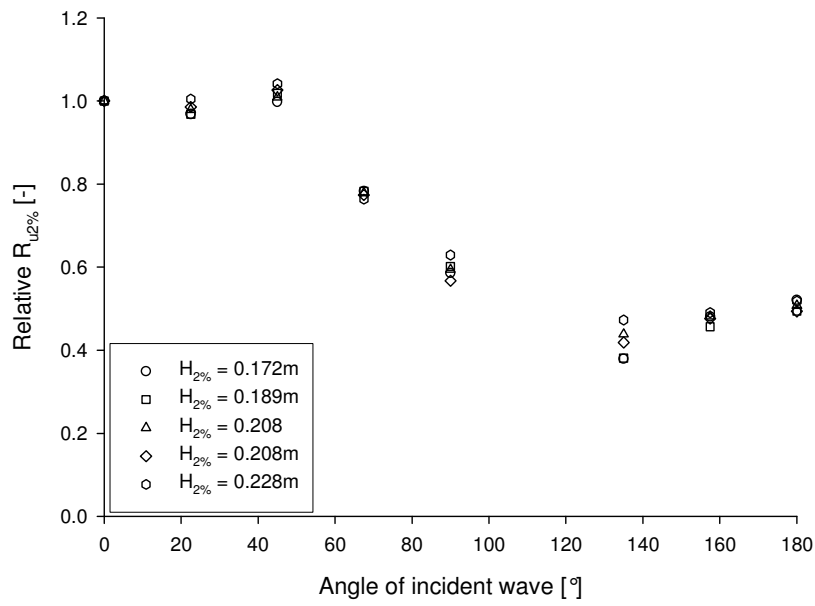


Figure 6-20: Variation of 2% run-up along the monopile, $s_0 = 0.044$.

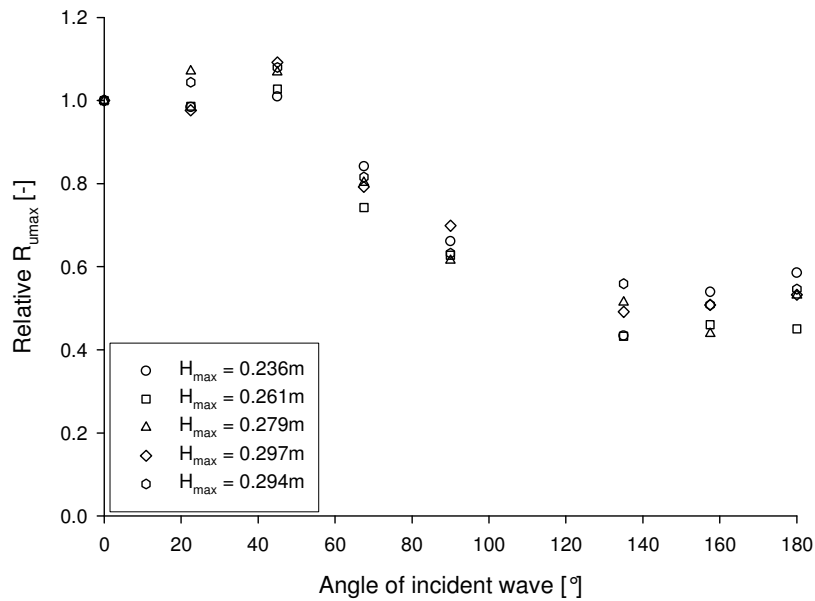


Figure 6-21: Variation of maximum run-up along the monopile, $s_0 = 0.044$.

6.3 Evaluation of run-up formula

In Andersen and Frigaard (2006) the data described in this chapter were reanalyzed to investigate the spreading of the m -value in equation (6.3). They found a significant spreading on the value of m . It was found that, for the monopile foundation, the value varies between 1.9 and 4.2 with a standard deviation equal to 0.62, while for the cone foundation the standard deviation is 0.71 and the value of m varies between 3.2 and 5.6.

Andersen and Frigaard (2006) found a strong dependency of m on the ratio of wave height to water depth H_s/d for the data described in this chapter. In Figure 6-22, m is plotted against H_s/d for the monopile data, with $d = 0.5m$, described in this chapter. From the figure it can be seen that indeed, m increases slightly with increasing values of H_s/d for values of the wave steepness $s = 0.02$ and 0.03 . For higher values of the wave steepness however, the value of m decreases as a function of H_s/d .

As described in section 6.2.3, the wave steepness has an influence on the wave run-up, with significantly higher run-up values for the lowest wave steepness. From Figure 6-22 it can be seen that this however does not result in higher values for m for the lowest wave steepness. When looking at the data, this can be explained by the fact that η_{max}/H_{max} is significantly higher for the low wave steepness, resulting in lower values of m , even when the measured run-up is higher.

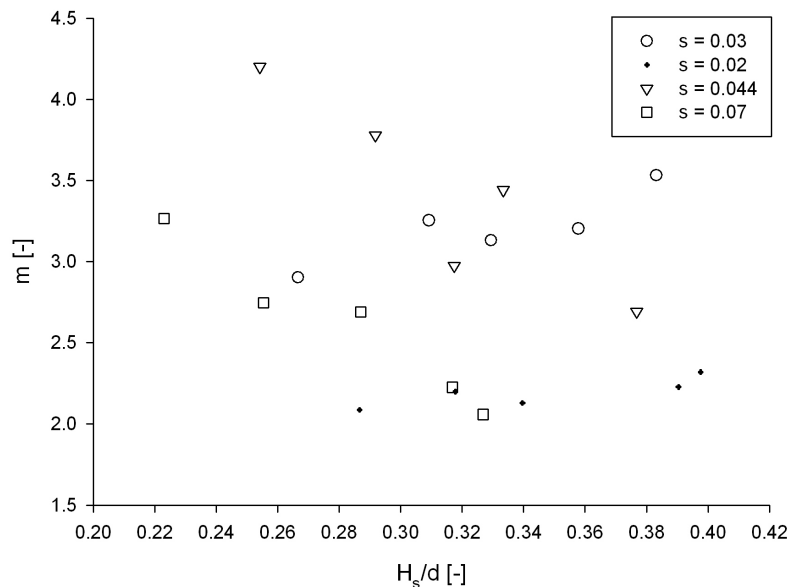


Figure 6-22: Influence of H_s/d on the value of m

Andersen and Frigaard (2006) performed a new test series, in which the water depth varied between 0.2 to 0.4m, and the wave steepness varied between 0.02 and 0.035. They found that the m values which were found lie in the same range as found in De Vos et al. (2007), described in this chapter, but that the dependency on H_s/d was less clear than expected.

It was noted by Andersen and Frigaard (2006) that the variation on the predicted run-up level was much lower than the variation of the m value would lead to suspect, due to the fact that the factor m only influences the second term in equation (6.3) and the first part has a significant influence on the result. Furthermore, they also observed that the wave steepness has a large influence on the wave run-up, with significantly higher run-up for the low steepness.

6.4 Conclusions

Wave run-up on offshore wind turbine foundations is much higher than often predicted by linear wave theory, causing problems for the access facilities. A possible countermeasure exists in placing the platforms higher, preventing the up-running waves to reach them.

In this chapter, equation (6.3) is given to predict wave run-up for irregular waves, based on a small-scale experimental study that examines both regular and irregular wave run-up on two different shapes of pile foundations: cylindrical and conical. The parameters selected for this study reflect a range useful for understanding the run-up phenomenon on a wind turbine foundation, placed in deeper water conditions ($d/L = 0.10 - 0.8$), with a flat bottom slope ($\tan\beta = 1:100$). As experience shows and as the formulae predict, run-up can often be so high that placing the platform on a level were it cannot be reached by the waves is hardly manageable. Designers of offshore foundations should therefore

take the wave forces from up-running waves into consideration. To obtain the prediction formula for the run-up caused by irregular waves, the velocity stagnation head theory was adjusted with a coefficient m as suggested by Niedzwecki et al. (1992), while using the second order Stokes theory for the wave kinematics. It was found that the shape of the foundation influences the expected run-up level, leading to a different value m for a cylindrical foundation and for the cone foundation. More research is needed to assess the run-up for other foundation shapes and types.

To find an optimal location for the access facilities of the wind turbines, the variation of the run-up around the pile was measured. The test results show that the position with the lowest run-up level $R_{u2\%}$ or $R_{u\max}$ is located under 135° , while the run-up at that position amounts to approximately 40% to 50% of the maximum run-up at the frontline.

References

- ACES, 1992. Automated Coastal Engineering System. Coastal Engineering Research Center, Department of the army, Mississippi.
- Andersen, T.L. and Frigaard, P., 2006. Horns Rev II, 2-D Model Tests; Wave Run-Up on Pile, Aalborg University, Aalborg, Denmark.
- De Vos, L., Frigaard, P. and De Rouck, J., 2007. Wave run-up on cylindrical and cone shaped foundations for offshore wind turbines. Coastal Engineering, 54(1): 17-29.
- Glukhovsky, B.H., 1966. Investigations of wind waves. Gidrometeoizdat, 284 pp.
- Mansard, E.P.D. and Funke, E.R., 1980. The measurement of Incident and Reflected Spectra using a Least Square Method, 17th Coastal Engineering Conference, Sydney, Australia.
- Martin, A.J., Easson, W.J. and Bruce, T., 2001. Runup on Columns in Steep, Deep Water Regular Waves. Journal of Waterway, Port, Coastal and Ocean Engineering, 127(1): 26-32.
- Niedzwecki, J.M. and Duggal, S.D., 1992. Wave Run-up and Forces on Cylinders in Regular and Random Waves. Journal of Waterway, Port, Coastal, and Ocean Engineering, 118(6): 615-634.
- Niedzwecki, J.M. and Huston, J.R., 1992. Wave interaction with tension leg platforms. Ocean Engineering, 19(1): 21-37.
- Randall, R.E., Zhang, J. and Longridge, J.K., 1993. Laser Doppler anemometer measurements of irregular water wave kinematics. Ocean Engineering, 20(6): 541-554.
- US Army Corps of Engineers, 1984. Shore Protection Manual, Vol2. Coastal Engineering Research Center, WES Vicksburg, MS.
- US Army Corps of Engineers, 2002. Coastal Engineering Manual. Engineer Manual 1110-2-1100, Washington, D.C. .

PART IV. PREDICTION TOOL

Chapter 7: Practical implementation of prediction tool

7.0 Introduction

The formulae which were derived during this thesis are grouped in this chapter, together with the underlying equations. The software, in which these formulae are programmed is also described in this chapter. The prediction tool allows to calculate the following aspects of an offshore wind turbines' design:

- required stone size for the top armour layer in case of a statically stable scour protection without stone displacement
- required stone size for the top armour layer for a statically stable scour protection with a prescribed acceptable damage level
- for a scour protection with given characteristics, it can be assessed whether the threshold of motion is surpassed
- for a scour protection with given characteristics, it can be estimated which damage number to expect for the given loading conditions
- required filter characteristics for given bed material and top armour layer material
- wave run-up height near the SWL.

Even though all necessary information to calculate these aspects are given throughout the thesis, the final methodology and formulae are assembled here for the convenience of the user.

7.1 Statically stable scour protection without stone movement

The steps which should be taken to calculate the required stone size for a scour protection in which all stones are statically stable are shown in Figure 7-1, together with a reference to the formulae which are to be applied.

The required input data are:

- water depth: d
- design depth-averaged flow velocity: U_c
- design wave conditions: significant wave height H_{m0}
peak wave period T_p
spectrum: Jonswap, PM or measured spectrum
- rock density: ρ_s
- water density: ρ_w
- rock grading: D_{85}/D_{15}
- pile diameter: D

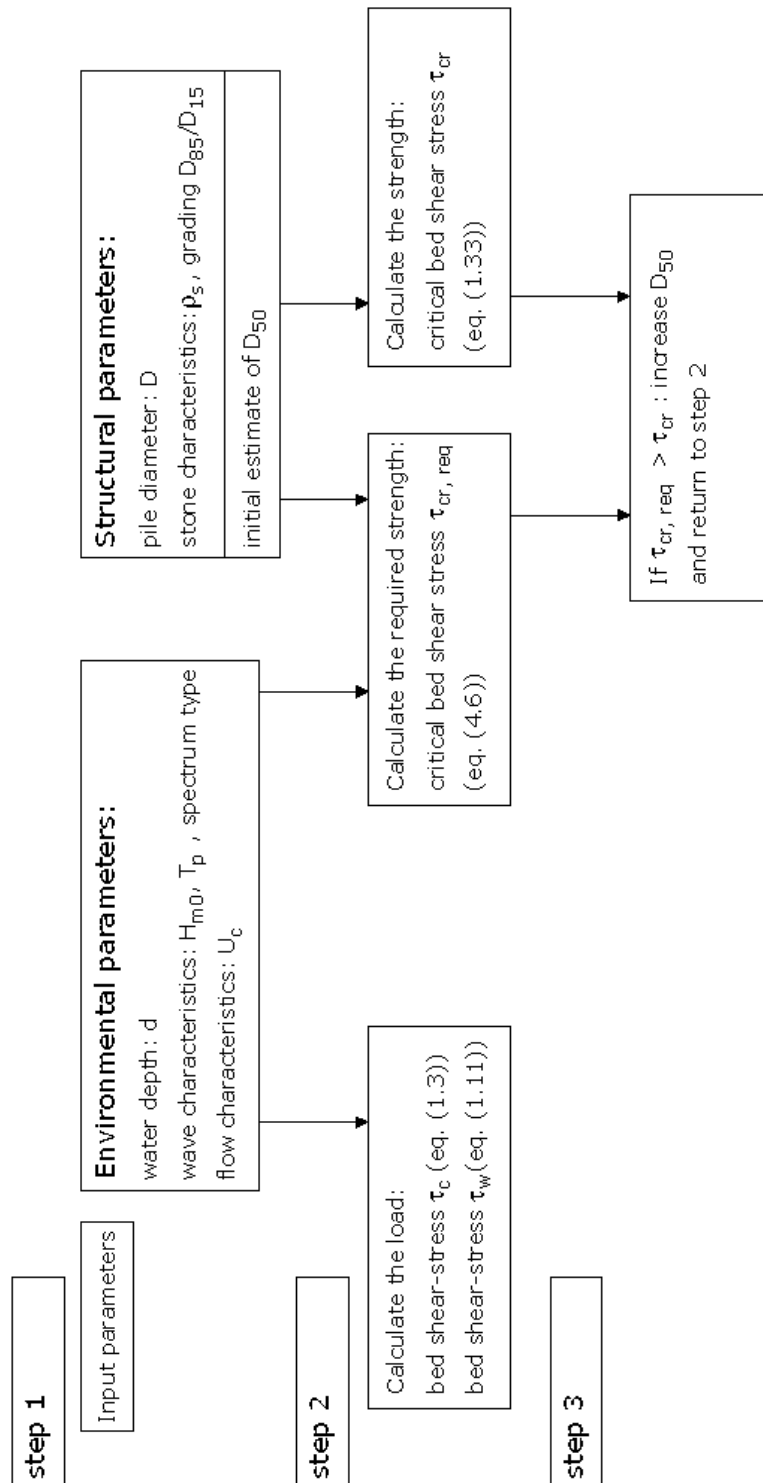


Figure 7-1: Design tree for statically stable scour protection

Equation (4.6) was derived to calculate the required stone size:

$$\frac{\tau_{cr}}{\rho_w \Delta g D} = 0.001 + 3.303 \frac{\tau_c}{\rho_w \Delta g D} + 1.015 \frac{\tau_w}{\rho_w \Delta g D} \quad (4.6)$$

and results in the required $D_{67.5}$ for the scour protection armour layer. In equation (4.6), τ_{cr} represents the critical bed shear-stress of the $D_{67.5}$; τ_c represents the current induced bed shear-stress; τ_w represents the wave induced bed shear-stress; ρ_w is the density of water; Δ is the relative density of the stones; g is the gravitational acceleration and D is the pile diameter.

From the critical bed shear-stress τ_{cr} , the required stone size can be calculated with:

$$\theta_{cr} = \frac{\tau_{cr}}{g(\rho_s - \rho_w)D_{67.5}} = 0.035 \quad (1.33)$$

or, when rearranging:

$$D_{67.5} = \frac{\tau_{cr}}{0.035g(\rho_s - \rho_w)}$$

The current induced bed shear-stress τ_c is calculated as:

$$\tau_c = \frac{1}{2} \rho_w f_c U_c^2 \quad (1.3)$$

with U_c the depth averaged flow velocity, ρ_w the density of water and f_c a dimensionless friction coefficient, determined as:

$$f_c = \frac{2g}{\left(\frac{\sqrt{g}}{\kappa} \ln \left(\frac{d}{z_0 e} \right) \right)^2} \quad (1.4)$$

with g the gravitational acceleration; $\kappa = 0.4$, the Von Karman constant; d the water depth; $e = 2.718$ and z_0 the roughness length, calculated with:

$$z_0 = \frac{k_s}{30} + \frac{\nu}{9u_*} \quad (1.6)$$

In equation (1.6), $k_s = 2.5D_{50}$ represents the bottom roughness; ν is the kinematic viscosity of water ($=10^{-6}$ m²/s) and u_* [m/s] is the friction velocity, which is defined as:

$$u_* = \sqrt{\frac{\tau_c}{\rho_w}} \quad (1.1)$$

The wave induced bed shear-stress τ_w is calculated as:

$$\tau_w = \frac{1}{2} \rho_w f_w U_{10\%}^2 \quad (1.11)$$

The bottom orbital velocity $U_{10\%}$ (exceeded by 10% of the waves) is derived from the design wave conditions, using the spectral information of the wave characteristics:

$$U_{10\%} = 1.52 U_m \quad (4.13)$$

with

$$U_m = \sqrt{2} \sigma_U \quad (4.9)$$

and

$$\sigma_U^2 = \int_0^\infty S_U(f) df \quad (4.10)$$

$$S_U(f) = \left(\frac{2\pi}{T \sinh(kd)} \right)^2 S(f) \quad (4.11)$$

in which $S(f)$ is the amplitude spectrum, defined as the ratio of $\frac{1}{2}$ wave amplitude squared and the frequency band width Δf :

$$S(f) = \frac{\frac{1}{2} a^2}{\Delta f} \quad (3.16)$$

with a the wave amplitude and Δf the frequency band width which depends on the duration of the measurement T_0 :

$$\Delta f = \frac{1}{T_0} \quad (3.17)$$

The wave friction factor f_w is determined as:

$$f_w = 0.32 \left(\frac{A}{k_s} \right)^{-0.8}, \quad 0.2 < \frac{A}{k_s} < 10 \quad (1.16)$$

and

$$f_w = 0.4 \left(\frac{A}{k_s} \right)^{-0.75}, \quad 10 < \frac{A}{k_s} < 50 \quad (1.15)$$

with $k_s = 2.5D_{50}$ the bottom roughness and A the amplitude of the orbital motion near the bottom, which is calculated as:

$$A = \frac{U_{10\%} T_p}{2\pi}$$

with T_p the peak wave period. For larger values of A/k_s ($A/k_s > 10$), the derived formula is used far outside the region for which it was derived and it is unsure whether it gives a correct estimate of the required stone size.

As shown in Figure 7-1, an initial, small estimate of D_{50} ($D_{50} = 0.1\text{mm}$) is used to calculate the resulting bed shear-stresses. When the required critical bed shear-stress is smaller than the actual bed shear-stress, the value of D_{50} is increased until the required critical bed shear-stress equals or exceeds the actual bed shear-stress.

To calculate the actual critical bed shear-stress for $D_{67.5}$ and for the given value of D_{50} , the following relationship is derived between D_{50} and $D_{67.5}$, departing from the given rock grading D_{85}/D_{15} :

$$\log \left(\frac{D_{67.5}}{D_{50}} \right) = \frac{(67.5 - 50)}{(85 - 15)} \log \left(\frac{D_{85}}{D_{15}} \right) = 0.25 \log \left(\frac{D_{85}}{D_{15}} \right)$$

Equation (4.6) can also be used to assess whether an existing scour protection is statically stable. In this case, the stone grading is known, and both the median stone size D_{50} and the stone size $D_{67.5}$ need to be provided. The median stone size D_{50} is used to calculate the value of τ_c and τ_w , necessary to calculate the critical bed shear-stress with equation (4.6). This value of τ_{cr} should then be compared to the value of τ_{cr} obtained by assuming $\theta_{cr} = 0.035$ and the value of $D_{67.5}$ in equation (1.33). When the predicted value of τ_{cr} (equation (4.6)) is larger than the actual value of τ_{cr} , the scour protection is statically stable (section 4.2, figure 4.10).

7.2 Stable scour protection with prescribed damage level

The steps which should be taken to calculate the required stone size for a stable scour protection for which some stone movement is allowed are shown in Figure 7-2, together with a reference to the formulae which are used.

The required input data are:

- water depth: d
- design depth-averaged flow velocity: U_c
- flow direction: following or opposing the waves
- design wave conditions:
 - significant wave height H_{m0}
 - peak wave period T_p
 - energy wave period $T_{m-1,0}$
 - spectrum type: Jonswap, Pierson
Moskowitz or a measured spectrum
- rock density: ρ_s
- water density: ρ_w
- number of waves: N
- accepted damage number: S_{3D}

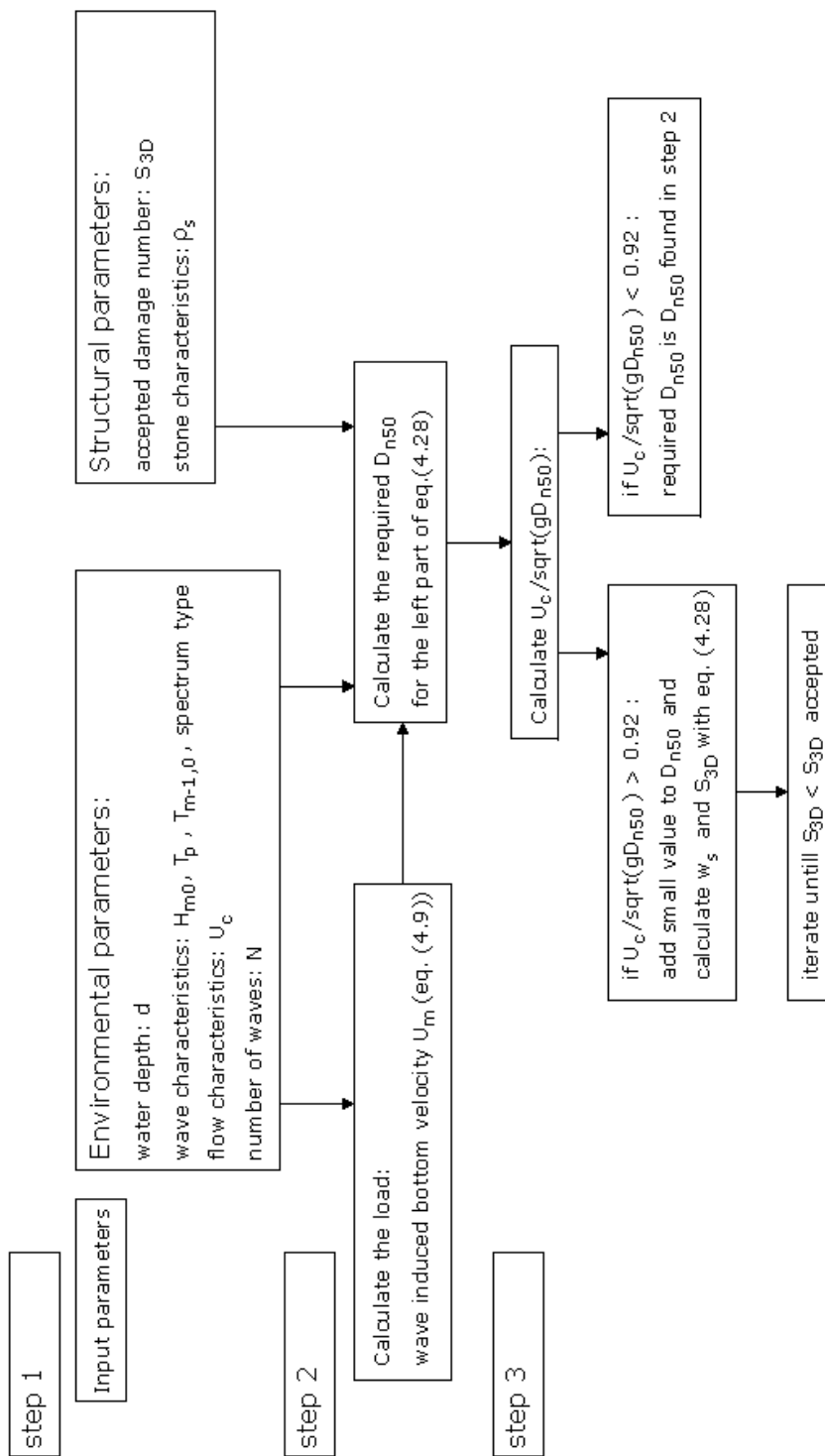


Figure 7-2: Design tree for static design criteria, including damage number

Equation (4.30) was derived to calculate the required stone size:

$$\frac{S_{3D}}{N^{b_0}} = a_0 \frac{U_m^3 T_{m-1,0}^2}{\sqrt{gd} (s-1)^{3/2} D_{n50}^2} + a_1 \left(a_2 + a_3 \frac{\left(\frac{U_c}{w_s} \right)^2 (U_c + a_4 U_m)^2 \sqrt{d}}{g D_{n50}^{3/2}} \right) \quad (4.30)$$

with S_{3D} the damage number. The designer of the scour protection (i.e. the user of this formula) has to decide which value of S_{3D} he wants to use. The value of S_{3D} may depend on the value of the structure, the return period, ... It is defined as:

$$S_{3D} = \max(S_{3D,sub}) \quad (4.17)$$

with $S_{3D,sub}$ the three dimensional damage number per sub area, defined as the ratio of eroded volume V_e and the surface of the sub area times the stone diameter:

$$S_{3D,sub} = \frac{V_e}{D_{n50} \cdot \pi \frac{D^2}{4}} \quad (4.16)$$

Each sub area has a surface equal to the pile's surface and $S_{3D,sub}$ represents the number of cubes with size D_{n50} which have disappeared over the height from the considered sub area.

In equation (4.30), the parameters b_0 , a_0 , a_2 en a_3 were determined through fitting and are equal to 0.243, 0.00076, -0.022 en 0.0079 respectively. The parameters a_1 and a_4 depend on both the current velocity/stone diameter ratio and the current direction and are determined as:

$$a_1 = 0 \text{ for } \frac{U_c}{\sqrt{gD_{n50}}} < 0.92 \text{ and waves following current} \quad (4.28)$$

$$a_1 = 1 \text{ for } \frac{U_c}{\sqrt{gD_{n50}}} \geq 0.92 \text{ or waves opposing current}$$

$$a_4 = 1 \text{ for waves following current} \quad (4.29)$$

$$a_4 = \frac{Ur}{6.4} \text{ for waves opposing current}$$

in which U_c is the depth averaged flow velocity; g is the gravitational acceleration = 9.81 m/s²; D_{n50} the nominal stone diameter, determined from the mean stone diameter D_{50} as:

$$D_{n50} / D_{50} = 0.84 \quad (3.40)$$

and Ur the Ursell number:

$$Ur = \frac{L^2 H}{d^3} \quad (4.25)$$

In equation (4.30), N represents the number of waves, g is the gravitational acceleration = 9.81 m/s²; d is the water depth; s is the relative density of the stones = ρ_s / ρ_w , with ρ_s the density of the scour protection material and ρ_w the density of the water; U_c is the depth averaged velocity and the bottom orbital velocity U_m has to be calculated from the spectrum as:

$$U_m = \sqrt{2} \sigma_U \quad (4.9)$$

with

$$\sigma_U^2 = \int_0^\infty S_U(f) df \quad (4.10)$$

$$S_U(f) = \left(\frac{2\pi}{T \sinh(kd)} \right)^2 S(f) \quad (4.11)$$

in which $S(f)$ is the amplitude spectrum, defined as the ratio of 1/2 wave amplitude squared and the frequency band width Δf :

$$S(f) = \frac{\frac{1}{2} a^2}{\Delta f} \quad (3.16)$$

with a the wave amplitude and Δf the frequency band width which depends on the duration of the measurement T_0 :

$$\Delta f = \frac{1}{T_0} \quad (3.17)$$

When the energy spectral wave period $T_{m-1,0}$ is not known, it can be calculated from the wave spectrum as:

$$T_{m-1,0} = T_e = \frac{m_{-1}}{m_0} \quad (3.20)$$

with the n^{th} moment of the spectral density m_n defined as:

$$m_n = \int_0^{\infty} f^n S(f) df \quad (3.23)$$

or, for a JONSWAP spectrum with $\gamma = 3.3$:

$$T_p = 1.107 T_{m-1,0} \quad (3.26)$$

An iterative approach is needed when the steady flow velocity is sufficiently large to have an influence on the damage development ($U_c / \sqrt{gD_{n50}} > 0.92$), as the fall velocity, used in equation (4.30) which then has to be determined depends on the stone size. As a first iteration, it is assumed that U_c is small, and an initial estimate of the required D_{n50} is obtained by using the left part of equation (4.30). The fall velocity w_s is then calculated as:

$$w_s = 1.1 \left[(s-1) g D_{50} \right]^{0.5} \text{ for } D_{50} \geq 1000 \mu\text{m} \quad (3.33)$$

with s the relative density of the stones = ρ_s / ρ_w and D_{50} the stone size for which 50% of the stones is lighter by weight. When the D_{n50} is known, the D_{50} can be calculated as:

$$D_{n50} / D_{50} = 0.84 \quad (3.40)$$

A number of waves = 5000 is recommended to calculate the required stone size. When experiments with 3000 waves are conducted, the damage after 5000 waves can be obtained by using equation (4.19), which says that the average damage after 5000 waves is approximately equal to 1.12 x (S_{3D} after 3000 waves).

$$S_{3D}(5000) / S_{3D}(3000) = 0.129 (5000)^{0.254} = 1.12 \quad (4.19)$$

Equation (4.30) can also be used to assess which damage number can be expected for an existing scour protection, with a given nominal stone diameter D_{n50} . In this case, the same formulae as above can be used, but no iteration is necessary when the steady current velocity is sufficiently large to have an influence on the damage development ($U_c / \sqrt{gD_{n50}} > 0.92$).

7.3 Filter characteristics

The formulae which are used to determine the filter characteristics are given in Appendix I.

7.4 Wave run-up

The required input data are:

- water depth: d
- design wave conditions:
 - 2% exceeding wave height $H_{2\%}$
 - peak wave period T_p
 - spectrum type: Jonswap, Pierson Moskowitch or a measured spectrum
- foundation type: monopile or cone shaped gravity based foundation

The following formula was derived to calculate the run-up $R_{u2\%}$, which is exceeded by 2% of the waves:

$$R_{u2\%} = \eta_{\max} + m \frac{u^2}{2g} \quad (6.3)$$

with g the acceleration due to gravity and:

$m = 2.71$ in case of a monopile foundation

$m = 4.45$ in case of a cone shaped gravity based foundation

The maximum elevation η_{\max} is determined with the second order Stokes theory as:

$$\eta_{\max} = \frac{H_{2\%}}{2} + k \frac{H_{2\%}}{2} \frac{H_{2\%}}{8} \frac{\cosh(kd)}{\sinh^3(kd)} (2 + \cosh(2kd)) \quad (6.1)$$

and the velocity u represents the velocity u_{top} at the top of the wave crest, also determined with second order Stokes theory as:

$$u_{top} = \frac{H_{2\%}}{2} \frac{gk}{\omega} \frac{\cosh(k(\eta_{\max} + d))}{\cosh(kd)} + \frac{3}{4} k \frac{H_{2\%}^2}{4} \omega \frac{\cosh(2k(\eta_{\max} + d))}{\sinh^4(kd)} \quad (6.2)$$

in which $H_{2\%}$ is the wave height which is exceeded by 2% of the waves; d is the water depth; ω is the angular frequency of the waves = $2\pi/T_p$, with T_p the peak wave period; k is the wave number = $2\pi/L$, with L the airy wave length, determined as:

$$L = \frac{gT_p^2}{2\pi} \tanh\left(\frac{2\pi d}{L}\right) \quad (3.2)$$

7.5 Practical use of prediction tool

The equations, described above were implemented in a software tool. The software prediction tool allows to calculate all of the aspects of an offshore wind turbines' design described in this chapter:

- required stone size for the top armour layer in case of a statically stable scour protection without stone displacement ;
- for a scour protection with given characteristics, it can be assessed whether the threshold of motion is surpassed;
- required stone size for the top armour layer for a statically stable scour protection with a prescribed acceptable damage level;
- for a scour protection with given characteristics, it can be estimated which damage number to expect for the given loading conditions;
- wave run-up height near the SWL;
- required filter characteristics for given bed material and top armour layer material.

The software tool is an executable of the Labview 7.1 software and is included on the DVD (Scour protection design.exe). On the front page, the user can choose one of the 6 sub-menus. A screen shot of the main menu is given in Figure 7-3.

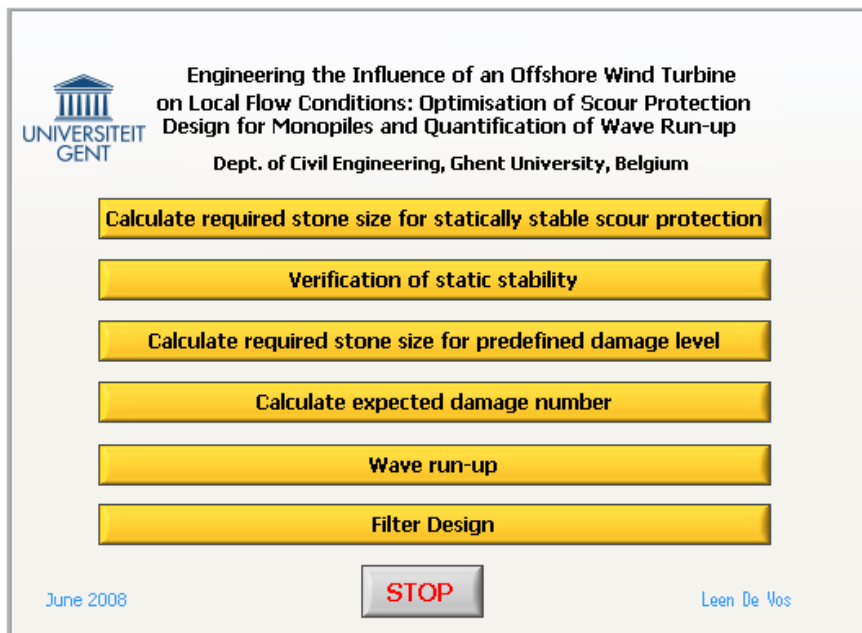


Figure 7-3: Main menu of software tool

When choosing one of the main menus, e.g. "calculate required stone size for predefined damage level", a sub-menu is opened as shown in Figure 7-4. The input parameters can be defined and the choice is offered to vary one of the input parameters within a certain range. The parameters which can be varied are the water depth d , the steady current velocity U_c , the significant wave height

H_{m0} , the peak wave period T_p , the stone density ρ_s , the number of waves N and the damage number S_{3D} . The input parameters can be changed and saved or loaded from a previously loaded file.

Figure 7-4: sub-menu “calculate required stone size for predefined damage level”: input

Input and output are located under a different tab in the same menu. When pressing the button “calculate” the program calculates the required output and automatically switches to the tab “output” when finished. For the menu “calculate required stone size for predefined damage level”, the calculated point is plotted in between the points from the experimental data and the required D_{n50} is also given. Under the tab “variation” the result of the calculation for the varied parameter is presented graphically. An example is given in Figure 7-5.

To return to the main menu, one has to push the button “stop”.

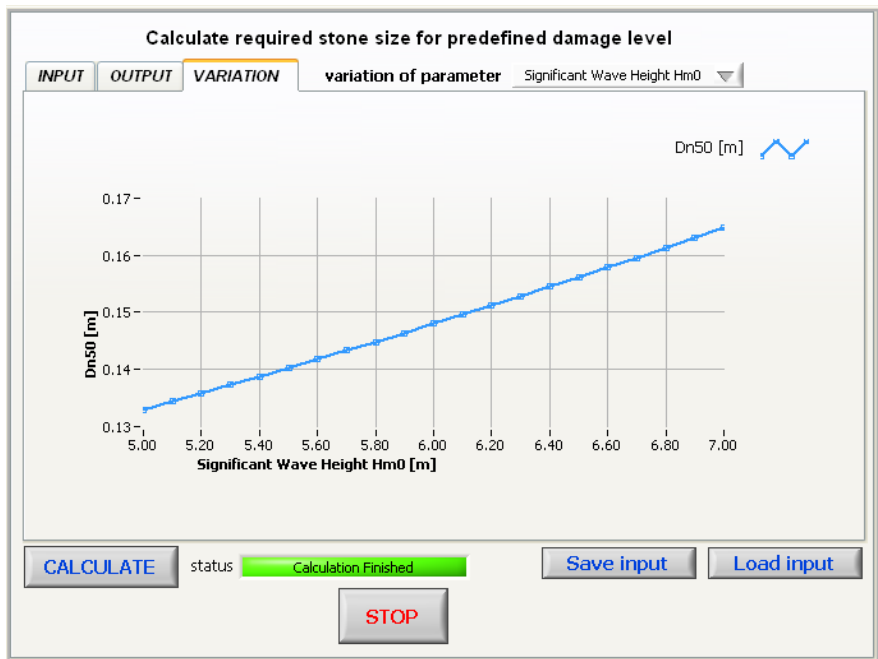
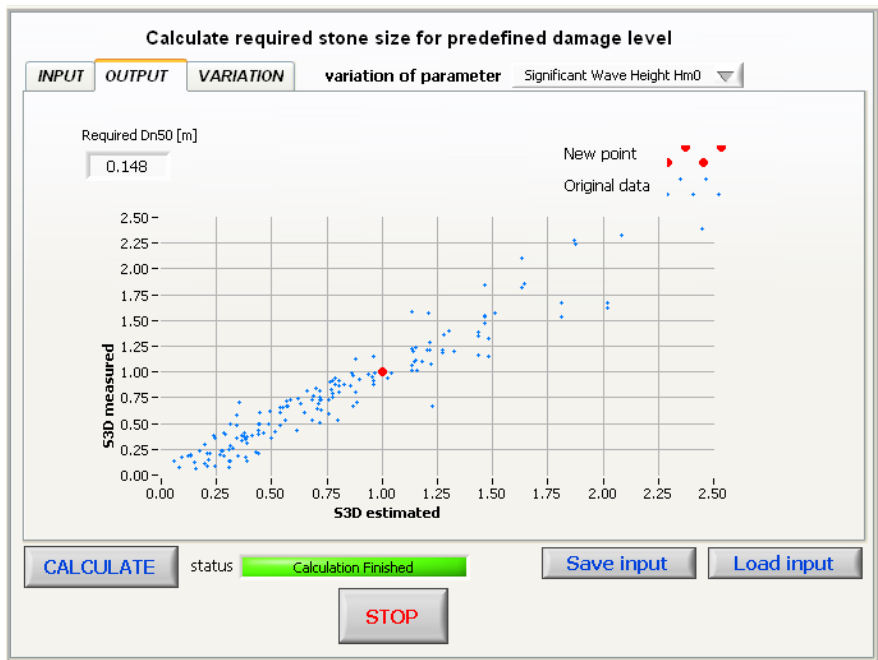


Figure 7-5: sub-menu "calculate required stone size for predefined damage level": output

Chapter 8 : Conclusions and recommendations

8.1 Conclusions

Two engineering problems, related to the disturbance of the local flow pattern, caused by placing a pile in a flow are discussed in this thesis.

The main focus lies on the influence of the disturbance caused by the pile on the bed, causing local scour development. The maximum scour depth develops in a steady current alone situation and empirical formulae predict equilibrium scour holes with a depth varying between 1 and 2 times the pile diameter. When accounting for the scour in the design of a monopile foundation, it is shown that scour has a significant influence and that placing a scour protection is a valuable solution for many of the experienced problems. An optimization of the existing design method was aspired and two empirical formulae were derived to determine the required stone size for the top layer of the scour protection. To derive the first formula, an optimization of the "no movement" condition, which is traditionally used, was performed. By simultaneously accounting for both waves and current in the physical model, the combined hydrodynamical loading on the scour protection is represented more accurately. Furthermore, a significant decrease in required stone size is obtained compared to the traditional calculation method. For the second formula, a similar approach as the design of breakwaters (Van der Meer (1988)) was pursued, including a damage number and the number of waves as extra parameters in the equation. When allowing even a limited amount of stone movement, this approach again leads to a significant decrease in required stone size. Unlike scour development, the damage development and scour protection design depend strongly on the wave induced horizontal orbital velocity U_m .

The formulae were derived for typical offshore wind turbine foundations in North Sea conditions considering water depth, wave characteristics, flow velocities and pile diameter. As only one pile diameter was tested, it is advised not to use the formulae outside the range for which they were derived ($D/L = 0.032 - 0.054$; $U_d/\sqrt{gD_{n50}} = 0 - 1.42$; $H/d = 0.17 - 0.42$).

The disturbance of the pile near the SWL causes high wave run-up on the pile. Serious damage to the smaller entrance facilities can be expected when the design does not account for these high run-up values. An empirical formula was derived to assess $R_{u2\%}$, the run-up which is exceeded by 2% of the waves.

8.2 Recommendations

Some remarkable observations were made during the experiments which were performed, leading to extensive possibilities for further research:

- although unexpected, a flow opposing the waves causes higher damage development. The increase in damage seems to depend on the degree of non-linearity of the waves. Further fundamental research may reveal the processes causing this observation. Both additional experimental research and numerical modelling might significantly contribute to the insight on this matter;
- while moderate flow velocities seem to have only a limited influence on the damage development, large current velocities lead to a significant increase in the damage. More experiments are required to fully understand the phenomenon which lies behind this;
- when applying large flow velocities to seriously damaged profiles, scour holes still develop near the pile when a granular filter is applied. When aspiring dynamically stable profiles, for which a large amount of stone displacement is allowed, higher scour protection thicknesses need to be investigated and an economical assessment of the advantage of smaller stone sizes versus larger scour protection thicknesses needs to be made;
- the few tests with small water depths show a possible significant influence of the water depth on the scour development. More in depth research is required to fully evaluate the effect of this parameter;
- as the pile diameter was not varied throughout the tests, more experiments with a different pile diameter for the same wave conditions might lead to new insights on the influence of the ratio of pile diameter to the amplitude of the orbital motion. The results from the opposing current lead to suspect that this might significantly influence the damage development;
- it should always be kept in mind that small scale experiments might be subject to scale and model effects. Verification of the results with large scale models and prototype measurements is indispensable;
- finally, wave run-up tests on larger scale will reveal the scale effects to which wave run-up is subject and allow for measurements of wave impacts on the platforms.

Appendix I: Filter criteria

A scour protection usually exists of two essential parts: the top armour layer and the filter. The armour layer provides protection against the hydraulic action, but cannot prevent the loss of subsoil through the scour protection. The filter keeps the grains of the subsoil in place, while allowing water flow across the soil boundary. One or more filter layers are applied between the top armour layer and the subsoil to be able to avoid winnowing of the subsoil through the armour layer. A filter can be either granular or geosynthetic.

Design rules for both geometrically open and closed granular filters are given, based on CUR (1993) and Schiereck (1998) and a reference is made to the filter criteria which can be used in the prediction tool. The most important characteristics of geotextile filters are presented, despite the fact that up till now they have seldom been used as a filter for a monopile scour protection, because some suggest the use of geotextile containers as a possible solution for a scour protection system, integrating the armour layer and the filter layer (Heibaum (2000), Grune et al. (2006)).

Both for granular and geosynthetic filters additional problems for filter placement arise with high water depths and situations where both currents or waves are present (marine environment). Although the correct placement of a filter is as important as its design, it is not described in this appendix, for this we refer to CUR (1993).

I.1. Granular filter

Several methodologies can be followed in designing a granular filter, two of which will be highlighted here: geometrically closed filters and stable, geometrically open filters. Figure AI-1 shows the relation between the gradient in porous flow and a representative ratio of the filter and base sediment size.

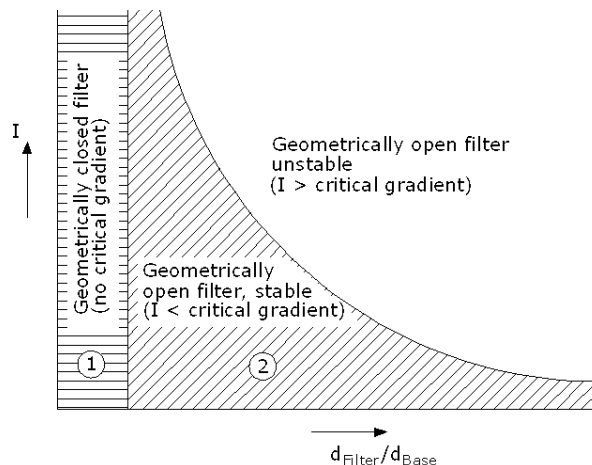


Figure AI-1: Different filter types (geometrically open - geometrically closed filter)

For small values of d_{Filter}/d_{Base} , the hydraulic gradient has no influence on the transportation of the base material and the filter is termed geometrically closed. For a geometrically open filter on the other hand, the grains of the filter are large enough to allow for transport of the base material through the filter. However, when the hydraulic load is not large enough to move the sediment the filter remains stable. Sometimes, some loss of material is accepted (unstable geometrically open filter), but the design of such a filter is outside the scope of this work.

The design of a geometrically closed filter only requires the knowledge of the grains size distribution, while for a geometrically open filter the hydraulic gradient also needs to be known. As it is much easier to obtain the grain size distribution than hydraulic gradients, geometrically closed filters are used more often (Heibaum (2004)).

I.1.1. Geometrically closed filters

The main goal of a geometrically closed filter is to prevent erosion of the subsoil, independent of the hydraulic load. This is obtained by making sure that the space between the filter grains is smaller than the base sediment's grain size. Next to the stability between the filter layer and the base layer, the permeability of the filter needs to be larger than the permeability of the base layer and the filter must be internally stable. (reason for this criterion)

These three criteria are translated into three quantitative criteria. Different empirical criteria are suggested. In the prediction tool, a distinction is made between the following three authors: CUR (1993), May et al. (2002) and CUR (1995). The criteria need to be applied to the interface between the armour layer and the filter, as well as to the interface between the filter and the base soil.

According to CUR (1993):

$$\text{Stability criterion: } \frac{d_{f15}}{d_{b85}} \leq 5 \quad (9.1)$$

$$\text{Permeability criterion: } \frac{d_{f15}}{d_{b15}} > 5 \quad (9.2)$$

$$\text{Internal stability criterion: } \frac{d_{f60}}{d_{f10}} < 10 \quad (9.3)$$

In which $d_{f\%}$ represents the particle size of the filter for which x% by weight of the filter material is smaller and $d_{b\%}$ represents the particle size of the base material for which x% by weight of the base material is smaller.

According to May et al. (2002):

The permeability criterion and internal stability criterion are identical to (9.2) and (9.3). An additional stability criterion to (9.1) is given, depending on the grading of the base material:

$$\text{For uniformly graded material: } \frac{d_{f50}}{d_{b50}} \leq 5 \quad (9.4)$$

$$\text{For well-graded material: } 5 \leq \frac{d_{f50}}{d_{b50}} \leq 20 \quad (9.5)$$

According to CUR (1995):

CUR (1995) gives additional criteria for the internal stability of the filter:

$$d_{f10} < 4d_{f5} \quad (9.6)$$

$$d_{f20} < 4d_{f10} \quad (9.7)$$

$$d_{f30} < 4d_{f15} \quad (9.8)$$

$$d_{f40} < 4d_{f20} \quad (9.9)$$

I.1.2. Geometrically open filters

Beside a geometrically closed filter, another possibility is to design a stable geometrically open filter by reducing the hydraulic load at the subsoil-armour layer interface. This is possible by applying a sufficiently thick armour layer. It is important that the hydraulic load at the interface does not create movement of the subsoil in any circumstance. As this can be quite difficult, a geometrically closed filter is used more often.

For a stationary flow parallel with the interface of the filter, Klein Breteler found a relationship between the critical Shields parameter of the base material and the critical filter velocity (CUR (1993)):

$$u_{f,cr} = \left\{ \frac{n_f}{c} \left(\frac{d_{f15}}{\nu} \right)^m (\theta_{cr,b} \Delta_b g d_{b50})^{0.5} \right\}^{\frac{1}{1-m}} \quad (9.10)$$

With $u_{f,cr}$ the critical velocity; n_f the porosity of the filter material; ν the kinematic viscosity of water; $\theta_{cr,b}$ the critical Shields parameter for the base material; Δ_b the relative density of the base material; g the acceleration due to gravity; c a coefficient; m a coefficient and d_{b50} the median grain size of the base material (for which 50% of the material is finer by weight).

Equation (9.10) is valid for base material with a diameter between 0.1 and 1 mm.

The values of c , m and $\theta_{cr,b}$ reproduced in CUR (1993) and originally given by Klein Breteler are given in Table I.1. In case d_{b50} exceeds 2 mm, a value for c of $0.23 + 1.9 d_{b50}$ can be used.

Table I.1: Values for c , m and θ_{cr} according to Klein Breteler; from CUR (1993)

d_{b50} [mm]	c [-]	m [-]	$\theta_{cr,b}$ [-]
0.1	1.18	0.25	0.11
0.15	0.78	0.20	0.073
0.2	0.71	0.18	0.055
0.3	0.56	0.15	0.044
0.4	0.45	0.11	0.038
0.5	0.35	0.07	0.036
0.6	0.29	0.04	0.034
0.7	0.22	0	0.034
0.8	0.22	0	0.034
1.0	0.22	0	0.035

Based on experimental results a relationship is deduced in CUR (1993) between the external velocity on the top layer and the internal hydraulic load on the interface:

$$\frac{u_t}{u_f} = \left\{ \frac{2.2 C^2 R}{g n_f C_0 d_{f15}} \right\}^{0.5} \quad (9.11)$$

With u_t the flow velocity in the top layer (assumed to be equal to the velocity just above the top layer); u_f the velocity at the interface; g the acceleration due to gravity; n_f the porosity of the filter material; C the Chézy coefficient; R the hydraulic radius = water depth for a wide channel; d_{f15} the stone diameter for which 15% of the filter material is finer by weight and C_0 a coefficient which can be calculated as:

$$C_0 = 1 + 1.8 \left(\frac{R}{d_{t50cr}} \right)^{0.33} \left(1 - \frac{t_s}{R} \right) \quad (9.12)$$

With R the hydraulic radius = water depth; d_{t50cr} the critical stone size of the top layer for the load acting on the top layer and t_s the thickness of the top layer.

Another relationship for a geometrically open filter is called the Bakker/Konter formula, which gives a relationship for the interface top layer - filter layer (equation (9.13)) and one for the interface filter layer-base material (equation (9.14)).

$$\frac{d_{t15}}{d_{f50}} = \frac{1}{\gamma} \frac{2.2 \theta_{cr,f} \Delta_f R}{e^2 C_0 \theta_{cr,t} \Delta_t d_{t50cr}} \quad (9.13)$$

$$\frac{d_{f15}}{d_{b50}} = \frac{1}{\gamma} \frac{2.2}{e^2 C_0} \frac{\theta_{cr,b} \Delta_b}{\theta_{cr,f} \Delta_f} \frac{R}{d_{f50cr}} \quad (9.14)$$

A value of 2 is recommended for the coefficient γ . C_0 is computed with equation (9.12); $\theta_{cr,f}$, $\theta_{cr,t}$ and $\theta_{cr,b}$ are the critical Shields parameters of respectively the filter material, the top material and the base material; Δ_f , Δ_t and Δ_b are the relative densities of filter material, top material and base material; R is the hydraulic radius; d_{t50cr} and d_{f50cr} are the critical stone size of the top and filter material and e gives the ratio of the shear stress and the flow velocity at the interface and can be calculated as:

$$e = c \text{Re}^{-m} \quad (9.15)$$

With c and m as in Table I.1.

CUR (1993) mentions that, according to Klein Breteler, the critical velocity for non-stationary flows parallel with the filter (e.g. waves) can be calculated as for stationary parallel flows, when the period of the flow exceeds 2s.

I.2. Geotextile filters

Two forms of geotextile are used in scour protection, woven and non-woven. Woven geotextiles have regularly placed fibres orientated at right angles and have uniform hole sizes. Non-woven geotextiles use randomly placed fibres, leading to a range of hole sizes. Woven geotextiles are generally stronger than non-woven geotextiles, whereas non-woven geotextiles can stretch more before failure (May et al. (2002)).

Geotextile filters are designed primarily according to three criteria: soil retention, permeability and strength. Soil retention is related to the size of the pores or holes in the geotextile, termed the characteristic opening size, which is normally defined in terms of O_{90} (90% of the pores are smaller) and the O_{95} (95% of the pores are smaller). The following criteria have been suggested in CUR/RWS Report 169 (Centre for Civil engineering Research & Codes, 1995):

For geotextiles laid against non-cohesive, uniform soils:

$$\frac{O_{95}}{d_{85base}} < 1 \quad (9.16)$$

To satisfy permeability requirements the following criteria is suggested:

$$\kappa_g \geq M \kappa_s \quad (9.17)$$

where κ_s (in m/s) is the permeability of the soil, κ_g (in m/s) is the permeability of the geotextile and M is a coefficient which depends on the type of geotextile:

$M = 10$ for woven geotextiles

$M = 50$ for non-woven geotextiles.

The strength criterion is based on the need to avoid damage caused by the armour layer being placed on the geotextile. Reference should be made to manufacturers' literature to determine the appropriate strength of a geotextile to cope with different sized stones being dropped onto it.

References

- CUR, 1993. Filters in de waterbouw. Report 161, Gouda.
- CUR, 1995. Geotextielen in de waterbouw. Report 174, Gouda.
- Grune, J., Sparboom, U., Schmidt-Koppenhagen, R., Wang, Z. and Oumeraci, H., 2006. Stability Tests of Geotextile Sand Containers for Monopile Scour Protection, International Conference on Coastal Engineering, San Diego, pp. 5093.
- Heibaum, M.H., 2000. Scour Countermeasures Using Geosynthetics and Partially Grouted Riprap. Transportation Research Record, 1696(-1): 244-250.
- Heibaum, M.H., 2004. Geotechnical filters, the important link in scour protection, International Conference on Scour and Erosion, Nanyang University, Nanyang, Singapore.
- May, R.W.P., Ackers, J.C. and Kirby, A.M., 2002. Manual on Scour at Bridges and Other Hydraulic Structures. CIRIA.
- Schierreck, G.J., 1998. Filter structures. In: K.W. Pilarczyk (Editor), Dikes And Revetments: Design, Maintenance And Safety Assessment. Taylor & Francis.

Appendix II: Installation of steady current circuit

An exterior pump circuit was installed within the framework of this study at of the department of civil engineering, Ghent University. The pump circuit allows a reversible current in the wave flume. This appendix describes the pump and the pump circuit (inlet, outlet...) as well as the steady current velocity profile.

II.1. Pump circuit

The pump is a centrifugal pump which is located next to the wave flume. The pump characteristics are given in Figure II.1. A maximum flow of 320 m³/h can be attained.

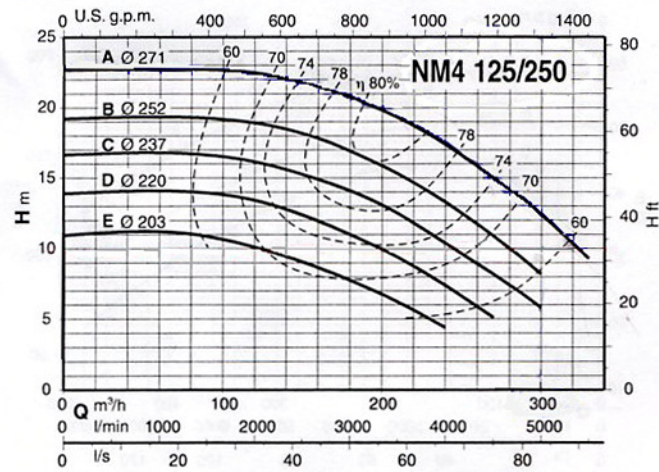


Figure II.1: Pump curve of the Calpeda NMW 125/250A

Figure II.2 shows a top view of the wave flume with the location of the pump circuit, while Figure II.3 shows a picture of the pump set-up, which allows to control and reverse the flow.

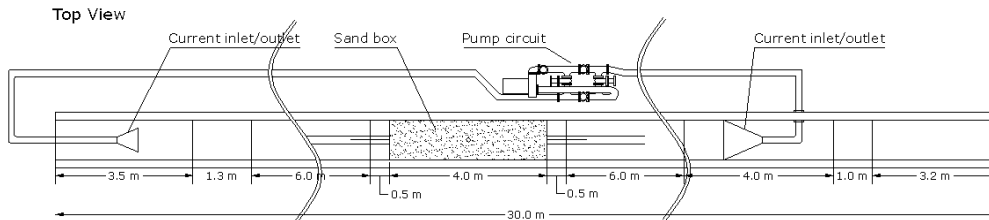


Figure II.2: Top view of the wave flume and pump set-up



Figure II.3: Picture of the pump set-up

The design of the in- and outlet is made to optimally guide the flow and to minimize turbulence at the flow inlet. Due to the large velocities which develop in the pipes and the limited height of the in- and outlet structure (the height is limited to reduce the obstruction for the waves) some distance is required to obtain a natural velocity profile. For this reason and to allow a reversible current, the test-section is placed just in between the in- and outlet structure. Some pictures of the in- and outlet structure are shown in Figure II.4 to Figure II.6. Figure II.5 shows the construction of the flow inlet: due to the gradual widening of the structure, the flow is distributed evenly along the width of the flume. Inside the inlet structure, an aluminium guidance is mounted to improve the flow distribution over the width of the flume. To allow for a reversible current, the in- and outlet structure are both constructed to optimize the flow distribution. The pump in-outlet at the end of the wave flume is made less wide than the width of the wave flume to permit a return flow in case of wave overtopping.



Figure II.4: Connection of the pipes with the in- (right) and outlet (left) structure

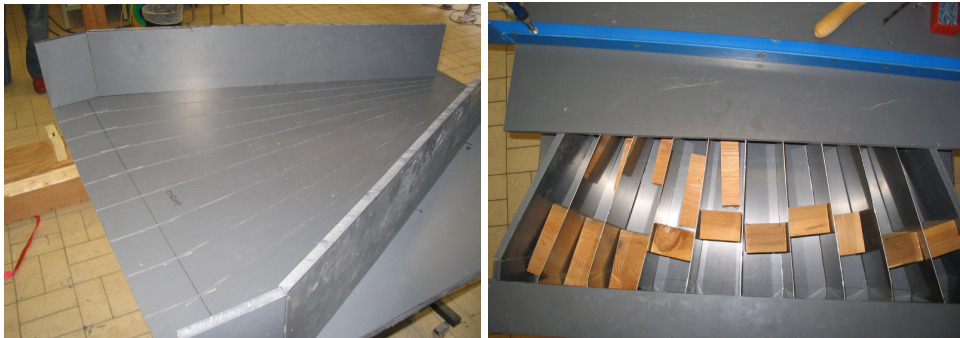


Figure II.5: Picture of the inside of the flow inlet



Figure II.6: Picture of the pump in- and outlet in the flume

II.2. Vertical distribution of the current

To measure the flow velocity, an electromagnetic velocity meter (Nautilus) is used (Figure II.7). The technical characteristics of the velocity meter are given in Table II.1.



Figure II.7: Electromagnetic velocity meter

The Nautilus works according to Michael Faraday's principle of electromagnetic induction. When an electric conductive environment displaces itself in a magnetic field, it produces a tension, induced in the conductor:

$$T_e = B_m L_c U_c \quad (10.1)$$

With T_e the measured tension; B_m the magnetic field; L_c the length of the conductor and U_c the flow velocity.

Table II.1: Technical characteristics of velocity meter

parameter	Value
Working temperature	-5°C - +40°C
Material of the sensor	epoxy resin, resistant against impact loading
Material of the electrodes	Titanium
Minimal required conductivity of the liquid	5 μ S
Dimensions	approx. 18cm x 5cm x 2cm
Weight	approx. 0.5kg
Measurement range	0.000 m/s - 1.5 m/s
Measurement rate	2Hz
Accuracy	1% of the measured value
Stability of the zero value	± 2 mm/s

The flow distribution near the test section is tested prior to the main tests. For this, measurements along a 3D measurement grid are made. Figure II.8 shows a top and side view of the measurement grid. At each location, 6 to 8 measurements are made along the height of the flume. The tests are performed with a water depth of 0.40m.

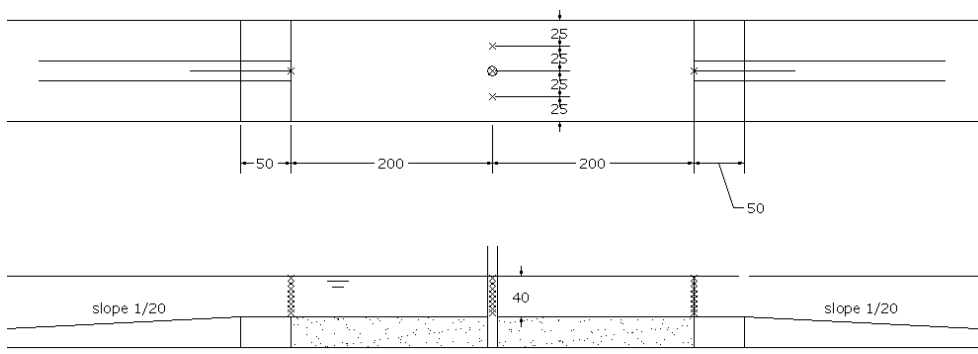


Figure II.8: Location of measurement points

The investigated topics are summed up below and the corresponding results are given in Figure II.9 until Figure II.13:

Repeatability of velocity measurements (Figure II.9)

The measurements are very repeatable. The standard deviation is less than 1% of the measured velocity, which is within the accuracy of the velocity meter, except for the measured velocity close to the bottom. The variation of the velocity close to the bottom can however be explained by the fact that a local scour hole developed at the location of the velocity meter.

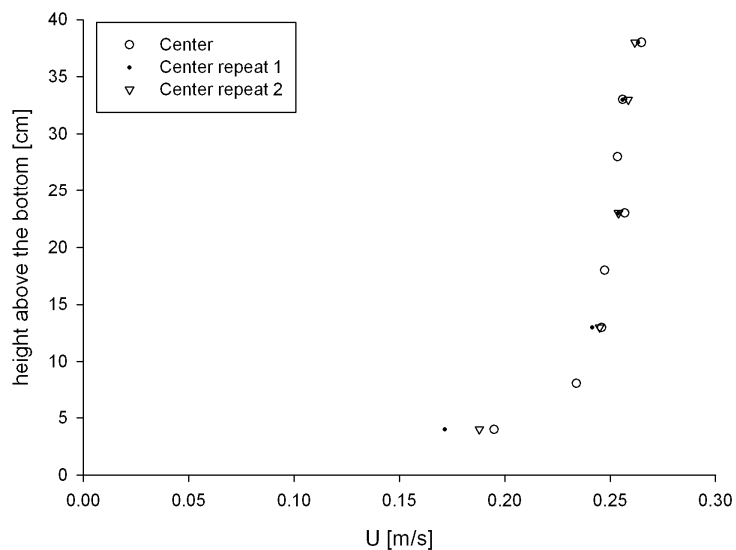


Figure II.9: Repeatability tests at the location of the pile, center of the flume

Distribution of velocity along the height of the flume (Figure II.10)

The distribution of the flow velocities u can be represented by the logarithmic form (Prandtl and von Karman):

$$u = \frac{u_*}{k} \ln\left(\frac{y}{y_0}\right) \quad (10.2)$$

With $\kappa = 0.40$ the von Karman constant.

For the measurements, the following logarithmic distribution was obtained (plotted along with the measurements in Figure II.10):

$$u = 20 \ln\left(\frac{y}{0.0000825}\right) \quad (10.3)$$

For the logarithmic velocity profile in equation (10.2), the average velocity U_c is measured at a height which is approx. equal to 40% of the water depth ($0.365d$), this would be at a height of 0.146m above the bottom.

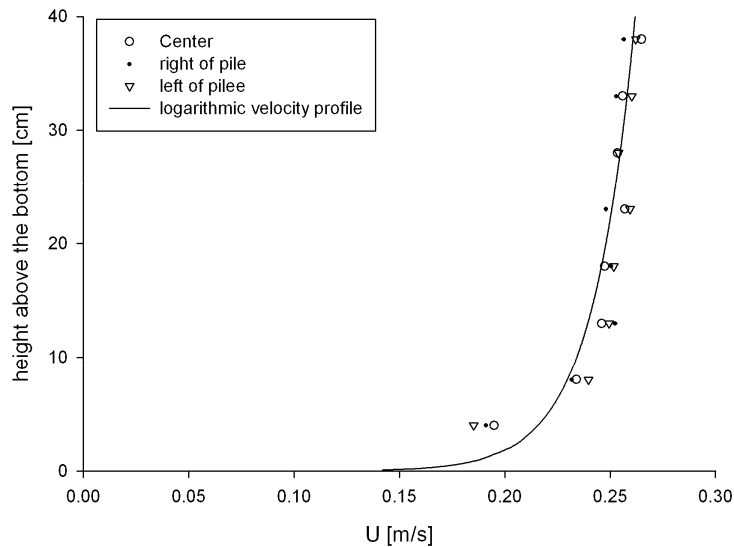


Figure II.10: Velocity distribution over the height of the flume

Distribution of the velocity along the width of the flume (Figure II.10)

The velocity profile at the center of the pile and at a distance of $1/4^{\text{th}}$ of the width of the flume are approximately the same. Although small variations are measured, it is not clear whether the velocity is smaller or higher near the walls (note that the velocities are not measured close by the wall, but still 0.25m from the wall). It can be concluded that the velocity is distributed evenly over the width of the wave flume.

Distribution of the velocity along the length of the test set-up (Figure II.11)

The velocity was measured at the beginning, centre and end of the test set-up.

Figure II.11 shows that the same velocity profile is obtained in each section, indicating that a constant velocity profile exists over the entire test set-up and more importantly that a stable velocity profile is formed.

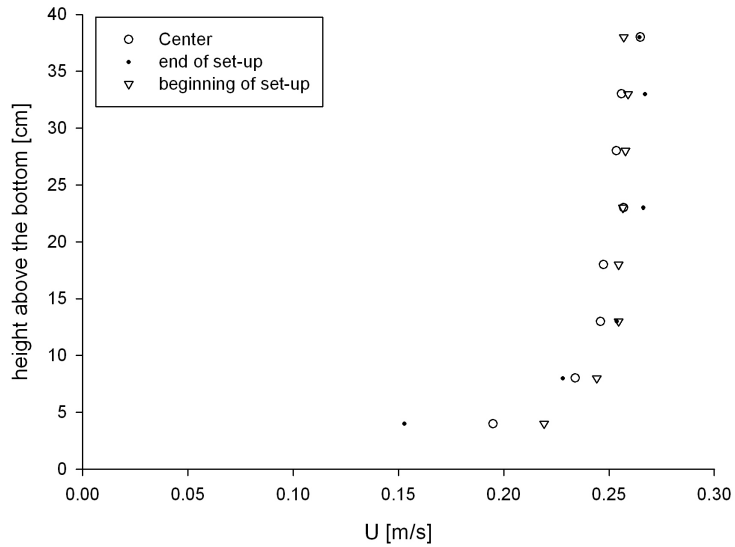


Figure II.11: Velocity distribution along the length of the test set-up

Influence of the presence of the pile (Figure II.12 and Figure II.13)

Figure II.12 and Figure II.13 respectively show the influence of the pile on the measurements made behind the pile and on the velocity measured beside the pile.

Figure II.12 shows the influence of the presence of the pile on the velocity measured at the end of the sand box (approx. 2 m behind the pile). A small influence is noted. For both tested flow velocities, the velocity decreases due to the presence of the pile, and the fluctuations (standard deviation) increases slightly. The advantage of this location however is that the flow near the pile is not influenced by the velocity meter. An adjustment for the measured velocity during the tests is derived below.

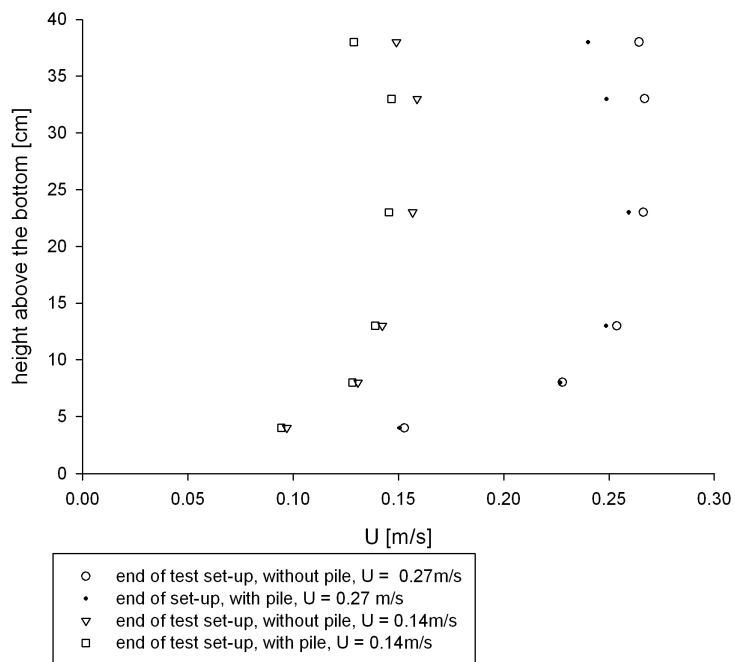


Figure II.12: Influence of presence of pile on velocity distribution behind the pile

Figure II.13 shows the influence of the presence of the pile on the velocity in the section of the pile. A velocity profile is shown, taken in the middle of the area between the pile and the side wall. The velocity in this section increases with approximately 6% due to the presence of the pile, due to the fact that the section is smaller.

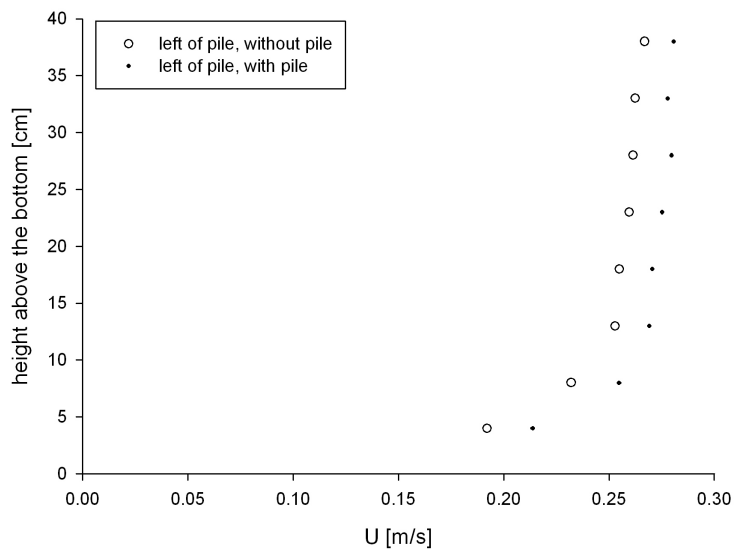


Figure II.13: Influence of presence of pile on velocity distribution beside the pile

As the flow was measured behind the pile during the tests, the measured flow velocity is disturbed by the pile's presence. Furthermore, the flow velocity is measured at a distance of 23 cm above the bottom, while the average flow velocity can be measured at a height of 14.6 cm ($= 0.365d$) above the bottom when the water depth is 40cm. For this reason, a conversion factor was determined between measurements without pile at a height of 14.6cm and measurements with pile at a height of 23cm above the bottom for the different flow velocities. In case of a smaller water depth (20cm), the respective heights with and without pile are 11cm (test situation) and 7.6cm (reference situation) above the bottom. The results are summarized in Table II.2.

Table II.2: Conversion factor for flow velocity

Water depth [m]	Target flow velocity [m/s]	Measured flow velocity with pile [m/s]	Measured flow velocity without pile [m/s]	Conversion factor [-]
0.40	0.07	0.0677	0.0752	1.11
0.40	0.14	0.1339	0.1408	1.05
0.40	0.21	0.1905	0.2034	1.07
0.40	-0.07	-0.0771	-0.7310	0.95
0.40	-0.14	-0.1489	-0.1444	0.97
0.20	0.14	0.1633	0.1728	1.06
0.20	0.28	0.2762	0.2887	1.05

To obtain the average flow velocities from the measured flow velocities during the tests, a conversion factor of 1.06 was used in the case of a current following the waves and a factor of 0.96 for a current opposing the waves.

Appendix III: Scour tests

Some tests were performed to estimate the scour depth at the flow velocities that are used as loading on the scour protections. The aim of the tests is to compare the measurements of the scour depths with previous research to see if the tests are reliable. The sand which is used for the tests is very fine, narrow graded sand, with a d_{50} of 100 μm . The pile diameter is 0.1m.

Only the current alone cases are tested, as it is generally accepted that a combination of waves and currents lead to smaller scour depths (chapter 1). The equilibrium scour depth and the time scale of the scour are compared with results or formulae found in literature (and described in chapter 1).

The scour tests are performed for approximately 2 to 3 hours. The scoured profiles are measured with the non-contact profiler and the result for each current velocity is given below. In the subtitle, the target flow velocities is mentioned. The measured flow velocity may deviate a little from this target value.

III.1. $u = 0.07 \text{ m/s}$

The water depth $d = 0.4\text{m}$ near the pile. There is no significant movement of the sediment, neither far away from the pile nor close to the pile. The test is stopped very quickly. No measurements are made.

III.2. $u = 0.14 \text{ m/s}$

The water depth $d = 0.4\text{m}$ near the pile. The velocity measurements give the following values for mean velocity U_c and standard deviation σ :

$$U_c = 0.147 \text{ m/s}$$

$$\sigma = 0.0146 \text{ m/s}$$

There is significant movement of the sediment near the pile, but no movement in the area before the pile, so this is clear-water scour. This means that the acquired scour depth might be subjected to scale effects, as the sediment size is not scaled correctly. As mentioned in chapter 3, it is often accepted that scale effects are limited when live bed scour occurs. Because the amplification of the shear stresses is modelled correctly, the amount of sediment moving towards the pile and moving away from the pile due to the increased shear stresses in prototype and in the model is assumed to be scaled correctly in the live bed situation.

After 3h, the test has reached an equilibrium stage and the profile is measured. Figure III.1 shows a picture of the scour and images of the measurement made with the profiler. The current flows from right to left on all images. The extent of the scour is added on the contour plot of the scour measurement, as is the location of the largest scour depth.

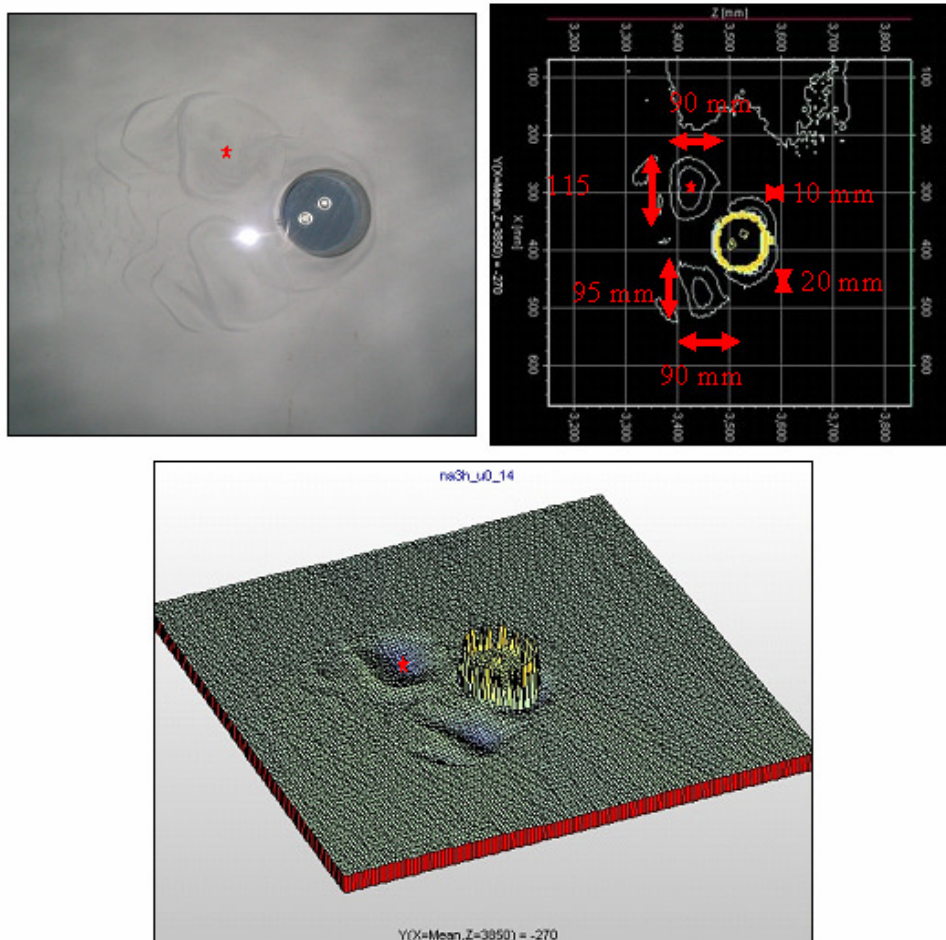


Figure III.1: Picture and measurement of the scour after 3h, $U_c = 0.147\text{m/s}$

The maximum scour depth is 24 mm, which leads to $S/D = 0.24$. The scour depth is calculated with the formulae given in chapter 1. The results are given in Table III.1.

Table III.1: Expected scour depth according to literature

Method	Breusers and Raudkivi (1991)	Melville (1997)	Whitehouse (1998)	Hoffmans and Verheij (1997)	Schiereck (2001)	Sheppard and Miller Jr (2006)
Eq. number	(1.49)	(1.53)	(1.59)	(1.60)	(1.63)	(1.65)
Scour depth S/D	1.73	0.58	0.27	0.23	0.31	0.69

III.3. $u = 0.21 \text{ m/s}$

The water depth $d = 0.4\text{m}$ near the pile. The velocity measurements give the following values for mean velocity U_c and standard deviation σ :

$$U_c = 0.203 \text{ m/s}$$

$$\sigma = 0.0405 \text{ m/s}$$

There is still no movement of the sediment in the region that is not influenced by the pile, which means this is again clearwater scour and the remarks made above on the scale effects and suggested values in literature for scour depth still apply. A reasonably large scour hole develops.

After 2h, the test has reached an equilibrium stage and the profile is measured. Figure III.2 shows a picture of the scour and images of the measurement made with the profiler. The current flows from right to left on all images. The extent of the scour is added on the contour plot of the scour measurement, as is the location of the largest scour depth.

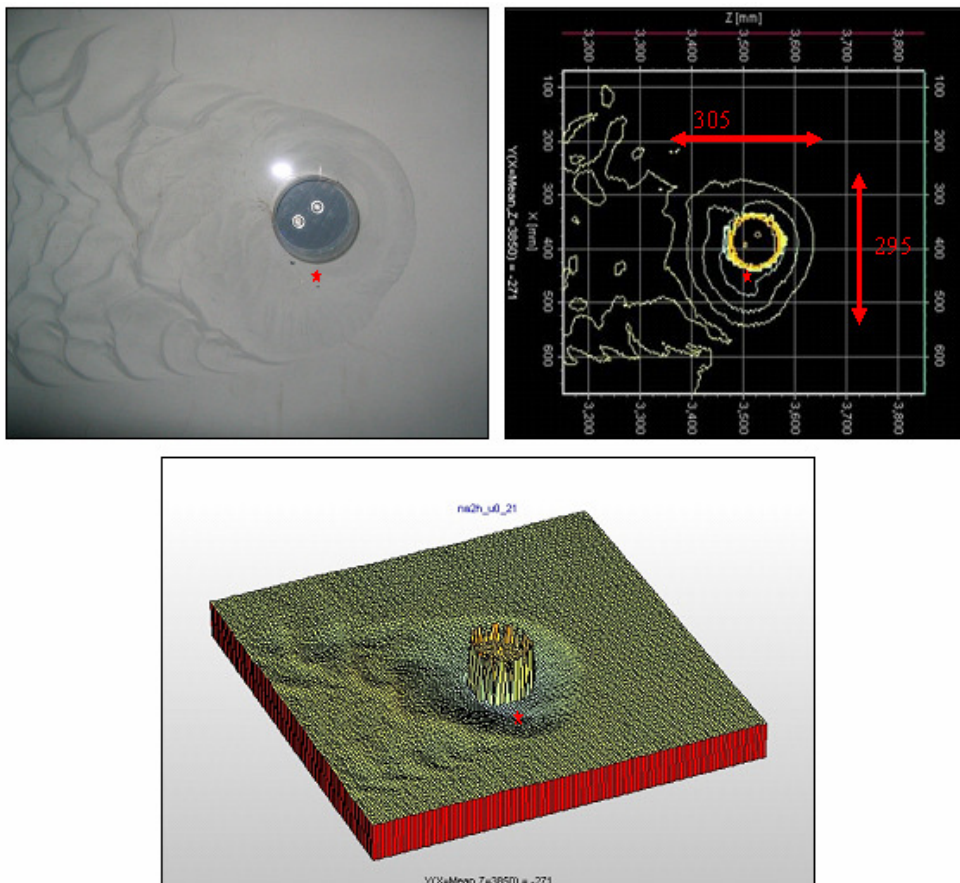


Figure III.2: Picture and measurement of the scour after 2h, $U_c = 0.203\text{m/s}$

The maximum scour depth is 67 mm, which leads to $S/D = 0.67$. The scour depth is again calculated with the formulae given in chapter 1. The results are given in Table III.2.

Table III.2: Expected scour depth according to literature

Method	Breusers and Raudkivi (1991)	Melville (1997)	Whitehouse (1998)	Hoffmans and Verheij (1997)	Schiereck (2001)	Sheppard and Miller Jr (2006)
Eq. number	(1.49)	(1.53)	(1.59)	(1.60)	(1.63)	(1.65)
Scour depth S/D	1.73	0.81	0.84	0.91	1.21	1.35

III.4. $u = 0.28$ m/s

The water depth $d = 0.2$ m near the pile. The velocity measurements give the following values for mean velocity U_c and standard deviation σ :

$$U_c = 0.298 \text{ m/s}$$

$$\sigma = 0.0151$$

The water depth near the pile is now only 0.2m, as this is the only way to generate the higher current velocity.

As can be seen on the pictures below (ribbles), this is a live bed situation, which means it can be assumed that scale effects are limited. The critical velocity, calculated according to equation (1.36), (1.2) and (1.3) is $U_{cr} = 0.253$ m/s. A very large scour hole develops.

After 2h, the test has reached an equilibrium stage and the profile is measured. Figure III.3 shows a picture of the scour and images of the measurement made with the profiler. The current flows from right to left on all images. The extension of the scour is added on the contour plot of the scour measurement, as is the location of the largest scour depth.

The maximum scour depth is 109 mm, which leads to $S/D = 1.09$. The scour depth is again calculated with the formulae given in chapter 1. The results are given in Table III.3.

Table III.3: Expected scour depth according to literature

Method	Breusers and Raudkivi (1991)	Sumer et al. (1992)	Melville (1997)	Hoffmans and Verheij (1997)	Schiereck (2001)	Sheppard and Miller Jr (2006)
Eq. number	(1.50)	(1.51)	(1.53)	(1.61)	(1.63)	(1.66)
Scour depth S/D	1.96	1.30	4.00	1.12	2.00	0.90

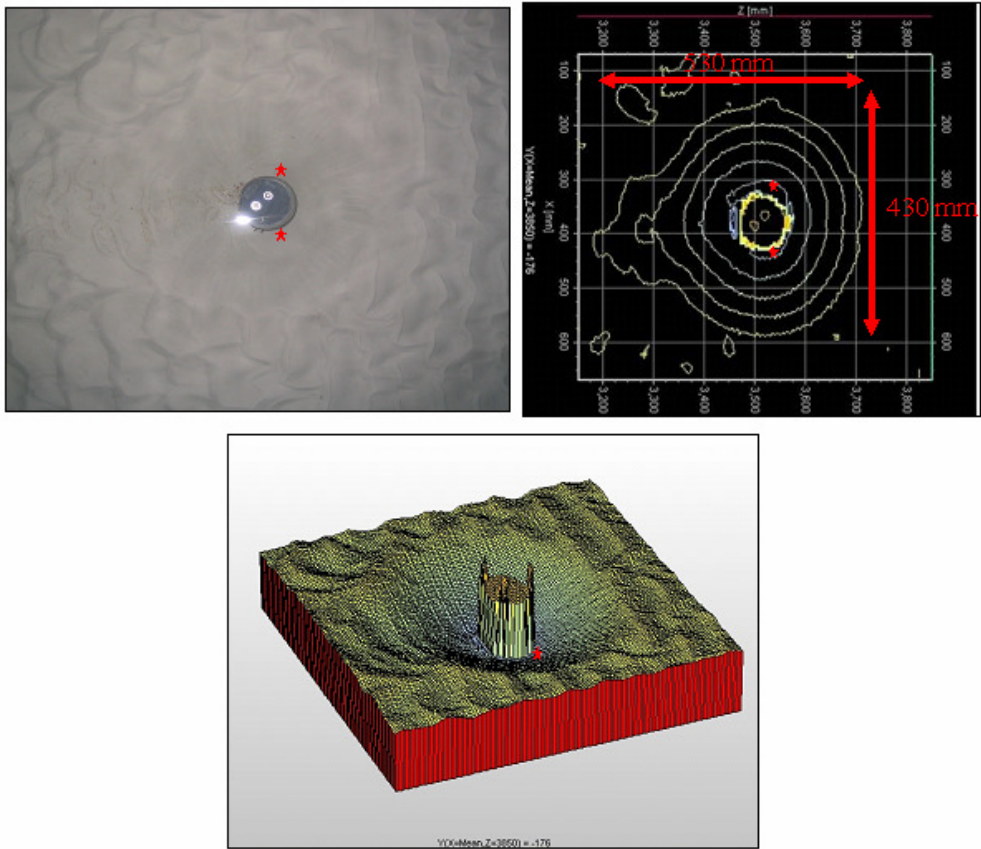


Figure III.3: Picture and measurement of the scour after 2h, $U_c = 0.298\text{m/s}$

References

- Breusers, H.N.C. and Raudkivi, A.J., 1991. Scouring. Balkema.
- Hoffmans, G.J.C.M. and Verheij, H.J., 1997. Scour manual. A.A. Balkema, Rotterdam, Netherlands ; Brookfield, VT, xv, 205 p. pp.
- Melville, B.W., 1997. Pier and Abutment Scour: Integrated Approach. Journal of Hydraulic Engineering, 123(2): 125-136.
- Schiereck, G.J., 2001. Introduction to Bed, Bank and Shore Protection. Delft University Press.
- Sheppard, D.M. and Miller Jr, W., 2006. Live-Bed Local Pier Scour Experiments. Journal of Hydraulic Engineering, 132: 635-642.
- Sumer, B.M., Fredsøe, J. and Christiansen, N., 1992. Scour Around Vertical Pile in Waves. Journal of Waterway, Port, Coastal and Ocean Engineering, 118(1): 15-31.
- Whitehouse, R., 1998. Scour at marine structures : a manual for practical applications. Thomas Telford, London, xix, 198 pp.

Appendix IV: Influence of steady current on wave characteristics

IV.1. Change of wave length and wave height

When a wave travels on a steady current with depth averaged velocity U_c , the wave characteristics are altered by the presence of the current. When considering a fixed reference frame and a constant current velocity, the wave period T_w does not change (Fredse and Deigaard (1992)). The celerity of the wave will however change from $C = L/T_w$ to $C + U_c$. The higher wave celerity of the waves will in return influence the wave length:

$$L = (C + U_c)T_w \quad (12.1)$$

An iterative approach can be used to calculate the correct wave celerity and wave length. A good estimate of the wave length can generally be obtained with 2 or 3 iterations.

The wave kinematics should however be calculated by considering a frame of reference, moving with the current, as in this case the equations and solutions for water motion are identical to the case of no current (Fredse and Deigaard (1992), Chawla and Kirby (1998)). The wave period $T_{w,r}$ in the moving reference frame can be calculated as:

$$T_{w,r} = T_w \frac{C + U_c}{C} \quad (12.2)$$

Many authors present this in the frequency shape:

$$\omega = \sigma + kU_c \quad (12.3)$$

With ω the angular frequency in the fixed reference frame, σ the angular frequency in the moving reference frame, k the wave number = $2\pi/L$ and U_c the steady current velocity. Equation (12.3) is also known as the Doppler equation. The maximum near bed velocity U_m should be calculated as (Fredse and Deigaard (1992)):

$$U_m = \frac{\pi H}{T_r} \frac{1}{\sinh(kd)} \quad (12.4)$$

Equation (12.2) leads to an increase in wave length (and celerity) in case of a wave following a current and a decrease in wave length (and wave celerity) in the case of a wave opposing a current. The same can be concluded for the wave period in the moving reference frame, thus an increased wave period for a wave

following the current, leading (with equation (12.4)) to an increased bottom velocity in the case of a wave following the current, and a decreased bottom velocity in the case of a wave opposing the current.

IV.2. Wave attenuation

Waves traveling a wave flume loose height along the length of the wave flume. Several authors (Simons et al. (1988), Nielsen (1992), Sato (1992)) have observed that waves traveling on an opposing current loose height more rapidly, whereas wave traveling on a following current loose height more slowly. Some suggest that this is caused by the influence of the current on the wave boundary layer (Simons et al. (1988)), but others note little difference to the wave friction factor when a current is superimposed (Sleath (1990)). Nielsen (1992) suggests that the change in wave attenuation can be explained by the change in wave group velocity (which together with the wave height determines the wave energy flux) rather than the change in boundary layer. When the wave height is measured at the location of the structure (as is the case for the tests performed within the framework of this study), this aspect does not have to be taken into consideration.

IV.3. Wave breaking and blocking

As described above, an opposing current slows down the waves leading to an increase in wave steepness, which can lead to wave breaking when the waves become too steep (Chawla and Kirby (1998)). When the current is strong enough, the wave velocity goes to zero and the current prevents the wave energy from traveling upstream. This is termed "wave blocking". In deep water, the condition where waves break depends on the ratio of wave celerity and the current velocity. In shallow water, the equations given by Miche for the breaker criterion without current remain available (Sakai et al. (1986)). In the case of a sloping bed, Sakai et al. (1986) note that the wave breaking is affected by an opposing current and that it depends on a normalized discharge, the bottom slope and the value of H_0/L_0 , with the index 0 denoting deep water conditions. The normalized discharge is defined per unit width and is equal to $q/(g^2T_w^3)$, with q the discharge per unit width, g the gravitational acceleration and T_w the wave period. Sakai et al. (1986) find that the breaking wave height increases (slightly) for an opposing current and a sloping bottom, but that the water depth at which breaking occurs increases significantly (so for a constant water depth, waves tend to break sooner).

References

- Chawla, A. and Kirby, J.T., 1998. Experimental study of wave breaking and blocking on opposing currents. In: B.L. Edge (Editor), International conference on coastal engineering, Copenhagen, Denmark, pp. 759-772.
- Fredsøe, J. and Deigaard, R., 1992. Mechanics of Coastal Sediment Transport. Advanced series on Ocean Engineering, Vol. 3. World Scientific.
- Nielsen, P., 1992. Coastal Bottom Boundary Layers and Sediment Transport. Advanced Series on Ocean Engineering, Vol. 4. World Scientific.
- Sakai, S., Hiyamizu, K. and Saeki, H., 1986. Irregular wave transformation affected by opposing currents. In: B.L. Edge (Editor), International conference on coastal engineering, Taipei, Taiwan pp. 563-575.
- Sato, M., 1992. On the attenuation of waves propagating with a current. In: B.L. Edge (Editor), International Conference on Coastal Engineering, Venice, Italy, pp. 563-575.
- Simons, R.R., Grass, A.J. and Kyriacou, A., 1988. The influence of currents on wave attenuation. In: B.L. Edge (Editor), International Conference on Coastal Engineering, Malaga, Spain, pp. 363-376.
- Sleath, J.F.A., 1990. Velocities and bed friction in combined flows. In: B.L. Edge (Editor), International Conference on Coastal engineering, Delft, The Netherlands, pp. 450-463.

Appendix V: 3D EPro measurements

In all cases the bed profile was measured with a non-contact laser profiler before each test and after 1000 waves, 3000 waves and 5000 waves. A picture of the profiler is shown in Figure 4-5. The profiler measures a rectangular area around the pile, which is 0.6m wide and 0.7m long on a grid of 5mm x 5mm. The profiler follows a track which can be specified by the user. The different possibilities are shown in Figure V.1. For the tests' measurements, the profiler measured according to track 9, which means that it stops along fixed positions in the length of the flume, while progressing continuously along the width of the flume.

Whenever possible, a test is completed in one day, to make sure the profiler keeps its offset settings. Furthermore the pile is fixed to the bottom and has a flat surface inside to provide an inspection point for the vertical offset.

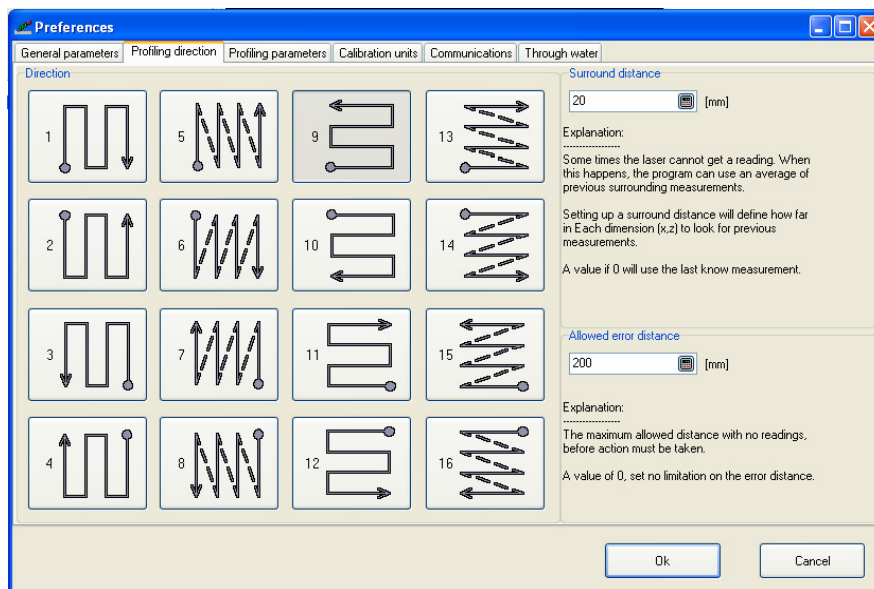


Figure V.1: Profiler tracking possibilities

A picture and example of an epro-file with the profiler's measurements is given in Figure V.2. In the picture, waves come from the right, while they come from the top in the profiler measurement. The epro-file gives a top view of the measurement, a 3D image and a cross section in both directions.

As can be seen on the pictures, some sand moves on top of the scour protection. The pictures in appendix VI show that the sand never settles on top of the inner ring of the scour protection or at the location of damage. As the damage is only defined by the loss of material, the sand's presence therefore does not influence the measured damage.

As can be seen in Figure V.2, the plexiglass sides of the pile result in large peaks or troughs in the measurements. These values are filtered out manually during the analysis.

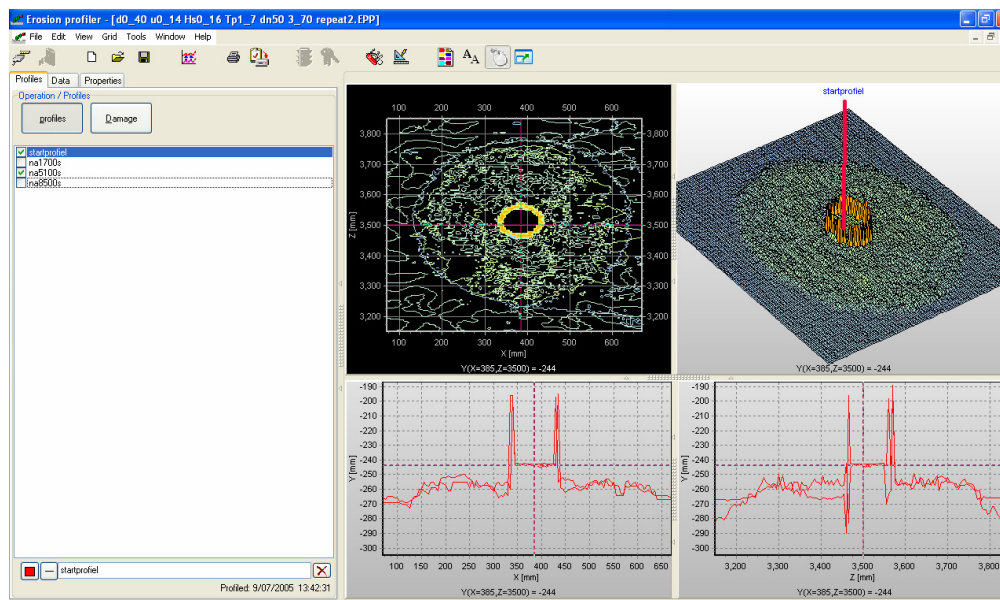
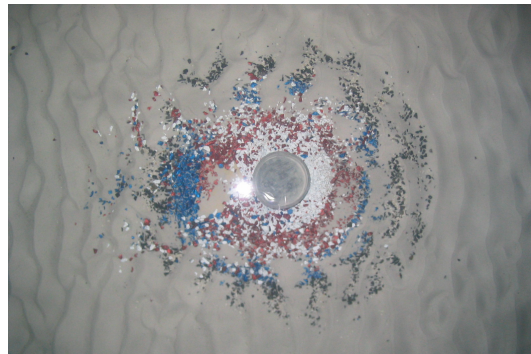


Figure V.2: Picture (top) and epro-file (profiler measurement, bottom) of scour protection: $U_{c, target} = 0.14\text{m/s}$, $H_s, target = 0.16\text{m}$, $T_p, target = 1.7\text{s}$, $d_{n50} = 3.45\text{mm}$


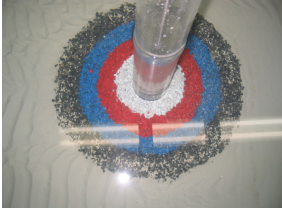

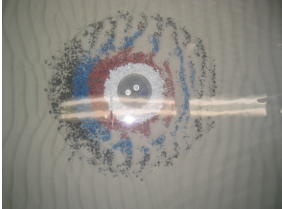
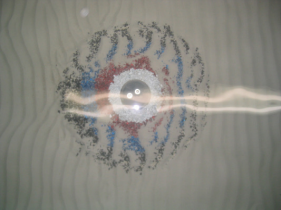
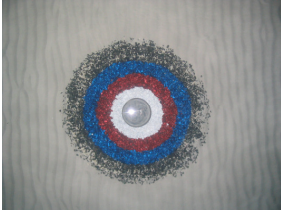

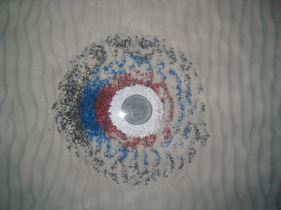
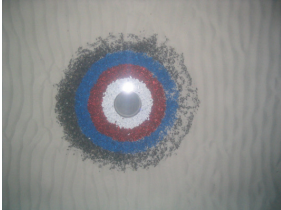


All profiler measurements are included on the DVD. Each measurement requires a *.txt, *.tee and *.EPP file. The file's name gives the specifics of the test and always lists: water depth – target current velocity – target significant wave height – target peak period – stone size – extra specifics. An example is given below for a water depth of 0.4m, a target velocity of 0.21m/s, a target significant wave height of 0.16m, a target peak period of 1.7s, a scour protection with $D_{n50} = 7.2\text{mm}$ and as extra specifics that the current opposes the waves:

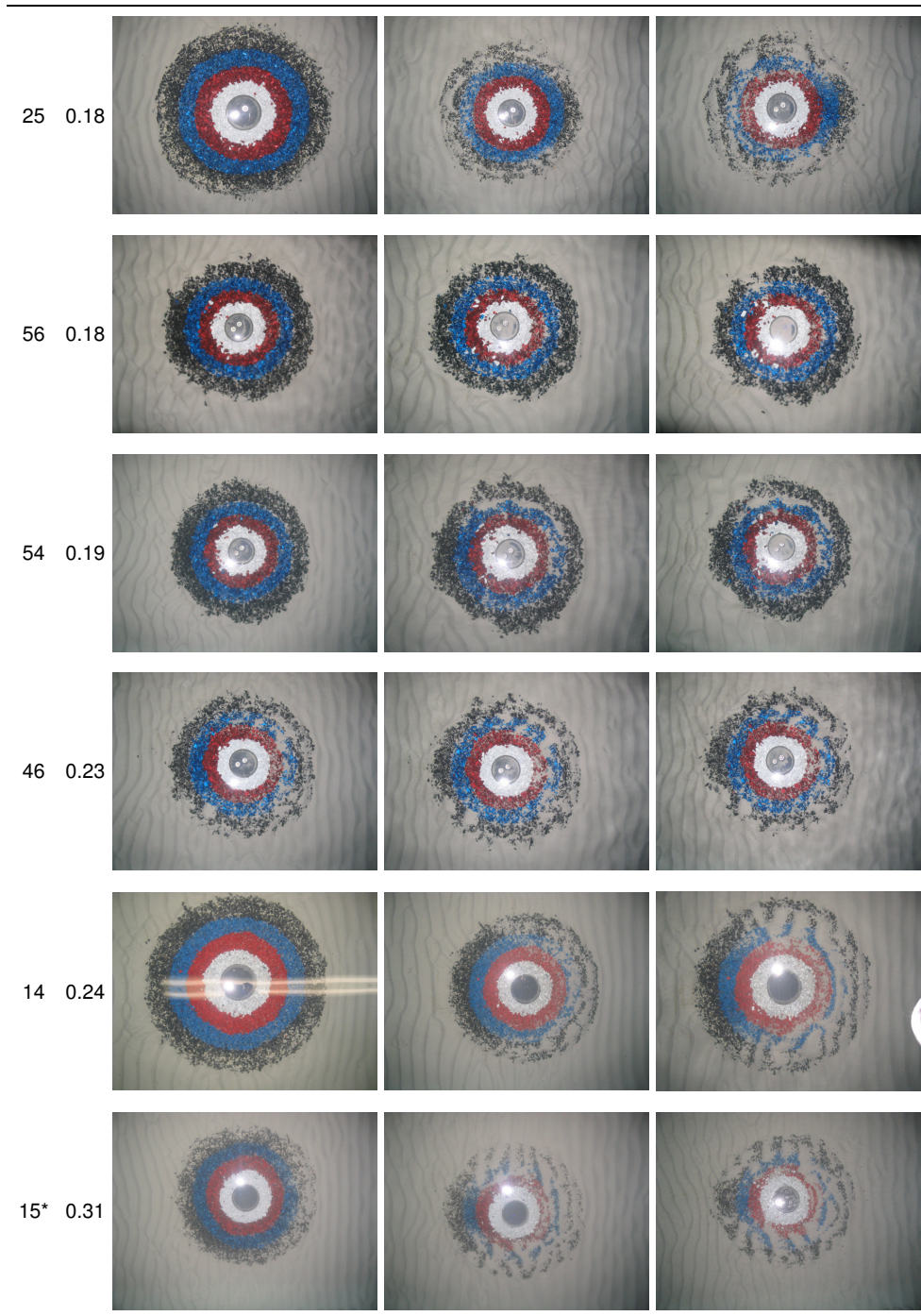
d0_40 u0_21 Hs0_16 Tp1_7 dn50 7_2 reverse current.txt

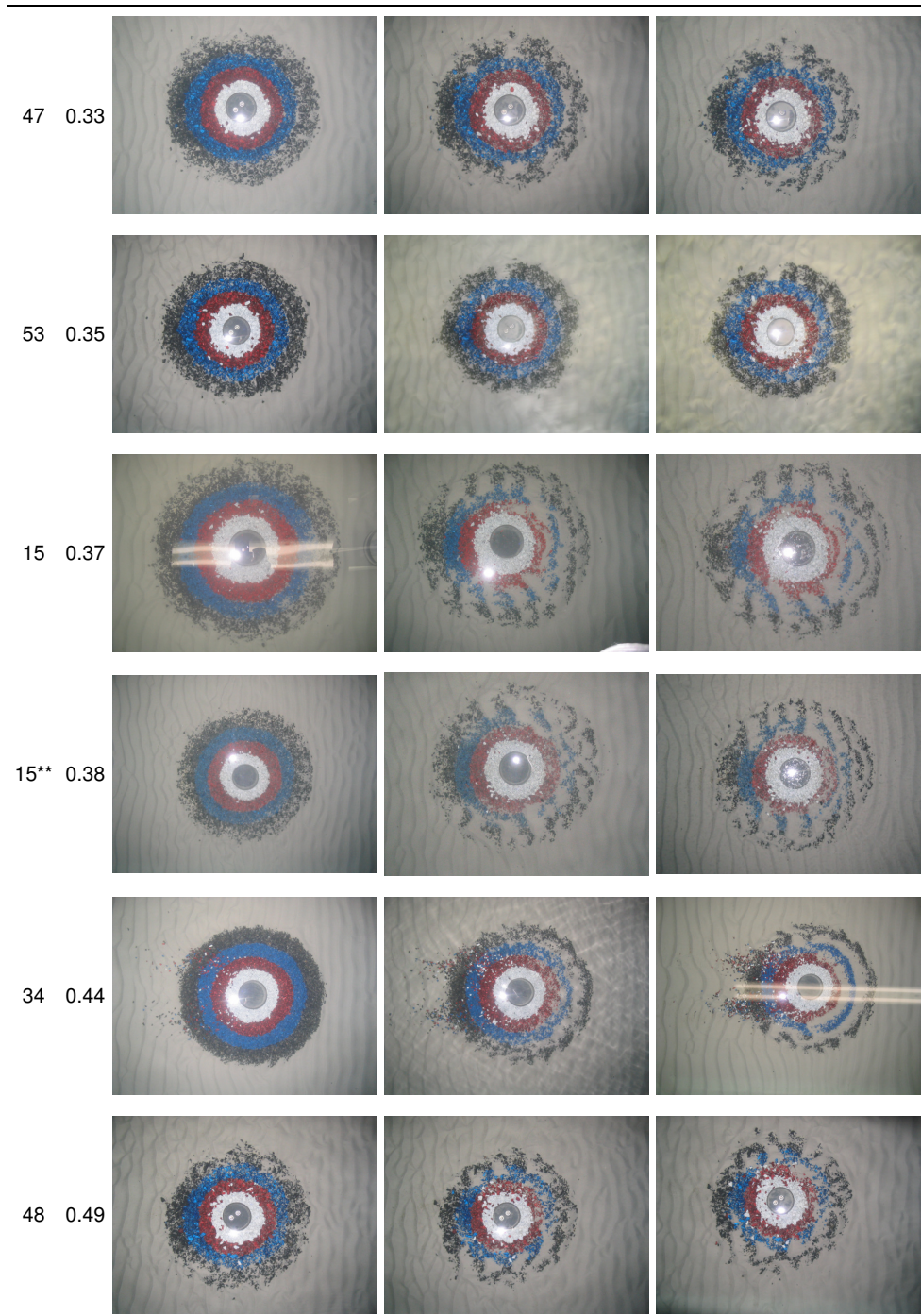
Appendix VI: Pictures of scour protection tests

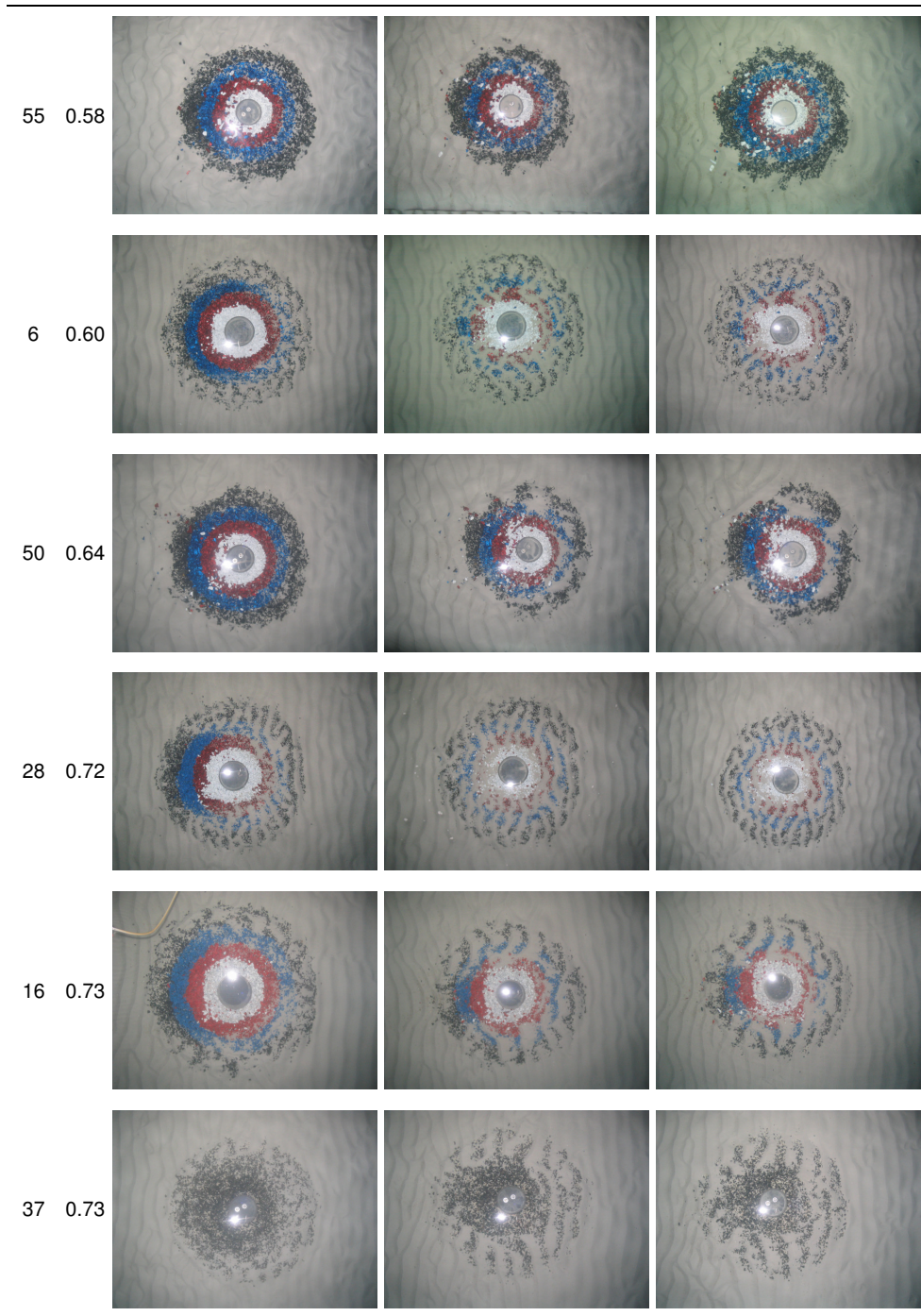
In this appendix, pictures of the top view of all scour protection tests with irregular waves are shown in Table VI.1. Pictures after 1000 waves, 3000 waves and 5000 waves are shown. The tests are shown in order of the measured damage. The damage (in volume % of eroded material) is included, as is the test number. The test matrix is given in chapter 4, Table 4-6. The pictures are also included on the DVD.

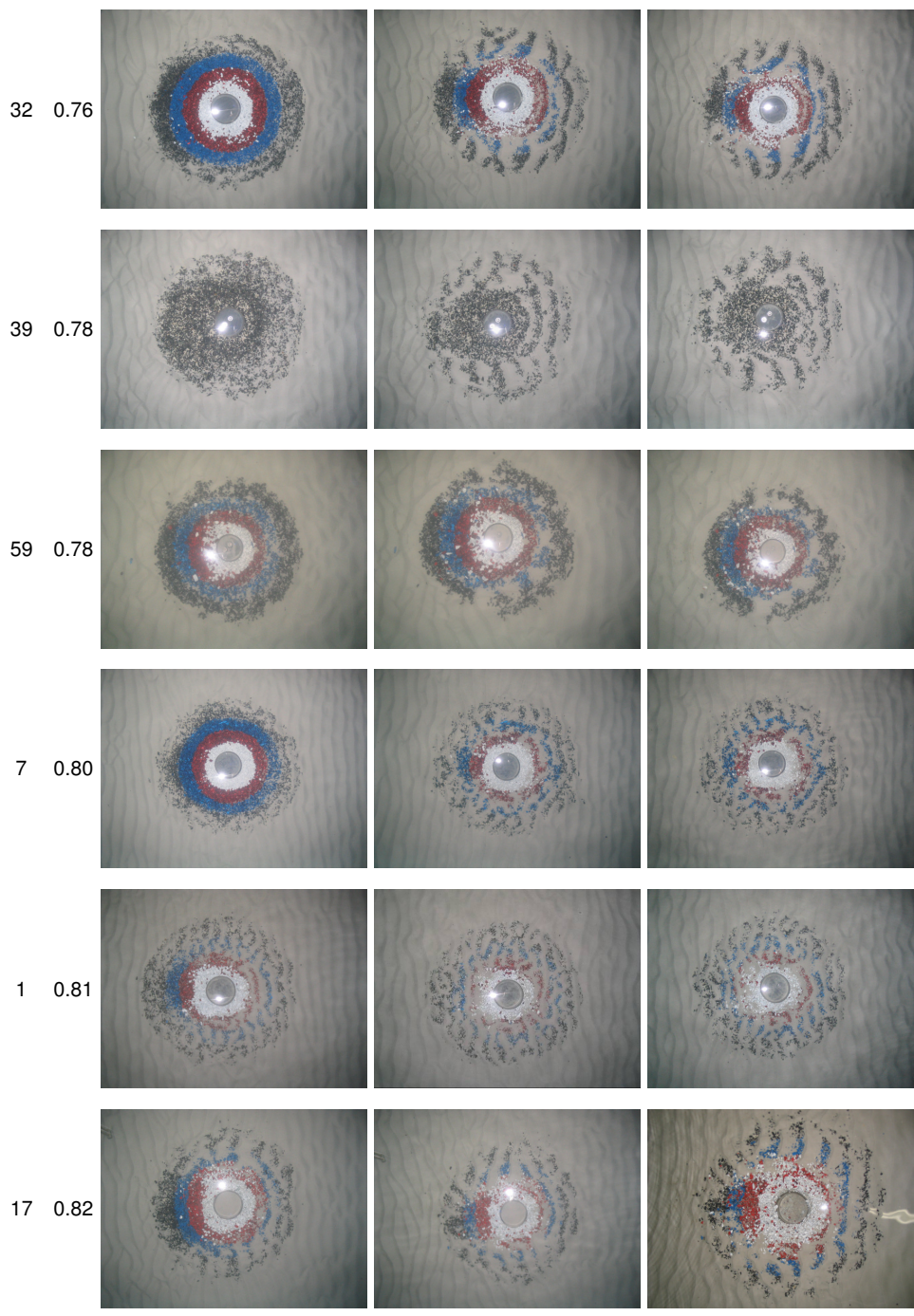
Table VI.1: Pictures of scour protection tests for increasing damage

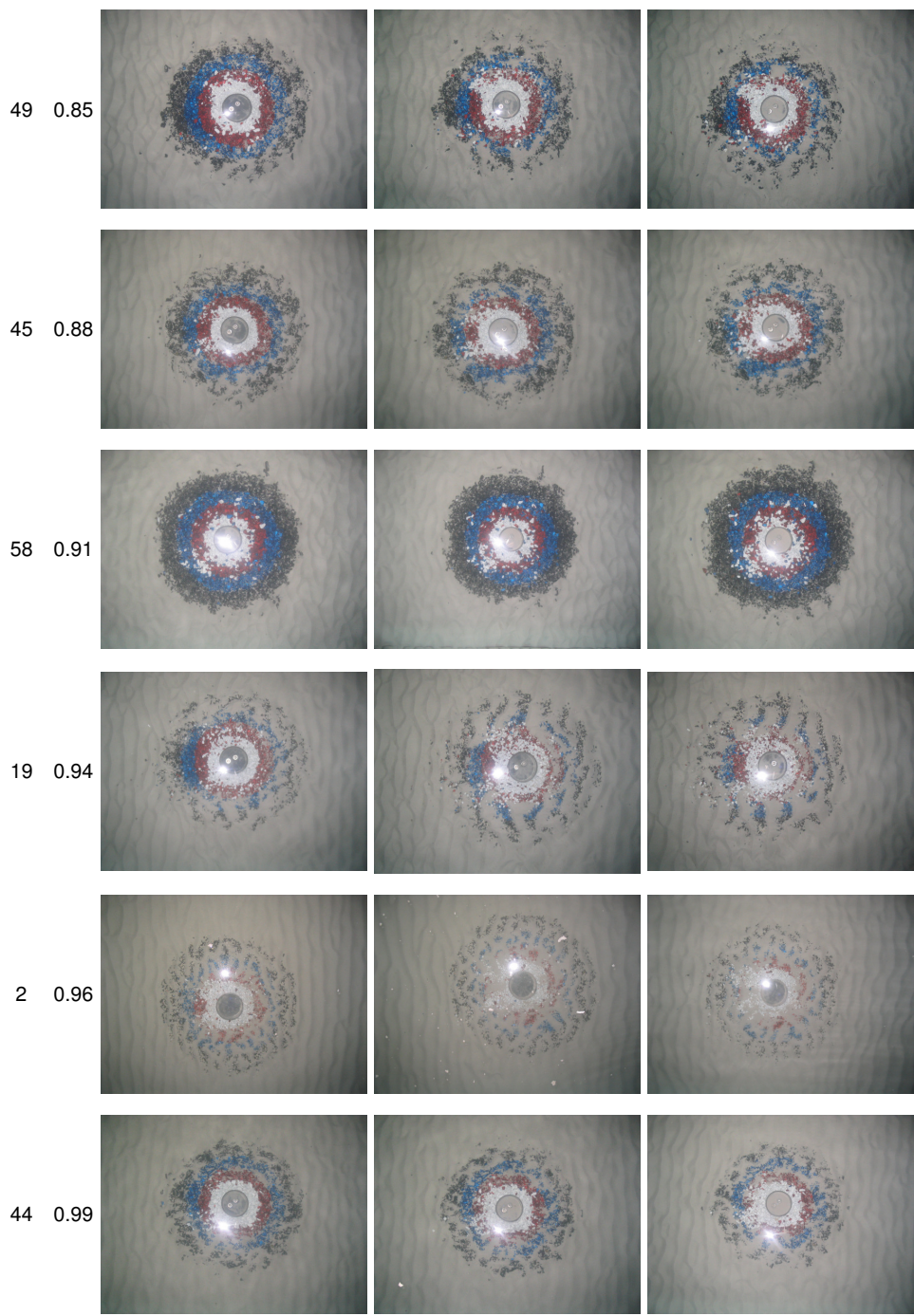
Test n°	S_{3D} [-]	Picture after 1000 waves	Picture after 3000 waves	Picture after 5000 waves
13	0.07			/
11	0.08			
5	0.11			
31	0.14			

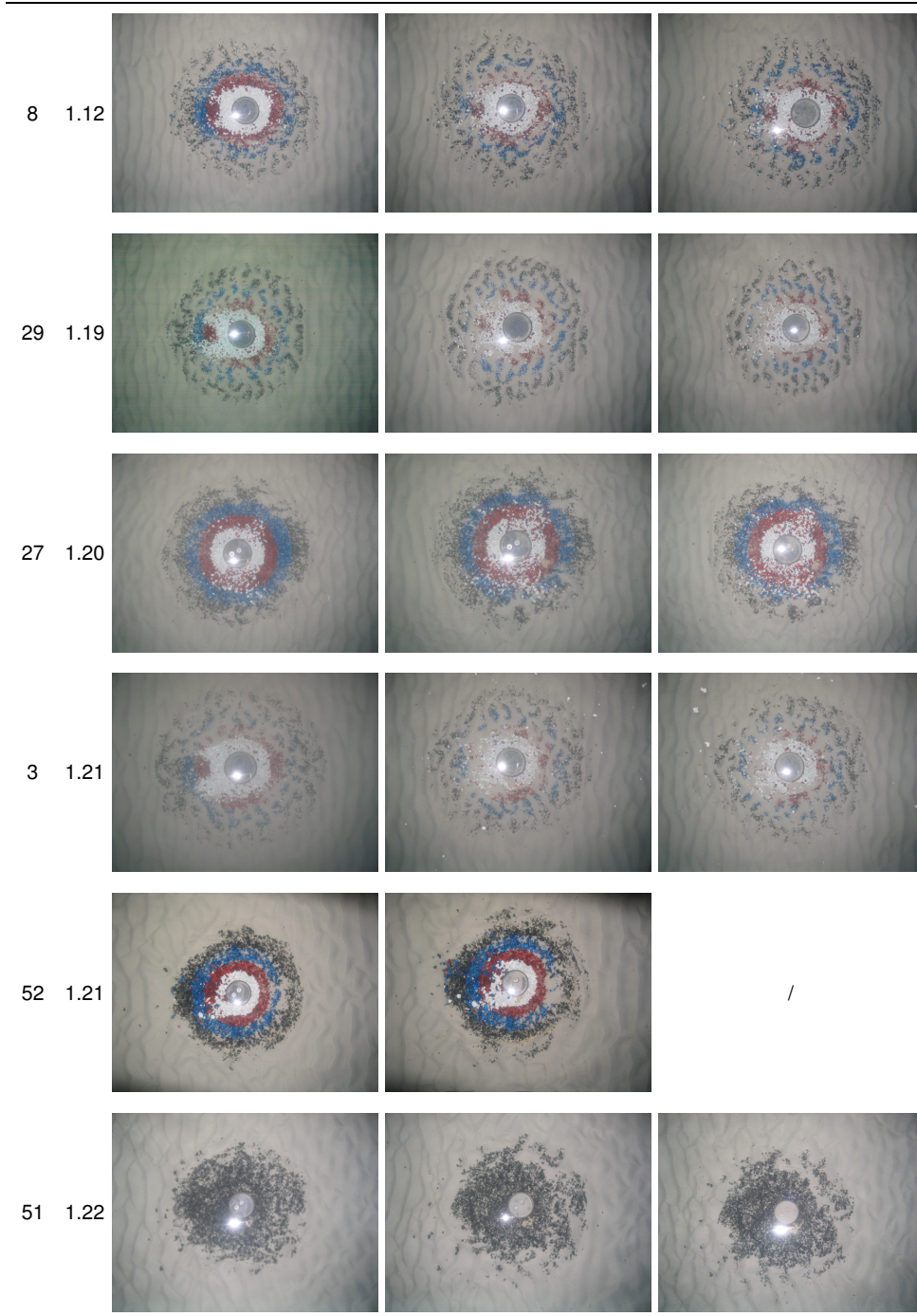


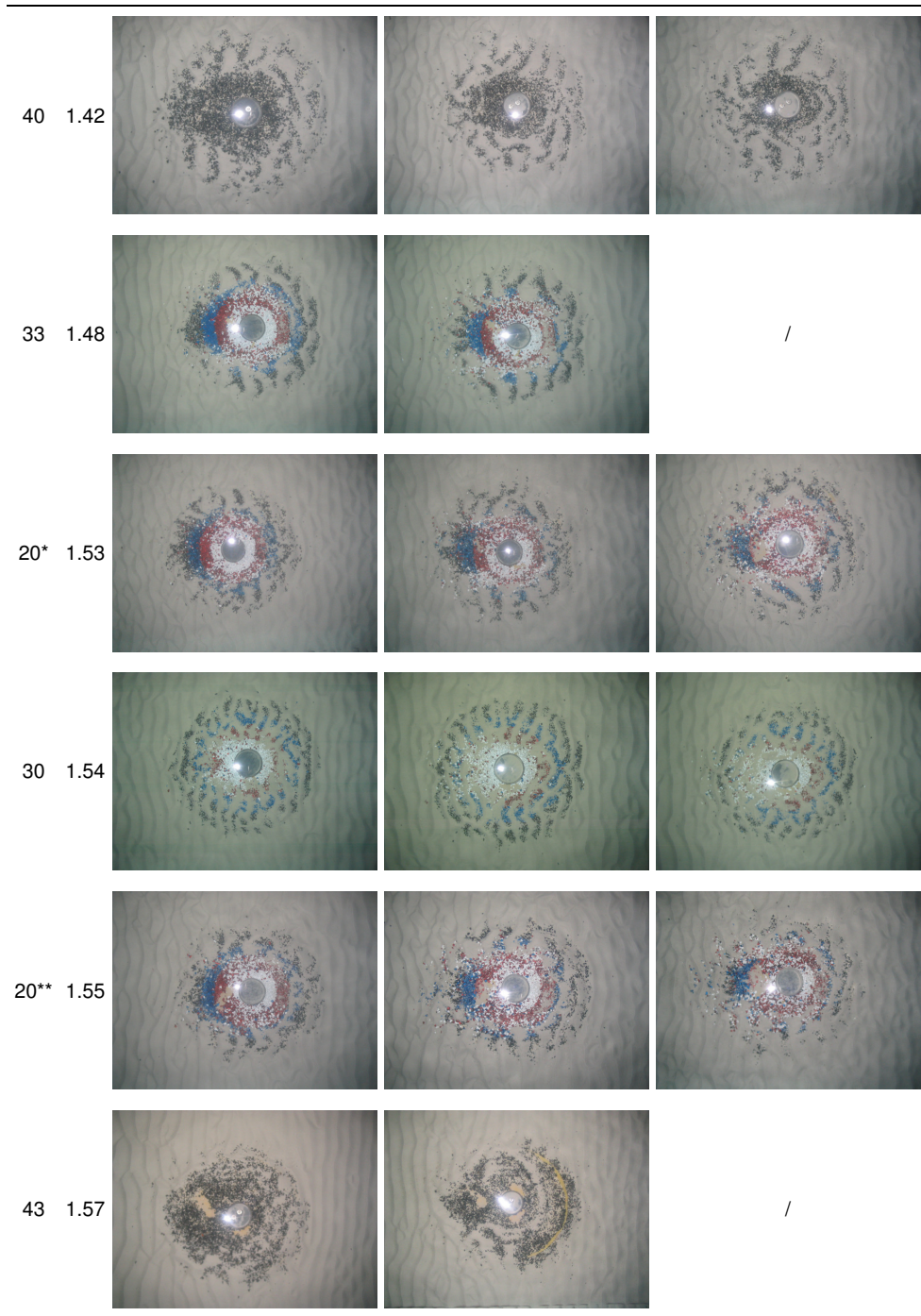


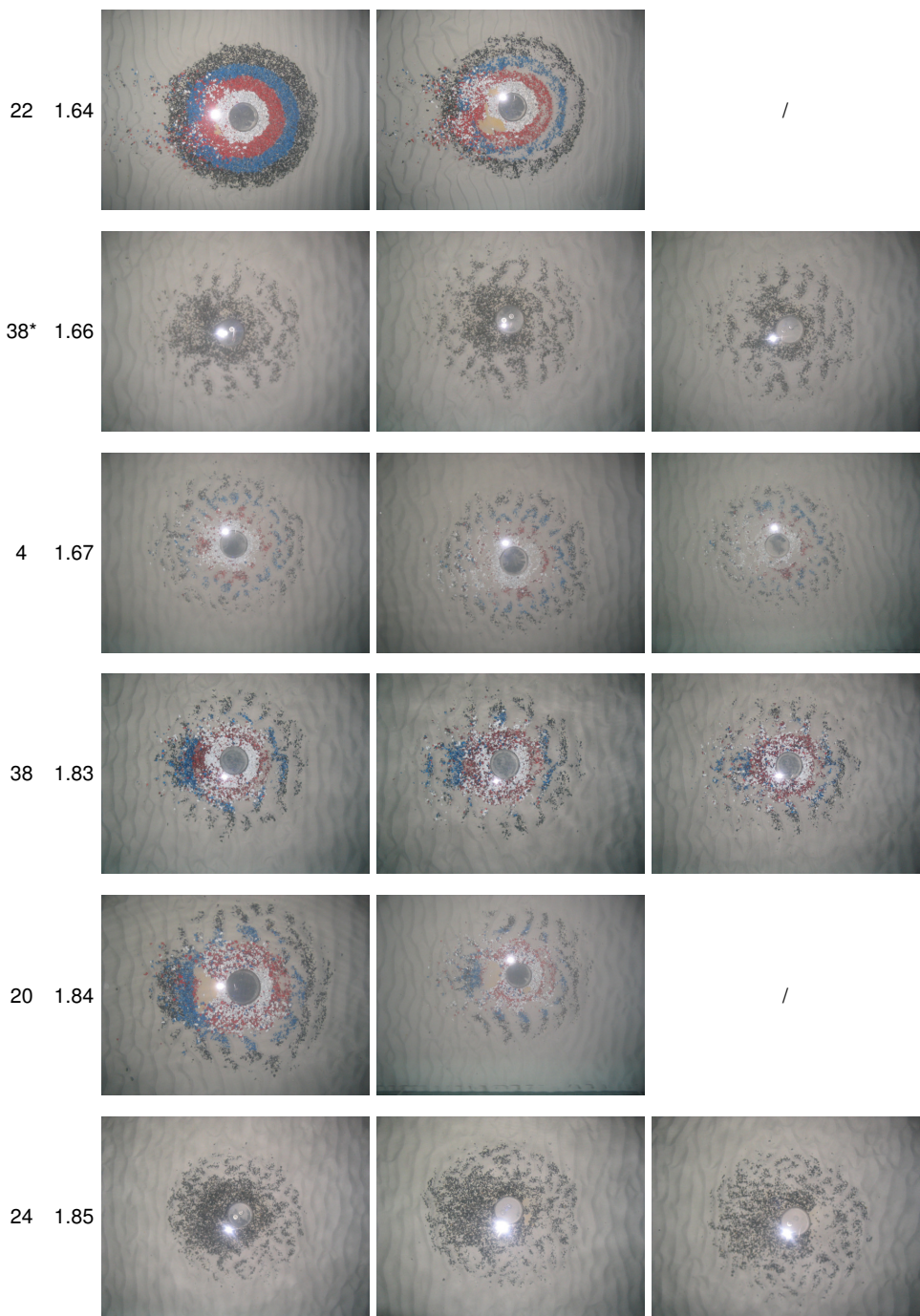


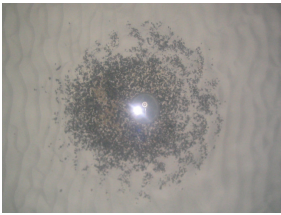
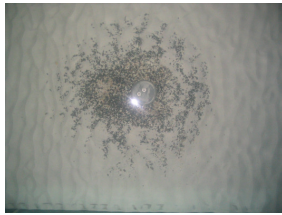

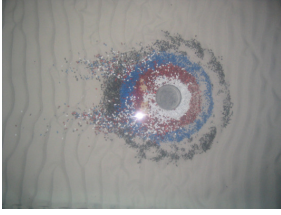
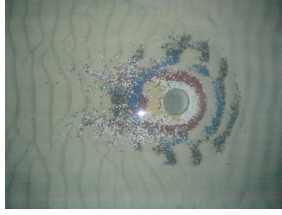
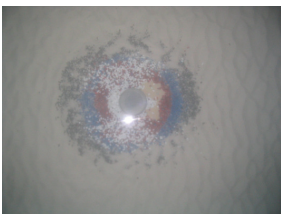
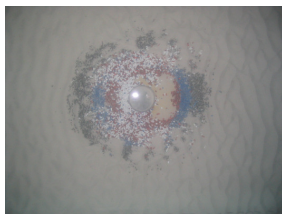










41 2.19			
35 2.33			/
36 2.39			/

Appendix VII: PIV experiments

In this appendix, more details are given on the Particle Image Velocimetry (PIV) test set-up that was used for the tests described in chapter 4, section 4.4.1.2. The PIV equipment, the set-up in both physical wave flumes and the data analysis are described below. The main advantages of the PIV technique are that it is a non-intrusive, indirect technique which can capture a whole flow field.

VII.1. PIV equipment

Particle Image Velocimetry is a powerful measuring technique to obtain instant whole flow field measurements. The working principle of the PIV technique is shown in Figure 4-78. This figure is repeated here in Figure VII-1. For the 2 dimensional PIV technique, a camera, a laser, a synchronizer and seeding particles are needed.

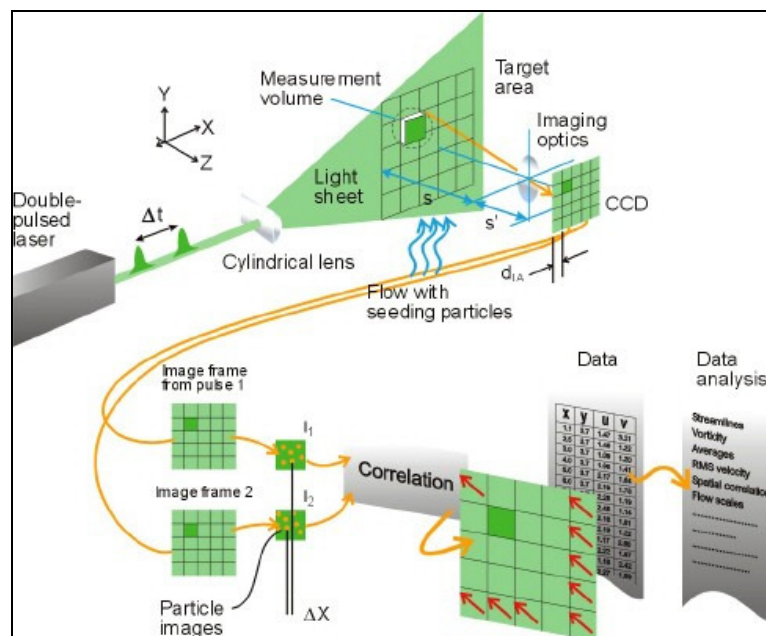


Figure VII-1: Particle Image Velocimetry, definition sketch; from Raffel et al. (1998)

VII.1.1. Seeding

Seeding particles are placed in the fluid. The particles are very small and need to fulfill two requirements. Firstly, they need to follow the flow without disturbing it, and secondly, they need to reflect the laser light, in order to be traceable by the camera. The first condition is met because the seeding particles are very small (and thus do not disturb the flow) and have a density close to the density of water (and therefore follow the water displacement very closely). The second

condition is met because the seeding particles have a coating, which increases the reflection of the laser light.

The seeding material which is used for the tests has a density of 1016 kg/m^3 , a diameter of approximately $56 \text{ }\mu\text{m}$ and a silver coating.

VII.1.2. Camera

The camera is a CCD (Charge Coupled Device) camera, which uses a chip instead of a film. This has the advantage that the data is recorded digitally, allowing to immediately process the images on a computer. Another advantage of a CCD camera is that it has a much higher light sensitivity than traditional camera's. The camera which is used is a PCO Sencicam QE 1380×1040 pixels with high sensitivity and an imaging frequency of 10fps.

VII.1.3. Laser

The laser illuminates a specific plane with two pulses. The laser light is reflected by the seeding particles and the camera captures the illuminated light sheet. The time between the two pulses determines the distance which the particles have travelled between the two images and must therefore be determined carefully. For the tests a Nd - YAG - laser is used. Light sheet optics with mirrors and prisms are used to get a thin light sheet (Figure VII-2), which illuminates only the particles in the plane of interest.



Figure VII-2: Laser arm, light sheet optic of the PIV system

VII.1.4. Synchronizer

The synchronizer provides synchronization between laser and camera. The synchronizer controls both camera and laser and can be externally triggered when a certain event occurs. In both test set-ups, the synchronizer is triggered by the wave elevation which is measured before the set-up. Each time the elevation exceeds a certain value on a rising flank of the wave, the synchronizer

gets a pulse. The synchronizer in its turn will trigger both laser and camera, with a certain time delay, adjustable by the user. The camera can only take a double image with an interval of 250ms. To obtain a measurement every 50 ms, the time delay by which camera and laser are triggered is each time increased with 50ms.

VII.2. Set-up

A drawing of the test-setup for the small wave flume (SWF) is shown in Figure VII-3, while the test set-up for the large wave flume (LWF) is shown in Figure VII-4.

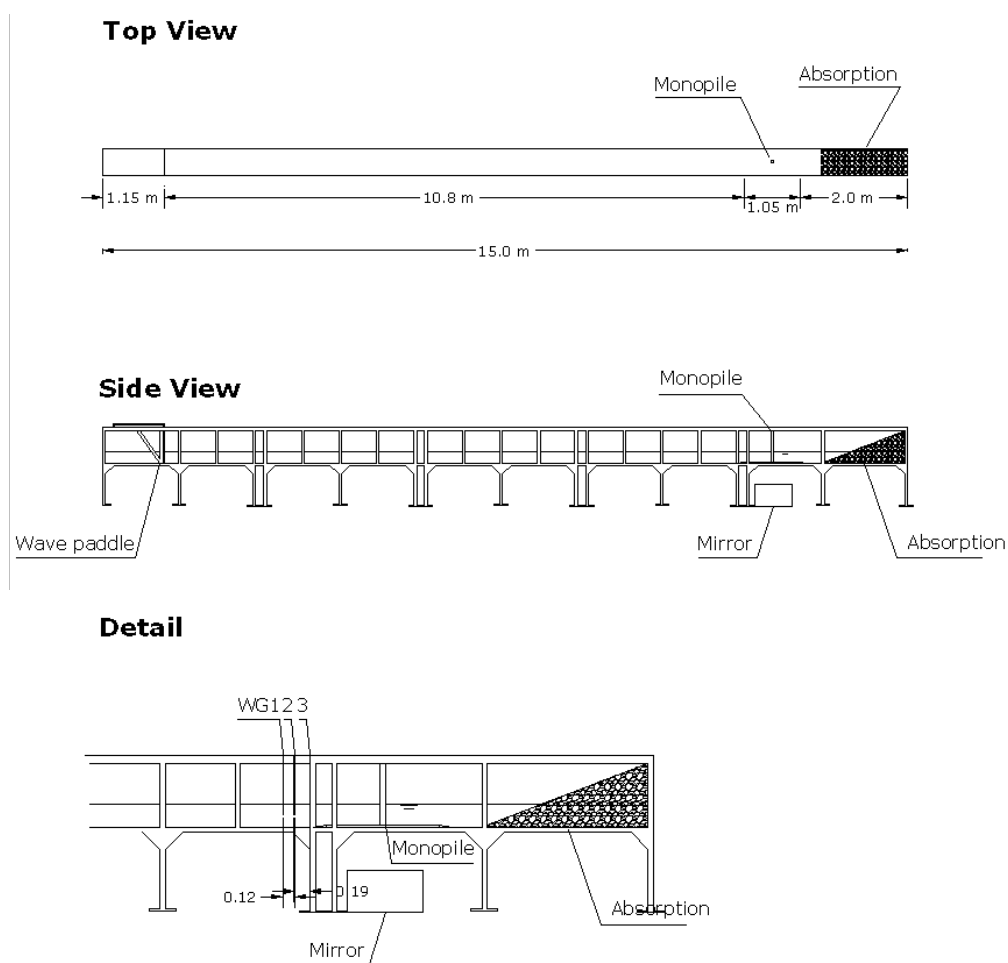


Figure VII-3: PIV set-up in the small wave flume (SWF)

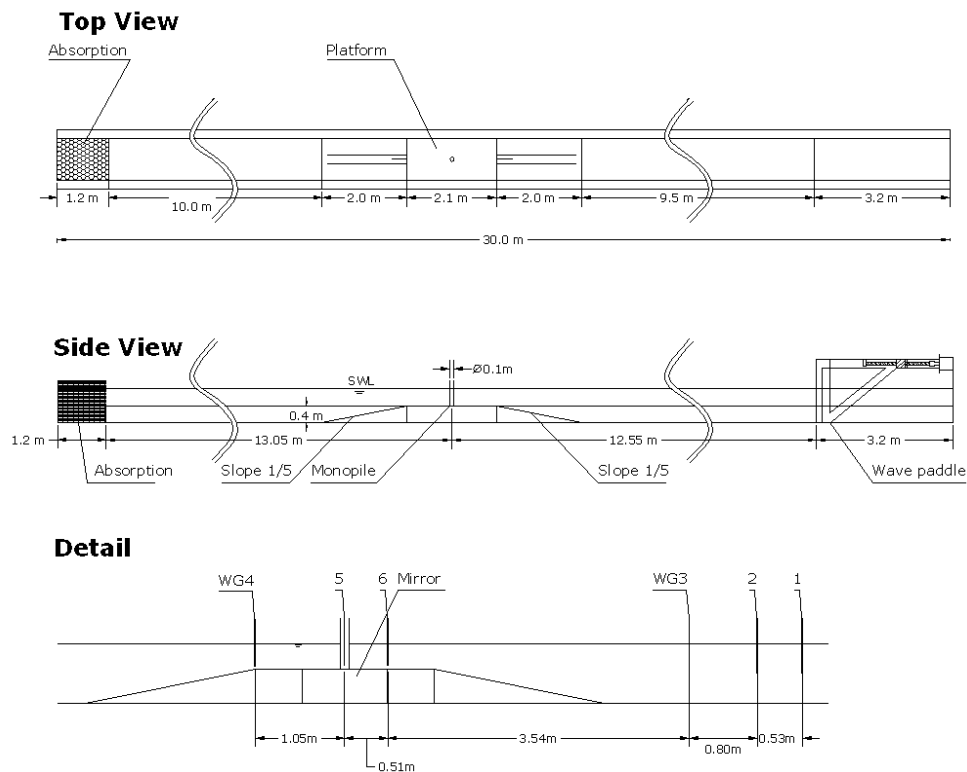
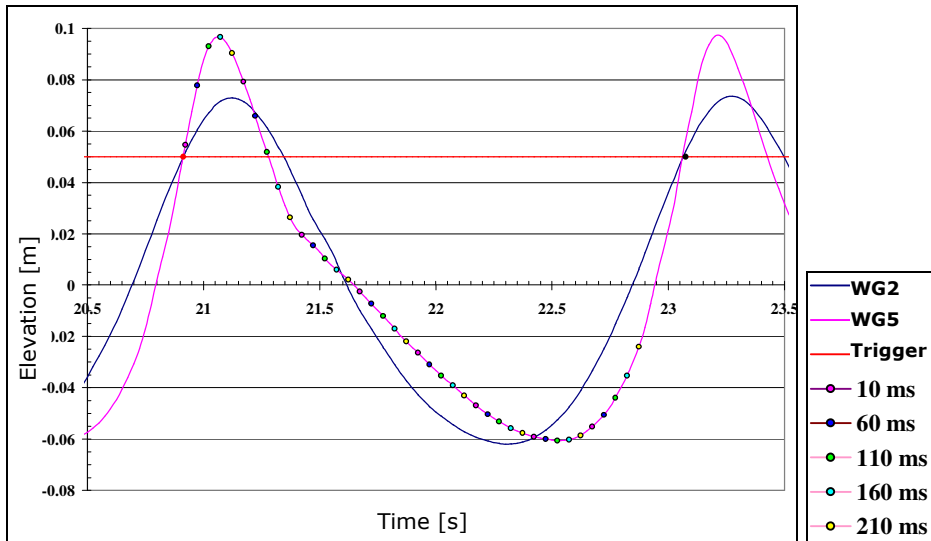


Figure VII-4: PIV set-up in the large wave flume (LWF)

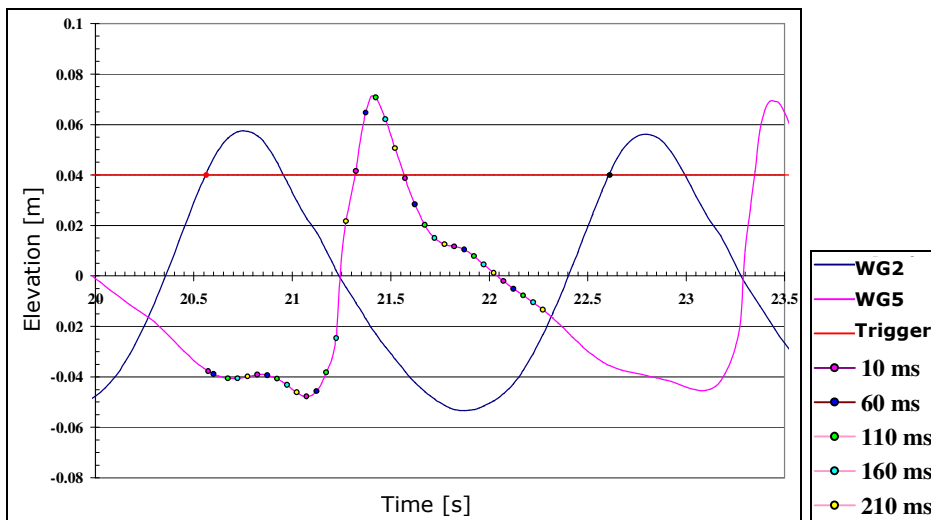
Four important elements can be distinguished: the wave gauges, the pile, the mirror and the PIV related equipment.

VII.2.1. Wave gauges

The wave height is measured with resistance type wave gauges (WG) at the locations shown in Figure VII-3 and Figure VII-4. As mentioned above, one of the wave gauges triggered the synchronizer which in his turn triggers the laser and camera. This was done by sending a signal from the wave gauge to the synchronizer at the exact moment the elevation exceeded 4cm on the rising flank of the wave. The location of the wave gauge which triggers the synchronizer determines the location of the wave near the pile at the moment of triggering. This is illustrated in Figure VII-5, which shows the wave at the location of the wave gauge used for triggering and at the location of the pile together with the moments at which laser and camera were triggered for the tests in the largest wave flume.



Non-breaking wave



Breaking wave

Figure VII-5: Elevation measured at the trigger wave gauge and at the location of the pile

The purpose of the tests is to measure the flow field around the base of the pile during an entire wave period. An interval of 50ms for the successive images was aspired, resulting in a measurement-frequency of 20Hz. As the time in between two captures needs to be at least 250ms due to the limitation of the camera to export the images to the computer, this could only be achieved by repeating the tests several times while adding a time delay to the triggering of 50ms. This implies that the moment of triggering needed to be very accurate in order to guarantee repeatability of the tests. This was accomplished by using a very high frequency to measure the wave elevation, resulting in an accuracy of 1ms.

VII.2.2. Structure and PIV equipment

A vertical cylindrical pile was placed in the flumes in front of a glass section. The location of the pile in the wave flumes is shown in Figure VII-3 and Figure VII-4. For the tests in the small wave flume, a dark tent was built around both the wave flume and the PIV set-up to avoid interference due to direct sunlight (Figure VII-8). For the same reason the complete room was darkened by covering the windows while testing in the large wave flume.

Both the flow field in a horizontal plane just above the bottom (approximately 0.5 - 1 cm above the bottom), and the flow field in the vertical plane through the centre of the pile are captured. The SWF has both plexiglass side walls and a plexiglass bottom. The experimental test set-up for the images of the horizontal flow field in the SWF is shown in Figure VII-6: images are captured using a mirror, positioned underneath the wave flume. As the LWF only has one vertical glass wall a different set-up had to be used, with under water light-sheet optics (behind the pile) and a mirror, placed on the bottom of the wave flume, as shown in Figure VII-7. This means that in the large wave flume, a platform had to be built in order to position the mirror underneath the pile. In the small wave flume, a platform was only used to create wave breaking near the pile. The test set-up for the images in the vertical field are shown in Figure VII-8 and Figure VII-9 for the SWL and the LWF respectively. In the SWF, the laser optics are placed underneath the flume. As this is not possible for the LWF, the mirror had to be used to direct the light in a vertical sheet through the centre of the pile.

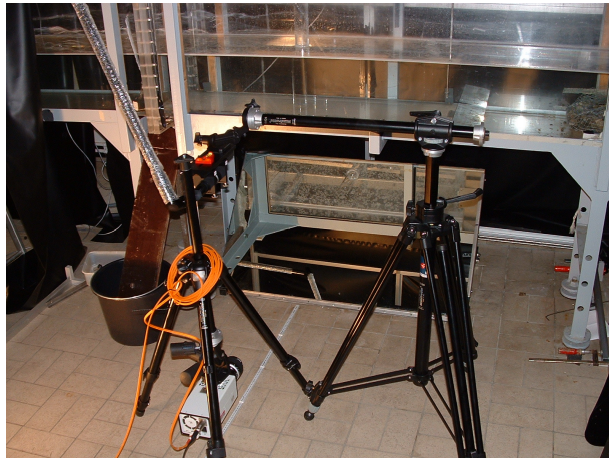


Figure VII-6: Set-up for capturing the flow field around the base of the vertical pile in the small wave flume



Figure VII-7: Set-up for capturing the flow field around the base of the vertical pile in the large wave flume: under water light sheet optics (left) and camera position, pile and mirror (right)

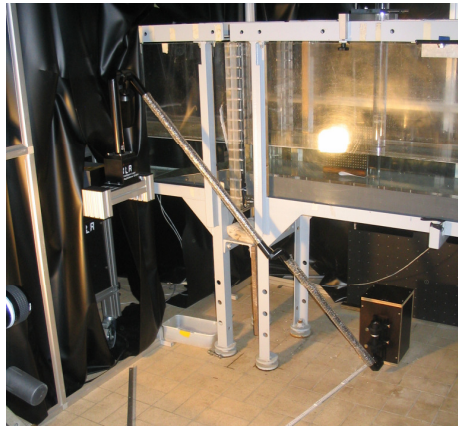


Figure VII-8: Set-up for the flow field in a vertical field through the centre of the vertical pile in the small wave flume

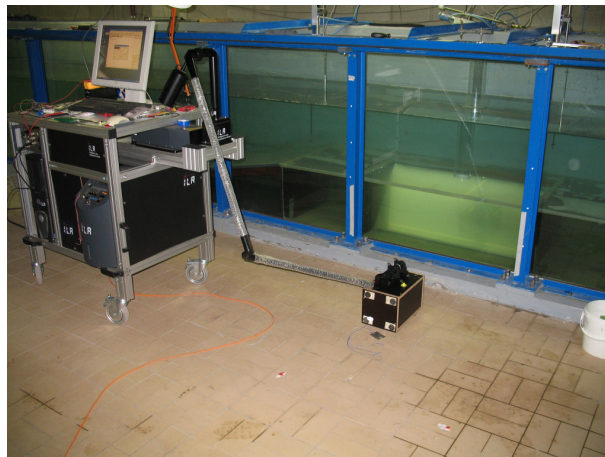


Figure VII-9: Set-up for the flow field in a vertical field through the centre of the vertical pile in the large wave flume: light sheet optics, pile and mirror

VII.3. Image capturing

The times at which images were captured are given in Table VII.1 and Table VII.2. Table VII.2 can be compared with Figure VII-5. As the breaking wave has a smaller wave period than the non-breaking wave in both cases, less images were sufficient to capture a complete wave period for the breaking wave (indicated in bold in the two tables).

Table VII.1: Time of image capture, small wave flume

Image series	trigger delay [ms]	Time of image capture [ms]					
1	10	10	260	510	760	1010	1260
2	60	60	310	560	810	1060	1310
3	110	110	360	610	860	1110	1360
4	160	160	410	660	910	1160	1410
5	210	210	460	710	960	1210	1460

Table VII.2: Time of image capture, large wave flume

Image series	trigger delay [ms]	Time of image capture [ms]								
1	10	10	260	510	760	1010	1260	1510	1760	
2	60	60	310	560	810	1060	1310	1560	1810	
3	110	110	360	610	860	1110	1360	1610	1860	
4	160	160	410	660	910	1160	1410	1660	1910	
5	210	210	460	710	960	1210	1460	1710	1960	

VII.4. Repeatability

As indicated above, the same test had to be repeated to obtain images with an interval of 50ms. Furthermore, each measurement was repeated three times and the average of the three measurements was used to calculate the flow field around the pile. This was done to improve the validity of the calculated velocity vectors. Repeatability of the tests was therefore one of the main requirements. The repeatability of the tests was estimated by running the same wave 10 times for all cases. The average measured value and the variance (in % of the average wave height) are given in Table VII.3 for all tests. As could be expected, both in the large as in the small wave flume, the repeatability is higher for the non-breaking wave than it is for the breaking wave. This can be explained by the fact that wave breaking is a turbulent event, which has therefore a random character. The repeatability in the large and small wave flume are comparable.

Table VII.3: Time of image capture, small wave flume

	Non-breaking wave		Breaking wave	
	SWF	LWF	SWF	LWF
water depth at the pile d [m]	0.2	0.4	0.12	0.22
H_{average} [m]	0.11	0.182	0.089	0.124
Standard deviation [%]		0.16		0.84

VII.5. Data analysis

To analyze the data, a series of processing needs to be done. The processing tree which was used to analyze the data is shown in Figure VII-10. The processing is done in de VIDPIV software, which is a software program developed by ILA (Intelligent Laser Applications) GmbH in Germany.

In the software, the images are loaded with the **Importation (Dual)** node, which loads the double image, captured by the camera.

The node **Linear mapping** is used to indicate the distances in the flow field. This is done by the aid of an image of a calibration target which is placed exactly in the laser sheet before a test series. Figure VII-12 gives the calibration image for the large wave flume, horizontal velocities. Note that the pile is removed in order to place the calibration target at the correct position (in the plane of the light-sheet which is generated by the laser).

In the node **Image annotations**, the areas where no flow can be expected (pile area, edges) can be specified and the velocities are not calculated in these zones, leading to a decrease of the computing time. An example is given in Figure VII-11

The node **Regular timing** is used to specify the distance between the two image captures (1.5 or 2ms). Both the node **Image annotations** and the node **Regular timing** are needed to translate the displacement into velocity vectors.

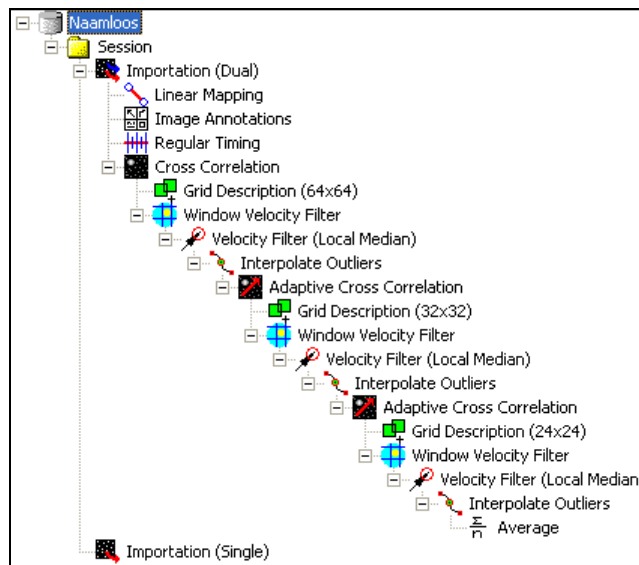


Figure VII-10: Processing tree for the PIV data

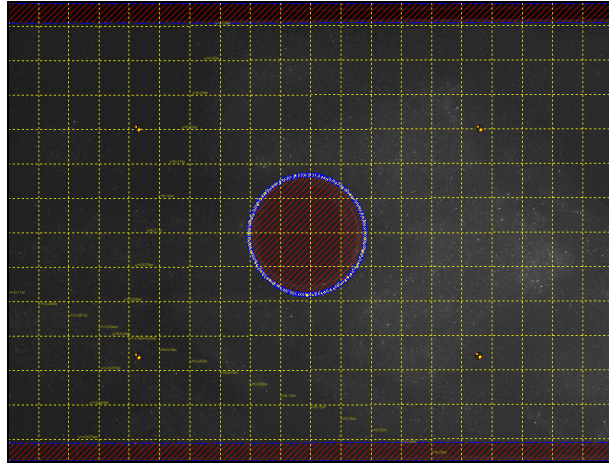


Figure VII-11: Image annotations: identifying the zones which do not require velocity calculations (pile, edges)

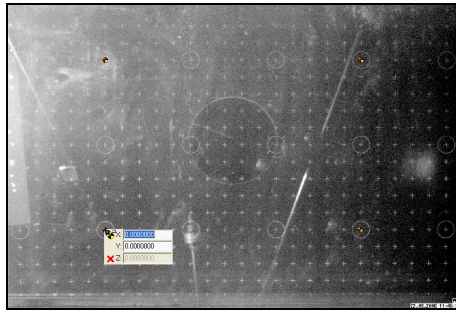


Figure VII-12: Calibration target placed at the base of the pile, horizontal flow field, LWF

The node **Cross correlation** calculates the displacement of the seeding particles between the two images. Cross correlation is the usual method for the evaluation of two images separated by a small finite time step - each with only one illumination of the seeded flow (Vansteenkiste (2007)). The assumption is that the lightened particles within a user defined interrogation volume are all displaced over the same distance d_s , which depends on the flow velocity. For a certain seeding pattern in the flow, a peak is found in the correlation function for a displacement d_s (Figure VII-13).

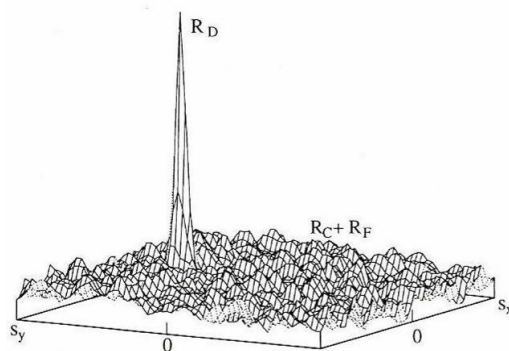


Figure VII-13: Cross correlation peak

After the initial cross correlation, the following steps are repeated, leading to an iterative calculation of the velocities in the flow field: **Window Velocity Filter**, **Velocity Filter (Local Median)**, **Interpolate Outliers**, **Adaptive cross correlation**. The velocity filters, filter out the velocity vectors which deviate too much from a given velocity window (**Window Velocity Filter**) or the adjacent velocity vectors (**Local Median**). These vectors are then excluded from the calculated vector field. The node **Interpolate Outliers** calculates an interpolated value for the excluded velocity vectors, based on adjacent vectors. After this, an **Adaptive cross correlation** is performed, which is basically a new cross correlation which uses the previously calculated velocity vectors as initial estimate for the displacement.

As mentioned above, an average of three images is taken to improve the validity of the calculated values, this is done with the **Average** node.

All processed images and the results of the tests are discussed in Smits (2005) and Vansteenkiste (2007). As an example, the vertical flow field and the horizontal flow field for the non-breaking wave in the LWF is given in Figure VII-14. The location of the wave elevation at the location of the pile, the vector field and a contour chart are given in Figure VII-14.

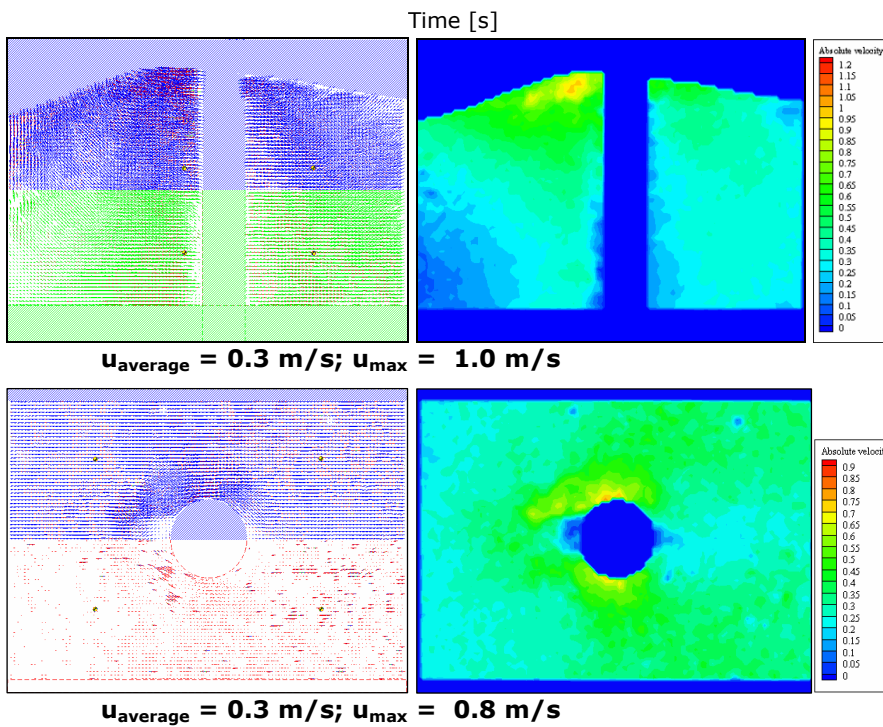
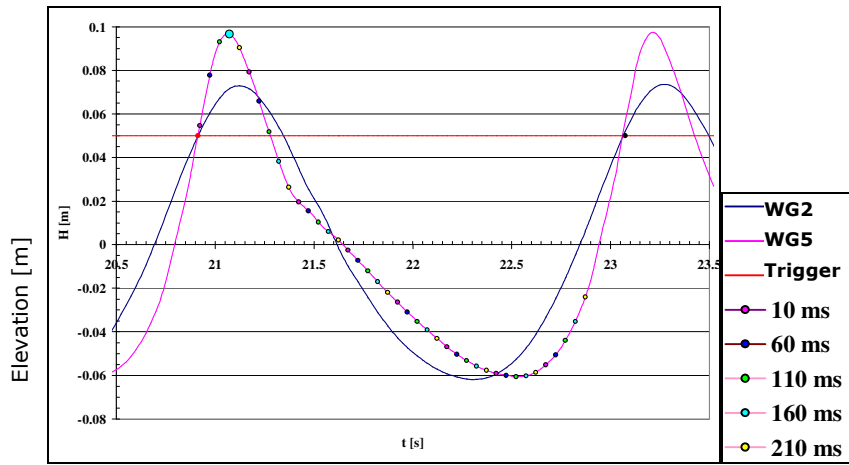


Figure VII-14: Vertical and horizontal flow field in the wave crest, non-breaking wave, LWF

References

- Raffel, M., Willert, C. and Kompenhans, J., 1998. Particle Image Velocimetry, a practical guide. Springer-Verlag Berlin Heidelberg.
- Smits, J., 2005. Bepalen van het stromingsprofiel rond een paal bij golfwerking met behulp van Particle Image Velocimetry. MSc Thesis, Ghent University, Ghent, 157 pp.
- Vansteenkiste, T., 2007. Vergelijken van PIV (Particle Image Velocimetry) metingen van het stromingsprofiel rond een paal met golven op grote en kleine schaal. MSc Thesis, Ghent University, Ghent, 161 pp.

